

Microscopic Mechanisms of Magnetism and Superconductivity Studied from First Principle Calculations

By

ZHIPING YIN
B.S. (Peking University) 2005

DISSERTATION

Submitted in partial satisfaction of the requirements for the degree of

DOCTOR OF PHILOSOPHY

in

PHYSICS

in the

OFFICE OF GRADUATE STUDIES

of the

UNIVERSITY OF CALIFORNIA

DAVIS

Approved:

Committee in Charge
2009

To my parents and Lu

Microscopic Mechanisms of Magnetism and Superconductivity
Studied from First Principle Calculations

Abstract

Density functional theory (DFT) based electronic structure calculations have been widely used to study, and have successfully described, various properties of many condensed matter systems. In my research, I have applied DFT to study the microscopic mechanisms of magnetism and superconductivity in several strongly correlated rare earth materials, conventional superconductor yttrium and calcium under high pressure, and the newly discovered iron-pnictide superconductors.

This dissertation is divided into 5 chapters. After a short introduction to electronic structure calculations and several condensed matter systems of current interests in chapter one, I briefly describe DFT, linear response method, tight binding approach and Wannier functions in chapter two.

Chapter three is devoted to three strongly correlated rare-earth materials. First, the evolution of the magnetic moment and various features of the electronic structure of fcc Gd metal under pressure are studied using the LDA+U correlated band method. I found that the Gd magnetic moment is very robust under pressure, even up to 500 GPa. The occupation of $4f$ orbitals is found to increase under pressure, which is consistent with experimental x -ray spectra. Then I apply the LDA+U method to study the chemical bonding and changes in $4f$ states across the lanthanide series in RB_4 (R = rare earth) compounds and find that a set of boron bonding bands are well separated from the antibonding bands. The trends in the mean $4f$ level for both majority and minority, and occupied and unoccupied, states are presented and interpreted. At last, I calculate the electronic structure of a heavy fermion

compound YbRh_2Si_2 in a relativistic framework using the LDA+U+SO method. The calculated band structure manifests a $4f^{13}$ spin-polarized configuration of Yb atom, leaving the unoccupied state at 1.4 eV above the Fermi energy. The calculated Fermi surfaces are nearly identical to experimental Fermi surfaces obtained from angle-resolved photoemission spectra (ARPES).

The electronic structures and lattice dynamics of two conventional elemental superconductors yttrium and calcium under pressure are discussed in chapter 4, using DFT and linear response calculations. In both systems, strong electron-phonon coupling ($\lambda > 1$) is found to be responsible for the rather high T_c (up to 20 K in Y and 25 K in Ca) over a wide pressure range. The contributions to λ are found to come from only a few specific vibration modes restricted in a small part of the Brillouin zone (BZ). The observed “simple cubic” structure of Ca at room temperature under 32-109 GPa pressure is badly unstable based on linear response calculations. However, the “sc” x -ray diffraction pattern can be explained as a locally noncrystalline, highly anharmonic phase derived from various structures, which are thermally accessible at room temperature, according to the small calculated differences in enthalpy at $T=0$ K of four sc-related (non-close-packed) structures, whose enthalpies are lower than the sc phase.

In the last chapter, I study the electronic structures of the newly discovered iron-pnictide superconductors. I first study LaFeAsO and find that the As position is crucial in determining the band structure. The stripe antiferromagnetic ordering is found to be the ground state. The effects of exchange-correlation functional, $z(\text{As})$, doping, and pressure on the electronic structure of LaFeAsO are studied and presented in details. The electronic field gradients (EFG) for all atoms in LaFeAsO are calculated and compared with available data. Then, I investigate the crucial role of

the pnictogen atom in this class and predict the structures and properties of the N and Sb counterparts that have not yet been reported experimentally. After that, I study the effect of antiphase magnetic boundary (with different densities) imposed on the stripe-AFM phase. Many experimental observations can be understood based on our calculated results, when dynamic antiphase boundaries are assumed. Finally, I try to understand the structural transitions and antiferromagnetic transitions in these compounds. I construct the Wannier functions for the Fe $3d$ orbitals and calculate the hopping parameters in tight binding approach. The resulting hopping parameters indicate that electrons in the Fe $3d_{xz}$ ($3d_{yz}$) orbital have a larger amplitude to hop in the y (x) direction rather than the x (y) direction. A weak stripe antiferromagnetism makes the spin-majority electron in Fe $3d_{xz}$ (but not the $3d_{yz}$) orbital hop in both x and y directions, which induces anisotropy, structural transition such that the lattice constant a (aligned-spin direction) is smaller than b . To take advantage of a kinetic energy gain from this additional hopping process, orbital fluctuation is favored, which reduces the ordered Fe magnetic moment in the stripe antiferromagnetic phase, consistent with experimental observations. I also find that the pnictide atom is influential to form the stripe antiferromagnetism. Interlayer hopping of Fe $3d$ electrons in the z direction may help to stabilize the ordered magnetic moment of Fe in the stripe antiferromagnetic phase.

Acknowledgments and Thanks

First of all, I would like to thank my research advisor, Prof. Warren E. Pickett. I have been working with him since Oct. 2005. Prof. Pickett is a very kind and knowledgeable person. He has guided me step by step in the research process and is an ideal advisor that I can imagine. Under his direction, I am a coauthor of 7 papers already published, one accepted for publication, and a few more to be published, in refereed journals. Without him, there wouldn't be these publications and this dissertation. I also thank him for supporting me as a research assistant most of time (including summers) in the past four years.

I would like to thank past and current group members in Prof. Pickett's group. At the early stage of my research, I got a lot of help from Deepa Kasinathan, Kwan-woo Lee, Alan B. Kyker and Erik R. Ylvisaker. I had many useful discussions with them and other group members including Quan Yin, Victor Pardo, Simone Chiesa, Hanhbidt Rhee, Brian Neal, Swapnonil Banerjee, Amandeep Kaur, and all others I forget to mention here.

I am grateful to all my collaborators including Prof. Sergey Savrasov, Prof. Francois Gygi, Dr. Sébastien Lèbegue, Dr. Myung Joon Han, Dr. Gerald Wigger, etc.

I appreciate Prof. Warren Pickett, Sergey Savrasov and Richard Scalettar to be in my dissertation committee to read and help to improve this dissertation.

At last, I would like to thank my parents, relatives and friends. Especially I thank my parents for raising me up and supporting me, my brother and sister for being there since my childhood, Jianguo Cheng and Ping Yan for sponsoring me since my college, Jianping Pan for many helps when I came to Davis, and Lu Yu for being (patient) with me in the past five years.

Contents

List of Tables	xii
List of Figures	xvii
1 Introduction	1
1.1 Electronic Structure Calculations	1
1.2 Strongly Correlated Systems	3
1.3 Conventional Superconductors	4
1.4 High T_c Superconductors: Cuprates and Iron-Pnictide Compounds	5
2 Theoretical Background	7
2.1 Density Functional Theory	7
2.1.1 The Many-Body System and Born-Oppenheimer (BO) Approximation	9
2.1.2 Thomas-Fermi-Dirac Approximation	11
2.1.3 The Hohenberg-Kohn (HK) Theorems	13
2.1.4 The Kohn-Sham (KS) Ansatz	16
2.1.5 Local (Spin) Density Approximation (L(S)DA)	20
2.1.6 Generalized-Gradient Approximation (GGA)	25
2.1.7 LDA+U Method	26
2.1.8 Solving Kohn-Sham Equations	30
2.2 Linear Response Calculations	33

2.2.1	Lattice Dynamics and Phonons	33
2.2.2	Electron-Phonon Interaction and T_c	35
2.2.3	Nesting Function	38
2.3	Tight Binding Method and Wannier Functions	39
2.3.1	Local Orbitals and Tight Binding	39
2.3.2	Wannier Functions	42
3	Strongly Correlated Systems	46
3.1	Gd	46
3.1.1	Introduction	46
3.1.2	Electronic Structure Methods	50
3.1.3	LDA+U Results	53
3.1.4	Summary	60
3.1.5	Acknowledgments	62
3.2	RB ₄	63
3.2.1	Background and Motivation	63
3.2.2	Crystal Structure	65
3.2.3	Computational Methods	69
3.2.4	General Electronic Structure	70
3.2.5	The Lanthanide Series	79
3.2.6	Summary	83
3.2.7	Acknowledgments	84
3.3	YbRh ₂ Si ₂	84
3.3.1	Introduction	84
3.3.2	Structure	86
3.3.3	Methods	88

3.3.4	Band Structure Results	89
3.3.5	Aspects of Kondo Coupling	93
3.3.6	Discussion of Bands and Fermi Surfaces	93
3.3.7	Summary	95
3.3.8	Acknowledgments	97
4	Conventional Superconductors	98
4.1	Introduction to Superconductivity	98
4.2	Yttrium under Pressure	102
4.2.1	Introduction	102
4.2.2	Structure and Calculation Details	104
4.2.3	Electronic Structure under Pressure	105
4.2.4	Results and Analysis	109
4.2.5	Summary	117
4.2.6	Acknowledgments	120
4.3	Calcium under Pressure	120
4.3.1	Introduction	120
4.3.2	Comparison to Related Metals	122
4.3.3	Objective of this Study	124
4.3.4	Computational Methods	125
4.3.5	Simple Cubic Calcium	127
4.3.6	$\bar{I}43m$ Ca	128
4.3.7	Other Possible Structures	137
4.3.8	Enthalpy and Competing Phases	137
4.3.9	Volume Collapse and First-order Isostructural Collapse	140
4.3.10	Stability and Lattice Dynamics	143

4.3.11	Coupling Strength and T_c	146
4.3.12	Conclusions	148
4.3.13	Acknowledgments	152
5	The Iron-based Superconductors	153
5.1	Introduction to Iron-based Superconductors	153
5.2	LaFeAsO	156
5.2.1	Background	157
5.2.2	Crystal Structure	159
5.2.3	Calculation Method	160
5.2.4	The Q_M AFM Ordering	160
5.2.5	Electronic Structure	162
5.2.6	Exchange Coupling	166
5.2.7	Influence of XC Functionals and Codes on the Electronic Structure of LaFeAsO	167
5.2.8	Effect of $z(\text{As})$ on the Electronic Structure of LaFeAsO	169
5.2.9	Effect of Virtual Crystal Doping on the Electronic Structure of LaFeAsO	172
5.2.10	Electric Field Gradients	173
5.2.11	Effect of Pressure on the Electronic Structure of LaFeAsO	176
5.2.12	Summary	179
5.2.13	Acknowledgments	180
5.3	$R\text{FeP}n\text{O}$	180
5.3.1	Background and Motivation	180
5.3.2	Overall Results	182
5.3.3	LaFePO	183

5.3.4	LaFeSbO	187
5.3.5	LaFeNO	190
5.3.6	Role of the Rare Earth Atom in <i>R</i> FeAsO	192
5.3.7	Summary	193
5.3.8	Acknowledgments	194
5.4	Antiphase Magnetic Boundary	194
5.4.1	Motivation	194
5.4.2	LDA VS. GGA	197
5.4.3	The Magnetic Moment and Hyperfine Field of Iron	199
5.4.4	The Energy Differences	199
5.4.5	The Electric Field Gradient	201
5.4.6	Summary	205
5.4.7	Acknowledgments	207
5.5	Wannier Functions	207
5.6	Tight Binding Analysis	210
5.6.1	Background and Motivation	210
5.6.2	The Fe $3d_{yz}$ and $3d_{xz}$ Bands in LaFeAsO and LaFePO	212
5.6.3	Possible Microscopic Orbital Ordering of the Fe $3d_{xz}$ and $3d_{yz}$ Orbitals	215
5.6.4	Tight Binding Hopping Parameters and Discussions	218
5.6.5	Summary	223
5.6.6	Acknowledgments	223

Bibliography **224**

List of Tables

3.1	Data on magnetic ordering in the RB_4 compounds.[112, 114, 129, 143] The columns provide the experimental ordering temperature(s) T_{mag} , the ordering temperature T_{th} predicted by de Gennes law (relative to the forced agreement for the GdB_4 compound), the orientation of the moments, and the measured ordered moment compared to the theoretical Hund's rule atomic moment (μ_B).	66
3.2	Site designations, symmetries, and atomic positions of the atoms in the RB_4 crystal.	68
3.3	Tabulation of the lattice constants and internal structural parameters used in our calculations. Considering the extreme regularity of the internal coordinates through this system, the irregularity in z_{B1} for Dy should be treated with skepticism.	69
4.1	For each volume v studied, the columns give the experimental pres- sure (GPa), the Fermi level density of states $N(0)$ (states/Ry spin), and calculated values of the mean frequency $\omega_1 = \langle \omega \rangle$ (meV), the logarithmic moment ω_{log} and second moment $\omega_2 = \langle \omega^2 \rangle^{1/2}$ (all in meV), the value of λ , the product $\lambda\omega_2^2$ (meV ²), and T_c (K). Exper- imental pressures are taken from ref. [221]. For T_c the value of the Coulomb pseudopotential was taken as $\mu^*=0.15$	115

4.2	Detailed structural data of the $\bar{I}43m$, $Pnma$, $Cmca$ and $P4_32_12$ Ca.	137
5.1	Calculated magnetic moment of Fe, the amounts of total energy per Fe lie below nonmagnetic state of FM, Q_0 AFM and Q_M AFM states from FPLO7 and Wien2K with different XC functionals of LaFeAsO with experimental structure. Positive ΔEE means lower total energy than NM state.	169
5.2	Calculated magnetic moment of Fe, total energy relative to the non-magnetic (ferromagnetic) states of NM/FM, Q_0 AFM and Q_M AFM of LaFeAsO with $z(\text{As})= 0.150$ (experimental), 0.145, and 0.139 (optimized) from FPLO7 with PW92 XC functional.	170
5.3	The EFG of Fe in LaFeAsO with NM, FM and Q_M AFM states at different doping levels from Wien2K with PBE(GGA) XC functional. The unit is 10^{21} V/m ² .	175
5.4	The EFG of As in LaFeAsO with NM, FM and Q_M AFM states at different doping levels from Wien2K with PBE(GGA) XC functional. The unit is 10^{21} V/m ² .	175
5.5	Structural parameters of LaFe P_n O ($P_n = \text{N, P, As, or Sb}$), as obtained experimentally for LaFePO[319] and LaFeAsO[191] or from our calculations for LaFeNO and LaFeSbO. Length units are in Å, $z(\text{La})$ and $z(P_n)$ are the internal coordinate of the lanthanum atom and the pnictide atom, and “Sum” means the sum of Fe covalent radius and the P_n covalent radius, which is quite close to the calculated value in all cases.	183

5.6	Calculated magnetic moment of Fe, total energy relative to the non-magnetic (ferromagnetic) states of Q_0 AFM, and Q_M AFM states of $LaFePnO$ from FPLO7 with PW92 XC functional.	183
5.7	Optimized structure parameters for $LaFeSbO$ at several volumes. The accuracy for c/a is within 0.3%, and within 0.8% for $z(La)$ and $z(Sb)$. A later calculation in the Q_M AFM phase using PBE XC functional gives $a= 4.196 \text{ \AA}$, $c= 9.296 \text{ \AA}$, $z(La)=0.128$, $z(Sb)=0.168$ at ambient pressure. ($V=1.150 V_0$.)	188
5.8	Calculated magnetic moment of Fe, total energy relative to the non-magnetic (ferromagnetic) states of Q_0 AFM and Q_M AFM with the optimized structure of $LaFeSbO$ at several volumes from FPLO7 with PW92 XC functional. Upper part: $z(Sb)$ is optimized. Lower part: $z(Sb)$ is optimized and shifted.	189
5.9	Calculated magnetic moment of Fe in $LaFeNO$, total energy relative to the nonmagnetic (ferromagnetic) states of Q_0 AFM and Q_M AFM with the optimized structure at several volumes, but shifted $z(N)$ up by 0.011, as a compensation PW92 does to $LaFeAsO$, where PW92 underestimates $z(As)$ by 0.011.	191
5.10	Collection of the lattice constants a (\AA) and c (\AA), volume V (\AA^3 of the primitive cell, T_c onset s (onset, middle, and zero, in K) of $RFeAsO$ reported from experiments.	193

- 5.11 The experimental magnetic moment of Fe m_{Fe} (in unit of μ_B) and the hyperfine field B_{hf} (in unit of Tesla) for Fe, and values calculated in the SDW and D-SDW ordered phases, using Wien2K with PW91 for the MFe_2As_2 (M =Ba, Sr, Ca), LaFeAsO and SrFeAsF compounds. The experimental values are in all cases much closer to the D-SDW values (with its maximally dense antiphase boundaries) than to the SDW values. [281, 340, 337, 335, 336, 343, 344, 345] For the Fe magnetic moment, results from both FPLO (denoted as FP) and Wien2k(denoted as WK) are given. Because these methods (and other methods) differ somewhat in their assignment of the moment to an Fe atom, the difference gives some indication of how strictly a value should be presumed. 200
- 5.12 Calculated total energies (meV/Fe) compared to NM state of the various SDW states (SDW, D-SDW, Q-SDW) in the MFe_2As_2 (M =Ba, Sr, Ca), LaFeAsO and SrFeAsF compounds. The energy tabulated in the last column, labeled Q' , is the average of the high spin (SDW) and low spin (D-SDW) energies. illustrating that the energy of the Q-SDW ordered phase follows this average reasonably well. The level of agreement indicates to what degree ‘high spin’ and ‘low spin’ is a reasonable picture of the energetics at an antiphase boundary. 201
- 5.13 The calculated EFG component V_a, V_b, V_c (in unit of 10^{21} V/m²), the asymmetry parameter η , spin magnetic moment of As (μ_B), hyperfine field at the As nuclei (Tesla) of BaFe₂As₂ in the SDW, D-SDW, Q-SDW and O-SDW states. Experimentally, V_c is around 0.62, η is in the range of 0.9 to 1.2, and the internal field at As site parallel to c axis is about 1.4 T.[283] See text for notation. 204

5.14	The calculated EFG component V_a, V_b, V_c (in unit of 10^{21} V/m ²) , the asymmetry parameter $\eta= V_{xx}-V_{yy} / V_{zz} $ (here $ V_{zz} > V_{xx} $ and $ V_{yy} $), $V_Q= V_{zz} /(1+\eta^2/3)^{1/2}$ of Fe in SrFe ₂ As ₂ in the NM, SDW, D- SDW, Q-SDW and O-SDW states. Experimentally, V_Q is around 0.83 at room temperature in the non-magnetic state, and it is about 0.58 at 4.2 K.[344]	206
5.15	The hopping parameters (in eV) of LaFeAsO in the nonmagnetic and Q_M AFM state. The onsite energies (in eV) of the $d_{z^2}, d_{x^2-y^2}, d_{yz}, d_{xz},$ and d_{xy} in the NM and Q_M AFM (both spin up and spin down) are (-0.11, -0.27, 0.02, 0.02, 0.18), (-0.95, -1.14, -0.67, -0.70, -0.50), (0.18, 0.07, 0.23, 0.21, 0.40), respectively.	218
5.16	The hopping parameters (in eV) of LaFePO in the nonmagnetic and Q_M AFM state. The onsite energies (in eV) of the $d_{z^2}, d_{x^2-y^2}, d_{yz},$ $d_{xz},$ and d_{xy} in the NM and Q_M AFM (both spin up and spin down) are (-0.17, -0.27, -0.04, -0.04, 0.23), (-0.35, -0.44, -0.19, -0.21, 0.13), (-0.04, -0.14, 0.07, 0.07, 0.30), respectively.	220
5.17	The hopping parameters t_{xy}, t_{yx}, t_{xx} and t_{yy} in the NM and Q_M AFM phases of a few iron-pnictides.	221

List of Figures

2.1.1	Flowchart of self-consistency loop for solving KS equations.	34
3.1.1	Log plot of the calculated pressure versus volume. The relatively small difference between the LDA+U and LDA results is evident. The relation is roughly exponential below $V/V_o < 0.8$. Current static diamond anvil cells will only take Gd to the $V/V_o \sim 0.35$ region.	54
3.1.2	Behavior of the calculated moment/cell ($4f$ spin moment plus conduction electron polarization) of Gd versus reduction in volume, from both LDA and LDA+U methods. For the more realistic LDA+U method, there is very little decrease in moment down to $V/V_o=0.45$ (~ 110 GPa), with a rapid decline beginning only around $V/V_o \approx 0.2$ (1.5 TPa).	55
3.1.3	View of the $4f$ projected density of states under compression, with majority spin plotted upward and minority plotted downward. The curves are displaced for clarity, by an amount proportional to the reduction in lattice constant. The legend provides the ratio a/a_o , which is decreasing from above, and from below, toward the middle of the figure.	57

3.1.4	Plot of band positions (lines) and widths (bars) of the majority and minority $4f$ states, the semicore $5p$ bands, and the valence $5d$ bands, for ferromagnetic Gd. The bar at $V/V_o=0.5$ (~ 59 GPa) marks the observed volume collapse transition, while the arrow at 113 GPa denotes the highest pressure achieved so far in experiment. These results were obtained from LDA+U method, with U varying with volume as given by McMahan <i>et al</i> [65].	59
3.1.5	Plot of the $4f$ bandwidths (both majority and minority), together with the volume-dependent Coulomb repulsion U from McMahan.[65] The simple crossover criterion $W_f \approx U$ occurs around $V/V_o = 0.20 - 0.25$, corresponding roughly to a pressure of 700-1000 GPa. Also pictured is $U^* \equiv U/\sqrt{7}$, see text for discussion.	61
3.2.1	Structure of RB_4 viewed from along the c direction. The large metal ion spheres (red) lie in $z=0$ plane. Apical B1 atoms (small black) lie in $z \simeq 0.2$ and $z \simeq 0.8$ planes. Lightly shaded (yellow) dimer B2 and equatorial B3 (dark, blue) atoms lie in $z=0.5$ plane. The sublattice of R ions is such that each one is a member of two differently oriented R_4 squares, and of three R_3 triangles.	66
3.2.2	Plot of experimental lattice constants of RB_4 vs position in the Periodic Table (atomic number), showing a lanthanide contraction of about 5% for a , 3% for c . The smooth lines show a quadratic fit to the data.	67

3.2.3	Band structure of YB ₄ (top panel) and CaB ₄ (lower panel) within 6 eV of the Fermi level along high symmetry directions, showing the gap that opens up around E _F (taken as the zero of energy) throughout much of the top and bottom portions of the tetragonal Brillouin zone. Notice the lack of dispersion along the upper and lower zone edges R-A-R ($k_z=\pi/c$, and either k_x or k_y is π/a). Note also that, due to the non-symmorphic space group, bands stick together in pairs along X-M (the zone ‘equator’) and along R-A (top and bottom zone edges).	71
3.2.4	Projected density of states per atom of each of the B atoms for YB ₄ . The curves are shifted to enable easier identification of the differences. The B 2 <i>p</i> bonding-antibonding gap can be identified as roughly from -1 eV to 4-5 eV.	72
3.2.5	Enlargement of the partial densities of states of Y 4 <i>d</i> and B 2 <i>p</i> states (per atom) near the Fermi level. The states at the Fermi level, and even for almost 2 eV below, have strong 4 <i>d</i> character. The apical B2 character is considerably larger than that of B1 or B3 in the two peaks below E _F , but is only marginally larger exactly at E _F	72
3.2.6	Fermi surfaces of YB ₄ . Light (yellow) surfaces enclose holes, dark (red) surfaces enclose electrons. The wide gap throughout the top and bottom edges of the zone account for the lack of Fermi surfaces there.	76

3.2.7	The full valence band structure of DyB ₄ , and up to 5 eV in the conduction bands. This plot is for ferromagnetic alignment of the spin moments, with the solid bands being majority and the lighter, dashed lines showing the minority bands. The flat bands in the -4.5 eV to -11 eV are 4 <i>f</i> eigenvalues as described by the LDA+U method.	78
3.2.8	Band structure of DyB ₄ on a fine scale around the Fermi energy, see Fig. 3.2.7. The exchange splitting (between solid and dashed bands) gives a direct measure of the coupling between the polarized Dy ion and the itinerant bands (see text).	79
3.2.9	Calculated mean 4 <i>f</i> eigenvalue position (symbols connected by lines) with respect to E _F , and the spread in eigenvalues, of RB ₄ compounds. The smooth behavior from Pr to Tm (except for Eu) reflects the common trivalent state of these ions. Eu and Yb are calculated to be divalent and deviate strongly from the trivalent trend. Ce has a higher valence than three, accounting for its deviation from the trivalent trend.	80
3.3.1	Crystal structure of YbRh ₂ Si ₂ .	87
3.3.2	Band structure of YbRh ₂ Si ₂ along tetragonal symmetry lines. The Cartesian symmetry line indices are Γ(0,0,0), X(1,0,0), M(1,1,0), Z(0,0,1), in units of $[\frac{\pi}{a}, \frac{\pi}{a}, \frac{2\pi}{c}]$. Top panel: bands with total Rh 4 <i>d</i> emphasized using the fatbands representation. Bottom panel: same bands with total Yb 5 <i>d</i> emphasized using the fatbands representation.	90

3.3.3	Total and projected (per atom) densities of states of YbRh_2Si_2 corresponding to the band structure in Fig. 3.3.2. Rh $4d$ character dominates around the Fermi level.	91
3.3.4	The three calculated Fermi surfaces of YbRh_2Si_2 with $4f^{13}$ configuration, pictured within the crystallographic Brillouin zone. Top panel: fluted donut \mathcal{D} surface centered around the upper zone face midpoint Z. Middle panel: multiply-connected jungle gym \mathcal{J} surface. Bottom panel: tall pillbox surface \mathcal{P} , containing electrons at the zone center Γ . The Fermi surfaces of LuRh_2Si_2 are very similar, see text.	94
4.2.1	Plot of the total DOS and projected $4d$ DOS per atom of fcc Y with different volumes. Both the total and the $4d$ density of states at Fermi level decrease with reduction in volume.	105
4.2.2	Plot along high symmetry directions of the bands of Y at $V/V_o=1.00$ and at $V/V_o=0.50$. The “fattening” of the bands is proportional to the amount of Y $4d$ character. Note that the $4d$ character goes substantially in the occupied bands under pressure (the lighter shading), although there is relatively little change in the Fermi surface band crossings.	106
4.2.3	Surface plot of the Fermi surface of fcc Y at a volume corresponding to ambient pressure. The surface is shaded according to the Fermi velocity. The surface is isomorphic to that of Cu, <i>except</i> for the tubes through the W point vertices that connect Fermi surfaces in neighboring Brillouin zones. The evolution with pressure is described in the text.	108

4.2.4	Plot of the calculated phonon spectrum along high symmetry directions (Γ -X, Γ -K, Γ -L) of fcc Y with different volumes. The longitudinal mode phonons increases with the distance from Γ points along all the three directions. Along Γ -X direction (left panel), the doubly degenerate transverse mode slightly softens near X point, while along Γ -K direction (left panel, only the T_2 mode slightly softens near K point. Along Γ -L direction (right panel), the already soft doubly degenerate transverse mode soften further near the L point with decreasing volume. At $V = 0.6V_0$, the frequency at L becomes negative, indicating lattice instability.	110
4.2.5	Plot of the calculated linewidths of fcc Y for varying volumes. The linewidths of the transverse modes at the X point increases from 1.3 to 5.5 as volume decreases from $V=0.9V_0$ to $V=0.6V_0$. The linewidths of the T_2 along $\langle 110 \rangle$ modes show the same increase. The linewidths along the $\langle 111 \rangle$ direction have been multiplied by four for clarity.	111
4.2.6	Plot of the product $\lambda_{Q\nu}\omega_{Q\nu}$ of fcc Y for different volumes, along the high symmetry directions. Note that the longitudinal (L) values along $\langle 111 \rangle$ have been multiplied by four for clarity. In addition, values corresponding to unstable modes near L have been set to zero. Differences in this product reflect differences in matrix elements; see text.	113

4.2.7	Top panel: Plot of $\alpha^2 F(\omega)$ versus ω As volume decreases, $\alpha^2 F(\omega)$ increases and gradually transfers to low frequency. Bottom panel: the frequency-resolved coupling strength $\alpha^2(\omega)$ for each of the volumes studied. The evolution with increased pressure is dominated by strongly enhanced coupling at very low frequency (2-5 meV). . .	116
4.3.1	Band structure and DOS of sc Ca at 36 GPa ($a=2.70 \text{ \AA}$, $0.451 V_0$) and 109 GPa ($a=2.35 \text{ \AA}$, $0.297 V_0$). The high symmetry points are $\Gamma(0, 0, 0)$, $X(1, 0, 0)$, $M(1, 1, 0)$ and $R(1, 1, 1)$ in the units of $(\pi/a, \pi/a, \pi/a)$	127
4.3.2	Fermi surface of sc Ca, $\bar{I}43m$ Ca and the sc* Ca which takes the symmetry of $\bar{I}43m$ space group, i.e., 8 atoms in the unit cell with $x=0.25$, at 109 GPa ($0.297 V_0$).	129
4.3.3	Phonon spectrum of sc Ca at 36 GPa and 109 GPa. The high symmetry points are $\Gamma(0, 0, 0)$, $X(0.5, 0, 0)$, $M(0.5, 0.5, 0)$ and $R(0.5, 0.5, 0.5)$ in the units of $(2\pi/a, 2\pi/a, 2\pi/a)$	130
4.3.4	Local coordination of the five structures of Ca, plotted as number of neighbors versus the distance d relative to the cubic lattice constant a_{sc} with the same density. The inset shows the unit cube of the $\bar{I}43m$ structure (which contains two primitive cells); this structure retains six near neighbors at equal distances but three different second neighbor distances. The $P4_32_12$ and $Pnma$ structures can be regarded to be seven-coordinated, albeit with one distance that is substantially larger than the other six.	131
4.3.5	Plot of volume dependence total energy and pressure of bcc, sc and $\bar{I}43m$ Ca.	133

4.3.6	Band structure and DOS of I43m Ca at 71GPa (a=5.00 Å, 0.358 V ₀) and 109 GPa (a=4.70 Å, 0.297 V ₀), and sc Ca at 109 GPa (a=4.70 Å, 0.297 V ₀) which takes the symmetry of I43m space group, i.e., 8 atoms in the unit cell with x=0.25. The high symmetry points are Γ(0, 0, 0), H(1, 0, 0), N(0.5, 0.5, 0) and P(0.5, 0.5, 0.5) in the units of (2π/a, 2π/a, 2π/a).	134
4.3.7	Phonon spectrum and phonon DOS of I43m Ca at 71 GPa (a=5.00 Å, 0.358 V ₀) and 109 GPa (a=4.70 Å, 0.297 V ₀). The high symmetry points are Γ(0, 0, 0), H(1, 0, 0), N(0.5, 0.5, 0) and P(0.5, 0.5, 0.5) in the units of (2π/a, 2π/a, 2π/a).	136
4.3.8	Nesting function ξ(Q) of I43m Ca on the (100), (110) and (111) planes at 83 GPa.	136
4.3.9	Structures of the I43m, Pnma, Cmca and P4 ₃ 2 ₁ 2 Ca.	138
4.3.10	Plot of the enthalpy H(P) of the four distorted Ca structures relative to that for Ca in the simple cubic structure. The inset gives an expanded picture of the 40-100 GPa regime.	139
4.3.11	Plot (right hand axis) of the volume-pressure V(P) - V _{sc} (P) behavior for each of the four distorted structures, relative to the behavior of sc Ca (shown as the dashed line and the left hand axis). The dips in the curves (70 GPa for Cmca, 80-100 GPa for P4 ₃ 2 ₁ 2, 90 GPa for Pnma, 140 GPa for I43m) reflect volume collapse regions.	141

4.3.12	Top: Pressure variation of the internal structural parameters of the four distorted Ca structures. Bottom: Pressure variation of the lattice constants of the Cmca and Pnma structures (the corresponding behavior for P4 ₃ 2 ₁ 2 is smooth). Note the first-order change in the Cmca quantities near 75 GPa.	142
4.3.13	Plot of $\alpha^2 F(\omega)$ (lower panel), $\alpha^2(\omega)$ (middle panel), and phonon DOS (upper panel) of $\bar{I}43m$ structure at about 61, 71, 83 and 97 GPa. This regime is characterized by strong coupling $\alpha^2(\omega)$ at very low frequency.	145
4.3.14	Plot of $\alpha^2 F(\omega)$ (bottom panel), $\alpha^2(\omega)$ (middle panel), and phonon DOS (upper panel) of Pnma structure at about 60, 85, 120, 160, and 200 GPa. The main trends are the stiffening of the modes with increasing pressure, and the retention of coupling strength $\alpha^2(\omega)$ over a wide frequency range.	147
4.3.15	Phonon spectrum, phonon DOS, α^2 and $\alpha^2 F$ of Cmca Ca at 0.251 V_0 (~ 130 GPa from PWscf). The high symmetry points are $\Gamma(0, 0, 0)$, $Y_1(1, 0, 0)$, $Y_2(0, 1, 0)$, $\Gamma'(1, 1, 0)$, $S(0.5, 0.5, 0)$, $Z(0, 0, 0.5)$, $T_1(1, 0, 0.5)$, $T_2(0, 1, 0.5)$, $Z'(1, 1, 0.5)$ and $R(0.5, 0.5, 0.5)$ in the units of $(2\pi/a, 2\pi/b, 2\pi/c)$	149
4.3.16	Upper panel: Calculated electron-phonon coupling constant λ , η and T_C of Ca in $\bar{I}43m$ (empty symbols), Pnma (filled symbols) and Cmca (crossing-line filled symbols) structures at a few pressures. Lower panel: T_c calculated from the Allen-Dynes equation, showing the dependence on the Coulomb pseudopotential for which two values, $\mu^*=0.10$ and 0.15 have been taken.	150

5.2.1	The Q_M antiferromagnetic structure of LaFeAsO, with different shades of Fe atoms (top and bottoms planes) denoting the opposing directions of spins in the Q_M AFM phase. Fe atoms lie on a square sublattice coordinated tetrahedrally by As atoms, separated by LaO layers (center of figure) of similar structure. The dashed lines indicate the nonmagnetic primitive cell.	158
5.2.2	Top panel: total DOS for the Q_M AFM phase. Bottom panel: spin resolved Fe 3 <i>d</i> DOS, showing majority filled and minority half-filled up to the pseudogap, and the As 4 <i>p</i> DOS.	161
5.2.3	Band structure of the \vec{Q}_M AFM phase along high symmetry directions. Note that two dispersive bands and one narrow band cross E_F along Γ -Y, while only the one flatter band crosses E_F (very near $k=0$) along Γ -X.	162
5.2.4	Fermi surfaces of LaFeAsO in the Q_M AFM phase. (A) and (B): the hole cylinders and electron tubes of the stoichiometric Q_M phase. (C) and (D): hole- and electron-doped surfaces doped away from the Q_M AFM phase.	165
5.2.5	The magnitude of the Fe magnetic moment, the change in energy, and the Fe-As distance, as the As height z_{As} is varied.	166
5.2.6	The bandstructure and total DOS of Q_M LaFeAsO at ambient pressure computed for $z(\text{As})=0.150$, $z(\text{As})=0.145$, $z(\text{As})=0.139$	171
5.2.7	Plot of LaFeAsO Q_M AFM Fe 3 <i>d</i> PDOS at ambient pressure with $z(\text{As})=0.150$, $z(\text{As})=0.145$, $z(\text{As})=0.139$	171

5.2.8	Plots of undoped, 0.1 and 0.2 electron-doped LaFeAsO Q_M AFM total DOS (displaced upward consecutively by 10 units for clarity, obtained using the virtual crystal approximation. Referenced to that of the undoped compound, the Fermi levels of 0.1 and 0.2 electron-doped DOS are shifted up by 0.20 eV and 0.26 eV, respectively.	173
5.2.9	Plot of the magnetic moment of Fe atom in the Q_M AFM state of LaFeAsO as a function of the Fe-As distance, both at ambient pressure and under pressure.	177
5.2.10	Plot of the optimized c/a ratio, the Fe-As distances (\AA), the total energy of the Q_M AFM state (eV), the total energy differences between NM and Q_M AFM state (EE(NM)-EE(Q_M AFM) (40 meV/Fe), the magnetic moment (μ_B) of the Q_M AFM states as a function of V/V_0 . 177	177
5.2.11	The bandstructure and total DOS of Q_M LaFeAsO computed for $0.975V_0$, $0.925 V_0$ and $0.875 V_0$. $z(\text{As})$ has been shifted.	178
5.2.12	The Fermi surface of Q_M LaFeAsO computed for $0.975V_0$, $0.925 V_0$ and $0.875 V_0$. $z(\text{As})$ has been shifted.	179
5.3.1	Plot of LaFePO band structure in Q_M AFM state and total DOS in both Q_M AFM and NM states at ambient conditions with experimental lattice parameters.	185
5.3.2	Fermi surface of Q_M AFM LaFePO, showing the very strong differences compared to LaFeAsO.	186
5.3.3	Plot of Q_M AFM LaFeSbO band structure and total DOS at $1.138 V_0$ with both optimized and shifted $z(\text{Sb})$	189

5.3.4	Plot of LaFeNO Q_M AFM band structure and total DOS at $0.850V'_0$, $0.825 V'_0$ and $0.800 V'_0$ with shifted $z(N)$	191
5.4.1	The structure of FeAs layer in the Q -SDW state showing the antiphase boundary in the center of the figure. Fe spin 1 (filled circle) and spin 2 (empty circle) have two different sites A ('bulklike') and B ('boundary-like'). As above Fe plane (filled square) and below Fe plane (empty square) have three sites 1, 2, 3 whose local environments differ.	196
5.4.2	The calculated errors of $z(\text{As})$ compared to experimental values in the NM and SDW states when using LDA (PW92) and GGA (PBE) XC functionals in CaFe_2As_2 , SrFe_2As_2 , BaFe_2As_2 , and LaFeAsO . . .	198
5.5.1	LaFeAsO band structure in the NM (top panel) and Q_M AFM (bottom panel) phases. Dash (red) lines are the Fe $3d$ tight-binding bands fitting to the DFT-LSDA Fe-derived bands (solid black), which generally have very good overall agreements.	209
5.5.2	LaFeAsO Wannier functions of Fe $3d$ orbitals in the NM (top panel) and Q_M AFM (bottom panel) phases: showing (a) $3d_{yz}$, (b) $3d_{xz}$, (c) $3d_{xy}$, (d) $3d_{z^2}$ and (e) $3d_{x^2-y^2}$. In the NM phase, these Wannier functions are well localized at the Fe site, however, in the Q_M AFM phase, the Wannier functions for $3d_{xy}$ and $3d_{xz}$ orbitals are more delocalized, especially for the d_{xz} orbital, with significant density at the nearest-neighbor As sites. The isosurface is at the same value (density) in each panel.	211

5.6.1	LaFeAsO band structure with highlighted Fe $3d_{yz}$ and $3d_{xz}$ fatband characters in the NM (top panel) and Q_M AFM (bottom panel) phases. Compared to the NM phase, the Fe $3d_{xz}$ bands near Fermi level in the Q_M AFM phase, especially along $\Gamma - X$ and $\Gamma - Y$ directions, change dramatically due to the formation of the stripe antiferromagnetism with large ordered Fe magnetic moment of $1.9 \mu_B$.	213
5.6.2	LaFePO band structure with highlighted Fe $3d_{yz}$ and $3d_{xz}$ fatband characters in the NM (top panel) and Q_M AFM (bottom panel) phase. Compared to LaFeAsO, the Fe $3d_{xz}$ bands near Fermi level in the Q_M AFM phase change less significantly from the NM phase, due to the relatively small ordered Fe magnetic moment of $0.5 \mu_B$.	214
5.6.3	Possible orbital orderings of iron in iron-pnictides. Left panel: Both (a) and (b) form the Q_M AFM ordering. However, (a) is favored because it gains more kinetic energy from nearest-neighbor hoppings according to second-order perturbation theory (see text). Right panel (from top to bottom) shows the simplified symbols for Fe $3d_{yz}$ and $3d_{xz}$ orbitals, the chosen x and y directions, up arrows for spin up electrons and down arrows for spin down electrons, where black arrows for $3d_{yz}$ orbital and red arrows for $3d_{xz}$ orbital.	216

Chapter 1

Introduction

1.1 Electronic Structure Calculations

The theory of electrons has been a great challenge to physicists since the discovery of the electron in 1896 by Lorentz and Zeeman and also by Thomson in 1897. There is no big progress until the establishment of quantum mechanics in the 1920s. In the 1930s, band theory for independent electrons was gradually formed, leading to the classification of materials into insulators, semiconductors, and metals, according to the number of electrons and filling of bands. Also in the 1930s, several methods were proposed which are still in use today, including Hartree-Fock method, augmented plane wave (APW) method (further developed in the 1950s), orthogonalized plane wave (OPW) method, and effective potential method (forerunner of pseudopotential method). Band structure calculations for high-symmetry simple metals (eg: Na and Cu) and ionic solids (eg: NaCl) were done in the 1930s and 1940s. Accurate calculations of bands for more difficult materials such as semiconductors were done in the early 1950s. Rapid developments in electronic structure calculations were made after the formation of density functional theory (DFT) in 1960s, based on the

Hohenberg-Kohn theorem which states that all properties of a many-body system are completely determined by the ground state charge density. Electronic structure calculations based on density functional theory were very limited by the inaccessibility of powerful computers from the 1960s to 1980s. With the rapid advancement in computer technology in the 1990s, especially after 2000, a single personal computer is able to do such calculations for small and medium systems (typically less than 100 atoms in one unit cell).

Since the 1990s, electronic structure calculations based on density functional theory become more and more popular in condensed matter physics, quantum chemistry and material science. Density functional theory is by far the most widely used approach for electronic structure calculations nowadays. It is usually called first principle method or *ab initio* method, because it allows people to determine many properties of a condensed matter system by just giving some basic structural information without any adjustable parameter. It provides an alternative way to investigate condensed matter systems, other than the traditional experimental method and pure theoretical method based on quantum (field) theory. It is becoming a useful tool used by both experimentalists and theorists to understand characteristic properties of materials and to make specific predictions of experimentally observable phenomena for real materials and to design new materials.

The most widely used programs today are based on the Kohn-Sham ansatz to the original density functional theory. The Kohn-Sham ansatz is to replace the original many-body problem by an auxiliary independent-particle system, specifically, it maps the original interacting system with real potential onto a fictitious non-interacting system whereby the electrons move within an effective Kohn-Sham single-particle potential. The many-body effects are approximated by a so-called

exchange-correlation functional in the effective Kohn-Sham single-particle potential. The most widely used exchange-correlation functionals are local (spin) density approximation (L(S)DA) and generalized gradient approximation (GGA). The former comes from the exchange-correlation functional of a homogeneous electron gas by a point-by-point mapping and the latter is a generalization of the former by including contributions from electron density gradient. In order to better describe correlation effects in some strongly correlated systems such as compounds with transition metals ($3d$ electrons) and lanthanides ($4f$ electrons), several extensions to LDA and GGA have been made, including L(S)DA(GGA)+U method and dynamical mean field theory (DMFT) (usually used as a combination of LDA and DMFT, so called LDA+DMFT).

Other methods for electronic structure calculations include quantum Monte Carlo, GW method, as well as some generalizations of DFT known as time-dependent DFT (TD-DFT), density functional perturbation theory (DFPT), etc. The field of electronic structure calculations is rapidly developing in basic theory, new algorithms, computational methods and computational power.

1.2 Strongly Correlated Systems

The term “strongly correlated systems” usually refers to materials containing transition metals, lanthanides or actinides, where the $3d$ or $4d$ electrons of the transition metals, the $4f$ electrons of the lanthanides, and $5f$ electrons of the actinides, are localized and strongly correlated. LDA and GGA usually fail in these systems. A famous example is the transition metal oxides. LDA (GGA) predicts them as metals but they are actually Mott insulators. To account for the strong correlations, orbital-dependent potentials are introduced for these d and f electrons. LDA+U method

is the most widely used one among such methods. In this approach, an additional screened Coulomb parameter U and Hund's exchange parameter J are included for the d and f electrons (see chapter 2 for details of this method). In this dissertation, LDA+ U method is applied to fcc Gd under pressure, the rare earth tetraborides RB_4 , and a heavy fermion compound $YbRh_2Si_2$. Detailed results are presented in chapter 3.

1.3 Conventional Superconductors

Conventional superconductors, also called phonon-mediated superconductors, are those solids for which superconductivity can be explained by electron-phonon interactions (electron motion coupled with lattice vibrations) which provide the (net) attractive force (between electrons) to pair electrons and form Cooper pairs—the central concept in BCS theory. BCS theory was proposed by Bardeen, Cooper, and Schrieffer in 1957 and is the most successful theory to explain superconductivity in certain superconductors, although superconductivity in many systems remains incompletely understood. The superconducting critical temperature (T_c) of phonon-mediated superconductors is usually very low, less than 10 K. Only a handful of conventional superconductors have T_c close to or higher than 20 K. The most striking one is the hexagonal MgB_2 with $T_c = 40$ K discovered in 2001. The next big surprise is the simple free electron metal Li with T_c up to 20 K under 35-50 GPa pressure. These superconductors with T_c close to or higher than 20 K are usually strongly electron-phonon coupled. Although its T_c can be explained well by Eliashberg theory (an extension of BCS theory), a simple physical picture of the rather high T_c is still lacking. In these superconductors, only a few specific lattice vibration modes restricted in a small region of the Brillouin zone (BZ) contribute most to the

rather high T_c , i.e., there are very sharp pictures of the “mode” λ . These specific phonon modes are varying from material to material and a clear physical explanation is still demanding. By applying linear response calculation, I have investigated yttrium and calcium under high pressure. Yttrium is conventionally classified as a rare earth metal and was found to superconduct at 20 K under 115 GPa pressure in early 2006. Calcium is a simple alkaline earth metal and was found to superconduct at 25 K under 161 GPa pressure in August, 2006. What is more peculiar of calcium is that it is simple cubic structurally at room temperature in a wide range of pressure from 32 GPa to 109 GPa observed in experiments. In the same range of pressure, it begins to superconduct and its T_c increases rapidly with pressure. The results and discussions of our calculations on these two metals are given in Chapter 4.

1.4 High T_c Superconductors: Cuprates and Iron-Pnictide Compounds

The cuprate superconductors are layered materials with two dimensional Cu and O planes sandwiched by layers with other elements such as lanthanides and alkali-earth metals. In 1986, Bednorz and Müller discovered a lanthanum-based cuprate perovskite material with T_c of 35 K. The highest T_c in this class by now is 150 K. The superconductivity in this class is believed to closely relate to Cu $3d_{x^2-y^2}$ orbital, but a convincing, generally accepted theory is still lacking. The mechanism of superconductivity in this class is still one of the major outstanding challenges of theoretical condensed matter physics.

A new class of iron-based superconductors—the iron-pnictide compounds was discovered in February 2008 by Hosono *et al.* in a fluorine-doped tetragonal material

LaFeAsO $_{1-x}$ F $_x$ with $T_c = 26$ K. The parent compound LaFeAsO contains FeAs layers sandwiched by LaO layers. Each FeAs layer consists of a square-lattice Fe plane with As atoms above and below the plane alternatively. Very soon after this discovery, the T_c in this class went up to 56 K by replacing La with other rare earth elements Ce, Pr, Nd, Sm, and Gd. Later on, a few other families of iron-based superconductors were found with similar values of T_c . Now in these iron-based superconductors, the parent compounds are R eFeAsO (1111-type), M Fe $_2$ As $_2$ (122-type), A FeAs (111-type), M' FeAsF (another 1111-type), FeTe and FeSe (11-type), Fe $_2$ As $_2$ Sr $_4$ X $_2$ O $_6$ (22426-type), where R = rare earth elements; M =Ca, Sr, Ba, and Eu; A =Li and Na, M' =Ca and Sr, X =Sc and Cr. With similarities and differences of these iron-based superconductors and cuprate superconductors, scientists have more chances to unveil the underlying theory of superconductivity in these materials.

I have done a lot of calculations on the parent compounds of these iron-based superconductors. I have obtained the basic electronic structures of the nonmagnetic and stripe antiferromagnetic states. I discussed the role of the rare earth elements and pnictide elements in R Fe Pn O (R =rare earth metal and Pn =pnictides). I predicted and calculated the electronic structure of the hypothetical materials LaFeSbO and LaFeNO. I analyzed the effect of antiphase boundary with varying density imposed on the stripe antiferromagnetic order in these iron pnictide compounds through calculations of total energies, electric field gradients and hyperfine fields of Fe and As. I have also constructed the Wannier functions for the Fe 3d orbitals, and calculated the hopping parameters in tight binding method. Based on these hopping parameters, I discussed the structural transition and antiferromagnetic transition associated with the change of one of the hopping parameters, which is closely related to the Fe 3d $_{xz}$ Wannier function. The detailed discussions are presented in Chapter 5.

Chapter 2

Theoretical Background: Density Functional Theory and Linear Response Calculations

2.1 Density Functional Theory

Over the past few decades, density functional theory (DFT) has been the most successful, widely used method in condensed-matter physics, computational physics and quantum chemistry to describe properties of condensed matter systems, which include not only standard bulk materials but also complex materials such as molecules, proteins, interfaces and nanoparticles. The main idea of DFT is to describe a many-body interacting system via its particle density and not via its many-body wavefunction. Its significance is to reduce the $3N$ degrees of freedom of the N -body system to only three spatial coordinates through its particle density. Its basis is the well known Hohenberg-Kohn (HK) theorem[1], which claims that all properties of a system can

be considered to be unique functionals of its ground state density. Together with the Born-Oppenheimer (BO) approximation[2] and Kohn-Sham (KS) ansatz[3], practical accurate DFT calculations have been made possible via approximations for the so-called exchange-correlation (XC) potential, which describes the effects of the Pauli principle and the Coulomb potential beyond a pure electrostatic interaction of the electrons. Since it is impossible to calculate the exact XC potential (by solving the many-body problem exactly), a common approximation is the so-called local density approximation (LDA) which locally substitutes the XC energy density of an inhomogeneous system by that of a homogeneous electron gas evaluated at the local density.

In many cases the results of DFT calculations for condensed-matter systems agreed quite satisfactorily with experimental data, especially with better approximations for the XC energy functional since the 1990s. Also, the computational costs were relatively low compared to traditional ways which were based on the complicated many-electron wavefunction, such as Hartree-Fock theory[4, 5] and its descendants. Despite the improvements in DFT, there are still difficulties in using DFT to properly describe intermolecular interactions; charge transfer excitations; transition states, global potential energy surfaces and some other strongly correlated systems; and in calculations of the band gap of some semiconductors.

2.1.1 The Many-Body System and Born-Oppenheimer (BO) Approximation

The Hamiltonian of a many-body condensed-matter system consisting of nuclei and electrons can be written as:

$$\begin{aligned}
 H_{tot} = & - \sum_I \frac{\hbar^2}{2M_I} \nabla_{\mathbf{R}_I}^2 - \sum_i \frac{\hbar^2}{2m_e} \nabla_{\mathbf{r}_i}^2 + \frac{1}{2} \sum_{\substack{I,J \\ I \neq J}} \frac{Z_I Z_J e^2}{|\mathbf{R}_I - \mathbf{R}_J|} \\
 & + \frac{1}{2} \sum_{\substack{i,j \\ i \neq j}} \frac{e^2}{|\mathbf{r}_i - \mathbf{r}_j|} - \sum_{I,i} \frac{Z_I e^2}{|\mathbf{R}_I - \mathbf{r}_i|}
 \end{aligned} \tag{2.1.1}$$

where the indexes I, J run on nuclei, i and j on electrons, \mathbf{R}_I and M_I are positions and masses of the nuclei, \mathbf{r}_i and m_e of the electrons, Z_I the atomic number of nucleus I. The first term is the kinetic energy of the nuclei, the second term is the kinetic energy of the electrons, the third term is the potential energy of nucleus-nucleus Coulomb interaction, the fourth term is the potential energy of electron-electron Coulomb interaction and the last term is the potential energy of nucleus-electron Coulomb interaction. The time-independent Schrödinger equation for the system reads:

$$H_{tot} \Psi(\{\mathbf{R}_I\}, \{\mathbf{r}_i\}) = E \Psi(\{\mathbf{R}_I\}, \{\mathbf{r}_i\}) \tag{2.1.2}$$

where $\Psi(\{\mathbf{R}_I\}, \{\mathbf{r}_i\})$ is the total wavefunction of the system. In principle, everything about the system is known if one can solve the above Schrödinger equation. However, it is impossible to solve it in practice. A so-called Born-Oppenheimer (BO) approximation was made by Born and Oppenheimer[2] in 1927. Since the nuclei are much heavier than electrons (the mass of a proton is about 1836 times the mass of an electron), the nuclei move much slower (about two order of magnitude slower) than the

electrons. Therefore we can separate the movement of nuclei and electrons. When we consider the movement of electrons, it is reasonable to consider the positions of nuclei are fixed, thus the total wavefunction can be written as:

$$\Psi(\{\mathbf{R}_I\}, \{\mathbf{r}_i\}) = \Theta(\{\mathbf{R}_I\})\phi(\{\mathbf{r}_i\}; \{\mathbf{R}_I\}) \quad (2.1.3)$$

where $\Theta(\{\mathbf{R}_I\})$ describes the nuclei and $\phi(\{\mathbf{r}_i\}; \{\mathbf{R}_I\})$ the electrons (depending parametrically on the positions of the nuclei). With the BO approximation, Eq. (2.1.2) can be divided into two separate Schrödinger equations:

$$H_e\phi(\{\mathbf{r}_i\}; \{\mathbf{R}_I\}) = V(\{\mathbf{R}_I\})\phi(\{\mathbf{r}_i\}; \{\mathbf{R}_I\}) \quad (2.1.4)$$

where

$$H_e = -\sum_i \frac{\hbar^2}{2m_e} \nabla_{\mathbf{r}_i}^2 + \frac{1}{2} \sum_{\substack{I,J \\ I \neq J}} \frac{Z_I Z_J e^2}{|\mathbf{R}_I - \mathbf{R}_J|} + \frac{1}{2} \sum_{\substack{i,j \\ i \neq j}} \frac{e^2}{|\mathbf{r}_i - \mathbf{r}_j|} - \sum_{I,i} \frac{Z_I e^2}{|\mathbf{R}_I - \mathbf{r}_i|} \quad (2.1.5)$$

and

$$\left[-\sum_I \frac{\hbar^2}{2M_I} \nabla_{\mathbf{R}_I}^2 + V(\{\mathbf{R}_I\}) \right] \Theta(\{\mathbf{R}_I\}) = E' \Theta(\{\mathbf{R}_I\}) \quad (2.1.6)$$

Eq. (2.1.4) is the equation for the electronic problem with the nuclei positions fixed. The eigenvalue of the energy $V(\{\mathbf{R}_I\})$ depends parametrically on the positions of the nuclei. After solving Eq. (2.1.4), $V(\{\mathbf{R}_I\})$ is known and by applying it to Eq. (2.1.6), which has no electronic degrees of freedom, the motion of the nuclei is obtained. Eq. (2.1.6) is sometimes replace by a Newton equation, i.e., to move the nuclei classically, using ∇V as the forces. Then the whole problem is solved.

The significance of the BO approximation is to separate the movement of electrons

and nuclei. Now we can consider that the electrons are moving in a static external potential $V_{ext}(\mathbf{r})$ formed by the nuclei, which is the starting point of DFT. The BO approximation was extended by Bohn and Huang known as Born-Huang (BH) approximation [6] to take into account more nonadiabatic effect in the electronic Hamiltonian than in the BO approximation.

2.1.2 Thomas-Fermi-Dirac Approximation

The predecessor to DFT was the Thomas-Fermi (TF) model proposed by Thomas[7] and Fermi[8] in 1927. In this method, they used the electron density $n(\mathbf{r})$ as the basic variable instead of the wavefunction. The total energy of a system in an external potential $V_{ext}(\mathbf{r})$ is written as a functional of the electron density $n(\mathbf{r})$ as:

$$E_{TF}[n(\mathbf{r})] = A_1 \int n(\mathbf{r})^{5/3} d\mathbf{r} + \int n(\mathbf{r})V_{ext}(\mathbf{r})d\mathbf{r} + \frac{1}{2} \int \int \frac{n(\mathbf{r})n(\mathbf{r}')}{|\mathbf{r} - \mathbf{r}'|} d\mathbf{r}d\mathbf{r}' \quad (2.1.7)$$

where the first term is the kinetic energy of the non-interacting electrons in a homogeneous electron gas (HEG) with $A_1 = \frac{3}{10}(3\pi^2)^{2/3}$ in atomic units ($\hbar = m_e = e = 4\pi/\epsilon_0 = 1$). The kinetic energy density of a HEG is obtained by adding up all of the free-electron energy state $\varepsilon_k = k^2/2$ up to the Fermi wavevector $k_F = [3\pi^2n(\mathbf{r})]^{1/3}$ as:

$$\begin{aligned} t_0[n(\mathbf{r})] &= \frac{2}{(2\pi)^3} \int_0^{k_F} \frac{k^2}{2} 4\pi k^2 dk \\ &= A_1 n(\mathbf{r})^{5/3} \end{aligned} \quad (2.1.8)$$

The second term is the classical electrostatic energy of the nucleus-electron Coulomb interaction. The third term is the classical electrostatic Hartree energy approximated by the classical Coulomb repulsion between electrons. In the original TF method, the exchange and correlation among electrons was neglected. In 1930, Dirac[9] extended

the Thomas-Fermi method by adding a local exchange term $A_2 \int n(\mathbf{r})^{4/3} d\mathbf{r}$ to Eq. (2.1.7) with $A_2 = -\frac{3}{4}(3/\pi)^{1/3}$, which leads Eq. (2.1.7) to

$$E_{TFD}[n(\mathbf{r})] = A_1 \int n(\mathbf{r})^{5/3} d\mathbf{r} + \int n(\mathbf{r}) V_{ext}(\mathbf{r}) d\mathbf{r} + \frac{1}{2} \int \int \frac{n(\mathbf{r})n(\mathbf{r}')}{|\mathbf{r} - \mathbf{r}'|} d\mathbf{r} d\mathbf{r}' + A_2 \int n(\mathbf{r})^{4/3} d\mathbf{r} \quad (2.1.9)$$

The ground state density and energy can be obtained by minimizing the Thomas-Fermi-Dirac equation (2.1.9) subject to conservation of the total number (N) of electrons. By using the technique of Lagrange multipliers, the solution can be found in the stationary condition:

$$\delta\{E_{TFD}[n(\mathbf{r})] - \mu(\int n(\mathbf{r}) d\mathbf{r} - N)\} = 0 \quad (2.1.10)$$

where μ is a constant known as a Lagrange multiplier, whose physical meaning is the chemical potential (or Fermi energy at T=0 K). Eq. (2.1.10) leads to the Thomas-Fermi-Dirac equation,

$$\frac{5}{3}A_1 n(\mathbf{r})^{2/3} + V_{ext}(r) + \int \frac{n(\mathbf{r}')}{|\mathbf{r} - \mathbf{r}'|} d\mathbf{r}' + \frac{4}{3}A_2 n(\mathbf{r})^{1/3} - \mu = 0 \quad (2.1.11)$$

which can be solved directly to obtain the ground state density.

The approximations used in Thomas-Fermi-type approach are so crude that the theory suffers from many problems. The most serious one is that the theory fails to describe bonding between atoms, thus molecules and solids cannot form in this theory.[10] Although it is not good enough to describe electrons in matter, its concept to use electron density as the basic variable illustrates the way DFT works.

2.1.3 The Hohenberg-Kohn (HK) Theorems

DFT was proven to be an exact theory of many-body systems by Hohenberg and Kohn[1] in 1964. It applies not only to condensed-matter systems of electrons with fixed nuclei, but also more generally to any system of interacting particles in an external potential $V_{ext}(\mathbf{r})$. The theory is based upon two theorems.

The HK theorem I:

The ground state particle density $n(\mathbf{r})$ of a system of interacting particles in an external potential $V_{ext}(\mathbf{r})$ uniquely determines the external potential $V_{ext}(\mathbf{r})$, except for a constant. Thus the ground state particle density determines the full Hamiltonian, except for a constant shift of the energy. In principle, all the states including ground and excited states of the many-body wavefunctions can be calculated. This means that **the ground state particle density uniquely determines all properties of the system completely.**

Proof of the HK theorem I:

For simplicity, here I only consider the case that the ground state of the system is nondegenerate. It can be proven that the theorem is also valid for systems with degenerate ground states.[11] The proof is based on minimum energy principle. Suppose there are two different external potentials $V_{ext}(\mathbf{r})$ and $V'_{ext}(\mathbf{r})$ which differ by more than a constant and lead to the same ground state density $n_0(\mathbf{r})$. The two external potentials would give two different Hamiltonians, \hat{H} and \hat{H}' , which have the same ground state density $n_0(\mathbf{r})$ but would have different ground state wavefunctions, Ψ and Ψ' , with $\hat{H}\Psi = E_0\Psi$ and $\hat{H}'\Psi' = E'_0\Psi'$. Since Ψ' is not the ground state of \hat{H} ,

it follows that

$$\begin{aligned}
E_0 &< \langle \Psi' | \hat{H} | \Psi' \rangle \\
&< \langle \Psi' | \hat{H}' | \Psi' \rangle + \langle \Psi' | \hat{H} - \hat{H}' | \Psi' \rangle \\
&< E'_0 + \int n_0(\mathbf{r}) [V_{ext}(\mathbf{r}) - V'_{ext}(\mathbf{r})] d\mathbf{r}
\end{aligned} \tag{2.1.12}$$

Similarly

$$\begin{aligned}
E'_0 &< \langle \Psi | \hat{H}' | \Psi \rangle \\
&< \langle \Psi | \hat{H} | \Psi \rangle + \langle \Psi | \hat{H}' - \hat{H} | \Psi \rangle \\
&< E_0 + \int n_0(\mathbf{r}) [V'_{ext}(\mathbf{r}) - V_{ext}(\mathbf{r})] d\mathbf{r}
\end{aligned} \tag{2.1.13}$$

Adding Eq. (2.1.12) and (2.1.13) lead to the contradiction

$$E_0 + E'_0 < E_0 + E'_0 \tag{2.1.14}$$

Hence, no two different external potentials $V_{ext}(\mathbf{r})$ can give rise to the same ground state density $n_0(\mathbf{r})$, i.e., the ground state density determines the external potential $V_{ext}(\mathbf{r})$, except for a constant. That is to say, there is a one-to-one mapping between the ground state density $n_0(\mathbf{r})$ and the external potential $V_{ext}(\mathbf{r})$, although the exact formula is unknown.

The HK theorem II:

There exists a universal functional $F[n(\mathbf{r})]$ of the density, independent of the external potential $V_{ext}(\mathbf{r})$, such that the global minimum value of the energy functional $E[n(\mathbf{r})] \equiv \int n(\mathbf{r})V_{ext}(\mathbf{r})d\mathbf{r} + F[n(\mathbf{r})]$ is the exact ground state energy of the system and the exact ground state density $n_0(\mathbf{r})$ minimizes this functional. Thus the exact ground state energy and density are fully determined by the functional $E[n(\mathbf{r})]$.

Proof of the HK theorem II:

The universal functional $F[n(\mathbf{r})]$ can be written as

$$F[n(\mathbf{r})] \equiv T[n(\mathbf{r})] + E_{int}[n(\mathbf{r})] \quad (2.1.15)$$

where $T[n(\mathbf{r})]$ is the kinetic energy and $E_{int}[n(\mathbf{r})]$ is the interaction energy of the particles. According to variational principle, for any wavefunction Ψ' , the energy functional $E[\Psi']$:

$$E[\Psi'] \equiv \langle \Psi' | \hat{T} + \hat{V}_{int} + \hat{V}_{ext} | \Psi' \rangle \quad (2.1.16)$$

has its global minimum value only when Ψ' is the ground state wavefunction Ψ_0 , with the constraint that the total number of the particles is conserved. According to HK theorem I, Ψ' must correspond to a ground state with particle density $n'(\mathbf{r})$ and external potential $V'_{ext}(\mathbf{r})$, then $E[\Psi']$ is a functional of $n'(\mathbf{r})$. According to variational principle:

$$\begin{aligned} E[\Psi'] &\equiv \langle \Psi' | \hat{T} + \hat{V}_{int} + \hat{V}_{ext} | \Psi' \rangle \\ &= E[n'(\mathbf{r})] \\ &= \int n'(\mathbf{r}) V'_{ext}(\mathbf{r}) d\mathbf{r} + F[n'(\mathbf{r})] \\ &> E[\Psi_0] \\ &= \int n_0(\mathbf{r}) V_{ext}(\mathbf{r}) d\mathbf{r} + F[n_0(\mathbf{r})] \\ &= E[n_0(\mathbf{r})] \end{aligned} \quad (2.1.17)$$

Thus the energy functional $E[n(\mathbf{r})] \equiv \int n(\mathbf{r}) V_{ext}(\mathbf{r}) d\mathbf{r} + F[n(\mathbf{r})]$ evaluated for the correct ground state density $n_0(\mathbf{r})$ is indeed lower than the value of this functional for any other density $n(\mathbf{r})$. Therefore by minimizing the total energy functional of the system with respect to variations in the density $n(\mathbf{r})$, one would find the exact ground state density and energy.

The HK theorems can be generalized to spin density functional theory with spin degrees of freedom.[12] In this theory, there are two types of densities, namely, the particle density $n(\mathbf{r}) = n_{\uparrow}(\mathbf{r}) + n_{\downarrow}(\mathbf{r})$ and the spin density $s(\mathbf{r}) = n_{\uparrow}(\mathbf{r}) - n_{\downarrow}(\mathbf{r})$ where \uparrow and \downarrow denote the two different kinds of spins. The energy functional is generalized to $E[n(\mathbf{r}), s(\mathbf{r})]$. In systems with magnetic order or atoms with net spins, the spin density functional theory should be used instead of the original one-spin density functional theory. DFT can also be generalized to include temperature dependence[13] and time dependence known as time-dependent density functional theory (TD-DFT).[14]

Although HK theorems put particle density $n(\mathbf{r})$ as the basic variable, it is still impossible to calculate any property of a system because the universal functional $F[n(\mathbf{r})]$ is unknown. This difficulty was overcome by Kohn and Sham[3] in 1965, who proposed the well known Kohn-Sham ansatz.

2.1.4 The Kohn-Sham (KS) Ansatz

It is the Kohn-Sham (KS) ansatz[3] that puts Hohenberg-Kohn theorems into practical use and makes DFT calculations possible with even a single personal computer. This is part of the reason that DFT became the most popular tool for electronic structure calculations. The KS ansatz was so successful that Kohn was honored the Nobel prize in chemistry in 1998.

The KS ansatz is to replace the original many-body system by an auxiliary independent-particle system and assume that the two systems have exactly the same ground state density. It maps the original interacting system with real potential onto a fictitious non-interacting system whereby the electrons move within an effective Kohn-Sham single-particle potential $V_{KS}(\mathbf{r})$. For the auxiliary independent-particle

system, the auxiliary Hamiltonian is

$$\hat{H}_{KS} = -\frac{1}{2}\nabla^2 + V_{KS}(\mathbf{r}) \quad (2.1.18)$$

in atomic units $\hbar = m_e = e = 4\pi/\epsilon_0 = 1$. For a system with N independent electrons, the ground state is obtained by solving the N one-electron Schrödinger equations,

$$\left(\frac{1}{2}\nabla^2 + V_{KS}(\mathbf{r})\right)\psi_i(\mathbf{r}) = \varepsilon_i\psi_i(\mathbf{r}) \quad (2.1.19)$$

where there is one electron in each of the N orbitals $\psi_i(\mathbf{r})$ with the lowest eigenvalues ε_i . The density of the auxiliary system is constructed from:

$$n(\mathbf{r}) = \sum_{i=1}^N |\psi_i(\mathbf{r})|^2 \quad (2.1.20)$$

which is subject to the conservation condition:

$$\int n(\mathbf{r})d\mathbf{r} = N \quad (2.1.21)$$

The non-interacting independent-particle kinetic energy $T_S[n(\mathbf{r})]$ is given by,

$$T_S[n(\mathbf{r})] = -\frac{1}{2} \sum_{i=1}^N \int \psi_i^*(\mathbf{r})\nabla^2\psi_i(\mathbf{r})d\mathbf{r} \quad (2.1.22)$$

Then the universal functional $F[n(\mathbf{r})]$ was rewritten as

$$F[n(\mathbf{r})] = T_S[n(\mathbf{r})] + E_H[n(\mathbf{r})] + E_{XC}[n(\mathbf{r})] \quad (2.1.23)$$

where $E_H[n(\mathbf{r})]$ is the classic electrostatic (Hartree) energy of the electrons,

$$E_H[n(\mathbf{r})] = \frac{1}{2} \int \int \frac{n(\mathbf{r})n(\mathbf{r}')}{|\mathbf{r} - \mathbf{r}'|} d\mathbf{r}d\mathbf{r}' \quad (2.1.24)$$

and $E_{XC}[n(\mathbf{r})]$ is the XC energy, which contains the difference between the exact and non-interacting kinetic energies and also the non-classical contribution to the electron-electron interactions, of which the exchange energy is a part. Since the ground state energy of a many-electron system can be obtained by minimizing the energy functional $E[n(\mathbf{r})] = F[n(\mathbf{r})] + \int n(\mathbf{r})V_{ext}(\mathbf{r})d\mathbf{r}$, subject to the constraint that the number of electrons N is conserved,

$$\delta\{F[n(\mathbf{r})] + \int n(\mathbf{r})V_{ext}(\mathbf{r})d\mathbf{r} - \mu(\int n(\mathbf{r})d\mathbf{r} - N)\} = 0 \quad (2.1.25)$$

and the resulting equation is

$$\begin{aligned} \mu &= \frac{\delta F[n(\mathbf{r})]}{\delta n(\mathbf{r})} + V_{ext}(\mathbf{r}) \\ &= \frac{\delta T_S[n(\mathbf{r})]}{\delta n(\mathbf{r})} + V_{KS}(\mathbf{r}) \end{aligned} \quad (2.1.26)$$

where μ is the chemical potential,

$$\begin{aligned} V_{KS}(\mathbf{r}) &= V_{ext}(\mathbf{r}) + V_H(\mathbf{r}) + V_{XC}(\mathbf{r}) \\ &= V_{ext}(\mathbf{r}) + \frac{\delta E_H[n(\mathbf{r})]}{\delta n(\mathbf{r})} + \frac{\delta E_{XC}[n(\mathbf{r})]}{\delta n(\mathbf{r})} \end{aligned} \quad (2.1.27)$$

is the KS one-particle potential with the Hartree potential $V_H(\mathbf{r})$

$$\begin{aligned} V_H(\mathbf{r}) &= \frac{\delta E_H[n(\mathbf{r})]}{\delta n(\mathbf{r})} \\ &= \int \frac{n(\mathbf{r}')}{|\mathbf{r} - \mathbf{r}'|} d\mathbf{r}' \end{aligned} \quad (2.1.28)$$

and the XC potential $V_{XC}(\mathbf{r})$

$$V_{XC}(\mathbf{r}) = \frac{\delta E_{XC}[n(\mathbf{r})]}{\delta n(\mathbf{r})} \quad (2.1.29)$$

Equations (2.1.19), (2.1.20), (2.1.27) together are the well-known KS equations, which must be solved self-consistently because $V_{KS}(\mathbf{r})$ depends on the density through the XC potential. In order to calculate the density, the N equations in Eq. (2.1.19) have to be solved in KS theory as opposed to one equation in the TF approach. However an advantage of the KS method is that as the complexity of a system increases, due to N increasing, the problem becomes no more difficult, only the number of single-particle equations to be solved increases.

Although exact in principle, the KS theory is approximate in practice because of the unknown XC energy functional $E_{XC}[n(\mathbf{r})]$. An implicit definition of $E_{XC}[n(\mathbf{r})]$ can be given as

$$E_{XC}[n(\mathbf{r})] = T[n(\mathbf{r})] - T_S[n(\mathbf{r})] + E_{int}[n(\mathbf{r})] - E_H[n(\mathbf{r})] \quad (2.1.30)$$

where $T[n(\mathbf{r})]$ and $E_{int}[n(\mathbf{r})]$ are the exact kinetic and electron-electron interaction energies of the interacting system respectively. It is crucial to have an accurate XC energy functional $E_{XC}[n(\mathbf{r})]$ or potential $V_{XC}(\mathbf{r})$ in order to give a satisfactory description of a realistic condensed-matter system. The most widely used approx-

imations for the XC potential are the local density approximation (LDA) and the generalized-gradient approximation (GGA).

The KS energy eigenvalues of Eq. (2.1.19) are not for the original interacting many-body system and have no physical meaning. They cannot be interpreted as one-electron excitation energies of the interacting many-body system, i.e., they are not the energies to add or subtract from the interacting many-body system, because the total energy of the interacting system is not a sum of all the eigenvalues of occupied states in equation (2.1.19), i.e., $E_{tot} \neq \sum_i^{occ.} \varepsilon_i$. The only exception is the highest eigenvalue in a finite system which is the negative of the ionization energy, $-I$, because it determines the asymptotic long-range density of the bound system which is assumed to be exact. No other eigenvalue is guaranteed to be correct by the KS theory. Nevertheless, within the KS theory itself, the eigenvalues have a well-defined meaning and they are used to construct physically meaningful quantities. They have a definite mathematical meaning, often known as the Slater-Janak theorem. The eigenvalue is the derivative of the total energy with respect to occupation of a state, i. e.

$$\begin{aligned} \varepsilon_i &= \frac{dE_{total}}{dn_i} \\ &= \int \frac{dE_{total}}{dn(\mathbf{r})} \frac{dn(\mathbf{r})}{dn_i} d\mathbf{r} \end{aligned} \quad (2.1.31)$$

2.1.5 Local (Spin) Density Approximation (L(S)DA)

The KS ansatz successfully maps the original interacting many-body system onto a set of independent single-particle equations and makes the problem much easier. In the meantime, without knowing the exact form of the XC energy functional $E_{XC}[n(\mathbf{r})]$, the KS equations are unsolvable. Although the exact XC energy functional $E_{XC}[n(\mathbf{r})]$ should be very complicated, simple but successful approximations to it have been

made, which not only predict various properties of many systems reasonably well but also greatly reduce computational costs, leading to the wide use of DFT for electronic structure calculations. Of these approximations, the local density approximation (LDA) is the most widely used one. In LDA, the XC energy per electron at a point \mathbf{r} is considered the same as that for a homogeneous electron gas (HEG) that has the same electron density at the point \mathbf{r} . The total exchange-correlation functional $E_{XC}[n(\mathbf{r})]$ can be written as,

$$\begin{aligned} E_{XC}^{LDA}[n(\mathbf{r})] &= \int n(\mathbf{r})\epsilon_{XC}^{hom}(n(\mathbf{r}))d\mathbf{r} \\ &= \int n(\mathbf{r})[\epsilon_X^{hom}(n(\mathbf{r})) + \epsilon_C^{hom}(n(\mathbf{r}))]d\mathbf{r} \\ &= E_X^{LDA}[n(\mathbf{r})] + E_C^{LDA}[n(\mathbf{r})] \end{aligned} \quad (2.1.32)$$

for spin unpolarized systems and

$$E_{XC}^{LSDA}[n_\uparrow(\mathbf{r}), n_\downarrow(\mathbf{r})] = \int n(\mathbf{r})\epsilon_{XC}^{hom}(n_\uparrow(\mathbf{r}), n_\downarrow(\mathbf{r}))d\mathbf{r} \quad (2.1.33)$$

for spin polarized systems[15], where the XC energy density $\epsilon_{XC}^{hom}(n(\mathbf{r}))$ is a function of the density alone, and is decomposed into exchange energy density $\epsilon_X^{hom}(n(\mathbf{r}))$ and correlation energy density $\epsilon_C^{hom}(n(\mathbf{r}))$ so that the XC energy functional is decomposed into exchange energy functional $E_X^{LDA}[n(\mathbf{r})]$ and correlation energy functional $E_C^{LDA}[n(\mathbf{r})]$ linearly. Note that $E_{XC}^{LSDA}[n_\uparrow(\mathbf{r}), n_\downarrow(\mathbf{r})]$ is not written in the way

$$E_{XC}^{LSDA}[n_\uparrow(\mathbf{r}), n_\downarrow(\mathbf{r})] = \int [n_\uparrow(\mathbf{r})\epsilon_{XC,\uparrow}^{hom}(n_\uparrow(\mathbf{r})) + n_\downarrow(\mathbf{r})\epsilon_{XC,\downarrow}^{hom}(n_\downarrow(\mathbf{r}))]d\mathbf{r} \quad (2.1.34)$$

as one may think. The exchange energy functional $E_X^{LDA}[n(\mathbf{r})]$ employs the expression for a HEG by using it pointwise, which is known analytically as[9]

$$\begin{aligned} E_X^{LDA}[n(\mathbf{r})] &= \int n(\mathbf{r})\epsilon_X^{hom}(n(\mathbf{r}))d\mathbf{r} \\ &= -\frac{3}{4}\left(\frac{3}{\pi}\right)^{1/3} \int n(\mathbf{r})^{4/3}d\mathbf{r} \end{aligned} \quad (2.1.35)$$

where

$$\epsilon_X^{hom}(n(\mathbf{r})) = -\frac{3}{4}\left(\frac{3}{\pi}\right)^{1/3}n(\mathbf{r})^{1/3} \quad (2.1.36)$$

is the exchange energy density of the unpolarized HEG introduced first by Dirac.[9] Analytic expressions for the correlation energy of the HEG are unknown except in the high and low density limits corresponding to infinitely weak and infinitely strong correlations. The expression of the correlation energy density of the HEG at high density limit has the form

$$\epsilon_C = A\ln(r_s) + B + r_s(C\ln(r_s) + D) \quad (2.1.37)$$

and the low density limit takes the form

$$\epsilon_C = \frac{1}{2}\left(\frac{g_0}{r_s} + \frac{g_1}{r_s^{3/2}} + \dots\right) \quad (2.1.38)$$

where the Wigner-Seitz radius r_s is related to the density as

$$\frac{4}{3}\pi r_s^3 = \frac{1}{n}. \quad (2.1.39)$$

In order to obtain accurate values of the correlation energy density at intermediate density, accurate quantum Monte Carlo (QMC) simulations for the energy of the

HEG are needed and have been performed at several intermediate density values.[16] Most local density approximations to the correlation energy density interpolate these accurate values from QMC simulations while reproducing the exactly known limiting behavior. Depending on the analytic forms used for ϵ_C , different local density approximations were proposed including Vosko-Wilk-Nusair[17] (VWM), Perdew-Zunger[18] (PZ81), Cole-Perdew[19] (CP) and Perdew-Wang[20] (PW92).

For spin polarized systems, the exchange energy functional is known exactly from the result of spin-unpolarized functional:

$$E_X[n_\uparrow(\mathbf{r}), n_\downarrow(\mathbf{r})] = \frac{1}{2}(E_X[2n_\uparrow(\mathbf{r})] + E_X[2n_\downarrow(\mathbf{r})]) \quad (2.1.40)$$

The spin-dependence of the correlation energy density is approached by the relative spin-polarization:

$$\zeta(\mathbf{r}) = \frac{n_\uparrow(\mathbf{r}) - n_\downarrow(\mathbf{r})}{n_\uparrow(\mathbf{r}) + n_\downarrow(\mathbf{r})} \quad (2.1.41)$$

The spin correlation energy density $\epsilon_C(n(\mathbf{r}), \zeta(\mathbf{r}))$ is so constructed to interpolate extreme values $\zeta = 0, \pm 1$, corresponding to spin-unpolarized and ferromagnetic situations.

The XC potential $V_{XC}(\mathbf{r})$ in LDA is

$$\begin{aligned} V_{XC}^{LDA} &= \frac{\delta E_{XC}^{LDA}}{\delta n(\mathbf{r})} \\ &= \epsilon_{XC}(n(\mathbf{r})) + n(\mathbf{r}) \frac{\partial \epsilon_{XC}(n(\mathbf{r}))}{\partial n(\mathbf{r})} \end{aligned} \quad (2.1.42)$$

Within LDA, the total energy of a system is:

$$\begin{aligned}
E_{tot}[n(\mathbf{r})] &= T_S[n(\mathbf{r})] + E_H[n(\mathbf{r})] + E_{XC}[n(\mathbf{r})] + \int n(\mathbf{r})V_{ext}(\mathbf{r})d\mathbf{r} \\
&= \sum_i^{occ.} \langle \psi_i(\mathbf{r}) | -\frac{1}{2}\nabla^2 | \psi_i(\mathbf{r}) \rangle + E_H[n(\mathbf{r})] + E_{XC}[n(\mathbf{r})] + \int n(\mathbf{r})V_{ext}(\mathbf{r})d\mathbf{r} \\
&= \sum_i^{occ.} \langle \psi_i(\mathbf{r}) | -\frac{1}{2}\nabla^2 + V_H(\mathbf{r}) + V_{XC}(\mathbf{r}) + V_{ext}(\mathbf{r}) | \psi_i(\mathbf{r}) \rangle \\
&\quad - \sum_i^{occ.} \langle \psi_i(\mathbf{r}) | V_H(\mathbf{r}) | \psi_i(\mathbf{r}) \rangle - \sum_i^{occ.} \langle \psi_i(\mathbf{r}) | V_{XC}(\mathbf{r}) | \psi_i(\mathbf{r}) \rangle \\
&\quad - \sum_i^{occ.} \langle \psi_i(\mathbf{r}) | V_{ext}(\mathbf{r}) | \psi_i(\mathbf{r}) \rangle + E_H[n(\mathbf{r})] + E_{XC}[n(\mathbf{r})] + \int n(\mathbf{r})V_{ext}(\mathbf{r})d\mathbf{r} \\
&= \sum_i^{occ.} \varepsilon_i - \frac{1}{2} \int \frac{n(\mathbf{r})n(\mathbf{r}')}{|\mathbf{r} - \mathbf{r}'|} d\mathbf{r}d\mathbf{r}' + \int n(\mathbf{r})(\epsilon_{XC}(\mathbf{r}) - V_{XC}(\mathbf{r}))d\mathbf{r} \\
&= \sum_i^{occ.} \varepsilon_i - \frac{1}{2} \int \frac{n(\mathbf{r})n(\mathbf{r}')}{|\mathbf{r} - \mathbf{r}'|} d\mathbf{r}d\mathbf{r}' - \int n(\mathbf{r})^2 \frac{\partial \epsilon_{XC}(n(\mathbf{r}))}{\partial n(\mathbf{r})} d\mathbf{r}.
\end{aligned} \tag{2.1.43}$$

As mentioned before, $E_{tot} \neq \sum_i^{occ.} \varepsilon_i$.

The LDA is very simple, corrections to the exchange-correlation energy due to the inhomogeneities in the electronic density are ignored. However it is surprisingly successful and even works reasonably well in systems where the electron density is rapidly varying. One reason is that LDA gives the correct sum rule to the exchange-correlation hole. That is, there is a total electronic charge of one electron excluded from the neighborhood of the electron at \mathbf{r} . In the meantime, it tends to underestimate atomic ground state energies and ionization energies, while overestimating binding energies. It makes large errors in predicting the energy gaps of some semiconductors. Its success and limitations lead to approximations of the XC energy functional beyond the LDA, through the addition of gradient corrections to incorporate longer range gradient effects (GGA), as well as LDA+U method to account for

the strong correlations of the d electrons in transition elements and f electrons in lanthanides and actinides.

2.1.6 Generalized-Gradient Approximation (GGA)

As mentioned above, the LDA neglects the inhomogeneities of the real charge density which could be very different from the HEG. The XC energy of inhomogeneous charge density can be significantly different from the HEG result. This leads to the development of various generalized-gradient approximations (GGAs) which include density gradient corrections and higher spatial derivatives of the electron density and give better results than LDA in many cases. Three most widely used GGAs are the forms proposed by Becke[21] (B88), Perdew *et al.*[22], and Perdew, Burke and Enzerhof[23] (PBE).

The definition of the XC energy functional of GGA is the generalized form in Eq. (2.1.33) of LSDA to include corrections from density gradient $\nabla n(\mathbf{r})$ as

$$\begin{aligned} E_{XC}^{GGA}[n_{\uparrow}(\mathbf{r}), n_{\downarrow}(\mathbf{r})] &= \int n(\mathbf{r}) \epsilon_{XC}^{hom}(n_{\uparrow}(\mathbf{r}), n_{\downarrow}(\mathbf{r}), |\nabla n_{\uparrow}(\mathbf{r})|, |\nabla n_{\downarrow}(\mathbf{r})|, \dots) d\mathbf{r} \\ &= \int n(\mathbf{r}) \epsilon_X^{hom}(n(\mathbf{r})) F_{XC}(n_{\uparrow}(\mathbf{r}), n_{\downarrow}(\mathbf{r}), |\nabla n_{\uparrow}(\mathbf{r})|, |\nabla n_{\downarrow}(\mathbf{r})|, \dots) d\mathbf{r} \end{aligned} \quad (2.1.44)$$

where F_{XC} is dimensionless and $\epsilon_X^{hom}(n(\mathbf{r}))$ is the exchange energy density of the unpolarized HEG as given in Eq. (2.1.36). F_{XC} can be decomposed linearly into exchange contribution F_X and correlation contribution F_C as $F_{XC} = F_X + F_C$. For a detailed treatment of F_X and F_C in different GGAs, please refer to Chapter 8 of the book by Martin.[24]

GGA generally works better than LDA, in predicting bond length and binding energy of molecules, crystal lattice constants, and so on, especially in systems where

the charge density is rapidly varying. However GGA sometimes overcorrects LDA results in ionic crystals where the lattice constants from LDA calculations fit well with experimental data but GGA will overestimate it. Nevertheless, both LDA and GGA perform badly in materials where the electrons tend to be localized and strongly correlated such as transition metal oxides and rare-earth elements and compounds. This drawback leads to approximations beyond LDA and GGA.

2.1.7 LDA+U Method

Strongly correlated systems usually contain transition metal or rare-earth metal ions with partially filled d or f shells. Because of the orbital-independent potentials in L(S)DA and GGA, they cannot properly describe such systems. For example, L(S)DA predicts transition metal oxides to be metallic with itinerant d electrons because of the partially filled d shells. Instead, these transition metal oxides are Mott insulators and the d electrons are well localized. In order to properly describe these strongly correlated systems, orbital-dependent potentials should be used for d and f electrons. There are several approaches available nowadays to incorporate the strong electron-electron correlations between d electrons and f electrons. Of these methods including the self-interaction correction (SIC) method [25], Hartree-Fock (HF) method [26], and GW approximation [27], LDA+U method [28] is the most widely used one.

In the LDA+U method, the electrons are divided into two classes: delocalized s , p electrons which are well described by LDA (GGA) and localized d or f electrons for which an orbital-dependent term $\frac{1}{2}U \sum_{i \neq j} n_i n_j$ should be used to describe Coulomb $d-d$ or $f-f$ interaction, where n_i are d - or f -orbital occupancies. The total

energy in L(S)DA+U method is given as[28]:

$$E_{tot}^{LDA+U}[\rho_\sigma(\mathbf{r}), \{n_\sigma\}] = E^{LSDA}[\rho_\sigma(\mathbf{r})] + E^U[\{n_\sigma\}] - E_{dc}[\{n_\sigma\}] \quad (2.1.45)$$

where σ denotes the spin index, $\rho_\sigma(\mathbf{r})$ is the electron density for spin- σ electrons and $\{n_\sigma\}$ is the density matrix of d or f electrons for spin- σ , the first term is the standard LSDA energy functional, the second term is the electron-electron Coulomb interaction energy given by[28]

$$\begin{aligned} E^U[\{n\}] = & \frac{1}{2} \sum_{\{m\}, \sigma} \{ \langle m, m'' | V_{ee} | m', m''' \rangle n_{mm', \sigma} n_{m''m''', -\sigma} \\ & - (\langle m, m'' | V_{ee} | m', m''' \rangle - \langle m, m'' | V_{ee} | m''', m' \rangle) n_{mm', \sigma} n_{m''m''', \sigma} \} \end{aligned} \quad (2.1.46)$$

where m denotes the magnetic quantum number, and V_{ee} are the screened Coulomb interactions among the d or f electrons. The last term in Eq. (2.1.45) is the double-counting term which removes an averaged LDA energy contribution of these d or f electrons from the LDA energy. It is given by[28]

$$E_{dc}[\{n_\sigma\}] = \frac{1}{2}UN(N-1) - \frac{1}{2}J[N_\uparrow(N_\uparrow-1) + N_\downarrow(N_\downarrow-1)] \quad (2.1.47)$$

where $N_\sigma = Tr(n_{mm', \sigma})$ and $N = N_\uparrow + N_\downarrow$. U and J are screened Coulomb and exchange parameters.

As a simple approximation, if the exchange and non-sphericity is neglected, Eq. (2.1.45) is simplified to[28]

$$E_{tot}^{LDA+U} = E_{LDA} + \frac{1}{2}U \sum_{i \neq j} n_i n_j - \frac{1}{2}UN(N-1) \quad (2.1.48)$$

The orbital energies ε_i are derivatives of Eq. (2.1.48) with respect to orbital occupations n_i :

$$\varepsilon_i = \frac{\partial E}{\partial n_i} = \varepsilon_{LDA} + U\left(\frac{1}{2} - n_i\right) \quad (2.1.49)$$

In this simple consideration, the LDA orbital energies are shifted by $-U/2$ for occupied orbitals ($n_i = 1$) and by $+U/2$ for unoccupied orbitals ($n_i = 0$), resulting in lower and upper Hubbard bands separated by U , which opens a gap at the Fermi energy in transition metal oxides.

In the general case, the effective single-particle potential is

$$\begin{aligned} V_{mm',\sigma} &= \frac{\partial(E^U[\{n_\sigma\}] - E_{dc}[\{n_\sigma\}])}{\partial n_{mm',\sigma}} \\ &= \sum_{\{m\}} \{ \langle m, m'' | V_{ee} | m', m''' \rangle n_{m''m''',-\sigma} - (\langle m, m'' | V_{ee} | m' m''' \rangle \\ &\quad - \langle m, m'' | V_{ee} | m''', m' \rangle) n_{m''m''',\sigma} \} - U\left(N - \frac{1}{2}\right) + J\left(N_\sigma - \frac{1}{2}\right) \end{aligned} \quad (2.1.50)$$

which is used in the effective single-particle Hamiltonian

$$\hat{H} = \hat{H}_{LSDA} + \sum_{mm'} |inlm\sigma\rangle V_{mm',\sigma} \langle inlm'\sigma| \quad (2.1.51)$$

where i denotes the site, n the main quantum number, and l the orbital quantum number.

The matrix elements of V_{ee} can be expressed in terms of complex spherical harmonics and effective Slater integrals F_k as[29]

$$\langle m, m'' | V_{ee} | m', m''' \rangle = \sum_k a_k(m, m', m'', m''') F_k \quad (2.1.52)$$

where $0 \leq k \leq 2l$ and

$$a_k(m, m', m'', m''') = \frac{4\pi}{2k+1} \sum_{q=-k}^k \langle lm | Y_{kq} | lm' \rangle \langle lm'' | Y_{kq}^* | lm''' \rangle \quad (2.1.53)$$

$$F_k \approx \int_0^\infty \int_0^\infty dr_1 dr_2 (r_1 R_i(r_1))^2 (r_2 R_i(r_2))^2 \frac{r_{<}^k}{r_{>}^{k+1}}, \quad \text{for } k > 0 \quad (2.1.54)$$

Here, $r_{<}$ is the smaller of r_1 and r_2 and $r_{>}$ the larger. The relations between the Slater integrals and the screened Coulomb and exchange parameters U and J are:

$$U = F_0; \quad J = (F_2 + F_4)/14, \quad \text{for 3d or 4d systems,} \quad (2.1.55)$$

$$U = F_0; \quad J = (286F_2 + 195F_4 + 250F_6)/6435, \quad \text{for 4f or 5f systems,}$$

The ratio F_4/F_2 and F_6/F_2 are taken from atomic situations. $F_4/F_2 \sim 0.625$ for 3d transition elements[30] and $F_4/F_2 \sim 2/3, F_6/F_2 \sim 1/2$ for 4f lanthanides. The screened Coulomb parameter U can be calculated from the constraint LDA method[31], so that the LDA+ U method remains a first principle method (no adjustable parameters).

For the double-counting term, there are two different treatments: the so-called around mean field (AMF) and fully localized limit (FLL) (also called atomic limit) approaches. The former is more suitable for small U systems[32] and the latter is more suitable for large U systems.[33] The energies for the double counting are given by[34]

$$\begin{aligned} E_{AMF}^{dc} &= \frac{1}{2} \sum_{m \neq m', \sigma \sigma'} [U_{mm'} - \delta_{\sigma, \sigma'} J_{mm'}] \bar{n} \bar{n} \\ &= \frac{1}{2} U N^2 - \frac{U + 2lJ}{2l+1} \frac{1}{2} \sum_{\sigma} N_{\sigma}^2 \end{aligned} \quad (2.1.56)$$

$$\begin{aligned}
E_{FLL}^{dc} &= \frac{1}{2} \sum_{m \neq m', \sigma \sigma'} [U_{mm'} - \delta_{\sigma, \sigma'} J_{mm'}] \bar{n}_\sigma \bar{n}_{\sigma'} \\
&= \frac{1}{2} U N(N-1) - \frac{1}{2} J \sum_{\sigma} N_{\sigma} (N_{\sigma} - 1)
\end{aligned} \tag{2.1.57}$$

where $\bar{n} = N/2(2l+1)$ is the average occupation of the correlated orbitals and $\bar{n}_{\sigma} = N_{\sigma}/(2l+1)$ is the average occupation of a single spin of the correlated orbitals. Note that, Eq. (2.1.57) is the same as Eq. (2.1.47). For a detailed comparison of the different double counting terms, please refer to [34].

2.1.8 Solving Kohn-Sham Equations

By using independent-particle methods, the KS equations provide a way to obtain the exact density and energy of the ground state of a condensed matter system. The KS equations must be solved consistently because the effective KS potential V_{KS} and the electron density $n(\mathbf{r})$ are closely related. This is usually done numerically through some self-consistent iterations as shown in Fig. 2.1.1. The process starts with an initial electron density, usually a superposition of atomic electron density, then the effective KS potential V_{KS} is calculated and the KS equation is solved with single-particle eigenvalues and wavefunctions, a new electron density is then calculated from the wavefunctions. After this, self-consistent condition(s) is checked. Self-consistent condition(s) can be the change of total energy or electron density from the previous iteration or total force acting on atoms is less than some chosen small quantity, or a combination of these individual conditions. If the self-consistency is not achieved, the calculated electron density will be mixed with electron density from previous iterations to get a new electron density. A new iteration will start with the new electron density. This process continues until self-consistency is reached. After the

self-consistency is reached, various quantities can be calculated including total energy, forces, stress, eigenvalues, electron density of states, band structure, etc..

The most timing consuming step in the whole process is to solve KS equation with a given KS potential V_{KS} . There are several different schemes to the calculation of the independent-particle electronic states in solids where boundary conditions are applied. They are basically classified into three types[24]:

1. Plane waves.

In this method, the wavefunctions (eigenfunctions of the KS equations) are expanded in a complete set of plane waves $e^{i\mathbf{k}\cdot\mathbf{r}}$ and the external potential of nuclei are replaced by pseudopotentials which include effects from core electrons. Such pseudopotentials have to satisfy certain conditions. Most widely used pseudopotentials nowadays include norm-conserving pseudopotentials[35] (NCPPs) and ultrasoft pseudopotentials[36] (USPPs). In norm-conserving pseudopotentials, five requirements should be satisfied:

- a.** the pseudo valence eigenvalues should agree with all-electron valence eigenvalues for the chosen atomic reference configuration;
- b.** the pseudo valence wavefunctions should match all-electron valence wavefunctions beyond a chosen core radius R_c ;
- c.** the logarithmic derivatives of the pseudo and the all-electron wavefunctions should agree at R_c ,
- d.** the integrated charge inside R_c for each wavefunction agrees (norm-conservation); and
- e.** the first energy derivative of the logarithmic derivatives of the all-electron and pseudo wavefunctions agree at R_c , and therefore for all $r \leq R_c$.

In ultrasoft pseudopotentials, the norm-conservation condition is not required so

that the pseudo wavefunctions are much softer than pseudo wavefunctions in norm-conserving pseudopotentials. As a result, it significantly reduces the number of plane waves needed to expand the wavefunctions (smaller energy cutoff for wavefunctions).

Plane waves have played an important role in the early orthogonalized plane wave[37, 38, 39] (OPW) calculations and are generalized to modern projector augmented wave[40, 41, 42] (PAW) method. Because of the simplicity of plane waves and pseudopotentials, computational load is significantly reduced in these methods and therefore it is most suitable for calculations of large systems. In this method, forces can be easily calculated and it can be easily developed to quantum molecular dynamics simulations as well as response to (small) external perturbations. However, results from plane wave methods using pseudopotentials are usually less accurate than results from all-electron full potential methods. And great care should be taken when one generates a pseudopotential and it should be tested to match results from all-electron calculations. The most widely used codes using plane waves and pseudopotentials are plane wave self-consistent field (now known as Quantum ESPRESSO)[43] (PWscf), ABINIT[44], VASP[45] (which uses PAW method too).

2. Localized atomic(-like) orbitals.

The most well-known methods in this category are linear combination of atomic orbitals[46] (LCAO), also called tight-binding[46] (TB) and full potential non-orthogonal local orbital[47] (FPLO). The basic idea of these methods is to use atomic orbitals as the basis set to expand the one-electron wavefunction in KS equations.

In FPLO, in addition to the spherical average of the crystal potential, a so-called confining potential $V_{con} = (r/r_0)^m$ is used to compress the long range tail of the local orbitals (wave functions), where m is the confining potential exponent with a typical value of 4, $r_0 = (x_0 r_{NN}/2)^{3/2}$ is a compression parameter with x_0 being

a dimensionless parameter and r_{NN} the nearest neighbor distance. Therefore, the atomic-like potential is written as

$$V_{at}(r) = -(1/4\pi) \int V(\mathbf{r} - \mathbf{R} - \boldsymbol{\tau}) d^3\mathbf{r} + V_{con}(r), \quad (2.1.58)$$

where the first term is the spherical average of the crystal potential mentioned above. For systems containing atom(s) with partially filled $4f$ and $5f$ shells, the confining potential exponent m needs to be increased to 5 or 6. In practice, the dimensionless parameter x_0 is taken as a variational parameter in the self-consistent procedure.

3. Atomic sphere methods.

Methods in the class can be considered as a combination of plane wave method and localized atomic orbitals. It uses localized atomic orbital presentation near the nuclei and plane waves in the interstitial region. The most widely used methods are (full potential) linear muffin-tin orbital[48] (LMTO) as implemented in LMTART[49] by Dr. Savrasov and (full potential) linear augment plane wave[48, 50] (LAPW) as implemented in WIEN2K[51].

2.2 Linear Response Calculations and Superconductivity

2.2.1 Lattice Dynamics and Phonons

To calculate the lattice dynamical properties, we have linear response method[52] and density functional perturbation theory (DFPT) [53], which are closely related. In both methods, it is essential to calculate the second-order perturbation of DFT total energy, i.e., $\delta^2 E$, in the framework of density functional theory. The perturbation

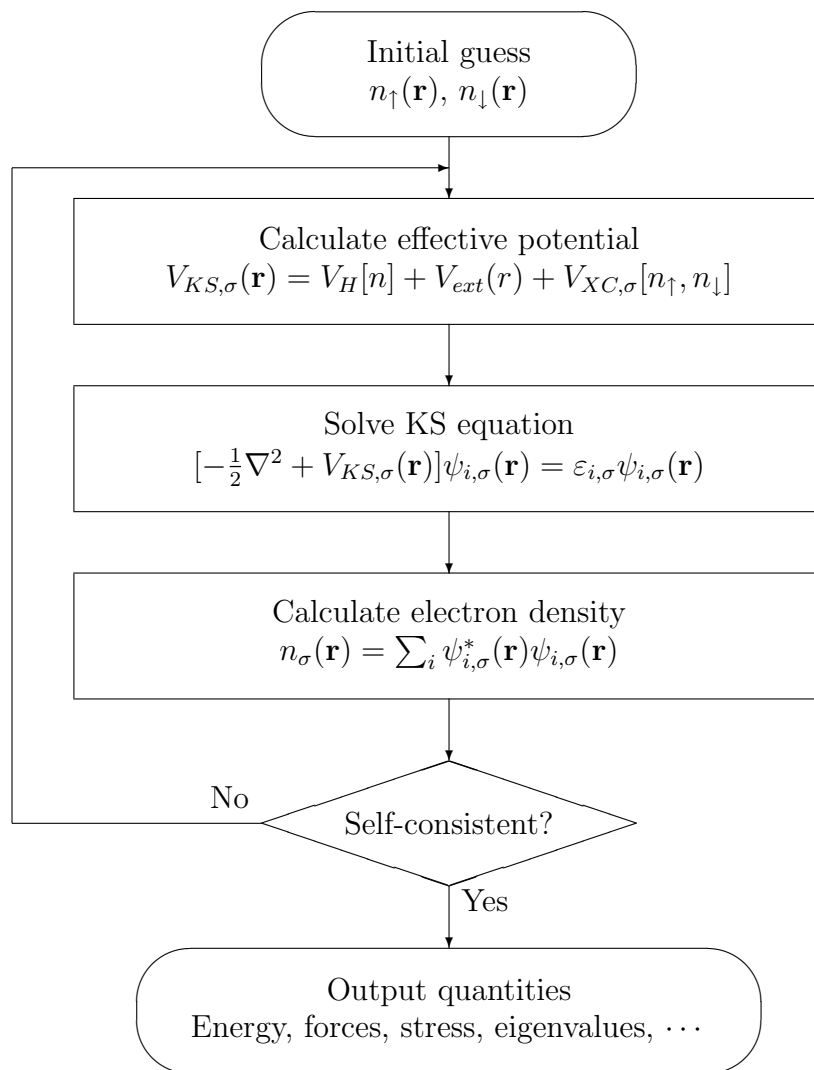


Figure 2.1.1: Flowchart of self-consistency loop for solving KS equations.

is induced by small displacements $\delta\mathbf{R}$ of the nuclei from their equilibrium positions, which result in changes in the external potential V_{ext} , the wave functions Ψ of the KS equations and hence the electron charge density. $\delta^2 E$ is obtained by expanding the DFT total energy with respect to the changes in the wave functions to first order and external potentials up to second order. Detailed expressions can be found in Ref[52, 53].

Phonon spectra can be obtained by first calculating the dynamical matrix

$$D_{ij}(\mathbf{q}) = \sum_{\mathbf{R}'} e^{-i\mathbf{q}\cdot\mathbf{R}'} \frac{\partial^2 E}{\partial u_i(\mathbf{R} + \mathbf{R}') \partial u_j(\mathbf{R})} \quad (2.2.1)$$

with respect to the atomic displacements $\mathbf{u}(\mathbf{R})$ for each atom in each direction, (i, j=1, 2, 3, corresponding to x, y and z directions), and then by solving the equation

$$D(\mathbf{q})\vec{\epsilon} = M\omega_{\mathbf{q}}^2\vec{\epsilon} \quad (2.2.2)$$

which gives the phonon frequencies $\omega_{\mathbf{q}}$ of the phonons with wave vector \mathbf{q} , where M is a diagonal matrix with the atomic masses on the diagonal.

2.2.2 Electron-Phonon Interaction and \mathbf{T}_c

Electron-phonon interaction plays a crucial role in conventional superconductivity. It provides the attractive interaction between electrons needed in BCS theory in order to form Cooper pairs. The physical picture is that the first electron attracts its nearby positive ions (to form phonons) which polarizes its nearby environment leading to a domain with positive charges, which in turn attracts the second electron, resulting in an effective attractive interaction between electrons. A net attractive interaction between electrons can be obtained if the above attraction is strong enough to override

the repulsive screened Coulomb interaction.

In the framework of density functional linear-response method, the electron-phonon (EP) interaction can be calculated by evaluating the EP matrix element[54]

$$g_{\mathbf{k}+\mathbf{q}j',\mathbf{k}j}^{\mathbf{q}\nu} = \langle \mathbf{k} + \mathbf{q}j' | \delta^{\mathbf{q}\nu} V_{eff} | \mathbf{k}j \rangle \quad (2.2.3)$$

which is the interaction between electronic potential and phonon mode $\omega_{\mathbf{q}\nu}$, or in other words, it is the probability of scattering from the one-electron state $|\mathbf{k}j\rangle$ to the state $|\mathbf{k} + \mathbf{q}j'\rangle$ via the phonon $\omega_{\mathbf{q}\nu}$, where $\delta^{\mathbf{q}\nu} V_{eff}$ is the change in the effective potential induced by the presence of a phonon mode $\omega_{\mathbf{q}\nu}$, and $\psi_{\mathbf{k}j}$ and $\psi_{\mathbf{k}+\mathbf{q}j'}$ have the Fermi energy ε_F .

The phonon linewidth $\gamma_{\mathbf{q}\nu}$ can be evaluated as

$$\gamma_{\mathbf{q}\nu} = 2\pi\omega_{\mathbf{q}\nu} \sum_{\mathbf{k}j j'} |g_{\mathbf{k}+\mathbf{q}j',\mathbf{k}j}^{\mathbf{q}\nu}|^2 \delta(\varepsilon_{\mathbf{k}j} - \varepsilon_F) \delta(\varepsilon_{\mathbf{k}+\mathbf{q}j'} - \varepsilon_F). \quad (2.2.4)$$

The electron-phonon spectral distribution functions $\alpha^2 F(\omega)$ can be written in terms of $\gamma_{\mathbf{q}\nu}$,

$$\alpha^2 F(\omega) = \frac{1}{2\pi N(\varepsilon_F)} \sum_{\mathbf{q}\nu} \frac{\gamma_{\mathbf{q}\nu}}{\omega_{\mathbf{q}\nu}} \delta(\omega - \omega_{\mathbf{q}\nu}), \quad (2.2.5)$$

where $N(\varepsilon_F) = \sum_{\mathbf{k}} \delta(\varepsilon_{\mathbf{k}} - \varepsilon_F)$ is the electronic density of states (DOS) per atom per spin at the Fermi level, $F(\omega) = \sum_{\mathbf{q}} \delta(\omega - \omega_{\mathbf{q}})$ is the phonon density of states.

The electron-phonon coupling parameter λ is given by

$$\lambda = 2 \int \frac{\alpha^2 F(\omega)}{\omega} d\omega, \quad (2.2.6)$$

and the average phonon frequency $\langle \omega^n \rangle$ is given by

$$\langle \omega^n \rangle = \frac{2}{\lambda} \int \omega^{n-1} \alpha^2 F(\omega) d\omega. \quad (2.2.7)$$

Alternatively, λ can be obtained from the “mode” λ

$$\begin{aligned} \lambda_{\mathbf{q}\nu} &= \frac{\gamma_{\mathbf{q}\nu}}{\pi \omega_{\mathbf{q}\nu}^2 N(\varepsilon_F)} \\ &= \frac{2}{\omega_{\mathbf{q}\nu} N(\varepsilon_F)} \sum_{\mathbf{k}j j'} |g_{\mathbf{k}+\mathbf{q}j', \mathbf{k}j}^{\mathbf{q}, \nu}|^2 \delta(\varepsilon_{\mathbf{k}j} - \varepsilon_F) \delta(\varepsilon_{\mathbf{k}+\mathbf{q}j'} - \varepsilon_F). \end{aligned} \quad (2.2.8)$$

by adding up the mode λ

$$\lambda = \sum_{\mathbf{q}\nu} \lambda_{\mathbf{q}\nu}. \quad (2.2.9)$$

The parameter λ plays the role of the BCS parameter $N(\varepsilon_F)V_{ph}$ and is the most important single number characterizing electron-phonon coupling.[55] In BCS theory, the superconducting critical temperature T_c is given by

$$T_c = 1.13 \langle \omega \rangle e^{-1/N(\varepsilon_F)V_{ph}}, \quad (2.2.10)$$

where V_{ph} is an effective interaction parameter to simplify the complicated net attractive interaction of electrons near Fermi energy, while here it is estimated by the McMillan equation[56]

$$T_c = \frac{\langle \omega \rangle}{1.20} e^{-\frac{1.04(1+\lambda)}{\lambda - \mu^*(1+0.62\lambda)}} \quad (2.2.11)$$

where μ^* is the screened Coulomb pseudopotential. In the strong coupling limit ($\lambda > 1$), the above McMillan equation is generalized to Allen-Dynes equation[57]

$$T_c = \frac{\omega_{log}}{1.20} f_1 f_2 e^{-\frac{1.04(1+\lambda)}{\lambda - \mu^*(1+0.62\lambda)}} \quad (2.2.12)$$

where ω_{log} is the average phonon frequency $\langle \omega^n \rangle^{1/n}$ with $n \rightarrow 0$, and

$$f_1 = (1 + (\lambda/\Lambda_1)^{3/2})^{1/3}, \quad f_2 = 1 + \frac{(\omega_2/\omega_{log} - 1)\lambda^2}{\lambda^2 + \Lambda_2^2} \quad (2.2.13)$$

contain the strong-coupling corrections which are important for $\lambda > 1$, with $\Lambda_1 = 2.46(1 + 3.8\mu^*)$, $\Lambda_2 = 1.82(1 + 6.3\mu^*)(\omega_2/\omega_{log})$, where ω_2 being the average phonon frequency $\langle \omega^n \rangle^{1/n}$ with $n = 2$.

2.2.3 Nesting Function

Note that $\lambda_{\mathbf{q}\nu}$, or $\gamma_{\mathbf{q}\nu}$, incorporates a phase space factor, the “nesting function” [58] $\xi(\mathbf{q})$ describing the phase space that is available for electron-hole scattering across the Fermi surface ($\varepsilon_F = 0$),

$$\xi(\mathbf{q}) = \frac{1}{N} \sum_{\mathbf{k}} \delta(\varepsilon_{\mathbf{k}}) \delta(\varepsilon_{\mathbf{k}+\mathbf{q}}) \propto \oint_{\mathcal{L}} \frac{d\mathcal{L}_{\mathbf{k}}}{|\vec{v}_{\mathbf{k}} \times \vec{v}_{\mathbf{k}+\mathbf{q}}|}. \quad (2.2.14)$$

Here \mathcal{L} is the line of intersection of an undisplaced Fermi surface and one displaced by \mathbf{q} , and $\vec{v}_{\mathbf{k}}$ is the electron velocity at \mathbf{k} . These equations presume the adiabatic limit, in which the phonon frequencies are small compared to any electronic energy scale. This limit applies to elemental Y and Ca, which will be discussed in details in chapter 4.

In the case of the free electron limit, $\varepsilon_{\mathbf{k}} = k^2/2$, in two dimension, the “Fermi surface” is a circle with a radius of k_F (or a cylinder in 3D), the nesting function is

$$\begin{aligned} \xi(\mathbf{q}) &\propto \frac{1}{|\mathbf{q}| \sqrt{4k_F^2 - \mathbf{q}^2}}, & \text{if } |\mathbf{q}| < 2k_F; \\ &= 0, & \text{if } |\mathbf{q}| > 2k_F, \end{aligned} \quad (2.2.15)$$

while in 3D, the Fermi surface is a sphere of radius k_F , the nesting function is then

$$\begin{aligned}\xi(\mathbf{q}) &\propto \frac{\pi}{2|\mathbf{q}|}, & \text{if } |\mathbf{q}| < 2k_F; \\ &= 0, & \text{if } |\mathbf{q}| > 2k_F.\end{aligned}\tag{2.2.16}$$

In real materials, the Fermi surfaces are usually very complicated and the nesting function needs to be calculated numerically.

2.3 Tight Binding Method and Wannier Functions

2.3.1 Local Orbitals and Tight Binding

Tight binding method provides a simple way to calculate electronic band structure and ground state energy, by expanding the wave function $\psi(\mathbf{r})$ in terms of atomic orbitals $\phi_n(\mathbf{r} - \mathbf{R})$ of isolated atoms at each atomic site, or in terms of other local orbitals (eg: Wannier functions). This method is sometimes also regarded as linear combination of atomic orbital (LCAO) approach and applies to non-crystalline materials (eg: molecules) and crystalline materials, although the latter is more common where the atoms are located on a periodic lattice. This approach is valid in systems where the electrons are more localized than itinerant, i.e., the electrons are bound to each atom instead of moving through the crystal. Therefore it applies to insulators and some semiconductors but certainly not simple metals. Recently, the tight binding method became a basic tool in the study of strongly correlated systems where the $3d$ and $4f$ electrons are highly localized.

In tight-binding model, the total Hamiltonian $H(\mathbf{r})$ of the crystal is a sum of the atomic Hamiltonians $H_{at}(\mathbf{r} - \mathbf{R} - \vec{\tau}_i)$ located at each atomic site plus an interaction

term $\delta U(\mathbf{r})$, which is considered as a small perturbation,

$$H(\mathbf{r}) = \sum_{\mathbf{R}} H_{at}(\mathbf{r} - \mathbf{R} - \vec{\tau}_i) + \delta U(\mathbf{r}). \quad (2.3.1)$$

where $\vec{\tau}_i$ is the atomic position to the origin of the cell at \mathbf{R} .

A basis state $\varphi_{ni,\mathbf{k}}(\mathbf{r})$ with wave vector \mathbf{k} (restricted to the first Brillouin zone) can be constructed from the atomic orbitals $\phi_n(\mathbf{r} - \mathbf{R} - \vec{\tau}_i)$, (which satisfy $H_{at}(\mathbf{r})\phi_n(\mathbf{r}) = E_n\phi_n(\mathbf{r})$), according to Bloch theorem

$$\varphi_{ni,\mathbf{k}}(\mathbf{r}) = \frac{1}{\sqrt{N}} \sum_{\mathbf{R}} e^{i\mathbf{k}\cdot(\mathbf{R}+\vec{\tau}_i)} \phi_n(\mathbf{r} - \mathbf{R} - \vec{\tau}_i). \quad (2.3.2)$$

The crystal wave function $\psi_{\mathbf{k}}(\mathbf{r})$ is then constructed from the above basis functions

$$\psi_{\mathbf{k}}(\mathbf{r}) = \sum_{ni} b_{ni}(\mathbf{k}) \varphi_{ni,\mathbf{k}}(\mathbf{r}), \quad (2.3.3)$$

where $b_{ni}(\mathbf{k})$ are coefficients depending on \mathbf{k} . It is easy to show that $\psi_{\mathbf{k}}(\mathbf{r})$ satisfies the Bloch theorem,

$$\psi_{\mathbf{k}}(\mathbf{r} + \mathbf{R}) = e^{i\mathbf{k}\cdot\mathbf{R}} \psi_{\mathbf{k}}(\mathbf{r}). \quad (2.3.4)$$

From the Schrödinger equation,

$$H\psi_{\mathbf{k}} = \varepsilon_{\mathbf{k}}\psi_{\mathbf{k}}, \quad (2.3.5)$$

we have

$$\sum_{nj} H_{mi,nj}(\mathbf{k}) b_{nj}(\mathbf{k}) = \varepsilon_{\mathbf{k}} \sum_{nj} S_{mi,nj}(\mathbf{k}) b_{nj}(\mathbf{k}), \quad (2.3.6)$$

where

$$\begin{aligned}
H_{mi,nj}(\mathbf{k}) &= \int \varphi_{mi,\mathbf{k}}^*(\mathbf{r}) H \varphi_{nj,\mathbf{k}}(\mathbf{r}) d\mathbf{r} \\
&= \frac{1}{N} e^{i\mathbf{k}\cdot(\vec{\tau}_j - \vec{\tau}_i)} \sum_{\mathbf{R}_1, \mathbf{R}_2} e^{i\mathbf{k}\cdot(\mathbf{R}_2 - \mathbf{R}_1)} \int \phi_m^*(\mathbf{r} - \mathbf{R}_1 - \vec{\tau}_i) H \phi_n(\mathbf{r} - \mathbf{R}_2 - \vec{\tau}_j) d\mathbf{r} \\
&= \frac{1}{N} e^{i\mathbf{k}\cdot(\vec{\tau}_j - \vec{\tau}_i)} \sum_{\mathbf{R}_1, \mathbf{R}_2} e^{i\mathbf{k}\cdot(\mathbf{R}_2 - \mathbf{R}_1)} H_{mi,nj}(\mathbf{R}_2 + \vec{\tau}_j - \mathbf{R}_1 - \vec{\tau}_i) \\
&= e^{i\mathbf{k}\cdot(\vec{\tau}_j - \vec{\tau}_i)} \sum_{\mathbf{R}} e^{i\mathbf{k}\cdot\mathbf{R}} H_{mi,nj}(\mathbf{R} + \vec{\tau}_j - \vec{\tau}_i)
\end{aligned} \tag{2.3.7}$$

and

$$\begin{aligned}
S_{mi,nj}(\mathbf{k}) &= \int \varphi_{mi,\mathbf{k}}^*(\mathbf{r}) \varphi_{nj,\mathbf{k}}(\mathbf{r}) d\mathbf{r} \\
&= \frac{1}{N} e^{i\mathbf{k}\cdot(\vec{\tau}_j - \vec{\tau}_i)} \sum_{\mathbf{R}_1, \mathbf{R}_2} e^{i\mathbf{k}\cdot(\mathbf{R}_2 - \mathbf{R}_1)} \int \phi_m^*(\mathbf{r} - \mathbf{R}_1 - \vec{\tau}_i) \phi_n(\mathbf{r} - \mathbf{R}_2 - \vec{\tau}_j) d\mathbf{r} \\
&= \frac{1}{N} e^{i\mathbf{k}\cdot(\vec{\tau}_j - \vec{\tau}_i)} \sum_{\mathbf{R}_1, \mathbf{R}_2} e^{i\mathbf{k}\cdot(\mathbf{R}_2 - \mathbf{R}_1)} S_{mi,nj}(\mathbf{R}_2 + \vec{\tau}_j - \mathbf{R}_1 - \vec{\tau}_i) \\
&= e^{i\mathbf{k}\cdot(\vec{\tau}_j - \vec{\tau}_i)} \sum_{\mathbf{R}} e^{i\mathbf{k}\cdot\mathbf{R}} S_{mi,nj}(\mathbf{R} + \vec{\tau}_j - \vec{\tau}_i)
\end{aligned} \tag{2.3.8}$$

which are usually called the Hamiltonian matrix and the overlap matrix. $H_{mi,nj}(\mathbf{R} + \vec{\tau}_j - \vec{\tau}_i)$ is the amplitude that an electron in the orbital ϕ_n at site $(\mathbf{R} + \vec{\tau}_j)$ will hop to the orbital ϕ_m at position $\vec{\tau}_i$ of origin under the action of the Hamiltonian \hat{H} , and is usually denoted as hopping parameter

$$t_{mi,nj}(\mathbf{R} + \vec{\tau}_j - \vec{\tau}_i) \equiv H_{mi,nj}(\mathbf{R} + \vec{\tau}_j - \vec{\tau}_i), \tag{2.3.9}$$

where the on-site ($\mathbf{R} = 0, \vec{\tau}_j - \vec{\tau}_i = 0$) term is

$$t_{mi,ni}(\mathbf{0}) = \varepsilon_n \delta_{m,n}. \tag{2.3.10}$$

Similarly $S_{mi,nj}(\mathbf{R} + \vec{\tau}_j - \vec{\tau}_i)$ is called the overlap of $\phi_m(\mathbf{r} - \vec{\tau}_i)$ and $\phi_n(\mathbf{r} - \mathbf{R} - \vec{\tau}_j)$, denoted as overlap matrix

$$s_{mi,nj}(\mathbf{R} + \vec{\tau}_j - \vec{\tau}_i) \equiv S_{mi,nj}(\mathbf{R} + \vec{\tau}_j - \vec{\tau}_i); s_{mi,ni}(\mathbf{0}) = \delta_{m,n}. \quad (2.3.11)$$

A general Hamiltonian matrix element involves three center integrals –contributions to the Hamiltonian \hat{H} from a third atom and the two sites upon which the orbitals are centered. But in practice, the three center contributions are neglected as in the two-center approximation introduced by Slater and Koster.[46]

In the simplest case with only a single atomic s-level on a lattice with only one atom per primitive cell, $m = n = s$, $i = j = 1$ and $\vec{\tau}_i = \vec{\tau}_j = 0$ are imposed on the above equations. Eq. (2.3.6) is simplified to

$$H_{s,s}(\mathbf{k})b_s(\mathbf{k}) = \varepsilon_{\mathbf{k}}S_{s,s}(\mathbf{k})b_s(\mathbf{k}). \quad (2.3.12)$$

The solution to the energy dispersion $\varepsilon_{\mathbf{k}}$ is then

$$\begin{aligned} \varepsilon_{\mathbf{k}} &= \frac{H_{s,s}(\mathbf{k})}{S_{s,s}(\mathbf{k})} \\ &= \frac{\sum_{\mathbf{R}} t(\mathbf{R})e^{i\mathbf{k}\cdot\mathbf{R}}}{\sum_{\mathbf{R}} s(\mathbf{R})e^{i\mathbf{k}\cdot\mathbf{R}}} \\ &= \frac{\varepsilon_s + \sum_{\mathbf{R}\neq 0} t(\mathbf{R})e^{i\mathbf{k}\cdot\mathbf{R}}}{1 + \sum_{\mathbf{R}\neq 0} s(\mathbf{R})e^{i\mathbf{k}\cdot\mathbf{R}}} \end{aligned} \quad (2.3.13)$$

2.3.2 Wannier Functions

As mentioned above, in tight binding method, the Bloch wave functions can also be expanded using other local orbitals instead of atomic orbitals. Wannier functions, first proposed by G. Wannier[59], is a candidate of such local orbitals, although they

are not localized in some cases when the bandwidths are large, where the Wannier functions are not like the atomic wave functions at all. Technically, Wannier functions are Fourier transformations of Bloch wave functions $\psi_{n\mathbf{k}}(\mathbf{r})$. Since $\psi_{n\mathbf{k}}(\mathbf{r})$ is periodic in the reciprocal lattice, i.e., $\psi_{n\mathbf{k}+\mathbf{G}}(\mathbf{r}) = \psi_{n\mathbf{k}}(\mathbf{r})$, where \mathbf{G} is a reciprocal lattice vector, $\psi_{n\mathbf{k}}(\mathbf{r})$ can be expanded in plane waves as

$$\psi_{n\mathbf{k}}(\mathbf{r}) = \sum_{\mathbf{R}} w_n(\mathbf{r} - \mathbf{R}) e^{i\mathbf{R}\cdot\mathbf{k}}, \quad (2.3.14)$$

where the coefficients $w_n(\mathbf{r} - \mathbf{R})$ are Wannier functions, which depend only on $\mathbf{r} - \mathbf{R}$ instead of \mathbf{r} and \mathbf{R} independently due to the Bloch theorem.

The Wannier functions $w_n(\mathbf{r} - \mathbf{R})$ can be obtained by inverse transformations

$$w_n(\mathbf{r} - \mathbf{R}) = \frac{\Omega_{cell}}{(2\pi)^3} \int_{BZ} e^{-i\mathbf{R}\cdot\mathbf{k}} \psi_{n\mathbf{k}}(\mathbf{r}) d\mathbf{k}, \quad (2.3.15)$$

where Ω_{cell} is the volume of the real-space primitive cell of the crystal.

The Wannier functions so obtained are not unique because any Bloch function $\psi_{n\mathbf{k}}(\mathbf{r})$ doesn't change any physically meaningful quantity under a "gauge transformation"

$$\psi_{n\mathbf{k}}(\mathbf{r}) \rightarrow \tilde{\psi}_{n\mathbf{k}}(\mathbf{r}) = e^{i\phi_n(\mathbf{k})} \psi_{n\mathbf{k}}(\mathbf{r}). \quad (2.3.16)$$

A more general construction of the Wannier functions is given by

$$w_n(\mathbf{r} - \mathbf{R}) = \frac{\Omega_{cell}}{(2\pi)^3} \int_{BZ} e^{i\phi_n(\mathbf{k})} e^{-i\mathbf{R}\cdot\mathbf{k}} \psi_{n\mathbf{k}}(\mathbf{r}) d\mathbf{k}, \quad (2.3.17)$$

The non-uniqueness of the Wannier functions is totally due to presence of the phase factor $\phi_n(\mathbf{k})$.

In addition to the freedom in the choice of phase factor $\phi_n(\mathbf{k})$, there is also a degree

of freedom associated with the choice of a full unitary matrix $U_{nm}^{\mathbf{k}}$, which transforms the N Bloch wave functions $\psi_{n\mathbf{k}}(\mathbf{r})$ between themselves at every wavevector \mathbf{k} , but leaves the electronic energy functional (in an insulator) invariant. This leads to the most general construction of Wannier functions from Bloch wave functions $\psi_{n\mathbf{k}}(\mathbf{r})$ in the form

$$w_n(\mathbf{r} - \mathbf{R}) = \frac{\Omega_{cell}}{(2\pi)^3} \int_{BZ} \sum_{m=1}^N U_{nm}^{\mathbf{k}} e^{-i\mathbf{R}\cdot\mathbf{k}} \psi_{m\mathbf{k}}(\mathbf{r}) d\mathbf{k}, \quad (2.3.18)$$

where $U^{\mathbf{k}}$ is a $M \times N$ unitary matrix with $M \leq N$. Note that $U^{\mathbf{k}}$ is not necessarily a square matrix, as one can use this procedure to construct M Wannier functions out of N bands. Again, in the procedure, the choice of $U^{\mathbf{k}}$ is not unique. Actually, one can use this freedom to construct Wannier functions with properties of one's own interest, such as the most symmetric, or maximally projected, or maximally localized. A widely used one is the maximally localized Wannier functions proposed by Vanderbilt and coworkers[60, 61], in which the quantity

$$\Omega = \sum_{n=1}^N (\langle \mathbf{r}^2 \rangle_n - \langle \mathbf{r} \rangle_n^2) \quad (2.3.19)$$

is minimized by choosing appropriate $U^{\mathbf{k}}$, where $\langle \dots \rangle_n$ is the expectation value over the n -th Wannier function in the unit cell. There are also other Wannier functions in use which are constructed by using projections onto local orbitals to emphasize symmetries.[62, 63]

The Wannier functions $w_n(\mathbf{r} - \mathbf{R})$ for all band n and \mathbf{R} form a complete orthogonal set. That is to say, the Wannier functions are orthogonal at different site and/or different band,

$$\int w_m(\mathbf{r} - \mathbf{R}_i) w_n(\mathbf{r} - \mathbf{R}_j) = \delta_{m,n} \delta_{i,j}. \quad (2.3.20)$$

In the tight binding approach, if Wannier functions are used as the local orbitals, the overlap matrix $s_{m,n}(\mathbf{R})$ is greatly simplified to

$$s_{m,n}(\mathbf{R}) = \delta_{m,n}\delta_{\mathbf{0},\mathbf{R}}. \quad (2.3.21)$$

As a result,

$$\begin{aligned} S_{m,n}(\mathbf{k}) &= \sum_{\mathbf{R}} e^{i\mathbf{k}\cdot\mathbf{R}} s_{m,n}(\mathbf{R}) \\ &= \sum_{\mathbf{R}} e^{i\mathbf{k}\cdot\mathbf{R}} \delta_{m,n}\delta_{\mathbf{0},\mathbf{R}} \\ &= \delta_{m,n} \end{aligned} \quad (2.3.22)$$

and Eq. (2.3.6) is simplified to

$$\sum_n H_{m,n}(\mathbf{k}) b_n(\mathbf{k}) = \varepsilon_{\mathbf{k}} b_m(\mathbf{k}). \quad (2.3.23)$$

This is a main advantage to use Wannier functions in tight binding method.

In practice, Wannier functions are constructed from the results of DFT calculations and used as the local orbitals in tight binding method. The hopping parameters ε_n (on-site energy) and $t_{m,n}(\mathbf{R})$ are obtained by fitting the $\varepsilon_n(\mathbf{k})$ (from the tight binding method) to the band structures of DFT calculations. (Note that the overlap matrix is the identity matrix due to the use of Wannier functions as local orbitals.) The hopping parameters are then used to construct model Hamiltonians to study many-body effects. As mentioned above, the Wannier functions are not localized if the bands have large bandwidths. Therefore, the above procedure works better for systems with an isolated set of narrow bands.

Chapter 3

Strongly Correlated Systems: the Lanthanide Metals and Compounds

3.1 Stability of the Gd Magnetic Moment under High Pressure

This section was published as[64] “*Stability of the Gd magnetic moment to the 500 GPa regime: An LDA+U correlated band method study*”, Z. P. Yin and W. E. Pickett, Phys. Rev. B **74**, 205106 (2006).

3.1.1 Introduction

The behavior of the $4f$ rare earth metals and their compounds under pressure has been discussed for decades, with the volume collapse transition under pressure attracting a great deal of attention. It has been known for some time that there are

volume collapse transitions in Ce (15% at 0.7 GPa, the famous γ -fcc to α -fcc phase transition, not structural transition.[65]), Pr (10% at 20 GPa, hR24(hexagonal) to α -uranium structural transition.[66]), Gd (5% at 59 GPa, dfcc-bcm (monoclinic) structural transition.[67]) and Dy (6% at 73 GPa, hR24 (hexagonal) to bcm (monoclinic) structural transition.[68]), while no significant volume collapses have been detected in Nd, Pm, and Sm. The equation of state of these metals, and references to the original work, has been collected by McMahan *et al.*[65] High temperature experiments[69] have seen signatures that are likely related to the localized \rightarrow itinerant transition, at 50 GPa in Nd and 70 GPa in Sm.

The question can be stated more generally as: what form does the localized \rightarrow itinerant transition of the $4f$ states take, and what is the correct description? This transition is intimately related to the question of behavior of magnetic moments,[65] although the questions are not the same. There have been two main viewpoints on the volume collapse transition. One is the “Mott transition of the $4f$ system” elaborated by Johansson,[70] in which the crucial ingredient is the change from localized (nonbonding) to more extended states (participating in bonding), with an accompanying drop in magnetic tendency. The other is the “Kondo volume collapse” view introduced by Allen and Martin[71] and Lavagna *et al.*[72], in which the main feature is the loss of Kondo screening of the local moment, with a decrease in localization of the $4f$ state not being an essential feature.

At ambient conditions the $4f$ electrons form a strongly localized f^n configuration that is well characterized by Hund’s rules. Under reduction of volume, several things might be anticipated to happen. At some point the $4f$ system begins to respond to the non-spherical environment. Initially, perhaps, it is just a matter of crystal field splitting becoming larger. Then the $4f$ orbitals actually begin to become involved

in the electronic structure, by overlapping orbitals of neighboring atoms. The consequences of this are possible participation in bonding, and that the orbital moment becomes less well defined (the beginning of quenching *i.e.* the loss of Hund's second rule, which has already occurred in magnetic $3d$ systems). Additionally, the $4f$ levels can shift and increase their interaction with the itinerant conduction (c) bands (Kondo-like coupling), which can change the many-body behavior of the coupled $4f - c$ system. At some point the kinetic energy increase, characterized by the $4f$ bandwidth W_f , compared to the on-site interaction energy U_f reaches a point where the spin moment begins to decrease. Finally, at small enough volume (large enough W_f) the $4f$ states simply form nonmagnetic conduction bands.

Just how these various changes occur, and in what order and at what volume reduction, is being addressed in more detail by recent high pressure experiments. Here we revisit the case of Gd, whose volume collapse was reported by Hua *et al.*[73] and equation of state by Akella *et al.*[74] The deviation from the series of close-packed structures below $P_c=59$ GPa and the lower symmetry bcm (body-centered monoclinic) high pressure structure signaled the expected onset of f -electron participation in the bonding, and Hua *et al.* seemed to expect that the moment reduction and delocalization of the $4f$ states would accompany this collapse.

New information has been reported by Maddox *et al.*,[75] who have monitored the resonant inelastic x-ray scattering and x-ray emission spectra of Gd through P_c and up to 113 GPa. They find that there is no detectable reduction in the magnetic moment at the volume collapse transition, so the volume-collapse is only a part of a more complex and more extended delocalization process of the $4f$ states. Maddox *et al* emphasize the Kondo-volume-collapse[76, 77] aspects of the transition at P_c .

The treatment of the $4f$ shell, and particularly the volume collapse and other

phenomena that may arise (see above), comprises a correlated-electron problem for theorists. Indeed there has been progress in treating this volume-collapse, moment-reduction problem in the past few years. The issue of the (in)stability of the local moment seems to involve primarily the local physics, involving the treatment of the hybridization with the conduction bands and interatomic $f - f$ interaction, with Kondo screening of the moment being the subsequent step. Dynamical mean field studies of the full multiband system have been carried out for Ce[65, 78, 79] and for Pr and Nd.[79] These calculations were based on a well-defined free-energy functional and included the conduction bands as well as the correlated $4f$ bands. One simplification was that only an orbital-independent Coulomb interaction U was treated, leaving the full orbital-dependent interaction (fully anisotropic Hund's rules) for the future. Density functional based correlated band theories have also been applied (at zero temperature). Self-interaction corrected local density approximation (LDA) was applied to Ce, obtaining a volume collapse comparable to the observed one.[80] Four correlated band theories have been applied[81] to the antiferromagnetic insulator MnO. Although their predictions for critical pressures and amount of volume collapse differed, all obtained as an $S=5/2$ to $S=1/2$ moment collapse rather than a collapse to a nonmagnetic phase.

Clearly there remain fundamental questions about how the magnetic moment in a multielectron atom disintegrates as the volume is reduced: catastrophically, to an unpolarized state, or sequentially, through individual spin flips or orbital-selective delocalization. If the latter, the total (spin + orbital) moment could actually *increase* initially in Gd. If the occupation change is toward f^8 , the decrease in spin moment (from $S=7/2$ to $S=3$) could be more than compensated by an orbital moment ($L=3$). If the change is toward f^6 , the onset of an $L=3$ orbital configuration could oppose

the $S=3$ spin (Hund's third rule), leaving a non-magnetic $J=0$ ion (as in Eu^{3+}) even though the $4f$ orbitals are still localized. Still another scenario would be that the increasing crystal field quenches the orbital moment (as in transition metals) and the remaining problem involves only the spins.

Our objective here is to look more closely at the stability of the Gd atomic moment, in the general context of the localized \rightarrow itinerant transition of the $4f$ system under pressure. Consideration of the changes in electronic structure under pressure go back at least to the broad study of Johansson and Rosengren[82] but most have not considered the magnetism in detail. We apply the LDA+U (local density approximation plus Hubbard U) method to study the evolution of the electronic structure and magnetism as the volume is reduced. Although this correlated band method neglects fluctuations and the dynamical interaction with the conduction electrons, it does treat the full multiorbital system in the midst of itinerant conduction bands. The resulting moment vs. volume surely provides only an upper limit to the pressure where the moment decreases rapidly. However, we can invoke studies of the insulator-to-metal transition in multiband Hubbard models to provide a more realistic guideline on when the localized \rightarrow itinerant (or at least the reduction in moment transition within the $4f$ system) may be expected to occur. The results suggest stability of the moment to roughly the 500 GPa region.

3.1.2 Electronic Structure Methods

In the section we apply the full potential local orbital code[47] (FPLO5.00-18) to Gd from ambient pressure to very high pressure (a few TPa). We use the fcc structure with space group Fm3m (#225) and ambient pressure atomic volume (corresponding to the fcc lattice constant $a_0=5.097\text{\AA}$). The basis set is (core)::(4d4f5s5p)/6s6p5d+.

We use 48^3 k point mesh and Perdew and Wang’s PW92 functional[20] for exchange and correlation. We have tried both 5.0 and 6.0 for the confining potential exponent (See Section 2.1.8 for definition of the confining potential and the related confining potential exponent), with very similar results, so only the results using exponent=5 will be presented here. We perform both LDA and LDA+U calculations (see below). Due to the extreme reduction in volume that we explore, any band structure method might encounter difficulties. For this reason we have compared the FPLO results on many occasions with parallel calculations with the full potential linearized augmented plane wave method WIEN2k.[51] The results compared very well down to $V/V_o=0.5$, beyond which the WIEN2k code became more difficult to apply. We use the notation $v \equiv V/V_o$ for the specific volume throughout the section.

We assume ferromagnetic ordering in all calculations. The Curie temperature has been measured only to 6 GPa,[83, 84, 85] where it has dropped from 293 K (P=0) to around 210 K. Linear extrapolation suggests the Curie temperature will drop to zero somewhat below 20 GPa. However, as the $4f$ bands broaden at reduced volume the physics will change substantially, from RKKY coupling at ambient pressure finally to band magnetism at very high pressure. Antiferromagnetic (AFM) ordering does not affect the $4f$ bandwidth[86] until $f - f$ overlap becomes appreciable. AFM ordering might affect some of the quantities that we look at in this study at very high pressure, but such effects lie beyond the scope of our present intentions.

LDA+U Method

For the strength of the $4f$ interaction we have used the volume dependent $U(V)$ calculated by McMahan *et al.*,[65] which is shown below. Due to the localized $4f$ orbital and the large atomic moment, we use the “fully localized limit” version of

LDA+U as implemented in the linearized augmented plane-wave method,[87] and as usual the ratio of Slater integrals is fixed at $F_4/F_2=0.688$, $F_6/F_2=0.495$. Since we are particularly interested in the stability of the atomic moment, the exchange integral J that enters the LDA+U method deserves attention. In atomic physics, and in the LDA+U method, the exchange integral plays two roles. It describes the spin dependence of the Coulomb interaction, that is, the usual Hund's rule coupling. In addition, it carries the orbital off-diagonality; with $J=0$ all $4f$ orbitals repel equally by U , whereas in general the anisotropy of the orbitals leads to a variation[88] that is described by J .

For a half filled shell for which the orbital occupations $n_{m\uparrow} = 1$ and $n_{m\downarrow}=0$ for all suborbitals m , the exchange effect primarily counteracts the effect of U , since the anisotropy of the repulsion averages out. As a result, using $U_{eff} \equiv U - J$ with $J_{eff}=0$ is almost equivalent, for a perfectly half-filled shell, to using U and J separately as normally is done. Since it could be argued that Hund's first rule is treated adequately by the LDA exchange-correlation functional, for our calculations we have set $J=0$. This becomes approximate for the off-diagonality effects when the minority $4f$ states begin to become occupied at high pressure. However, we have checked the effect at $a/a_o=0.8$ ($v = 0.5$, $P=60$ GPa). Comparing $U = 6.9$ eV, $J=1$ eV with $U = 5.9$ eV, $J=0$, we find the energy is exactly the same (to sub-mRy level) and the moment is unchanged. This result is in line with the U_{eff}, J_{eff} argument mentioned above. Changing J from 1 eV to 0 with $U = 5.9$ eV also leaves the energy unchanged, illustrating the clear unimportance of J . The $J=1$ eV calculation does result in a $0.03 \mu_B$ larger moment. At much smaller volumes, where the minority bands overlap the Fermi level, the changes become noticeable and would affect the equation of state, but only in a very minor way. In general, neglect of J will tend to *underestimate*

the stability of the magnetic moment, which we show below already to be extremely stable.

Structure

The observed structures of Gd follow the sequence $\text{hcp} \rightarrow \text{Sm-type} \rightarrow \text{dhcp} \rightarrow \text{dfcc} \rightarrow \text{bcm}$ ($\text{dfcc} \equiv \text{distorted fcc}$, which is trigonal; $\text{bcm} \equiv \text{body-centered monoclinic}$). All except the bcm phase are close-packed arrangements, differing only in the stacking of hexagonal layers. The bcm phase is a lower symmetry phase that suggests f -electron bonding has begun to contribute.

For our purpose of studying trends relating only to the atomic volume, it is best to stay within a single crystal structure. We expect the results to reflect mostly local physics, depending strongly on the volume but only weakly on the long-range periodicity. Therefore we have kept the simple fcc structure for the results we present.

3.1.3 LDA+U Results

The overall result of our study is that evolution of the volume and the Gd moment are predicted by LDA+U to be continuous under reduction of volume, with no evidence of a volume-collapse transition (or any other electronic phase change) in the region where one is observed (59 GPa), or even to much higher pressure. This result provides some support for the suggestion that the volume collapse is Kondo-driven, or involves in an essential way fluctuations, neither of which are accounted for in our approach.

While we will usually quote volumes or the relative volume v , it is useful to be able to convert this at least roughly to pressure. We provide in Fig. 3.1.1 the calculated equation of state, plotted as $\log P$ vs. V/V_o . It can be seen that the pressure is very roughly exponential in $-V/V_o$ from $v=0.8$ down to $v=0.15$ (2 GPa to 4 TPa). The

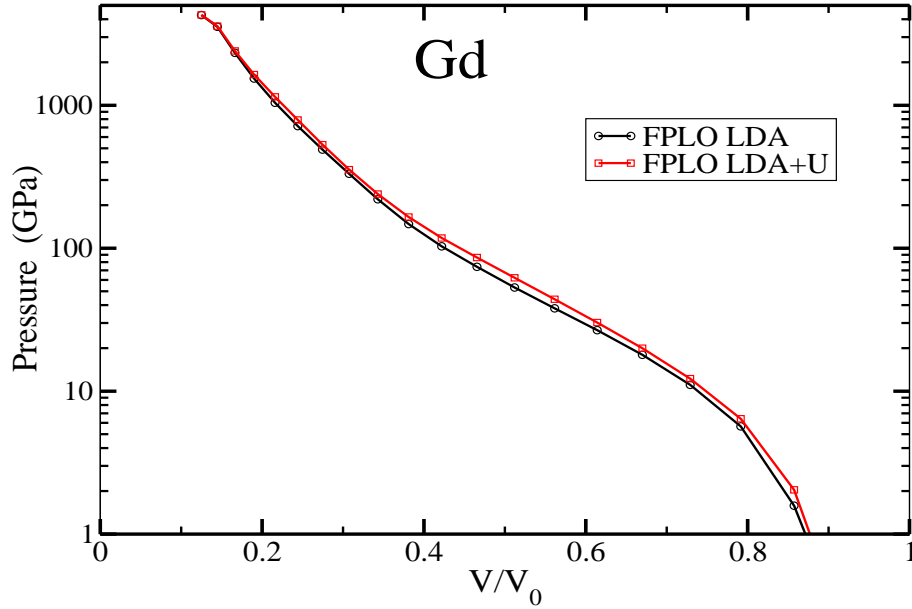


Figure 3.1.1: Log plot of the calculated pressure versus volume. The relatively small difference between the LDA+U and LDA results is evident. The relation is roughly exponential below $V/V_0 < 0.8$. Current static diamond anvil cells will only take Gd to the $V/V_0 \sim 0.35$ region.

change in slope around $v=0.4$ (in the vicinity of 100-200 GPa) is discussed below.

Magnetic Moment vs. Volume

The behavior of the total spin moment ($4f$ plus conduction) in LDA+U is compared in Fig. 3.1.2 with that of LDA. The general trend is similar, but the decrease in moment is extended to smaller volume by the correlations in LDA+U. Specifically, the moment is reduced not by decrease of majority spin population (which would be $f^7 \rightarrow f^6$) but rather by increase in the minority spin population ($f^7 \rightarrow f^8$; see discussion below). Thus LDA+U enhances the stability of the moment by raising the unoccupied minority $4f$ states in energy, thus reducing and delaying compensation of

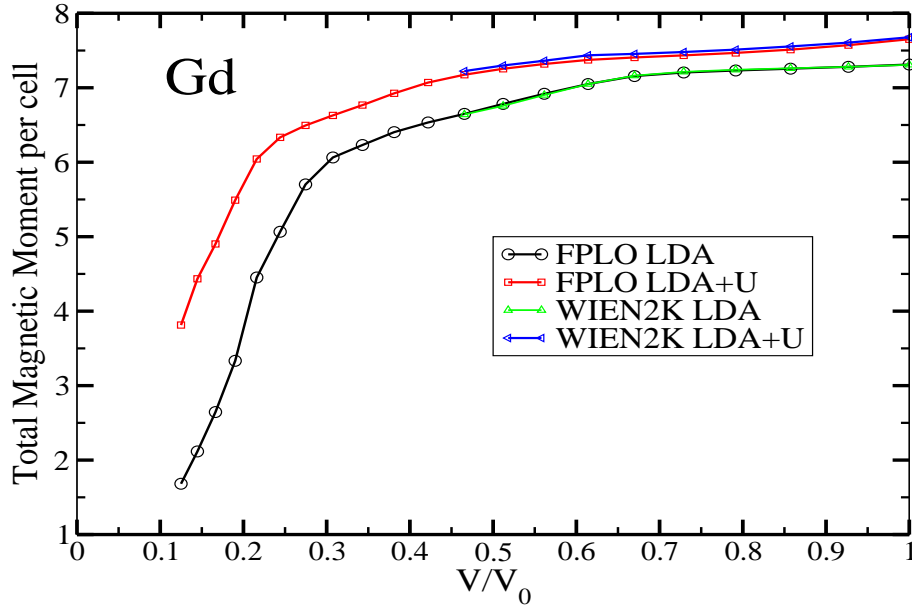


Figure 3.1.2: Behavior of the calculated moment/cell ($4f$ spin moment plus conduction electron polarization) of Gd versus reduction in volume, from both LDA and LDA+U methods. For the more realistic LDA+U method, there is very little decrease in moment down to $V/V_0=0.45$ (~ 110 GPa), with a rapid decline beginning only around $V/V_0 \approx 0.2$ (1.5 TPa).

the filled majority states. It has been noted elsewhere[89] that raising the minority states is the main beneficial effect of the LDA+U method for Gd at ambient pressure.

The decrease in moment is minor down to $v = 0.45$ (~ 90 -100 GPa) beyond which the decrease from $7\mu_B$ to $6\mu_B$ occurs by $v = 0.2$ ($P \sim 1$ TPa). Only beyond this incredibly high pressure does the moment decrease more rapidly, as the $4f$ states become band-like. Even in LDA this collapse does not occur until below $v=0.3$ ($P \sim 300$ -400 GPa). With the neglect of fluctuations, the simplistic interpretation of the LDA+U results is that the Gd “bare” spin moment is relatively stable to ~ 1 TPa.

It might be thought that, for the region of spin moment of $6\mu_B$ and below, where the minority occupation is one or more, there might be an orbital moment of the minority system. However, at these volumes (see below) the minority $4f$ bandwidth

is 5 eV or more, which we think makes an orbital moment unlikely. Therefore we have not pursued this possibility.

4f Bandwidth

The behavior of the 4f states, which become bands, is better illustrated in Fig. 3.1.3, where the evolution of the 4f “bands” (the 4f projected density of states (PDOS)) is provided graphically. At $a/a_o=0.80$ ($v=0.51$, $P \approx 60$ GPa, where the volume collapse is observed) the majority PDOS is somewhat less than 2 eV wide and still atomic-like, since it does not quite overlap the bottom of the conduction band. Above this pressure range the 4f states begin to overlap the conduction bands, primarily due to the broadening of the conduction bandwidth. By $a/a_o=0.70$ ($v=0.34$, $P \approx 200$ GPa) the width is at least 3 eV and the shape shows the effect of hybridization and formation of bands. For yet smaller volumes the bandwidth becomes less well defined as the bands mix more strongly with the conduction states and broaden. The minority PDOS lies in the midst of Gd 5d bands and is considerably broader down to $a/a_o=0.70$, beyond which the difference becomes less noticeable.

The position of the 4f states relative to the semicore 5p, and conduction 5d states, and their evolution with volume, are pictured in Fig. 3.1.4. The semicore 5p bands broaden to ~ 10 eV by 200 GPa, but it requires supra-TPa pressures to broaden them into the range of the majority 4f states. The upturn in the $\log P$ vs. V curve in Fig. 3.1.1 in the vicinity of 100-200 GPa is probably due to 5p semicore overlap on neighboring atoms (repulsion of closed shells as they come into contact). The 5d bands broaden in the standard way under pressure, and begin to rise noticeably with respect to the 4f states beyond 60 GPa.

The minority 4f bands fall somewhat with respect to E_F as they broaden, both

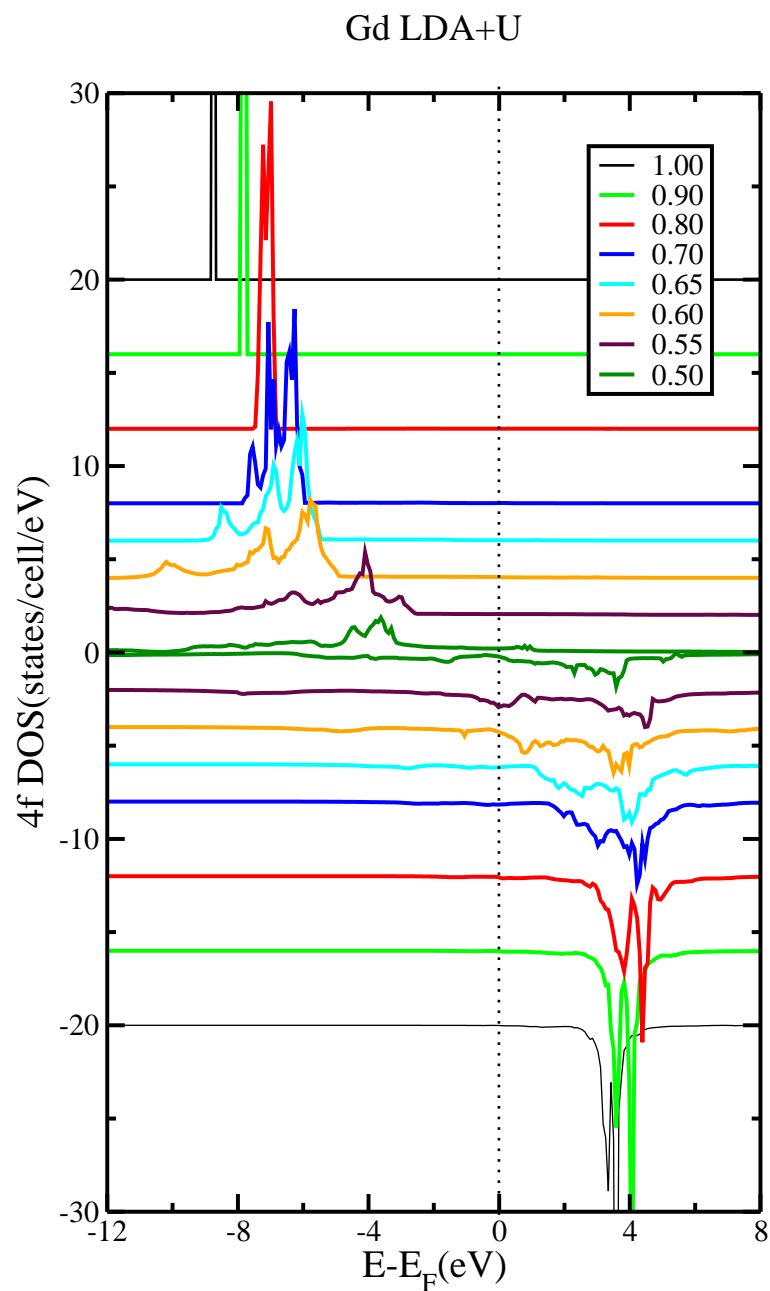


Figure 3.1.3: View of the $4f$ projected density of states under compression, with majority spin plotted upward and minority plotted downward. The curves are displaced for clarity, by an amount proportional to the reduction in lattice constant. The legend provides the ratio a/a_o , which is decreasing from above, and from below, toward the middle of the figure.

effects contributing to an increase in the minority $4f$ occupation at the expense of $5d$ and $6sp$ character. Since the majority $4f$ states remain full, the effect is that the total f count increases and the spin moment decreases (as discussed above).

The volume dependence of the $4f$ bandwidth in nonmagnetic Gd has been looked at previously by McMahan *et al.*[65] They identified the intrinsic width W_{ff} from the bonding and antibonding values of the $4f$ logarithmic derivative; W_{ff} lies midway (roughly halfway) between our majority and minority bandwidths, see Fig. 3.1.4. McMahan *et al.* also obtained a hybridization contribution to the $4f$ width; both of these would be included in our identified widths. Our widths, obtained for ferromagnetically ordered Gd, are difficult to compare quantitatively with those of McMahan *et al.*, because the positions of our minority and majority states differ by 12 eV at $P=0$, decreasing under pressure. Note that our minority and majority widths, obtained visually from Fig. 3.1.3 differ by a factor of ~ 6 at $v=1.0$, still by a factor of 2.5 at $v=0.3$, and only become equal in the $v < 0.2$ range.

Comments on Mott Transition

In the simplest picture (single-band Hubbard model) the Mott transition is controlled by the competition of kinetic (W) and potential (U) energies, with the transition occurring around $W \approx U$. This transition is normally pictured as a simultaneous insulator-to-metal, moment collapse, and presumably also volume collapse transition. In Gd, however, no change in moment is observed[75] across the volume collapse transition at 59 GPa.

In Fig. 3.1.5 the $4f$ bandwidths (majority and minority) and the Coulomb U of McMahan *et al.*[65] are plotted versus volume. The region $W \approx U$ occurs around $v \sim 0.20-0.25$. This volume corresponds to a calculated pressure in the general neigh-

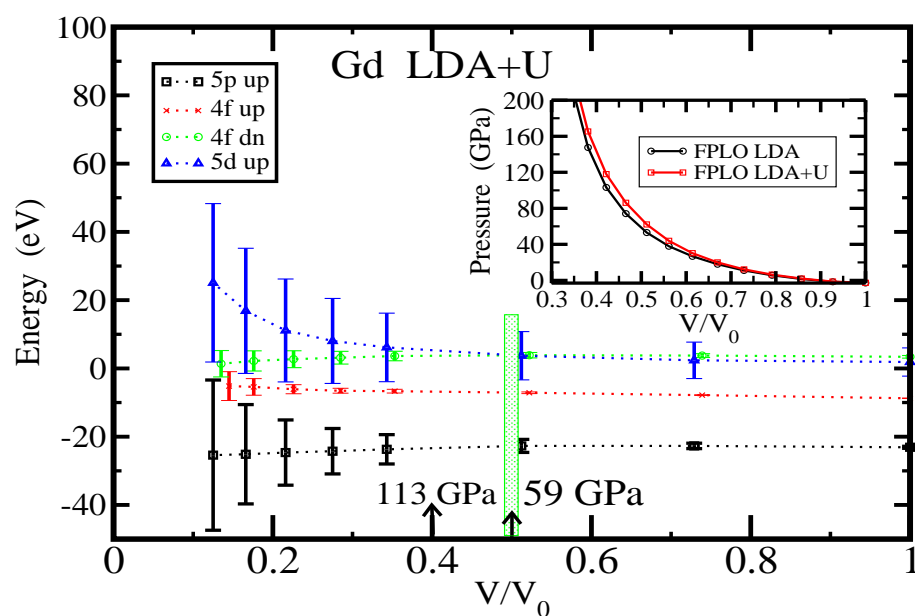


Figure 3.1.4: Plot of band positions (lines) and widths (bars) of the majority and minority $4f$ states, the semicore $5p$ bands, and the valence $5d$ bands, for ferromagnetic Gd. The bar at $V/V_0=0.5$ (~ 59 GPa) marks the observed volume collapse transition, while the arrow at 113 GPa denotes the highest pressure achieved so far in experiment. These results were obtained from LDA+U method, with U varying with volume as given by McMahan *et al*[65].

borhood of 1 TPa, indicative of an extremely stable moment well beyond present capabilities of static pressure cells. This criterion however presumes a simple single band system, which Gd is not.

Gunnarsson, Koch, and Martin have considered the Mott transition in the multi-band Hubbard model,[90, 91, 92] and found that the additional channels for hopping favored kinetic processes that reduced the effect of the Coulomb repulsion. They argued that the criterion involved the inverse square root of the degeneracy, which can be characterized by an effective repulsion $U^* = U/\sqrt{f}$ (for f states the degeneracy is $2\ell + 1 = 7$). The Mott transition could then be anticipated in the range $W \approx U^*$, for which $U^*(V)$ has also been included in Fig. 3.1.5. Taking W as the average of the majority and minority widths gives the crossover around $v_c \sim 0.35$ ($P_c \sim 200$ GPa); taking W more realistically as the majority bandwidth gives $v_c \sim 0.25$ ($P_c \sim 750$ GPa).

Another viewpoint on the ‘‘Mott transition’’ in the $4f$ system is that it can be identified with the ‘metallization’ of the $4f$ bands, which might be expected to be where the occupied and unoccupied bands overlap. These are respectively the majority and minority bands. Significant overlap occurs only above 2 TPa ($v < 0.20$) in Fig. 3.1.5. The fact is that metallization (however defined for a $4f$ system in the midst of uncorrelated itinerant conduction bands) and moment collapse need not coincide, and the concept of Mott transition may need to be generalized.

3.1.4 Summary

In this section we have applied the correlated band theory LDA+U method to probe the electronic and magnetic character of elemental Gd under pressure. The calculated moment decreases slowly down to $V/V_o = 0.20$ ($P > 1$ TPa), and only at

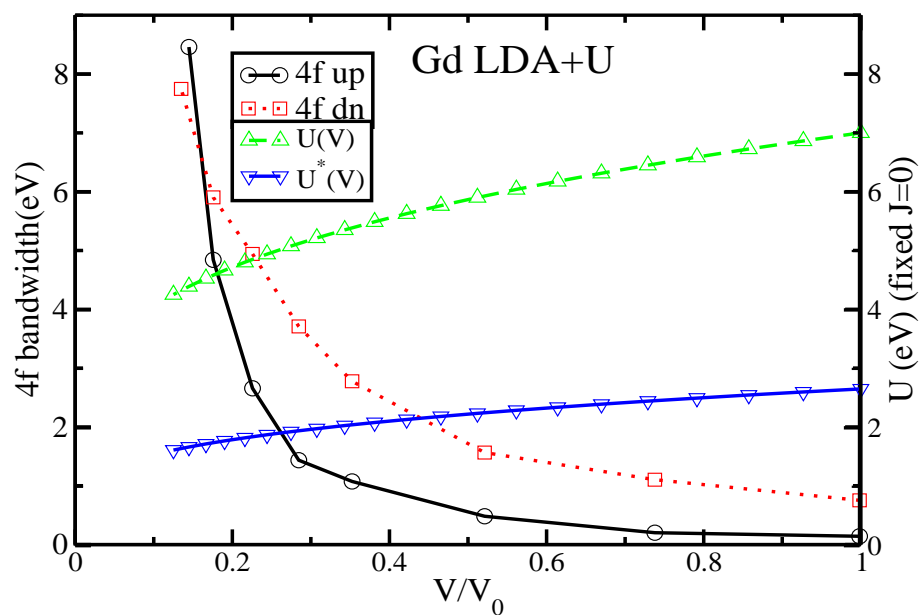


Figure 3.1.5: Plot of the 4f bandwidths (both majority and minority), together with the volume-dependent Coulomb repulsion U from McMahan.[65] The simple crossover criterion $W_f \approx U$ occurs around $V/V_0 = 0.20 - 0.25$, corresponding roughly to a pressure of 700-1000 GPa. Also pictured is $U^* \equiv U/\sqrt{7}$, see text for discussion.

smaller volumes does the moment decrease more rapidly. Still, no identifiable moment collapse has been obtained. Metallization, defined as overlap of unoccupied with occupied bands, also does not occur until the same range of volume/pressure. However, information from studies of the multiband Hubbard model, and comparison of the bandwidth to U/\sqrt{N} ratio ($N=7$ is the $4f$ degeneracy) suggests a “Mott transition” might be expected in the broad vicinity of 500 GPa.

The same LDA+U method, and three different correlated band methods have been applied to antiferromagnetic MnO. The manganese configuration is half-filled and fully polarized, as is Gd, with the difference being that it is $3d$ and an antiferromagnetic insulator rather than $4f$ in a background of itinerant bands. All methods obtained a volume collapse from a high-spin to low-spin configuration. Surprisingly, the collapse was not to nonmagnetic but rather to a spin-half result.

The critical pressures for transitions suggested by the present study (minimum of 200 GPa, more likely around 750 GPa) lie well above the volume collapse transition that is observed at 59 GPa. At this point in our understanding of the $4f$ shell in Gd, there seems to be no viable alternative to the suggestion by Maddox *et al.* that Gd provides an example of the Kondo volume collapse mechanism.[75]

3.1.5 Acknowledgments

This work has benefited greatly from a number of exchanges of information and ideas with A. K. McMahan. I have profited from many discussions on Gd with C. S. Yoo, B. Maddox, R. T. Scalettar, and A. Lazicki, and on the moment collapse question with M. D. Johannes and J. Kuneš. I thank M. D. Johannes and R. T. Scalettar for a careful reading of the manuscript. This work was supported by Department of Energy grant DE-FG03-01ER45876, by Strategic Science Academic Alliance Program grant

DE-FG03-03NA00071, and by the DOE Computational Materials Science Network.

3.2 Rare-earth-boron Bonding and $4f$ State Trends in RB_4 Tetraborides

This section was published as[93] “Rare-earth-boron bonding and $4f$ state trends in RB_4 tetraborides”, Z. P. Yin and W. E. Pickett, Phys. Rev. B **77**, 035135 (2008).

3.2.1 Background and Motivation

The tendency of the metalloid boron to form clusters has led to widespread study of the properties of condensed boron. Of the many classes of compounds that B forms, B-rich metal borides include classes with very important, and intensely studied, properties. One example is MgB_2 , which is the premier phonon-coupled superconductor[94] (at 40 K). Although this structural class includes several transition metal borides and other simple metal borides (such as LaB_2), MgB_2 is unique in this single-member class of quasi-two-dimensional s - p metal with very high superconducting transition temperature due to strong covalent B-B bonds that are driven metallic[95] by the crystal structure and chemistry.

Another class that has received great attention is the hexaborides MB_6 formed from vertex-linked B_6 octahedra that enclose the metal ion in the cubic interstitial site. This class includes the divalent metals ($M=Ca, Sr, Ba$) that are small gap semiconductors.[96, 97, 98, 99, 100, 101, 102, 103, 104, 105] The stability of this structure was understood decades ago, when cluster studies established[96, 97] that the bonding states of linked B_6 clusters are filled by 20 electrons, which requires two per B_6 unit in addition to the B valence electrons. There are many trivalent hexa-

borides as well, including lanthanide members which have very peculiar properties: unusual magnetic ordering, heavy fermion formation, and superconductivity.[99, 100, 104, 106, 107, 108, 109] Two monovalent members, NaB_6 [110] and KB_6 [111], have been reported.

Yet another class that has been known for decades is the metal (mostly rare earths) tetraboride RB_4 family, which is richer both structurally and electronically and for which considerable data is available (see: for several RB_4 , Refs. [112, 113, 114, 115]; YB_4 , Refs. [116, 117, 118, 119, 120]; LaB_4 , Ref. [121]; CeB_4 , Refs. [122, 123, 124]; NdB_4 , Ref. [125]; GdB_4 , Refs. [126, 127, 128, 129, 130, 131]; TbB_4 , Refs. [132, 133, 134, 135, 136, 137]; DyB_4 , Refs. [138, 139, 140, 141, 142, 143]; ErB_4 , Refs. [137, 144, 145]). Yttrium and all the lanthanides except Eu and Pm form isostructural metallic tetraborides RB_4 with space group $P4/mbm$ (#127), described below and pictured in Fig. 3.2.1. Presumably Eu is not stable in the tetraboride structure because of its preference for the divalent configuration in such compounds. The Sr and Ba tetraborides also are not reported. A “calcium tetraboride” with formula $Ca(B_{1-x}C_x)_4$, $x \approx 0.05$ was reported[146] recently.

These rare-earth tetraborides exhibit an unusual assortment of magnetic properties. While CeB_4 and YbB_4 (f^1 and f^{13} respectively) don’t order and PrB_4 orders ferromagnetically at $T_c=25$ K,[129] all of the others ($R=Nd, Sm, Gd, Tb, Dy, Ho, Er, Tm$) order antiferromagnetically, with Néel temperature T_N (see Table I) spanning the range 7-44 K. A noteworthy peculiarity is that T_N doesn’t obey de Gennes’ scaling law, which says that the magnetic transition temperature is proportional to $(g_J - 1)^2 J(J + 1)$ across an isostructural series where the rare-earth atom is the only magnetic component.[136, 147] (here J is the Hund’s rule total angular momentum index, g_J is the corresponding Landé g -factor.) In the rare earth nickel borocarbide

series, for example, de Gennes scaling is obeyed faithfully.[148] This lack of scaling indicates that magnetic coupling varies across the series, rather than following a simple RKKY-like behavior with a fixed Fermi surface.

Both the ferromagnetic member PrB_4 and antiferromagnetic ones RB_4 show strong magnetic anisotropy. For ferromagnetic PrB_4 the c axis is the easy axis. The situation is more complicated for the antiferromagnetic compounds, which display varying orientations of their moments below T_N , and some have multiple phase transitions. GdB_4 and ErB_4 have only one second order phase transition, while both TbB_4 and DyB_4 have consecutive second order phase transitions at distinct temperatures. A yet different behavior is shown by HoB_4 and TmB_4 , which have a second order phase transition followed by a first order phase transition at lower temperature. The magnetic ordering temperatures, primary spin orientations, and experimental and theoretical effective (Curie-Weiss) magnetic moments have been collected in Table I.

The variety of behavior displayed by these tetraborides suggests a sensitivity to details of the underlying electronic structure. Unlike the intense scrutiny that the tetraborides have attracted, there has been no thorough study of the tetraboride electronic structure, which contains a new structural element (the “boron dimer”) and an apical boron that is inequivalent to the equatorial boron in the octahedron. We provide here a detailed analysis, and in addition we provide an initial look into the trends to be expected in the $4f$ shells of the rare earth ions.

3.2.2 Crystal Structure

The full RB_4 structure was first reported by Zalkin and Templeton[124] for the Ce, Th, and U members. These tetraborides crystallize at room temperature in the tetragonal space group P_4/mbm , D_{4h}^5 with four formula units occupying the positions

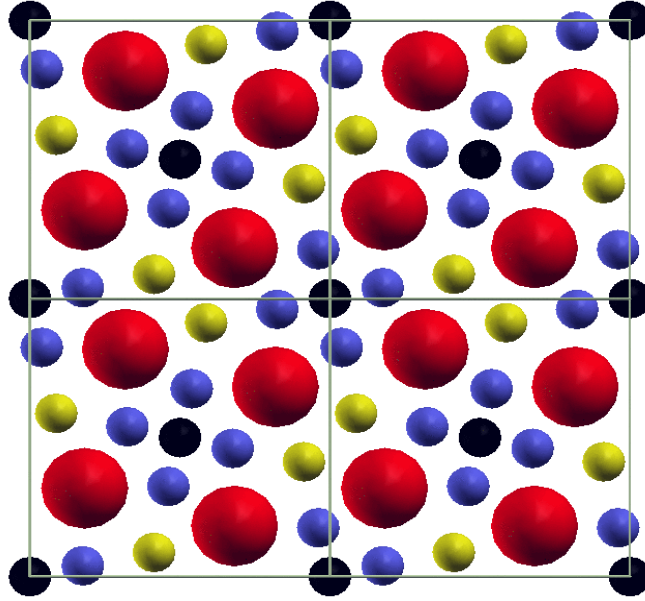


Figure 3.2.1: Structure of RB_4 viewed from along the c direction. The large metal ion spheres (red) lie in $z=0$ plane. Apical B1 atoms (small black) lie in $z \simeq 0.2$ and $z \simeq 0.8$ planes. Lightly shaded (yellow) dimer B2 and equatorial B3 (dark, blue) atoms lie in $z=0.5$ plane. The sublattice of R ions is such that each one is a member of two differently oriented R_4 squares, and of three R_3 triangles.

Table 3.1: Data on magnetic ordering in the RB_4 compounds.[112, 114, 129, 143] The columns provide the experimental ordering temperature(s) T_{mag} , the ordering temperature T_{th} predicted by de Gennes law (relative to the forced agreement for the GdB_4 compound), the orientation of the moments, and the measured ordered moment compared to the theoretical Hund's rule atomic moment (μ_B).

	T_{mag} (K)	T_{th} (K)	direction	$\mu(\text{exp})$	$\mu(\text{th})$
PrB_4	24	2.1	$\parallel c$	3.20	3.58
SmB_4	26	12	–	–	0.84
GdB_4	42	42	$\perp c$	7.81	7.94
TbB_4	44, 24	28	$\perp c$	9.64	9.72
DyB_4	20.3, 12.7	19	$\parallel c$	10.44	10.63
HoB_4	7.1, 5.7(1st)	12	$\parallel c$	10.4	10.6
ErB_4	15.4	7	$\parallel c$	9.29	9.60
TmB_4	11.7, 9.7(1st)	3	$\perp c$	7.35	7.56

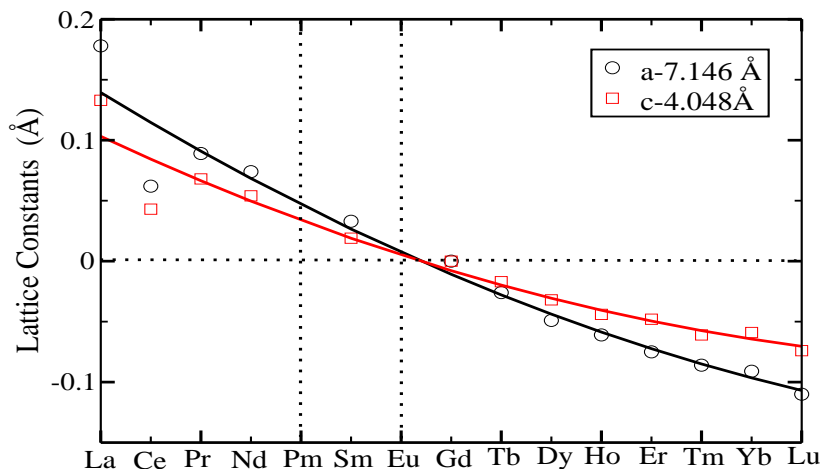


Figure 3.2.2: Plot of experimental lattice constants of RB_4 vs position in the Periodic Table (atomic number), showing a lanthanide contraction of about 5% for a , 3% for c . The smooth lines show a quadratic fit to the data.

listed in Table 3.2. The lattice constants for the reported rare earth tetraborides are presented in Table 3.3.

The B1 and B3 atoms form B_6 octahedra (apical and equatorial vertices, respectively) that are connected by B2 dimers in the $z=1/2$ plane. The B_6 octahedra, which are arrayed in centered fashion in the $x-y$ plane within the cell, are flattened somewhat, with distances from the center being 1.20 \AA along the c axis and 1.29 \AA in the $x-y$ plane (taking GdB_4 as an example). Each B2 atom is bonded to two B1 atoms in separate octahedra and to one other B2 atom. A suggestive form for the chemical formula then is $[R_2B_2B_6]_2$. The rare-earth atoms lie in the large interstitial holes in the $z=0$ plane, and form a 2D array that can be regarded as fused squares and rhombuses.[128]

The R site symmetry is mm . The symmetry of an R site is important for the properties of the compounds, as it dictates the crystal field splitting of the ion with

Table 3.2: Site designations, symmetries, and atomic positions of the atoms in the RB_4 crystal.

R	4g	mm	$(x, \frac{1}{2}+x, 0)$
B1	4e	4	$(0, 0, z)$
B2	4h	mm	$(x, \frac{1}{2}+x, \frac{1}{2})$
B3	8j	m	$(x, y, \frac{1}{2})$

total angular momentum $\vec{J} = \vec{L} + \vec{S}$ and thereby the resulting magnetic state at low temperature. The R ion is coordinated by seven B atoms in planes both above and below, three of them being dimer B2 atoms (two 2.88 Å distant and one at a distance of 3.08 Å) and four of them equatorial B3 atoms (two each at distances of 2.76 Å and 2.84 Å). Within the unit cell the four R sites form a square of side $d = 0.518a = 3.70\text{Å}$, oriented at about 15° with respect to the square sublattice of B_6 octahedra. The (low) site symmetries of the apical B1, dimer B2, and equatorial B3 atoms are $4, mm, m$, respectively.

The reported lattice constants for the lanthanides are plotted in Fig. 3.2.2. It is evident that most fall on smooth lines reflecting the lanthanide contraction in this system. The behavior is representative of trivalent behavior, from La through to Lu. The big exception is Ce, which has smaller volume suggesting that, rather than being simple trivalent, the $4f$ electron is participating in bonding. Pm with all unstable isotopes has not been reported. EuB_4 also has not been reported; Eu typically prefers the divalent state (due to the gain in energy of the half-filled $4f$ shell) so it is not surprising that it is different. However, some divalent tetraborides do form in this structure (*e.g.* CaB_4 , see Sec. IV) so it cannot be concluded that EuB_4 is unstable simply on the basis of divalency. Finally, the small deviation of Yb from the smooth curves suggest it maybe be mixed or intermediate valent (although close to trivalent).

Table 3.3: Tabulation of the lattice constants and internal structural parameters used in our calculations. Considering the extreme regularity of the internal coordinates through this system, the irregularity in z_{B1} for Dy should be treated with skepticism.

R	a(\AA)	c(\AA)	x_R	z_{B1}	x_{B2}	x_{B3}	y_{B3}	Ref.
Y	7.111	4.017	0.318	0.203	0.087	0.176	0.039	[116]
La	7.324	4.181	0.317	0.209	0.088	0.174	0.039	[115],[121]
Ce	7.208	4.091	0.318	0.203	0.087	0.176	0.039	[115],[123]
Pr	7.235	4.116	0.318	0.203	0.087	0.176	0.039	[114]
Nd	7.220	4.102	0.318	0.203	0.087	0.176	0.039	[115],[125]
Pm	7.193	4.082	0.318	0.203	0.087	0.176	0.039	
Sm	7.179	4.067	0.318	0.203	0.087	0.176	0.039	[114]
Eu	7.162	4.057	0.318	0.203	0.087	0.176	0.039	
Gd	7.146	4.048	0.317	0.203	0.087	0.176	0.038	[128]
Tb	7.120	4.042	0.317	0.202	0.087	0.176	0.039	[134],[136]
Dy	7.097	4.016	0.319	0.196	0.086	0.175	0.039	[114],[144]
Ho	7.085	4.004	0.318	0.203	0.087	0.176	0.039	[114]
Er	7.071	4.000	0.318	0.203	0.086	0.177	0.038	[136],[144]
Tm	7.057	3.987	0.318	0.203	0.087	0.176	0.039	[115]
Yb	7.064	3.989	0.318	0.203	0.087	0.176	0.039	[115]
Lu	7.036	3.974	0.318	0.203	0.087	0.176	0.039	[115]

3.2.3 Computational Methods

The full potential local orbital (FPLO) code[47] (version 5.18) was used in our calculations. Both LDA (PW92 of Perdew and Wang[20]) and LDA+U (using the atomic limit functional) are used. We used a k mesh of 12^3 in the full Brillouin zone. For the density of states (DOS) plot and Fermi surface plot, we used a k mesh of 24^3 for more precision. The basis set was $1s2s2p3s3p3d4s4p::(4d4f5s5p)/6s6p5d+$ for all metal elements(except Y($1s2s2p3s3p3d::(4s4p)/5s5p4d+$) and Ca($1s2s2p::(3s3p)/4s4p3d+$)). For boron atoms we used the basis $::1s/(2s2p3d)+$.

In the LDA+U calculations we used values typical for $4f$ atoms $U = 8$ eV and $J = 1$ eV (corresponding to Slater integrals $F_1=8.00$, $F_2=11.83$, $F_4=8.14$, $F_6=5.86$) throughout all calculations. The high symmetry points in the tetragonal zone are

$\Gamma=(0,0,0)$, $X = (\frac{\pi}{a}, 0, 0)$, $M = (\frac{\pi}{a}, \frac{\pi}{a}, 0)$, $Z = (0, 0, \frac{\pi}{c})$, $R = (\frac{\pi}{a}, 0, \frac{\pi}{c})$, and $A = (\frac{\pi}{a}, \frac{\pi}{a}, \frac{\pi}{c})$.

3.2.4 General Electronic Structure

The valence-conduction band structure of YB_4 (where there are no $4f$ bands) is shown in Fig. 3.2.3. For LaB_4 , which differs in volume and conduction d level position, the bands are very similar, with only slightly differing Fermi level crossings along the M- Γ direction. The occupied valence bandwidth is 11 eV (not all bands are shown in this figure). One striking feature of the bands is the broad gap of more than 3 eV along the top (and bottom) edges R-A-R of the Brillouin zone. Bands along these lines stick together in pairs due to the non-symmorphic space group, and nearly all bands disperse very weakly with k_x (or k_y) along these edges. This gap closes along the $k_z = \pi/c$ plane of the zone only for small in-plane components of the wavevectors. It is such gaps enclosing E_F that often account for the stability of a crystal structure, and the stability of boride structures, including this one, has been a topic of interest for decades.[96, 97, 150, 151]

The band structure of a divalent cation member (CaB_4) is also included in Fig. 3.2.3 for comparison. The largest difference is the band filling, as expected, although some band positions differ in important ways near the Fermi level. Still the $3d$ bands of Ca are not quite empty, as a band with substantial $3d$ character lies at E_F at R and is below E_F all along the R-A line. CaB_4 can be fairly characterized, though, as having nearly filled bonding B $2p$ bands and nearly empty Ca $3d$ bands.

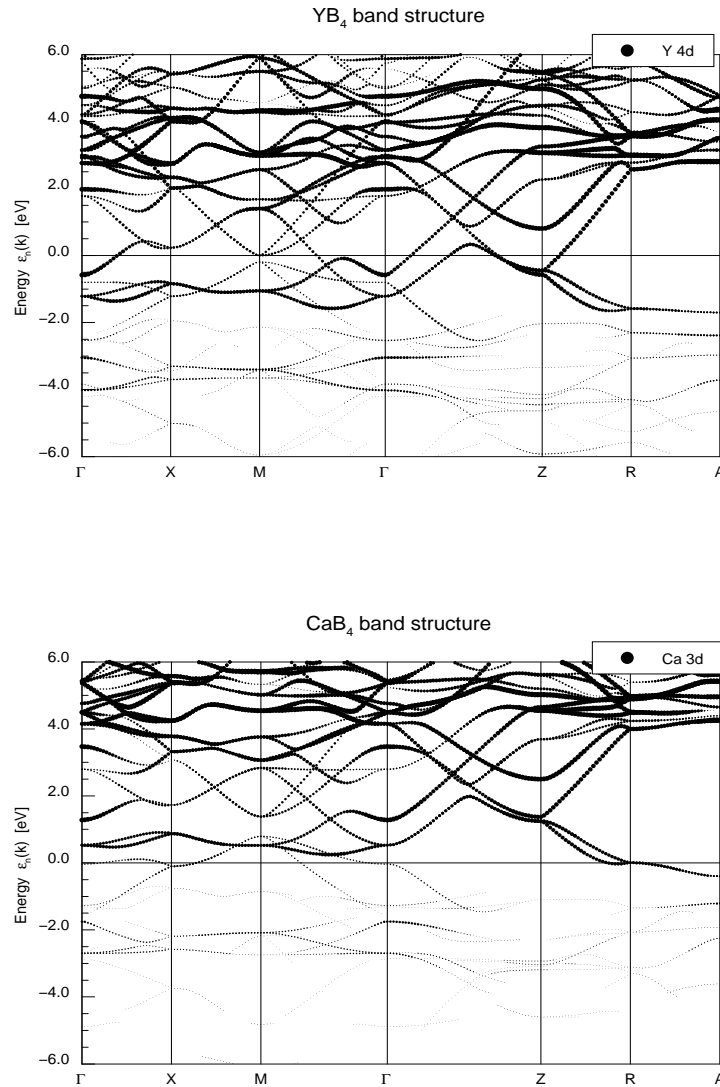


Figure 3.2.3: Band structure of YB₄ (top panel) and CaB₄ (lower panel) within 6 eV of the Fermi level along high symmetry directions, showing the gap that opens up around E_F (taken as the zero of energy) throughout much of the top and bottom portions of the tetragonal Brillouin zone. Notice the lack of dispersion along the upper and lower zone edges R-A-R ($k_z = \pi/c$, and either k_x or k_y is π/a). Note also that, due to the non-symmorphic space group, bands stick together in pairs along X-M (the zone ‘equator’) and along R-A (top and bottom zone edges).

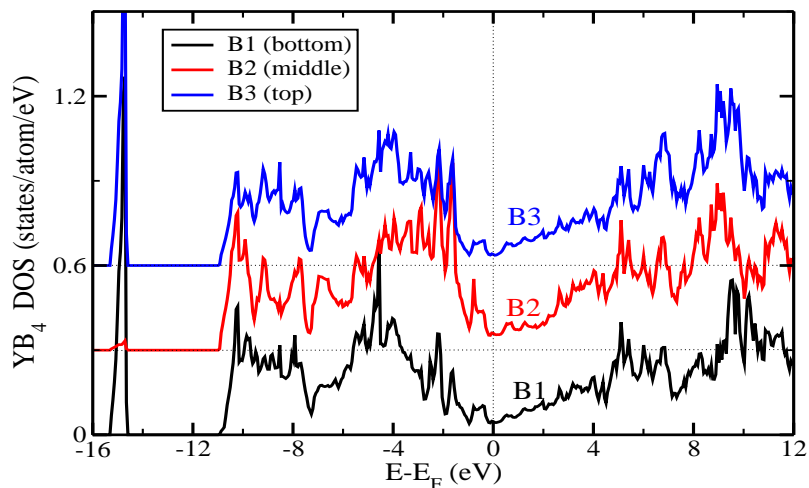


Figure 3.2.4: Projected density of states per atom of each of the B atoms for YB_4 . The curves are shifted to enable easier identification of the differences. The B $2p$ bonding-antibonding gap can be identified as roughly from -1 eV to 4-5 eV.

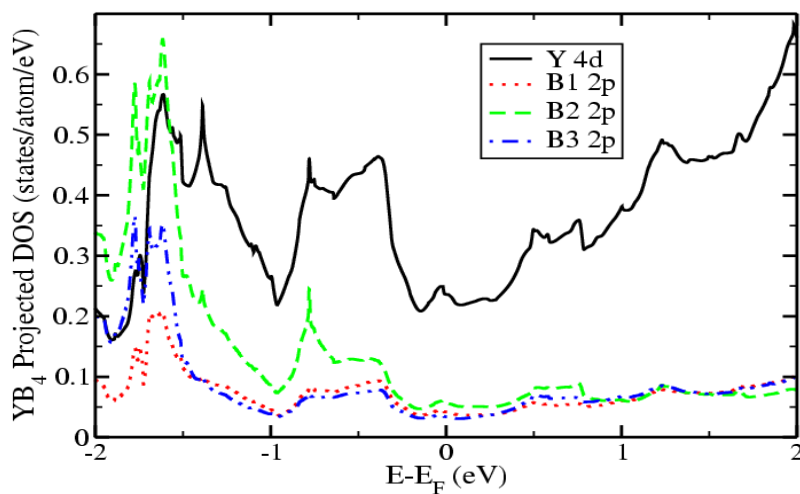


Figure 3.2.5: Enlargement of the partial densities of states of Y $4d$ and B $2p$ states (per atom) near the Fermi level. The states at the Fermi level, and even for almost 2 eV below, have strong $4d$ character. The apical B2 character is considerably larger than that of B1 or B3 in the two peaks below E_F , but is only marginally larger exactly at E_F .

Bonding and Antibonding Bands

As mentioned in the Introduction, the stability of the hexaborides is understood in terms of ten bonding molecular orbitals of the B_6 octahedron. This octahedron occurs also in these tetraborides, along with one additional B_2 dimer that is bonded only in the layer (sp^2). Lipscomb and Britton[96, 97] started from this point, and argued that each of the B_2 atoms in a dimer forms single bonds with two B_3 atoms but a double bond with its dimer neighbor, so each B_2 atom needs four electrons. The total of $20+8$ electrons for each set of $6+2$ boron atoms leaves a deficit of four electrons, or a deficit of 8 electrons in the cell. This amount of charge can be supplied by four divalent cations, with CaB_4 as an example. Most tetraborides contain trivalent cations, however, so this is an issue worth analyzing.

An empirical extended Hückel band structure study[146] for CaB_4 indeed gave a gap, albeit a very narrow one. The Hückel method can be very instructive but is not as accurate as self-consistent density functional methods. Our FPLO calculation on CaB_4 , shown in Fig. 3, gives a metallic band structure. However, the ‘valence’ (occupied) and ‘conduction’ (unoccupied) bands in the bands (Hückel, and also FPLO) are readily identified, and it clear that there are disjoint sets of bands with different characters. There are the boron bonding bands (at E_F and below) that can be clearly distinguished from conduction bands at and above E_F . These conduction bands are primarily metal d bands (with an interspersed nonbonding $B_2 p_z$ band, see below). If they were ~ 0.5 eV higher it would result in an insulating band structure in CaB_4 . The boron antibonding bands lie higher, above 5 eV at least and mix strongly with the metal d bands.

The separation into bonding and antibonding $B 2p$ bands agrees (almost) with the ideas of Lipscomb and Britton, and confirms their counting arguments. However, the

existence of numerous $R^{3+}B_4$ compounds and only one divalent member shows that the extra electron is not a destabilizing influence, while it increases the conduction electron density (hence, the conductivity, and magnetic coupling).

In covalently bonded materials it is common to be able to identify the distinction between the bonding bands and the antibonding bands. In covalent semiconductors, for example, they lie respectively below and above the band gap, an absolutely clean separation. In the RB_4 system the d bands lie within the corresponding bonding-antibonding gap and complicate the picture. Analysis of the orbital-projected bands clarify this aspect. The B1 and B3 atoms, being engaged in three-dimensional bonding (within an octahedron *and* to another unit (octahedron or dimer)), have a clear bonding-antibonding splitting of a few eV (beginning just below E_F). Likewise, the dimer B2 p_x, p_y states display a similar splitting.

The B2 p_z orbital is quite different. As is the case in MgB_2 (whose planar structure is similar to the local arrangement of a B2 atom), p_z bands extend continuously through the gap in the B bonding/antibonding bands, and mix fairly strongly with the rare earth d states in that region. There is considerable B2 p_z character in the bands near (both below and above) E_F at the zone edge M point, as well as the Y $4d$ character that is evident in Fig. 3.2.3. So while there is some B1 and B3 character in the rare earth metal d bands that lie within the boron bonding-antibonding gap, the amount of B2 p_z character is the primary type of B participation in these bands that provide conduction and magnetic coupling.

Pseudogap in the Density of States

From the projected DOS of the three types of B atoms of YB_4 (see Fig. 3.2.4), one can detect only relatively small differences in the distribution of B1, B2, and B3

character arising from their differing environments. First, note that in the DOS of B1 and B3 there is a peak around -15 eV, while there is no such peak for B2. This peak arises from the overlap of $2s$ and $2p_\sigma$ states of each of the boron atoms forming the B_6 octahedra (B1 and B3); the $2s$ character is about three times as large as the $2p_\sigma$ character, and the remaining $2s$ character is mixed into the lower $2p$ bands. This state is a well localized B_6 cluster orbital, and there are two such orbitals (octahedral clusters) per cell. The bridging B2 atoms do not participate in any such bound state.

Another difference in characters of the B sites is that, in the region below but within 2 eV of the Fermi level, the DOS of the dimer B2 atom is significantly larger than that of B1 and B3 atoms, as can be seen in Fig. 3.2.5. Together with plots showing the band character (not shown), this difference reflects the fact that all of the $2p$ orbitals of B1 and B3 (octahedron) atoms are incorporated into bonding (filled) and antibonding (empty) bands. The distinct characteristic of the B2 p_z state was discussed in the previous subsection. All B $2p$ states do hybridize to some degree with the metal d bands, however, and all B atoms have some contribution at the Fermi level.

The full Y $4d$ DOS (not shown) establishes that these bands are centered about 4 eV above E_F , with a ‘bandwidth’ (full width at half maximum) of 6-7 eV (a ‘full bandwidth’ would be somewhat larger). The largest Y character near E_F along symmetry lines is $4d(x^2 - y^2)$, primarily in the bands dispersing up from -0.5 eV at Z toward Γ . The flat bands around -1 eV along $\Gamma - X - M - \Gamma$ are strongly $4d(z^2)$ character, indicative of a nonbonding, almost localized state in the x - y plane. Note that these bands disperse strongly upward along $(0, 0, k_z)$ and lie 3-4 eV above E_F in the $k_z = \pi/c$ plane. Thus the $4d(z^2)$ orbitals form two nearly separate one-dimensional bands along k_z , and give rise to flat parts of some Fermi surfaces (see following sub-

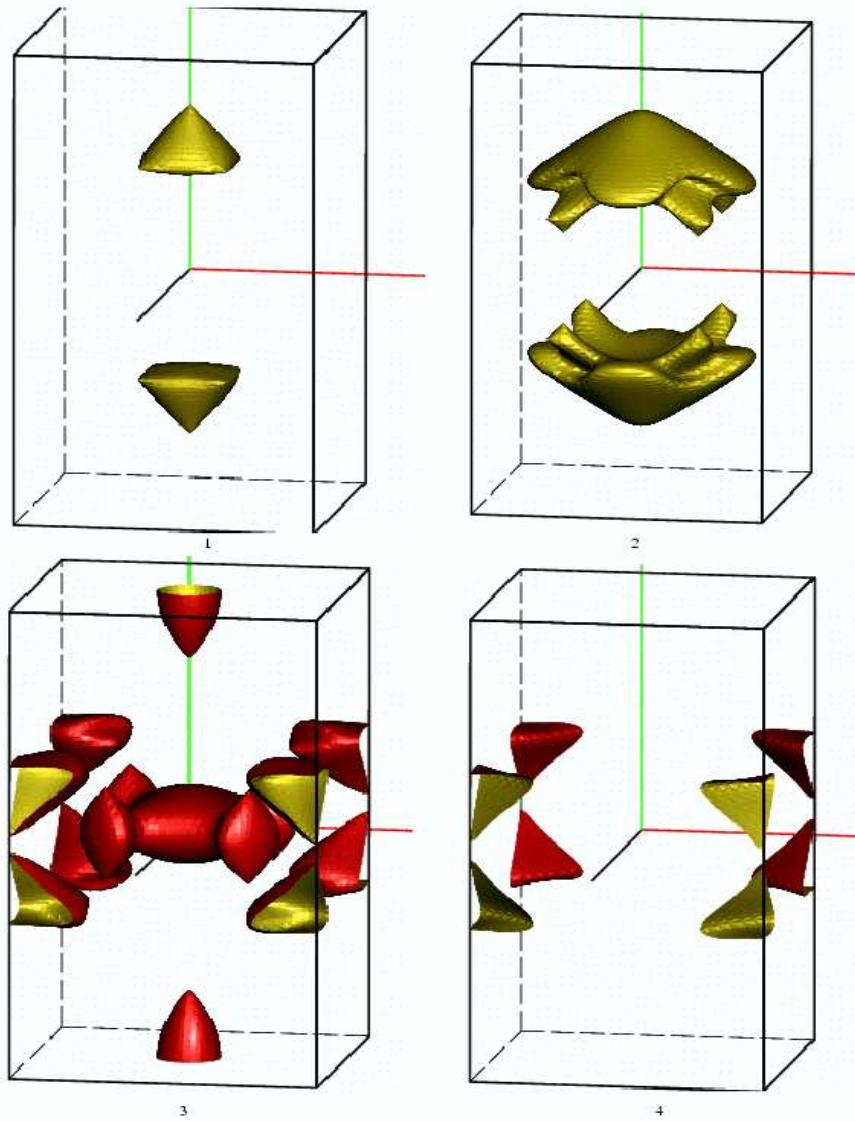


Figure 3.2.6: Fermi surfaces of YB_4 . Light (yellow) surfaces enclose holes, dark (red) surfaces enclose electrons. The wide gap throughout the top and bottom edges of the zone account for the lack of Fermi surfaces there.

section). These bands can be modeled by a tight-binding band $-t_{dd\sigma}\cos k_z c$ with hopping amplitude $t_{dd\sigma} \approx 1$ eV. Most of the $4d(xz), 4d(yz)$ character and $4d(xy)$ character lies above E_F , and is centered 3-4 eV above E_F . The B2 $2p_z$ state mixes primarily with Y $4d_{xz}, 4d_{yz}$ near the M point (near E_F and above). The B2 $2p_z$ orbitals are shifted up somewhat with respect to the $2p_x, 2p_y$ states by the ligand field effects (there is a bonding interaction within the $x-y$ plane only).

Fermi Surface

The Fermi surfaces of YB_4 , shown in Fig. 3.2.6, will be representative of those of the trivalent RB_4 compounds although small differences may occur due to element-specific chemistry of trivalent rare earths and due to the lanthanide contraction. The large gap along the R-A-R edges precludes any FS on or near most of the $k_z = \frac{\pi}{c}$ face. The Fermi surfaces can be pictured as follows. Square hole pyramids with only slightly rounded vertices lie midway along the $\Gamma - Z$ line, and similar nested electron pyramids lie along the $M - A$ line near the M point. A pointed ellipsoid oriented along k_z sits at the Z point. Surrounding Γ is lens-type electron surface joined to pointed ellipsoids along the (110) directions. Finally, there are two “tortoise shell” shaped hole surfaces within the zone, centered along the $\Gamma - Z$ lines.

These surfaces, and the small variation through the lanthanide series, is surely relevant to the varying magnetic behavior observed in RB_4 compounds. There are nesting possibilities between the bases of the square pyramids, for example, which will appear as RKKY coupling as the associated nesting vectors. The ellipsoidal attachments on the zone-centered lens surface may provide some weak nesting.

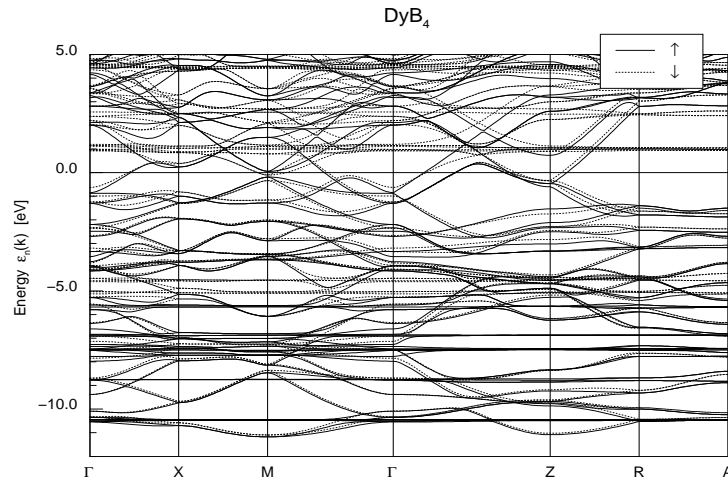


Figure 3.2.7: The full valence band structure of DyB_4 , and up to 5 eV in the conduction bands. This plot is for ferromagnetic alignment of the spin moments, with the solid bands being majority and the lighter, dashed lines showing the minority bands. The flat bands in the -4.5 eV to -11 eV are $4f$ eigenvalues as described by the LDA+U method.

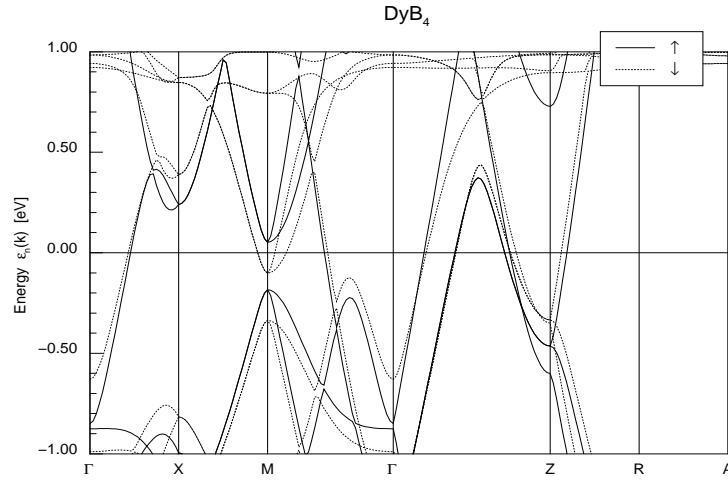


Figure 3.2.8: Band structure of DyB₄ on a fine scale around the Fermi energy, see Fig. 3.2.7. The exchange splitting (between solid and dashed bands) gives a direct measure of the coupling between the polarized Dy ion and the itinerant bands (see text).

3.2.5 The Lanthanide Series

Any effective one-electron treatment of the electronic structure of $4f$ electron systems faces serious challenges. The root of the difficulty is that the ground state of an open $4f$ shell has intrinsic many-body character, being characterized by the spin S and angular momentum L of all of the $4f$ electrons, and the resulting total angular momentum J , following Hund's rules. Although it is possible to delve into the extent to which the LDA+U method can reproduce the z -components of such configurations,[152] that is not the intention here. LDA+U reliably gets the high spin aspect, which contains much of the physics that determines relative $4f$ level positions and hence trends across the series. There is recent evidence from calculations on rare earth nitrides[153] that, if spin-orbit coupling is neglected and the symmetry is lowered appropriately, the high orbital moment (Hund's second rule) can usually

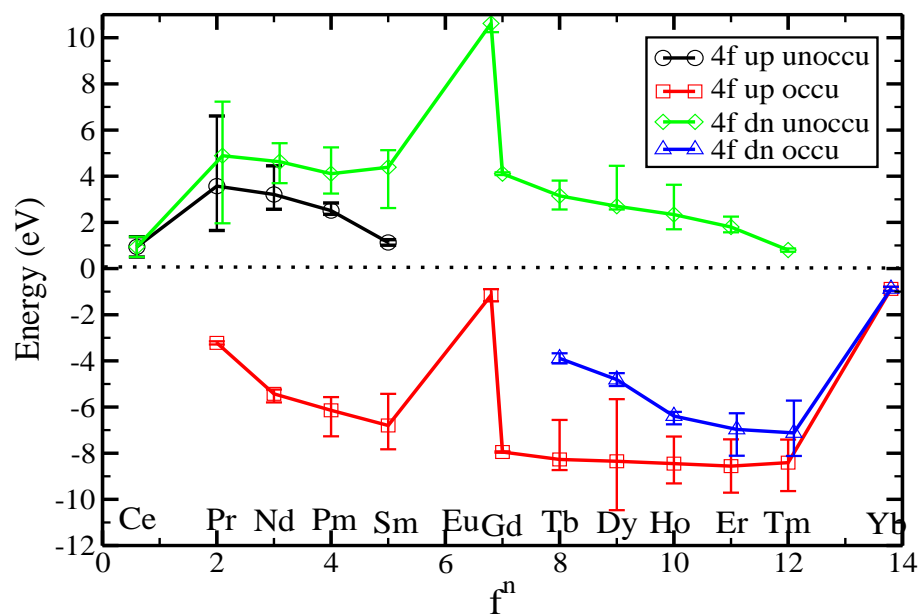


Figure 3.2.9: Calculated mean $4f$ eigenvalue position (symbols connected by lines) with respect to E_F , and the spread in eigenvalues, of RB_4 compounds. The smooth behavior from Pr to Tm (except for Eu) reflects the common trivalent state of these ions. Eu and Yb are calculated to be divalent and deviate strongly from the trivalent trend. Ce has a higher valence than three, accounting for its deviation from the trivalent trend.

be reproduced. The exceptions are the usual difficult (and interesting) cases of Eu and Yb.

The Hund's rule ground state of the ion often breaks the local symmetry of the site, and if one is exploring that aspect the site symmetry should be allowed to be lower than the crystalline symmetry. As stated, we are not interested here in those details. In the calculations reported here, the crystal symmetry is retained. The site symmetry of the lanthanide ion is already low (mm), reflected in its 14-fold coordination with B atoms. In addition, spin-orbit coupling has not been included.

Band Structure

Most of the RB_4 lanthanide tetraborides follow the usual trivalent nature of these ions, and the itinerant parts of their band structures are very similar to those of YB_4 and LaB_4 . The exceptions are $R = \text{Eu}$ and Yb , which tend to be divalent to achieve a half-filled or filled shell, respectively.

By way of illustration of the complexity of the full RB_4 bands, the full band structure of DyB_4 is presented in Fig. 3.2.7 for ferromagnetic ordering. The $4f$ bands themselves can be identified by their flat (weakly hybridizing) nature. An enlarged picture of the bands within 1 eV of E_F is given in Fig. 8. The splitting of the majority and minority itinerant bands provide a direct measure of the Kondo coupling of the $4f$ moment to the band states. Note that the sign of this splitting can vary from band to band.

Figure 8 suggests that the Fermi surfaces will be different in the magnetic tetraborides (compared to YB_4) in specific ways. For Dy, the Γ -centered surface splits almost imperceptibly. The surfaces that cross the Γ -Z line also are relatively unaffected by exchange splitting. At the M point, however, a new surface appears due to

the magnetism: an electron surface of minority spin. For this band, the polarization is opposite to the direction of the Dy spins. This figure is specifically for ferromagnetic alignment, while DyB_4 actually orders antiferromagnetically (see Sec. I).

Position of $4f$ Levels

The mean position of $4f$ levels is displayed in Fig. 3.2.9, separated into occupied and unoccupied, and majority and minority, and trends are more meaningful than absolute energies. Simple ferromagnetic alignment is used here, in order to follow the chemical trends in the simplest manner. For the occupied majority states, the $4f$ level drops rapidly from Pr (-3 eV) to Sm (-7 eV), then becomes almost flat for Gd-Tm (around -8 eV). For the unoccupied minority states, the mean $4f$ level drops almost linearly from Pr (+5 eV) to Er (+2 eV), and for Tm the $4f$ level is very close to E_F . The unoccupied majority levels, which become occupied minority levels beyond the middle of the series, drop more steeply, with slope almost -1 eV per unit increase in nuclear charge.

There are the usual exceptions to these overall trends. Ce is very different, indicating that it is very untypical (the calculational result is tetravalent and nonmagnetic). Both Eu and Yb are divalent in the calculation; an ‘extra’ $4f$ state is occupied so their mean $4f$ level position is 6 eV (8 eV for Yb) higher than the trivalent line.

The spread in $4f$ eigenvalues is also displayed in Fig. 3.2.9. This spread is sensitive to the specific configuration that is obtained, and also has no direct relation to spectroscopic data, although it does reflect some of the internal potential shifts occurring in the LDA+U method. The distinctive features are unusually large spread for the occupied majority levels in Dy (two electrons past half-filled shell), and for the unoccupied minority (and also unoccupied majority) levels in Pr (two electrons

above the empty shell).

3.2.6 Summary

In this section we have provided an analysis of the electronic structure of trivalent tetraborides, using YB_4 as the prototype, and compared this with a divalent member CaB_4 . In agreement with earlier observations on the likely bonding orbitals in the B atoms, it is found that bonding states are (nearly) filled and antibonding states are empty. The states at the Fermi level in the trivalent compounds are a combination of the (dimer) B2 p_z nonbonding orbitals whose bands pass through the bonding-antibonding gap, and the cation d orbitals. Since the extra electron in the trivalent compounds does not go into an antibonding state, there is no significant destabilization of the crystal structure.

The trends in the energy positions of the $4f$ states in the rare earth tetraborides has been found to be consistent with expectations based on other rare earth systems, as is the fact that Eu and Yb tend to be divalent rather than trivalent. Investigations of the magnetic behavior of rare earth tetraborides will require individual study. Nearest neighbor magnetic interactions may involve a combination of $4f-4d-2p_z-4d-4f$ interactions, and longer range RKKY interactions that may bring in the Fermi surface geometry. Another possible coupling path is the direct $4f-2p_z-4f$ path. The coupling is likely to be even more complicated than in the rocksalt EuO and Eu chalcogenides, where competition between direct and indirect magnetic coupling paths has received recent attention.[154] The tetraboride structure is fascinating in several respects. A relevant one, if coupling does proceed directly via $4f-2p_z-4f$, is that the (dimer) B2 atom coordinates with *three* neighboring rare earths ions, which will introduce frustration when the interaction has antiferromagnetic sign.

3.2.7 Acknowledgments

I have benefited from discussion of the calculations with D. Kasinathan, K. Koepf, and M. Richter, and from communication about data on DyB_4 with E. Choi. This work was supported by National Science Foundation Grant No. DMR-0421810.

3.3 Electronic Band Structure and Kondo Coupling in YbRh_2Si_2

The work presented in this section is a part of the published paper[155]: *Electronic band structure and Kondo coupling in YbRh_2Si_2* , G. A. Wigger, F. Baumberger, and Z.-X. Shen, Z. P. Yin, W. E. Pickett, S. Maquilon, and Z. Fisk, Phys. Rev. B **76**, 035106 (2007).

3.3.1 Introduction

Heavy fermion (HF) systems on the border of a zero-temperature magnetic transition have been particularly attractive in the past years[156] because of their anomalous low-temperature thermodynamic, transport, and magnetic properties that deviate strongly from Landau Fermi liquid theory. Recently, an increasing number of examples of Ce- and U-based systems such as $\text{CeCu}_{6-x}\text{Au}_x$, CePd_2Si_2 , CeIn_3 , and $\text{U}_2\text{Pt}_2\text{In}$ have been found to exhibit magnetic quantum criticality by either doping or pressure tuning.[157, 158, 159, 160] YbRh_2Si_2 has attracted attention as the first observed Yb-based and stoichiometric HF system with competing Kondo and Ruderman-Kittel-Kasuya-Yosida interaction, i.e., the dominant exchange mechanisms in metals where the moments interact through the intermediary conduction electrons.[161, 162] In-

deed, in YbRh_2Si_2 , a very weak antiferromagnetic order with a tiny magnetic moment of Yb $\mu \approx (10^{-2} - 10^{-3})\mu_B$ is observed[163] at ambient pressure below the Néel temperature $T_N \simeq 70$ mK. Pronounced non-Fermi liquid behavior has been observed in the resistivity $\rho(T)$ and the electronic specific heat $\Delta C(T)$ at low temperatures, showing $\Delta\rho = \rho - \rho_0 \propto T$ and $\Delta C/T \propto -\ln(T)$, respectively.[164, 165] The ground-state properties of YbRh_2Si_2 can be easily tuned around the magnetic quantum critical point by control parameters such as pressure, magnetic field, or doping.[156] An external pressure compresses the atomic lattice leading to an increase of the antiferromagnetic coupling with a maximal Néel temperature of 1 K at 2.7 GPa.[164, 166] On the other hand, expanding the lattice by replacing Si by Ge [167] or Yb by La favors the Kondo coupling and reduces T_N . Approximately 5% Ge or La doping completely destroys the antiferromagnetic order in YbRh_2Si_2 . Electron-spin-resonance and nuclear-magnetic-resonance experiments have demonstrated the importance of magnetic fluctuations at low T.[163, 168] At intermediate temperatures, a regime emerges for which it is believed that the quantum critical fluctuations dominate and the notion of a well defined quasiparticle breaks down. Remarkably, in YbRh_2Si_2 , this regime extends up to 10 K.[165]

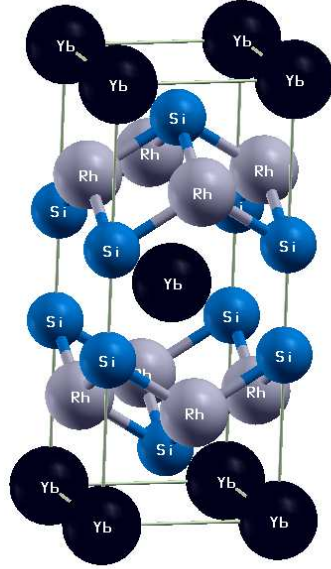
A Hall-effect measurement suggested a discontinuity in the Fermi-surface (FS) volume of one charge carrier across the quantum phase transition.[169] Based on a local-density approximation (LDA) calculation, the change in the FS volume by unit charge was suggested to arise from a shift of the f levels across a quantum transition from the antiferromagnetic phase to the Kondo Fermi liquid.[170] Concurring theories on critical heavy Fermi liquids assume f electrons to be partly integrated into a large FS and distinguish between visible quasiparticle peaks spin-density wave case versus a vanishing Kondo resonance.[171] A direct measurement of the electronic

band structure and especially the location and renormalization of f -derived electronic bands, their hybridization with the conduction bands, and their incorporation into the FS could provide a stringent test of such theories. Angle-resolved photoemission spectroscopy (ARPES) has proven to be uniquely powerful in its capability to directly probe the electronic structure of solids.[172]

We report here the band-structure calculations reflecting the Yb^{3+} ion that is observed by macroscopic experiments at elevated temperatures. Previous calculations have only modeled a nonmagnetic Yb^{2+} ion. We compare the angle-resolved photoemission spectra for YbRh_2Si_2 in the ordinary Kondo-screened state with those for LuRh_2Si_2 . The comparison of the Yb and Lu compounds provides a definitive identification of the $4f$ -derived states in the Yb compound. Most importantly, we have directly observed evidence of hybridization between the $4f$ state and valence states, yielding hybridization gaps ranging from 30 to 80 meV. We performed an analysis[155] of the $4f$ -derived spectrum within the single-impurity Anderson model[173] using parameters suggested by the band-structure calculation, which leads to a picture that differs from those presented in previous studies. This analysis explains $\rho_\nu(\epsilon)$ and macroscopic parameters such as the Kondo temperature T_K in reasonable agreement with the experiments.

3.3.2 Structure

The crystal structure of YbRh_2Si_2 , displayed in Fig. 3.3.1, is body-centered tetragonal (bct) with $I4/mmm$ space group (space group 139). The Yb ion occupies the $2a$ site which has full tetragonal $4/mmm$ symmetry and forms a bct sublattice, which becomes important in the interpretation of its magnetic behavior. Rh resides in a $4d$ site ($\bar{4}m2$ symmetry), and lie on a simple tetragonal sublattice rotated by 45° in

Figure 3.3.1: Crystal structure of YbRh_2Si_2 .

the plane and having lattice constants $a/\sqrt{2}$ and $c/2$. Si is in the $4e$ site ($4mm$); the Si-Si interatomic distances 2.46 \AA is only 5% longer than in diamond structure Si, so one view of the structure is in terms of Si_2 dimers oriented along the \hat{z} axis. Yb atoms and the dimers form a centered square lattice in the $x - y$ plane. Yb is eightfold coordinated by Rh at a distance of 3.17 \AA . The atomic positions are [in units of (a, a, c)]: Yb $(0,0,0)$, Rh $(0, \frac{1}{2}, \frac{1}{4})$, Si $(0,0,0.375)$; note that the Si height is not determined by symmetry and is accidentally equal to $\frac{3}{8}$. The experimental lattice constants $a = 4.010 \text{ \AA}$ and $c = 9.841 \text{ \AA}$ have been used in our calculations.

For reference, we have also calculated the band structure of isostructural and isovalent LuRh_2Si_2 ($a = 4.090 \text{ \AA}$, $c = 10.18 \text{ \AA}$). In this compound, Lu has a filled $4f$ shell under all conditions and the compound is a conventional nonmagnetic metallic Fermi liquid.

3.3.3 Methods

Rare earth atoms, and other atoms with strong effective intra-atomic Coulomb repulsion U (Hubbard U) pose a serious challenge for band theoretical methods. Density functional theory addresses at the most basic level the ground state, which gives the Hund's rule ground state of the Yb ion a central role. Hund's rule implies that one leaves consideration of spin-orbit coupling (SOC) until after the spin S and angular momentum L have been maximized. For interpreting single-particle-like excitations, which is the main topic of this section, one wants to obtain the $j = \ell \pm \frac{1}{2}$ character of the excitations (which is evident in spectra). Thus one must include SOC at the one-electron level, and that is the viewpoint that we take here. From the Curie-Weiss susceptibility at high temperature in YbRh_2Si_2 it is clear that the Yb ion is primarily in an $4f^{13}$ configuration (at elevated temperature, at least), corresponding to $S = \frac{1}{2}$, $L = 3$, $J = \frac{7}{2}$ in the absence of crystal fields.

To be able to include the necessary combination of exchange splitting (magnetic order), SOC, and also the LDA+ U approach that is necessary for rare earth atoms, we have used the WIEN2K electronic structure code.[51] An f^{13} configuration necessarily requires a magnetic ion, and we consider only the simplest (ferromagnetic) alignment of Yb spins. With magnetization along (001) direction, spin-orbit coupling reduces the symmetry to $Abm2$ (space group 39). The around-mean-field version of LDA+ U (appropriate for small spin) was used, with $U=8.0$ eV and $J=1.0$ eV ($U_{eff} = U - J = 7.0$ eV). In the result presented below, the $m=0$ $4f$ orbital was unoccupied. We have also obtained a solution with the $m = -2$ orbital unoccupied. (The Hund's rule state would have $m = +3$ unoccupied.) There is no difference in the results that are discussed here, only minor difference in the placement of the Yb $4f$ bands. The filled f^{14} shell of Lu does not present any of these complications. To obtain an

accurate determination of the Fermi surface, we have used a k mesh of 20^3 (641 k-points in the IBZ), $R K_{max}=9$, and the Perdew-Burke-Ernzerhof generalized gradient approximation[23] for exchange correlation potential. An energy range from -7.00 Ry to 7.00 Ry is used when SOC is incorporated.

3.3.4 Band Structure Results

The band structure shown in Fig. 3.3.2 is characterized by the expected $4f^{13}$ spin-polarized configuration of the Yb ion. Without SOC this would correspond to one hole in the minority $4f$ shell. With SOC included, as here, the flat $4f$ band complex is spin-mixed and split into a $4f_{5/2}$ complex and a $4f_{7/2}$ complex separated by the spin-orbit splitting of roughly 1.3 eV. Although each $4f$ band is quite flat, each of these complexes of $2j + 1$ bands ($j = \frac{5}{2}, \frac{7}{2}$) is split somewhat due to the anisotropy of the Coulomb interaction[174] within the $4f$ shell, which is included fully in the LDA+U method. However, the $4f$ electrons are polarized (one hole, $S=\frac{1}{2}$) so there is also an exchange splitting which complicates the identification in the figure of the $4f_{5/2}$ and $4f_{7/2}$ states separately. However, the result that is pertinent to this section is that this electronic structure calculation fully includes magnetic and relativistic effects, and leaves one hole in the $4f$ shell consistent with the Curie-Weiss susceptibility.

The unoccupied $4f$ band lies 1.4 eV above the Fermi level E_F and can be seen to mix exceedingly weakly with the itinerant (Rh+Yb+Si) bands. The occupied levels lie 2.5 eV or more below E_F and also hybridize weakly. Hence at the band structure level the $4f$ states are well away from the Fermi level. Many-body interactions arising through coupling to the conduction bands may, of course, lead to large renormalizations as reflected in the experimental data.[155] We focus first on the states near and at E_F , and then return to the (Kondo) coupling of the $4f$ moment to the

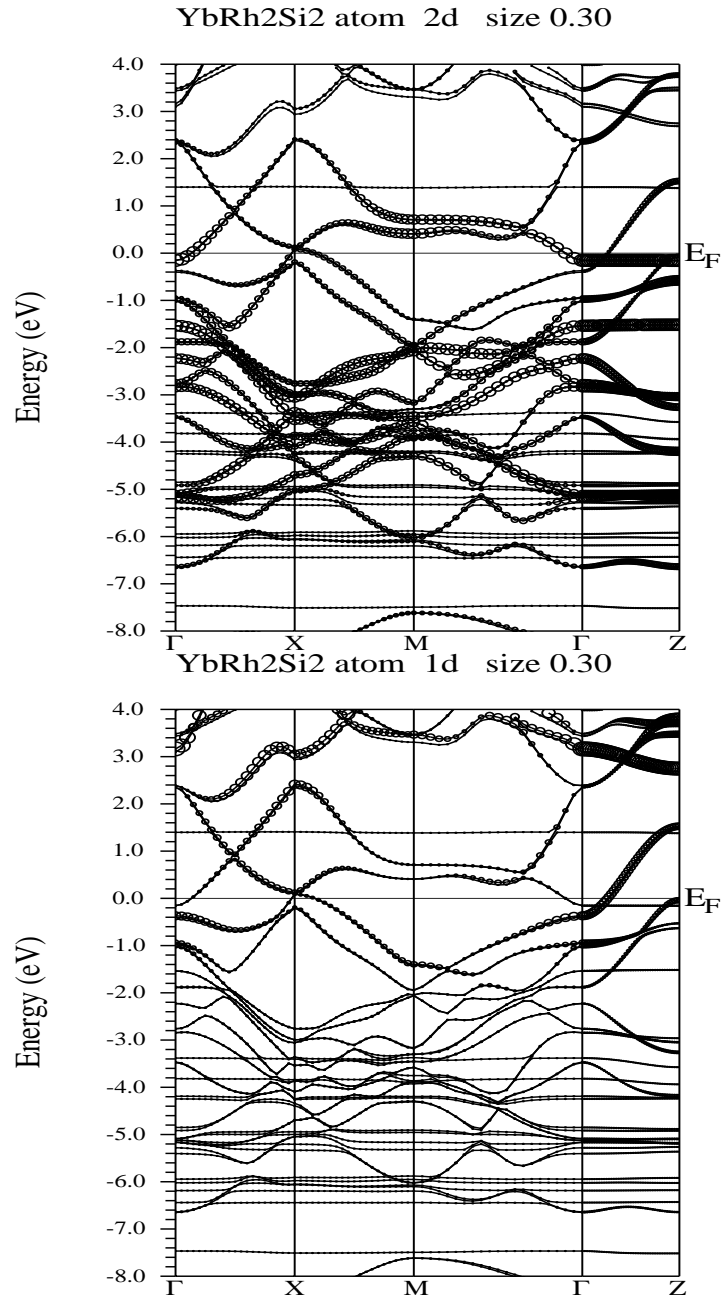


Figure 3.3.2: Band structure of YbRh_2Si_2 along tetragonal symmetry lines. The Cartesian symmetry line indices are $\Gamma(0,0,0)$, $X(1,0,0)$, $M(1,1,0)$, $Z(0,0,1)$, in units of $[\frac{\pi}{a}, \frac{\pi}{a}, \frac{2\pi}{c}]$. Top panel: bands with total Rh $4d$ emphasized using the fatbands representation. Bottom panel: same bands with total Yb $5d$ emphasized using the fatbands representation.

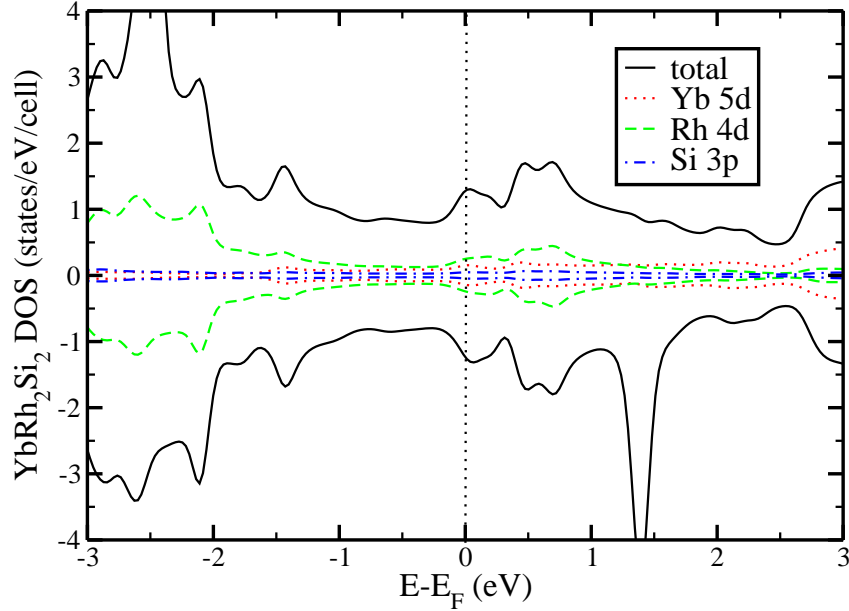


Figure 3.3.3: Total and projected (per atom) densities of states of YbRh_2Si_2 corresponding to the band structure in Fig. 3.3.2. Rh $4d$ character dominates around the Fermi level.

Fermi surfaces.

The total Rh $4d$ and total Yb $5d$ character are shown separately in the projected orbital character (fatband) representations in Fig. 3.3.2. (see Fig. 3.3.3 for the density of states.) Much of the Rh $4d$ bands are occupied, while most of the Yb $5d$ bands are unoccupied, however there is Yb $5d$ character around and below the Fermi level. The Si $3p$ character is spread fairly evenly through the valence and conduction bands. The bands around E_F have mostly Rh $4d$ character, with some Yb $5d$ mixed in, and the bands along symmetry lines are clearly associated with certain symmetry-determined irreducible representations a_g ($d_{3z^2-r^2}$), b_{1g} ($d_{x^2-y^2}$), b_{2g} (d_{xy}) or e_g (d_{xz} , d_{yz}) of the Rh and Yb d states.

The first noteworthy feature is the band lying 0.1 eV below E_F at Γ , which is

completely flat along $\Gamma - Z$ [(0, 0, k_z) line] and disperses upward in the plane: this is a pure Rh $d_{x^2-y^2}$ band, whose two-dimensionality near the band edge will give rise to a (small) step increase in the density of states $N(E)$. There is also strong Rh $4d_{x^2-y^2}$ character at -5 eV (within the 4*f* bands), presumably the bonding combination of $d_{x^2-y^2}$ orbitals on the two Rh atoms in the cell. The Rh $d_{x^2-y^2}$ band crossing E_F contributes the cylindrical faces of the electron-type tall pillbox \mathcal{P} Fermi surface with (near circular) mean radius in the plane of $k_F=0.133 \frac{\pi}{a}$. All three FSs are displayed in Fig. 3.3.4. The Fermi level is intersected along $\Gamma - Z$ by a band composed of Rh $4d_{3z^2-r^2}$, Yb $5d_{3z^2-r^2}$ character and 2 eV wide. This band defines the top and bottom faces of the Γ -centered pillbox, with Fermi wavevector $k_F = 0.265 \frac{2\pi}{c}$ along the \hat{z} axis. This pillbox contains $\sim 4 \times 10^{-3}$ carries/f.u.

From the bands in Fig. 3.3.2 it can be observed that a hole-type surface nearly closes at the $X=(\frac{\pi}{a}, 0, 0)$ point. Because the point we call X is not on the bct Brillouin zone boundary (the true zone is shown in Fig. 3.3.4), this is not a small ellipsoid as might be guessed, but rather part of tubes of a multiply connected jungle gym surface \mathcal{J} . The largest part of this surface encircles nearly all of the upper zone face centered on the $Z=(0, 0, \frac{2\pi}{c})$ point. The character near X is Rh $4d_{xz}, 4d_{yz}$, and some Yb $5d$ character. There is also strong Rh $4d_{xz}, 4d_{yz}$ character in the flat band along $\Gamma - Z$ near -3 eV. Rh $4d_{xy}$ character dominates the flat band at -1.5 eV along $\Gamma - Z$, which disperses downward from there within the plane.

The other Fermi surface, also shown in Fig. 3.3.4, is a fluted donut \mathcal{D} centered at the Z point and oriented in the $x - y$ plane. It arises partially from the upward dispersion in the $x - y$ plane of the band that lies at 30 meV at Z . This donut \mathcal{D} surface contains electrons. The FS of $LuRh_2Si_2$ is nearly identical, as anticipated from the identical structures and the isovalence of the rare-earth ions. One change occurs

due to a small difference in band energy at and near the X point. The \mathcal{J} surface changes its connectivity and shape as a result but remains a large (and generally similar) FS.

3.3.5 Aspects of Kondo Coupling

YbRh_2Si_2 is a heavy fermion compound, whose $J = L + S = \frac{7}{2}$ ion and associated local moment will be affected by crystal fields and finally screened by conduction electrons at low temperature (a tiny moment survives and orders in YbRh_2Si_2). Thus, while our ferromagnetic state with $S = \frac{1}{2}$ is not expected to describe the interacting ground state, it has the virtue of providing a measure of the degree of Kondo coupling of the Yb moment to the two Fermi surfaces, because the exchange splitting of the Fermi surfaces reflects the coupling of the local moment to the itinerant bands.

The exchange splitting of the Γ cylinder is 6 meV around its waist (in the $x - y$ plane) and 30 meV at top and bottom, a strong anisotropy resulting from the different characters of wave functions on the different parts of the surface. For points on the \mathcal{J} surface near the X point, the exchange splitting is 20 meV at both $(0.95, 0, 0)\frac{\pi}{a}$ and $(1, 0.2, 0)\frac{\pi}{a}$. Thus, the Kondo coupling, and likewise the carrier scattering by the moments, differs by at least a factor of 5 around the Fermi surfaces.

3.3.6 Discussion of Bands and Fermi Surfaces

This fully relativistic, spin-polarized LDA+U band structure and resulting Fermi surfaces can be compared with previous unpolarized relativistic LDA prediction. [170, 175, 176] Not surprisingly there are substantial differences, as expected from LDA's $4f^{14}$ configuration versus our magnetic $4f^{13}$ bands; this difference in Yb $4f$ charge state puts Norman's Fermi level one electron lower with respect to the Rh $4d + \text{Yb}$

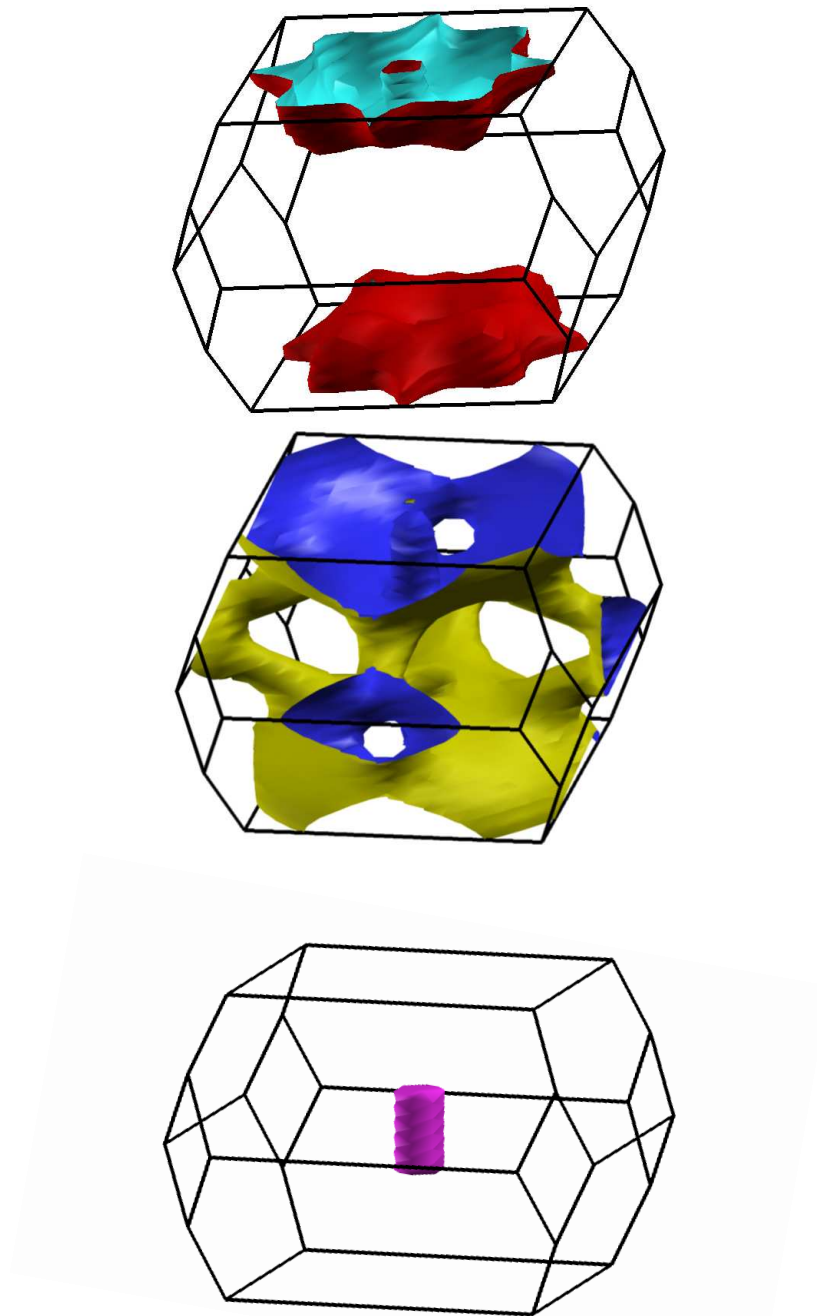


Figure 3.3.4: The three calculated Fermi surfaces of YbRh_2Si_2 with $4f^{13}$ configuration, pictured within the crystallographic Brillouin zone. Top panel: fluted donut \mathcal{D} surface centered around the upper zone face midpoint Z . Middle panel: multiply-connected jungle gym \mathcal{J} surface. Bottom panel: tall pillbox surface \mathcal{P} , containing electrons at the zone center Γ . The Fermi surfaces of LuRh_2Si_2 are very similar, see text.

$5d + \text{Si } 3p$ itinerant bands. As a result, the flat Rh $4d_{x^2-y^2}$ band that lies 0.1 eV below E_F in our bands lies 0.1 eV *above* E_F in the LDA bands, and the Fermi surfaces are entirely different. This will lead to a different prediction for the Hall coefficient.

On the qualitative level, our Fermi surfaces include large sheets with canceling positive and negative contributions to the Hall coefficient, as do Norman's. The Hall coefficient, usually thought of (in the constant relaxation times approximation) as being an average of the Fermi-surface curvature, will bear no relation to the number of carriers. Discussion of the Hall tensor will be deferred to a future publication. No doubt it will be quite anisotropic, given the strong tetragonality of the FSs. The edges of the pillbox \mathcal{P} may give large contributions (and make evaluation difficult); likewise, the sharp edges on the donut \mathcal{D} will also have large curvatures.

The ‘‘curvature’’ interpretation of the Hall tensor relies on the isotropic scattering time approximation. This situation is unlikely to be the case in YbRh_2Si_2 , where the main scattering arises from the Kondo coupling to local moments. As pointed out in the previous subsection, this coupling varies strongly over the Fermi surface (by at least a factor of 5). Hence, this system is an example of a multiband (correlated) metal with large Fermi surfaces of varying curvature, having large and anisotropic scattering. Its Hall tensor, versus temperature, field, and magnetic ordering, promises to be very challenging to understand.

3.3.7 Summary

In this section, we have presented the results of an electronic band-structure calculation within a relativistic framework including correlation corrections for YbRh_2Si_2 . The characteristic of the electronic structure is the $4f^{13}$ ground state as required by the Curie-Weiss moment that is observed at high temperature. A small FS cylinder

of $4d_{x^2-y^2}$ symmetry is centered at Γ , a fluted donut \mathcal{D} surface situated around the upper zone face midpoint Z , and a multiply connected jungle-gym \mathcal{J} surface. The angle-resolved photoemission spectrum manifests true many-body intensities originating from $4f_{7/2}^{13}$ and $4f_{5/2}^{13}$ final-state excitations separated by 1.3 eV, the value for the spin-orbit interaction obtained from the calculation. These excitations are eight-fold (sixfold) degenerate and do not manifest the splitting due to the anisotropic Coulomb interaction inherent to the single-particle energy states.

An analysis[155] of the $4f$ spectrum according the degenerate Anderson impurity model using the parameters obtained from the band-structure calculations explains the appearance of a peak related to the $4f_{7/2}$ excitations at 45 meV below E_F . The Kondo splittings obtained from the bandstructure calculations can be compared to the electronic gaps in the photoemission spectra. In a GS framework, the splittings are $V(\epsilon_F) = V/\pi \approx 33$ meV at Γ and 16 meV at the BZ boundaries. These values agree with those obtained from the LDA+U+SOC calculation. The Kondo temperature $T_K \sim 30$ K and full Yb^{3+} moment are in agreement with the results from macroscopic experiments.

The band structure and FS of LuRh_2Si_2 and YbRh_2Si_2 are compared. The absence of very flat bands in the Lu compound provides confirmation for the $4f$ nature of these bands in the Yb compound. Both compounds show very similar Fermi-surface features. There is no clear difference between the FS of both materials observed, neither theoretically nor experimentally. This indicates that the spectral weight of the $4f$ bands do not contribute significantly in forming the FS at 14 K.

3.3.8 Acknowledgments

I acknowledge important interactions within DOE's Computational Materials Science Network team studying strongly correlated materials. This work was supported by Department of Energy grant DE-FG03-01ER45876 and by the DOE Computational Materials Science Network.

Chapter 4

Conventional Superconductors: Yttrium and Calcium under Pressure

4.1 Introduction to Superconductivity

Superconductivity is one of the most peculiar phenomena in nature. Its zero electrical resistance and full repulsion of magnetic field (known as Meissner effect[177]) have great potential uses in practical applications. The first superconducting phenomenon was discovered in 1911 by Heike Kamerlingh Onnes,[178] who found that the resistance of solid mercury disappeared abruptly at 4.2 K. Since this discovery, scientists have never been stopped seeking superconductors with higher temperatures. In 1913, lead was found to superconduct at 7 K and in 1941 niobium nitride was found to superconduct at 16 K.

Since the first discovery of superconductivity in mercury in 1911, the underly-

ing mechanism has been a major challenge to condensed matter physics community. In 1935, the brothers of F. and H. London[179] explained the Meissner effect as a result of the minimization of the electromagnetic free energy carried by superconducting current. The famous London equations described the two basic electrodynamic properties mentioned above very well. In 1950, Landau and Ginzburg[180] developed the phenomenological Ginzburg-Landau theory by introducing a complex pseudowavefunction ψ as an order parameter within Landau's general theory of second-order phase transitions which led to a Schrödinger-like wave function equation. The Ginzburg-Landau theory explained the macroscopic properties of superconductors successfully. By applying the Ginzburg-Landau theory, Abrikosov[181] showed that superconductors could be grouped into Type I and Type II superconductors in 1957. Also in 1950, Maxwell and Reybold *et al.*[182, 183] found the isotope effect which showed that the critical temperature of a superconductor depends on the isotopic mass of the constituent element. This important discovery pointed to the electron-phonon interaction as the microscopic mechanism responsible for superconductivity. The complete microscopic theory of superconductivity was finally proposed in 1957 by Bardeen, Cooper, and Schrieffer known as the BCS theory.[184] In the BCS theory, they showed that pairs of electrons (known as Cooper pairs) could form through even a weak attractive interaction between electrons, such as electron-phonon interaction. The supercurrent is explained as a superfluid of Cooper pairs. The superconductivity phenomenon was explained independently in 1958 by Nikolay Bogoliubov,[185] who was able to use a canonical transformation of the electronic Hamiltonian to derive the BCS wavefunction, which was obtained from a variational method in the original work of Bardeen, Cooper, and Schrieffer. In 1959, Lev Gor'kov[186] shown that the Ginzburg-Landau theory was a limiting form of the BCS theory close to the critical

temperature. BCS theory is the most successful theory to explained superconductivity in conventional superconductors.

Nevertheless, superconductivity in many superconductors remains unexplained, including (but not limit to) the high temperature superconductors (HTS, namely, the cuprates), the newly discovered iron-based superconductors, some organic superconductors and heavy fermion superconductors (eg: the 115 materials). The most wellknown superconductors are the cuprates, which was first discovered by Bednorz and Müller[188] in 1986 in a lanthanum-based cuprate perovskite material with T_c of 35 K (Nobel Prize in Physics, 1987). It was shortly found by Wu *et al.*[189] that replacing the lanthanum with yttrium , i.e. making YBCO, raised T_c to 92 K. The highest T_c superconductor of this class (and among all superconductors) is the $\text{HgBa}_2\text{Ca}_2\text{Cu}_3\text{O}_{8+x}$ compound under pressure with T_c about 150 K. [190]

The other class is the iron-based superconductors, first discovered in February 2008 by Hosono *et al.*,[191] in a fluorine-doped tetragonal material $\text{LaFeAsO}_{1-x}\text{F}_x$ with $T_c=26$ K. Replacing the lanthanum in $\text{LaFeAsO}_{1-x}\text{F}_x$ with other rare earth elements such as cerium (Ce), [192] praseodymium (Pr), [193] neodymium (Nd), [194] samarium (Sm), [195, 196], and gadolinium (Gd) [197] increases T_c up to 56 K.(the highest T_c in this class up to now) More details of these iron-pnictide compounds are presented in Chapter 5.

A few other (doped) materials were also found to superconduct at a relatively high temperature in the range of 10-40 K. A partial list of these materials[187] is doped C_{60} (T_c up to 40 K), $\text{Ba}_{1-x}\text{K}_x\text{BiO}_3$ (T_c up to 35 K), doped HfNCl (25 K) and ZrNCl (15 K), Y_2C_3 (18 K), $\text{Ba}_2\text{Nb}_5\text{O}_x$ and BaNbO_{3-x} (22 K), $\text{YPd}_2\text{B}_2\text{C}$ (23 K), PuCoGa_5 (18 K). All of these material are structurally complex and are not phonon mediated superconductors. The mechanism(s) responsible for their relatively high T_c

superconductivity is (are) less known.

Due to the lack of mechanism(s) of the above superconductors, the topic of this chapter is restricted to phonon-mediated superconductors with relatively high T_c , whose T_c can be evaluated by using the well known McMillan equation, where the electron-phonon coupling strength and averaged phonon frequency can be calculated by performing linear response calculation.

The biggest surprise in conventional superconductors is the discovery of superconductivity in MgB_2 with $T_c = 40$ K in 2001 by Akimitsu *et al.*[198] Following that is the discovery that free-electron metal lithium superconducts at up to 20 K under 35 - 50 GPa pressure.[199, 200, 201] In early 2006, rare earth metal yttrium was also found to have T_c up to 20 K under 115 GPa pressure by Schilling *et al.* [202] The highest T_c in elemental superconductors is calcium with T_c up to 25 K under 161 GPa found by Yabuuchi *et al.* in August 2006.[203] All of these material are confirmed to be phonon-mediated superconductors but with their own characteristic properties. A common feature, if there is any, is that only a few specific phonon modes localized in a small part of the BZ contributing strongly to electron-phonon coupling strength (and thus to enhance superconductivity).

In this chapter, the focus is on yttrium and calcium under high pressure, where linear response calculations are applied and detailed results are presented. In addition, I also discuss possible structures of Ca under pressure, and manage to explain the observed “simple cubic” structure at room temperature in the pressure range of 32-109 GPa, whereas at $T=0$ K, this simple cubic structure is badly unstable from linear response calculations.

4.2 Linear Response Study of Strong Electron-Phonon Coupling in Yttrium under Pressure

This section was published as[204] “*Linear response study of strong electron-phonon coupling in yttrium under pressure*”, Z. P. Yin, S. Y. Savrasov, and W. E. Pickett, Phys. Rev. B **74**, 094519 (2006).

4.2.1 Introduction

The remarkable discovery[198] in 2001 of MgB₂ with superconducting critical temperature $T_c=40\text{K}$, and the fact that the simple free-electron-like metal lithium[199, 200, 201] also has T_c in the 14-20K under 30-50 GPa pressure, has greatly increased efforts in seeking higher T_c in elements and simple compounds. Of all the elements (over 110), currently there are 29 elements known to be superconducting at ambient pressure and 23 other elements superconduct only under pressure[205, 206]. Among these superconducting elements there is a clear trend for those with small atomic number Z to have higher values of T_c , although much variation exists. For example, under pressure[207, 208] Li, B, P, S, and V all have T_c in the range 11-20 K. Hydrogen[209, 210, 211], the lightest element, is predicted to superconduct at much higher temperature at pressures where it becomes metallic.

While light elements tend to have higher T_c among elemental superconductors, Hamlin *et al.*[202] recently reported that Y ($Z=39$) superconducts at $T_c=17\text{K}$ under 89 GPa pressure and 19.5 K at 115 GPa, with the trend suggesting higher T_c at higher pressure. This result illustrates that heavier elements should not be neglected; note that La ($Z=57$) has T_c up to 13 K under pressure.[212, 213] The superconductivity of La has been interpreted in terms of the rapidly increasing density of states of

4*f* bands near Fermi level with increasing pressure, causing phonon softening and resulting stronger coupling under pressure.[214, 215] Such a scenario would not apply to Y, since there are no *f* bands on the horizon there. No full calculations of the phonon spectrum and electron-phonon coupling have been carried out for either Y or La to date.

La and Y are two of the few elemental transition metals to have T_c above[207, 208] 10 K, and the case of Y is unusually compelling, since its value of T_c is at least as high that of Li, qualifying it as having the highest T_c of any elemental superconductor. (And now it is surpassed by Ca of $T_c = 25$ K under 161 GPa pressure) Moreover, the reduced volume $v \equiv V/V_0=0.42$ corresponds to the value of $T_c \approx 20$ K in Y [202] (115 GPa) and also to the report of $T_c \approx 20$ K in (strained) Li [199] above 50 GPa.[216, 217] For our study of Y reported here, it is first necessary to understand its phase diagram. Under pressure, it follows a structure sequence[218, 219] through close-packed phases that is typical of rare earth metals: hcp \rightarrow Sm-type \rightarrow dhcp \rightarrow dfcc (dfcc is distorted fcc, with trigonal symmetry). The transitions occur around 12 GPa, 25 GPa, and 30-35 GPa. Superconductivity was first found[220] in Y by Wittig in the 11-17 GPa range (1.2-2.8 K), in what is now known to be the Sm-type structure. From 33 GPa to 90 GPa T_c increases smoothly (in fact T_c increases linearly with decrease in v over the entire 35-90 GPa range[202]) suggesting that Y remains in the fcc phase, perhaps with the distortion in the dfcc phase vanishing (the tendency is for the c/a ratio in these structures to approach ideal at high pressure[218]). Calculations[221] predict it adopts the bcc structure at extremely high pressure(>280 GPa), but this is far beyond our interest here.

We have studied the electronic structure and electron-phonon coupling calculations of Y for reduced volumes in the range $0.6 \leq v \leq 1$ (pressures up to 42 GPa).

Our results indeed show strong electron-phonon coupling and phonon softening with increasing pressure. A lattice instability (in the harmonic approximation used in linear response calculations) is encountered at $v=0.6$ and persists to higher pressures. The instability arises from the vanishing of the restoring force for transverse displacements for $Q \parallel < 111 >$ near the zone boundary, corresponding to sliding of neighboring close-packed layers of atoms. It is only the stacking sequence of these layers that distinguishes the various structures in the pressure sequence of structures (see above) that is observed in rare earth metals. Near-vanishing of the restoring force for sliding of these layers is consistent with several stacking sequences being quasi-degenerate, as the structural changes under pressure suggest.

4.2.2 Structure and Calculation Details

Yttrium crystallizes in the hcp structure at ambient pressure with space group $P63/mmc$ (#194) and lattice constants $a=3.647 \text{ \AA}$ and $c=5.731 \text{ \AA}$. [222]

Since the observed structures are all close packed (or small variations from) and above 35 GPa Y is essentially fcc, we reduce the calculational task by using the fcc structure throughout our calculations. The space group is $Fm3m$ (#225), with the equivalent ambient pressure lattice constant $a=5.092 \text{ \AA}$. We do note however that results for electron-phonon strength can be sensitive to the crystal symmetry, both through the density of states and through the nesting function.

We use the full potential local orbital (FPLO) code [47] to study the electronic structure, and apply the full-potential linear-muffin-tin-orbital (LMTART) code [49] to calculate the phonon frequencies and the electron-phonon coupling spectral function α^2F . For FPLO, a k mesh of 36^3 and the Perdew-Wang (PW92) [20] exchange-correlation potential are used. The basis set is $1s2s2p3s3p3d::(4s4p)/5s5p4d+$. For

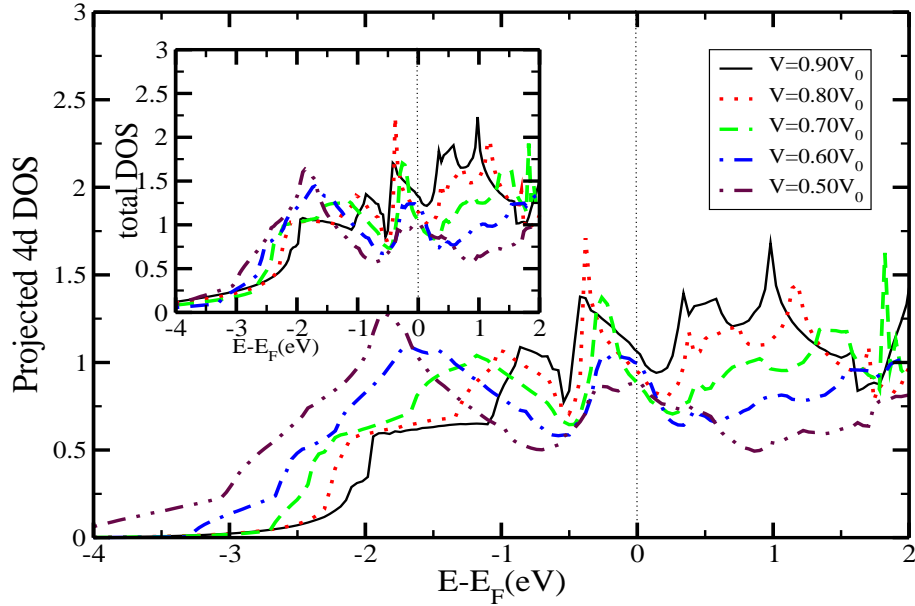


Figure 4.2.1: Plot of the total DOS and projected $4d$ DOS per atom of fcc Y with different volumes. Both the total and the $4d$ density of states at Fermi level decrease with reduction in volume.

LMTART, a k mesh of 48^3 and GGA96 (PBE) approximation[23] for exchange-correlation potential are used. For the electron-phonon coupling calculations we used a phonon Q mesh of 16^3 , which has 145 Q points in the irreducible Brillouin zone.

4.2.3 Electronic Structure under Pressure

Many studies suggest that the general character of an elemental rare earth metal is influenced strongly by the occupation number of the d electrons, which changes under pressure. Our calculations show that the $4d$ occupation number of trivalent Y increases from 1.75 at ambient pressure, to a little above 2 at $V=0.7V_0$ and then finally close to 3 at $V=0.3V_0$ (which is extreme pressure). Such an increase can be seen from the projected density of states (PDOS) of $4d$ states (Fig. 4.2.1) at different

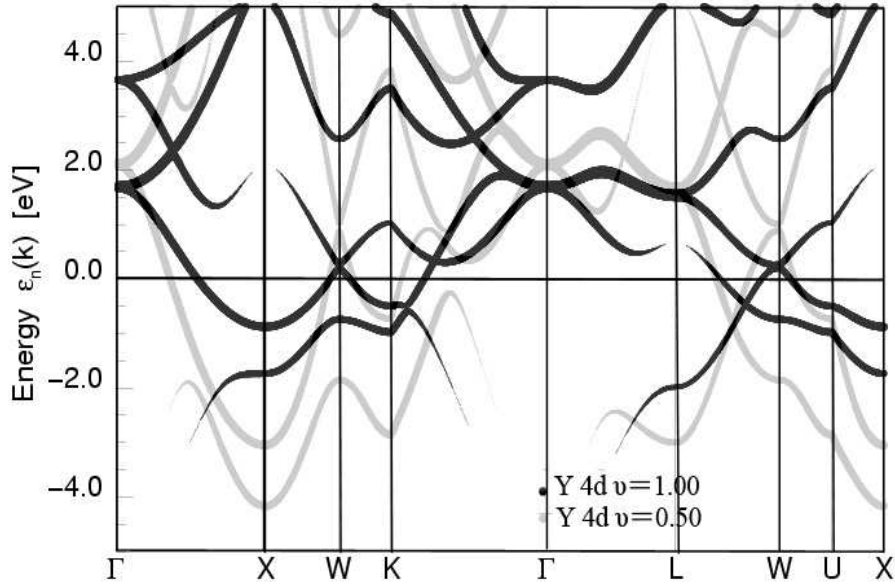


Figure 4.2.2: Plot along high symmetry directions of the bands of Y at $V/V_0=1.00$ and at $V/V_0=0.50$. The “fattening” of the bands is proportional to the amount of Y 4d character. Note that the 4d character goes substantially in the occupied bands under pressure (the lighter shading), although there is relatively little change in the Fermi surface band crossings.

volumes. From Fig. 4.2.1 broadening of the density of states with reduction in volume can be seen, but is not a drastic effect. The main occupied 4d PDOS widens from 2 eV to 3 eV with reduction of the volume to $v=0.5$. The value of the density of states at the Fermi level (taken as the zero of energy) $N(0)$ decreases irregularly with volume reduction; the values are given in Table 4.1.

The pressure evolution of the band structure is indicated in Fig. 4.2.2, where the 4d character at $v=1.00$ (black) and $v=0.50$ (gray) is emphasized. First, the relative positions of the Fermi level crossings change smoothly, indicating there is little change in the Fermi surface topology. This slow change is also seen in Fermi surface plots, of which we show one (below). Second, the overall band widths change moderately, as was noted above in the discussion of the density of states. The change in position

of $4d$ character is more substantial, however. $4d$ bands at X lying at -1 eV and -2 eV at ambient volume are lowered to -3 eV and -4 eV at $v=0.50$. Lowering of $4d$ character bands at K and W is also substantial. Thus Y is showing the same trends as seen in alkali metals. For Cs and related alkalis and alkaline earths under pressure, $6s$ character diminishes as $5d$ character grows strongly with pressure.[225] In Li, $2s$ character at the Fermi surface evolves to strong $2p$ mixture[58] at the volume where T_c goes above 10 K.

The Fermi surface of Y at ambient pressure (hcp) has been of interest for some time, from the pioneering calculation of Loucks[223] to the recent measurements and calculations of Crowe *et al.*[224] However, the unusual Fermi surface in the hcp structure (having a single strong nesting feature) is nothing like that in the fcc phase we are addressing, which is unusual in its own way. At $v=1.00$ the fcc Fermi surface is a large ‘belly’ connected by wide necks along $\langle 111 \rangle$ directions as in Cu, but in addition there are tubes (‘wormholes’) connecting a belly to a neighboring zone’s belly through each of the 24 W points. The belly encloses holes rather than electrons as in Cu; that is, the electrons are confined to a complex multiply-connected web enclosing much of the surface of the Brillouin zone.

As the volume is reduced, the wormholes slowly grow in diameter until in the range $0.5 < v < 0.6$, they merge in certain places with the necks along the $\langle 111 \rangle$ directions, and the change in topology leaves closed surfaces around the K points as well as a different complex multiply-connected sheet. The point we make is that, at all volumes, the Fermi surface is very complex geometrically. There is little hope of identifying important “nesting” wavevectors short of an extensive calculation. Even for the simple Fermi surface of fcc Li, unexpected nesting vectors were located[58] in three high symmetry planes of the zone. The rest of the zone in Li still remains

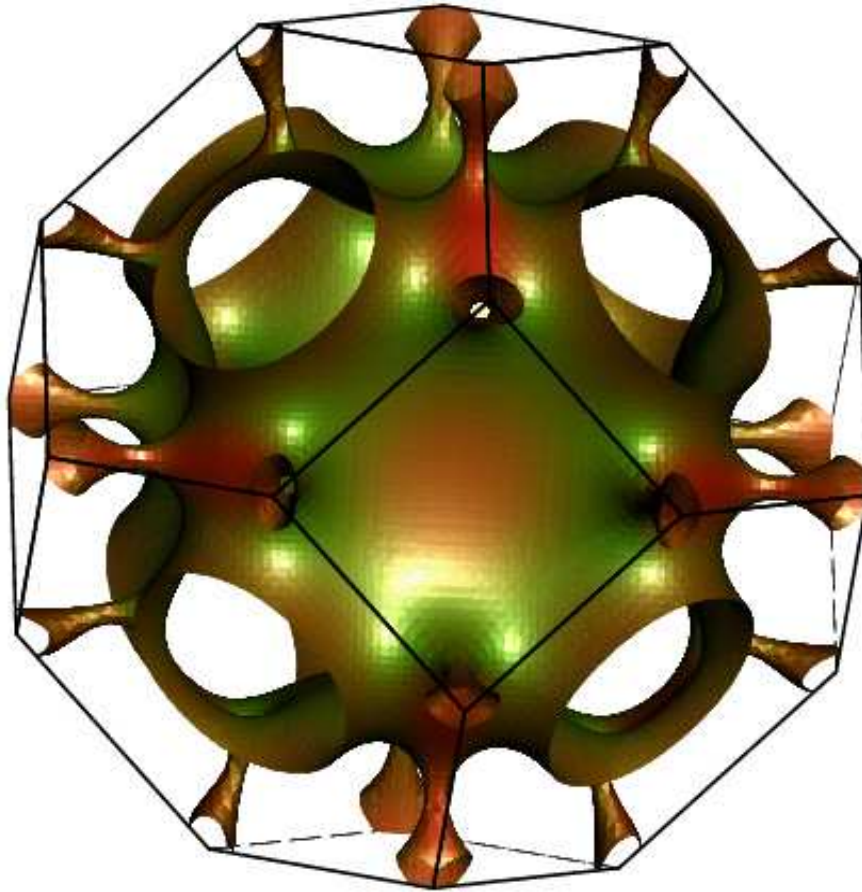


Figure 4.2.3: Surface plot of the Fermi surface of fcc Y at a volume corresponding to ambient pressure. The surface is shaded according to the Fermi velocity. The surface is isomorphic to that of Cu, *except* for the tubes through the W point vertices that connect Fermi surfaces in neighboring Brillouin zones. The evolution with pressure is described in the text.

unexplored.

4.2.4 Results and Analysis

Behavior of Phonons

The calculated phonon branches are shown along the high symmetry lines, from $v=0.90$ down to $v=0.60$, in Fig. 4.2.4. The longitudinal modes behave normally, increasing monotonically in frequency by $\sim 30\%$ in this range. The transverse modes along $\langle 100 \rangle$ and $\langle 110 \rangle$ show little change; the doubly degenerate transverse mode at X *softens* by 20%, reflecting some unusual coupling. Along $\langle 110 \rangle$, T_1 and T_2 denote modes polarized in the $x - y$ plane, and along the z axis, respectively.

The interesting behavior occurs for the (doubly degenerate) transverse branch along $\langle 111 \rangle$. It is quite soft already at $v=0.9$ (7 meV, only 25% of the longitudinal branch), softer than the corresponding mode in hcp Y at ambient pressure.[226] With decreasing volume it *softens* monotonically, and becomes unstable between $v=0.65$ and $v=0.60$. It should not be surprising that the transverse mode at the L point is soft in a rare earth metal. The sequence of structural transitions noted in the introduction (typically hcp \rightarrow Sm-type \rightarrow dhcp \rightarrow dfcc \rightarrow fcc for trivalent elements) involves only different stacking of hexagonal layers of atoms along the cubic (111) direction. So although these various periodic stackings may have similar energies, the soft (becoming unstable) transverse mode at L indicates also that the barrier against sliding of these planes of atoms is very small. At $v=0.60$ (see Fig. 4.2.4) the largest instability is not at L itself but one-quarter of the distance back toward Γ . At $v=0.65$ there are surely already anharmonic corrections to the lattice dynamics and coupling from the short wavelength transverse branches.

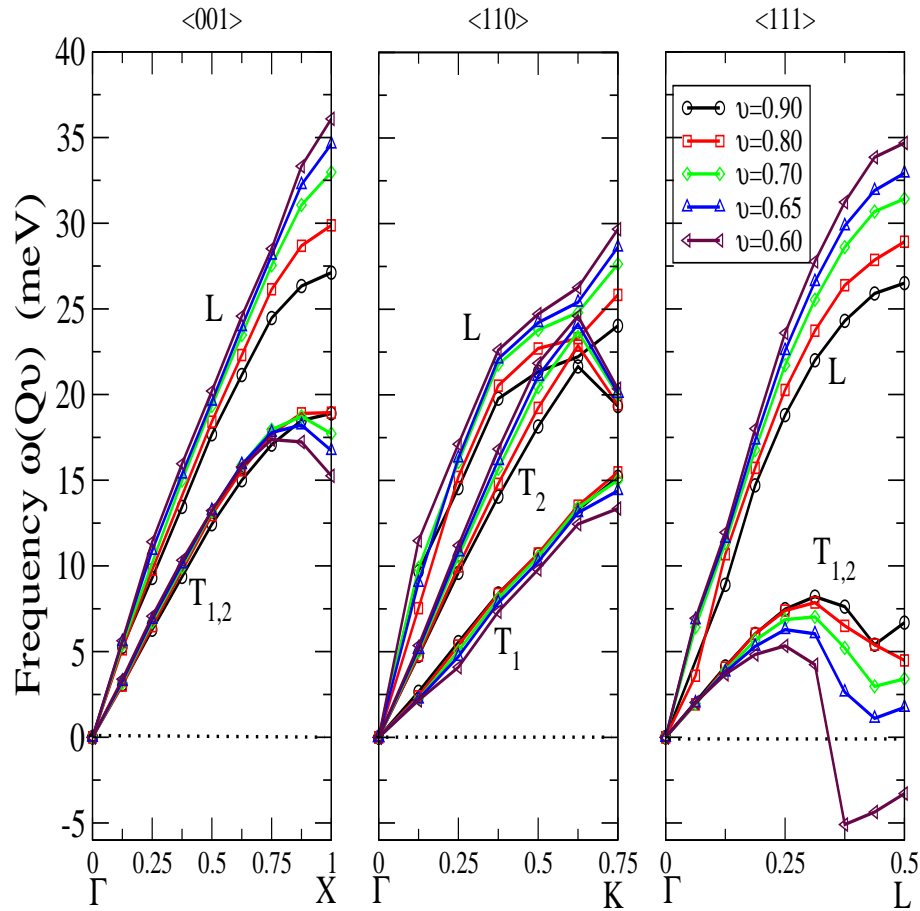


Figure 4.2.4: Plot of the calculated phonon spectrum along high symmetry directions (Γ -X, Γ -K, Γ -L) of fcc Y with different volumes. The longitudinal mode phonons increases with the distance from Γ points along all the three directions. Along Γ -X direction (left panel), the doubly degenerate traverse mode slightly softens near X point, while along Γ -K direction (left panel, only the T_2 mode slightly softens near K point. Along Γ -L direction (right panel), the already soft doubly degenerate traverse mode soften further near the L point with decreasing volume. At $V = 0.6V_0$, the frequency at L becomes negative, indicating lattice instability.

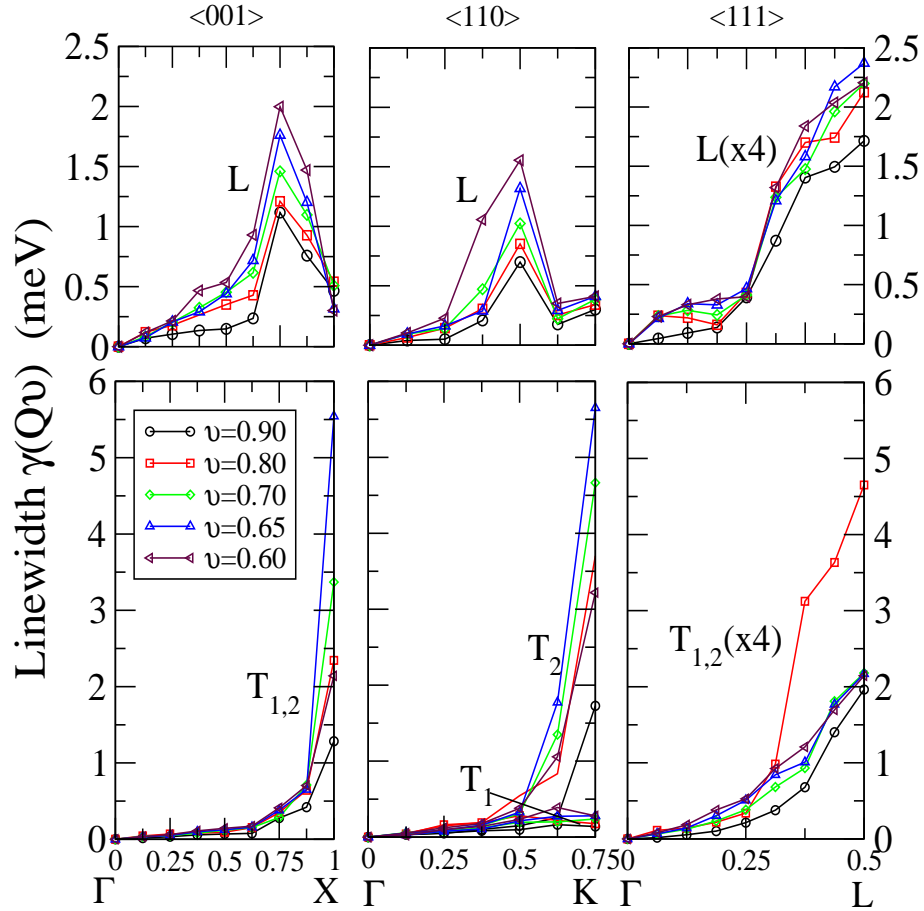


Figure 4.2.5: Plot of the calculated linewidths of fcc Y for varying volumes. The linewidths of the transverse modes at the X point increases from 1.3 to 5.5 as volume decreases from $V=0.9V_0$ to $V=0.6V_0$. The linewidths of the T_2 along $\langle 110 \rangle$ modes show the same increase. The linewidths along the $\langle 111 \rangle$ direction have been multiplied by four for clarity.

Linewidths

The linewidths $\gamma_{Q\nu}$, one indicator of the mode-specific contribution to T_c , are shown in Fig. 4.2.5. To understand renormalization, one should recognize that in lattice dynamical theory it is ω^2 , and not ω itself, that arises naturally. At $v=0.90$, ω^2 for the T modes is only 1/16 of the value for the longitudinal mode at the L point. A given amount of coupling will affect the soft modes much more strongly than it does the hard modes.

For the $\langle 110 \rangle$ direction, the strong peak in $\gamma_{Q\nu}$ for the T_2 (\hat{z} polarized) mode at the zone boundary point K (5.7 meV) is reflected in the dip in this mode at K that can be seen in Fig. 4.2.4. At $v=0.60$ the linewidth is 1/3 of the frequency. The coupling to the T_1 mode along this line is negligible. Note that it is the T_1 mode that is strongly coupled in Li and is the first phonon to become unstable. A peak in the linewidth of the L modes correlates with a depression of the frequency along this line. Along $\langle 001 \rangle$ the T modes again acquire large linewidths near the zone boundary under pressure. This electron-phonon coupling is correlated with the dip in the T frequency in the same region.

The coupling along the $\langle 111 \rangle$ direction is not so large, either for T or for L branches (note, they have been multiplied by a factor of four in Fig. 4.2.5). The coupling is strongest at the zone boundary, and coupled with the softness already at $v=0.90$, the additional coupling causes an instability when the volume is reduced to $v=0.60$ ($P = 42$ GPa). This seems to represent an example where a rather modest amount of coupling has a potentially catastrophic result: instability of the crystal. Evidently Y is stabilized in the fcc structure by anharmonic effects, coupled with the fact that being already close-packed there may be no simple structural phase that is lower in energy.

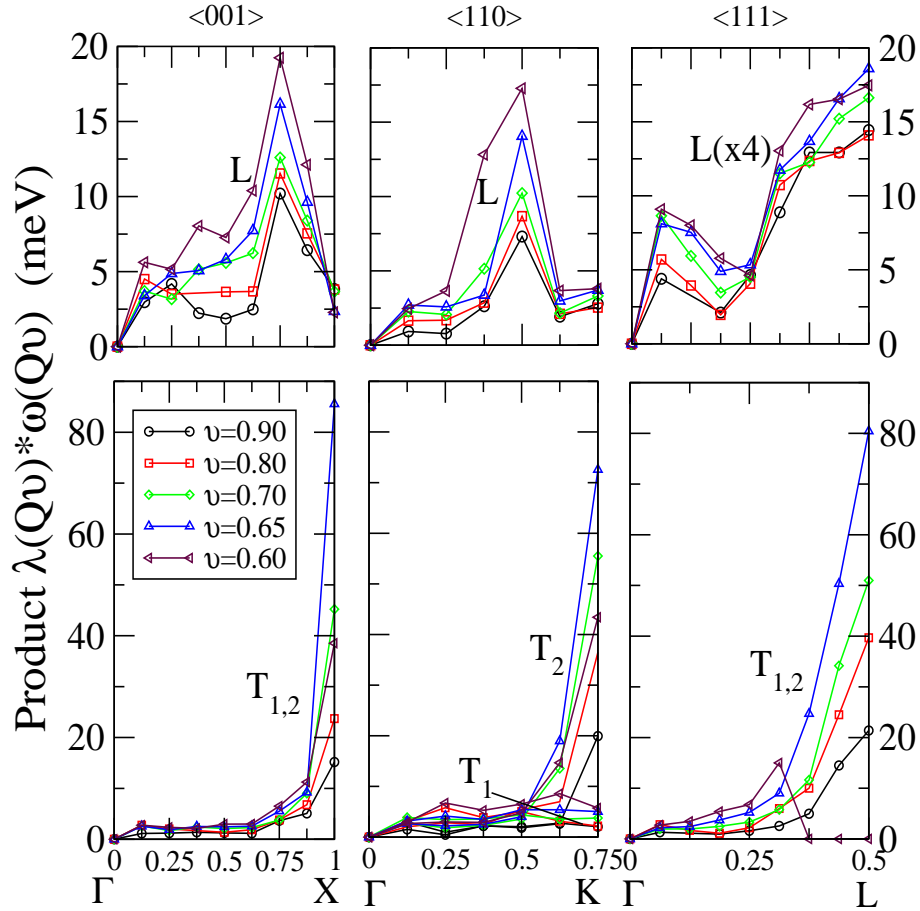


Figure 4.2.6: Plot of the product $\lambda_{Q\nu}\omega_{Q\nu}$ of fcc Y for different volumes, along the high symmetry directions. Note that the longitudinal (L) values along $\langle 111 \rangle$ have been multiplied by four for clarity. In addition, values corresponding to unstable modes near L have been set to zero. Differences in this product reflect differences in matrix elements; see text.

Coupling Strength

It is intuitively clear that strong coupling to extremely low frequency modes is not as productive in producing high T_c as coupling to higher frequency modes. This relationship was clarified by Bergmann and Rainer,[227] who calculated the functional derivative $\delta T_c / \delta \alpha^2 F(\omega)$. They found that coupling at frequencies less than $\bar{\omega} = 2\pi T_c$ has little impact on T_c (although coupling is never harmful). Since we are thinking in terms of Y's maximum observed $T_c \approx 20$ K, this means that coupling below $\bar{\omega} = 10$ meV becomes ineffective.

The product $\lambda_{Q\nu}\omega_{Q\nu} \propto \gamma_{Q\nu}/\omega_{Q\nu}$ gives a somewhat different indication of the relative coupling strength[228] than does either $\lambda_{Q\nu}$ or $\gamma_{Q\nu}$. It is also, up to an overall constant, just the nesting function defined earlier, with electron-phonon matrix elements included within the sum. Since the nesting function is a reflection of the phase space for scattering, it is independent of the polarization of the mode, hence differences between the three branches are due solely to the matrix elements.

This product $\lambda_{Q\nu}\omega_{Q\nu}$ is shown in Fig. 4.2.6. The weight in the transverse modes is concentrated near the zone boundary, with the region being broader around L than at X or K and growing in width with pressure. The T_1 branch along $\langle 110 \rangle$, which is polarized along $[1\bar{1}0]$, shows essentially no coupling. The weight in this product for the longitudinal modes is peaked *inside* the zone boundary along the $\langle 001 \rangle$ and $\langle 110 \rangle$ directions with a mean value of 7-8 meV, and is weaker along the $\langle 111 \rangle$ direction.

$\alpha^2 F(\omega)$

The results for $\alpha^2 F$ are displayed in Fig. 4.2.7. The longitudinal peak in the 20-35 range hardens normally with little change in coupling strength. The 7-20 meV

Table 4.1: For each volume v studied, the columns give the experimental pressure (GPa), the Fermi level density of states $N(0)$ (states/Ry spin), and calculated values of the mean frequency $\omega_1 = \langle \omega \rangle$ (meV), the logarithmic moment ω_{log} and second moment $\omega_2 = \langle \omega^2 \rangle^{1/2}$ (all in meV), the value of λ , the product $\lambda\omega_2^2$ (meV²), and T_c (K). Experimental pressures are taken from ref. [221]. For T_c the value of the Coulomb pseudopotential was taken as $\mu^*=0.15$.

v	P	$N(0)$	ω_{log}	ω_1	ω_2	λ	$\lambda\omega_2^2$	T_c
0.90	6	9.7	12.5	13.6	14.7	0.75	162	4.0
0.80	14	11.3	11.6	13.2	14.5	1.30	273	11.9
0.70	26	9.1	10.1	12.0	13.8	1.53	291	13.0
0.65	32	8.4	7.6	10.2	12.6	2.15	341	14.4
0.60	42	7.9	6.9	9.5	12.1	2.80	410	(16.9)

range of transverse modes at $v=0.90$ increases in width to 2-24 meV at $v=0.60$, and the strength increases monotonically and strongly. The strong peak in $\alpha^2(\omega) = \alpha^2 F(\omega)/F(\omega)$, shown in the bottom panel of Fig. 4.2.7, reflects the very soft modes that have been driven into the 2-5 meV range, and the fact that they are very relatively strongly coupled. The substantial increase in coupling, by a factor of ~ 2.5 , in the range 7-25 meV is important for T_c , as noted in the next subsection.

Estimates of T_c

This background helps in understanding the trends displayed in Table 4.1, where T_c from the Allen-Dynes equation[57] (choosing the standard value of $\mu^*=0.15$) and the contributing materials constants are displayed. The calculated values of λ increases strongly, by a factor of 3.7 in the volume range we have studied. Between $v=0.65$ and $v=0.60$ (the unstable modes are removed from consideration) λ increases 30% but T_c increases by only 2.5 degrees. The cause becomes clear in looking at the frequency moments. These moments are weighted by $\alpha^2 F(\omega)/\omega$. $\alpha^2(\omega)$ itself become strongly peaked at low frequency under pressure, and it is further weighted by ω^{-1} . The frequency moments set the scale for T_c (ω_{log} in particular) and they *decrease* strongly

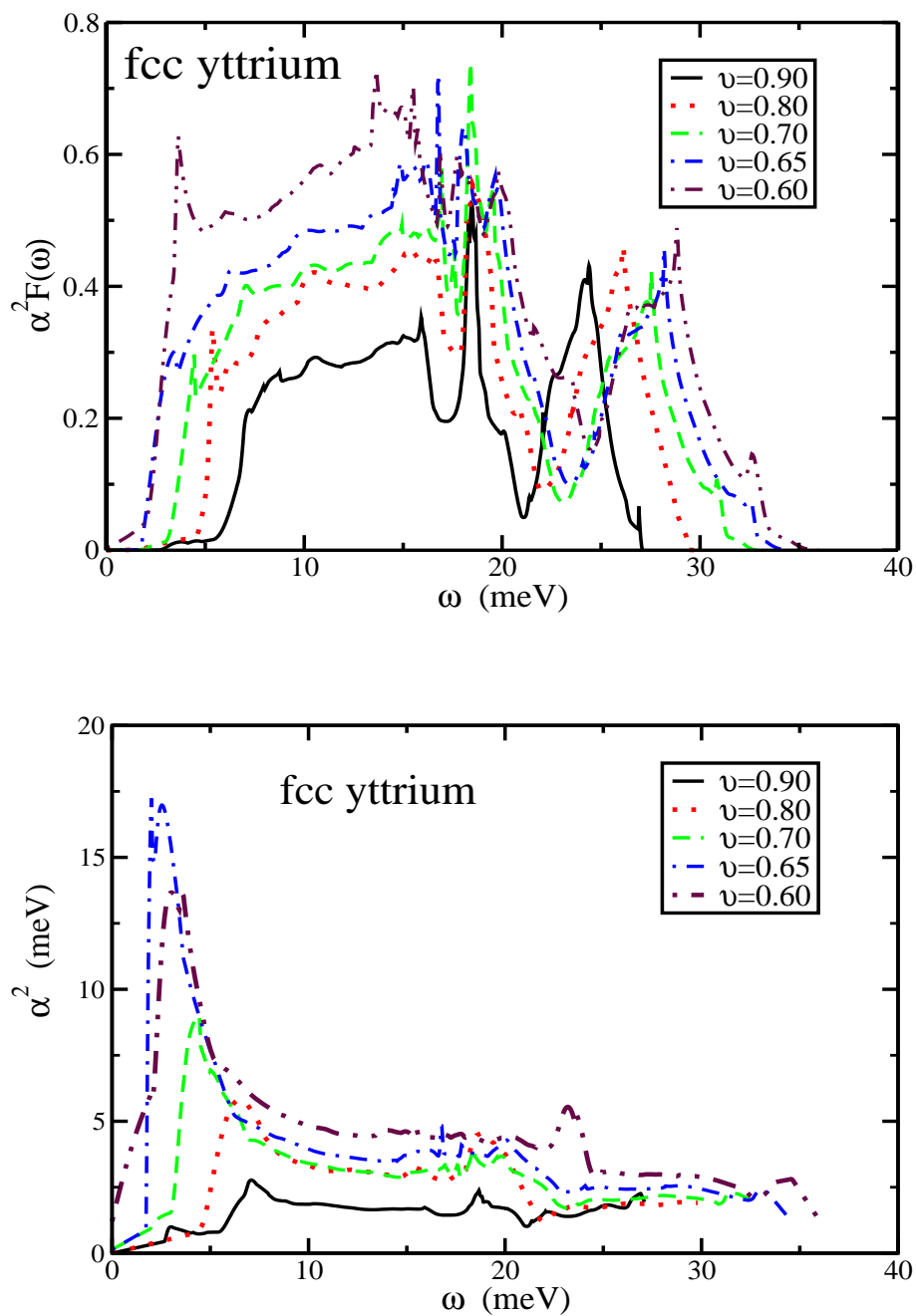


Figure 4.2.7: Top panel: Plot of $\alpha^2 F(\omega)$ versus ω . As volume decreases, $\alpha^2 F(\omega)$ increases and gradually transfers to low frequency. Bottom panel: the frequency-resolved coupling strength $\alpha^2(\omega)$ for each of the volumes studied. The evolution with increased pressure is dominated by strongly enhanced coupling at very low frequency (2-5 meV).

with decreasing volume. In particular, ω_{log} decreases by 45% over the volume range we have studied, reflecting its strong sensitivity to soft modes.

The increase in T_c probably owes more to the increase in coupling in the 10-25 meV range (see $\alpha^2(\omega)$ plot in Fig. 4.2.7; a factor of roughly 2.5) than to the more spectacular looking peak at very low frequency. Put another way, the very low frequency peak in α^2F looks impressive and certainly contributes strongly to λ , but is also very effective in lowering the temperature scale (ω_{log}). For $\alpha^2(\omega)$ shapes such as we find for Y, the quantities λ and ω_{log} which go into the Allen-Dynes equation for T_c do not provide a very physical picture of the change in T_c . For this reason we provide also in Table 4.1 the product $\lambda\omega_2^2 = N(0) \langle I^2 \rangle / M$ ($\langle I^2 \rangle$ is the conventional Fermi surface average of square of the electron-ion matrix element and M is the atomic mass). For the volumes $0.60 \leq v \leq 0.80$ in the table, the ratio of $\lambda\omega_2^2/T_c$ is nearly constant at 23 ± 1.5 (in the units of the table), illustrating the strong cancellation of the increase of λ with the decrease in frequency moments in producing the resulting T_c .

4.2.5 Summary

In this section we have presented the evolution of elemental Y over a range of volumes ranging from low pressure to 40+ GPa pressure ($V/V_o = 0.60$). Lattice instabilities that emerge near this pressure (and persist to higher pressures) make calculations for smaller volumes/higher pressures unrealistic. For simplicity in observing trends the structure has been kept cubic (fcc); however, the observed phases are also close-packed so it was expected that this restriction may still allow us to obtain the fundamental behavior underlying the unexpectedly high T_c in Y. On the other hand, the Fermi surface geometry varies strongly with crystal structure, and the nesting function

$\xi(Q)$ and perhaps also the matrix elements may have some sensitivity to the type of long-range periodicity.

In addition to the band structure, Fermi surface, and electronic density of states, we have also presented the phonon dispersion curves and linewidths along the high symmetry directions, and also have presented $\alpha^2 F(\omega)$ and the resulting value of T_c . The results show indeed that Y under pressure becomes a strongly coupled electron-phonon system, readily accounting for value of T_c in the range that is observed.

In spite of having used a relatively dense mesh of Q points for the phonons, it seems clear that this Brillouin zone integral is still not well converged. Evaluation of $\xi(Q)$ on a very fine Q mesh in three planes for fcc Li, which has a very simple Fermi surface, has shown[58] that this nesting factor contains (thickened) surfaces of fine structure with high intensity. The convergence of this zone integral (and for example the resulting $\alpha^2 F$ function) has rarely been tested carefully in full linear response evaluations of phonons; such a test could be very computationally intensive. Nevertheless, the general finding of strong coupling is clear.

Very recently it has been found that isovalent Sc is superconducting at 8.1 K under 74 GPa pressure.[229] Note that if the lattice were harmonic and the only difference between Sc and Y were the masses (which differ by a factor of two), $T_c = 20$ K for Y would translate to $T_c = 28$ K for Sc. (For an element with a harmonic lattice, λ is independent of mass.) The corresponding argument for (again isovalent) La gives $T_c = 16$ K. La has $T_c = 13$ K at 15 GPa, and has not been studied beyond[207] 45 GPa.

Another comparison may be instructive. Dynes and Rowell obtained and analyzed tunneling data[233] on Pb-Bi alloys where λ is well into the strong coupling region, becoming larger than two as is the case for Y under pressure in Table 4.1. The

Pb_{0.65}Bi_{0.35} alloy has $\lambda=2.13$, $\langle \omega^2 \rangle=22.6$ meV². We can compare directly with the $v=0.65$ case in Table 4.1, which has $\lambda=2.15$, $\langle \omega^2 \rangle=159$ meV². The product $M \langle \omega^2 \rangle$ for Y is three times as large as for the heavy alloy. Since the λ 's are equal, the value of $N(0) \langle I^2 \rangle$ (equal to $\lambda M \langle \omega^2 \rangle$) is also three times as large as in the alloy. The values of T_c are 14.4 K (Y) and 9 K (alloy) [somewhat different values of μ^* were used.] The values of ω_{log} differ by less than a factor of two, due to the low-frequency coupling in $\alpha^2(\omega)$ in Y that brings that frequency down, and that is why the values of T_c also differ by less than a factor of two.

While this study is in some sense a success, in that it has become clear that strong electron-phonon coupling can account for the remarkable superconductivity of Y under pressure, there remains a serious shortcoming, one that is beyond the simple lack of numerical convergence that would pin down precisely λ , T_c , etc. What is lacking is even a rudimentary physical picture for what distinguishes Y and Li (T_c around 20 K under pressure) from other elemental metals which show low, or vanishingly small, values of T_c .

The rigid muffin-tin approximation (RMTA) of Gaspari and Gyorffy,[230] which approximates the phonon-induced change in potential and uses an isotropic idealization for the band structure to derive a simple result, seemed fairly realistic for the electronic contribution (the Hopfield η) for transition metal elements and intermetallics.[231, 232] On top of these idealizations, there is an additional uncertainty in $\langle \omega^2 \rangle$ that must be guessed to obtain λ and T_c . One would not 'guess' the values of the frequency moments that we have obtained for Y under pressure.

In addition, the RMTA expression does not distinguish between the very different matrix elements for the various branches, giving only a polarization and Fermi surface average. Nevertheless, it gave a very useful understanding of trends[231] in

electron-phonon coupling in elemental transition metals and in some intermetallic compounds. While the linear response evaluation of the phonon spectrum and the resulting coupling seems to work well, this more detailed approach has not yet provided – even for elemental superconductors – the physical picture and simple trends that would enable us to claim that we have a clear understanding of strong coupling superconductivity.

4.2.6 Acknowledgments

I have benefited from substantial exchange of information with J. S. Schilling, and help with computer codes from D. Kasinathan. This work was supported by National Science Foundation Grant No. DMR-0421810.

4.3 Competing Phases, Strong Electron-Phonon Interaction and Superconductivity in Elemental Calcium under High Pressure

The work presented in this section was done in collaboration with Prof. Warren E Pickett and Prof. Francois Gygi. Part of the work was accepted for publication in Phys. Rev. B.[234] The preprint for the accepted manuscript is available at <http://arxiv.org/abs/0911.0040> (arXiv: 0911.0040).

4.3.1 Introduction

One of the most unanticipated developments in superconducting critical temperatures (T_c) in the past few years has been achievement of much higher values of T_c in

elemental superconductors by the application of high pressure, and that these impressive superconducting states evolve from simple metals (not transition metals) that are non-superconducting at ambient pressure. The first breakthrough arose in Li, with T_c approaching [199, 200, 201] 20 K, followed by yttrium [202, 235] at megabar pressure also superconducting up to 20 K and showing no sign of leveling off. Both of these metals have electron-phonon (EP) coupled pairing, according to several linear response calculations [236, 58, 204, 237] of the phonon spectrum, EPC strength, and application of Eliashberg theory. These impressive superconductors have been surpassed by Ca, with T_c as high as 25 K reported [203] near 160 GPa. Perhaps more unusual is the report, from room temperature x-ray diffraction (XRD), of a simple cubic (hence far from close-packed) structure over a volume reduction of 45→30% (32-109 GPa). Whether these two unique phenomena are connected, and in what way, raises fundamental new issues in an area long thought to be well understood.

At room temperature, Ca undergoes a series of structural transitions under pressure. [250] It crystallizes in a four-atom fcc cell with lattice constant 5.588 Å at ambient pressure. Under pressure, it first transforms to a body-centered cubic (bcc) space group at about 20 GPa and then surprisingly it remains in a simple cubic (sc, Pm-3m, #221) structure from 32 GPa to 109 GPa. Further compressing makes Ca transform to some unknown structures which are denoted as Ca-IV and Ca-V structure.

A simple cubic (sc) structure for an element is rare, occurring at ambient pressure only in polonium and under pressure only in a handful of elemental metals. [239, 240] This identification of a sc structure for Ca is particularly problematic, since it has been shown by linear response calculations of the phonon spectrum by a few groups [241, 242, 243] that (at least at zero temperature) sc Ca is highly unstable dynamically at *all volumes (pressures)* in the region of interest. Since these calculations are reliable

for such metals, there are basic questions about the “sc” structure itself.

4.3.2 Comparison to Related Metals

Strontium, which is isovalent with Ca, like Ca superconducts under pressure and undergoes a series of structural transitions from close-packed structure to non-close-packed structure at high pressure. Sr transforms from a fcc phase to a bcc phase at 3.5 GPa and then transforms to Sr-III at 24 GPa, to Sr-IV at 35 GPa and to Sr-V at 46 GPa.[244] The Sr-III structure was first believed to be a distorted sc and later found to be an orthorhombic structure.[245] However, later experiments have found that there are two phases coexisting in the Sr-III phase, namely, a tetragonal phase with a distorted β -tin structure and an unidentified additional phase.[245] The Sr-IV structure is very complex and was showed recently to be a monoclinic structure with the Ia space group and 12 atoms per unit cell.[246] The structure is more complex in Sr-V, and was identified as an incommensurate structure similar to that of Ba-IV.[247] Sr begins to superconduct at 20 GPa, its T_c is 8 K at 58 GPa, and is believed to be higher beyond 58 GPa.[244]

Sc, with one more ($3d$) electron than Ca, undergoes phase transitions from hcp to Sc-II at 20 GPa and to a Sc-III phase at 107 GPa.[248, 249] Although Sc is conventionally grouped together with Y and the lanthanide metals as the rare-earth metals, due to their similarities in their outer electron configurations, its structural transition sequence is rather different from the common sequence of lanthanide metals and Y from hcp \rightarrow Sm-type \rightarrow dhcp \rightarrow fcc \rightarrow distorted fcc. The Sc-II structure is very complicated, and was recently found to be best fitted to a pseudo bcc structure with 24 atoms in the unit cell.[248] The structure of Sc-III is not identified to date. Sc begins to superconduct at 20 GPa. Its T_c increases monotonically to 19.6 K with

pressure to 107 GPa. Its T_c drops dramatically to 8 K at the phase transition from Sc-II to Sc-III around 107 GPa.[249]

Considering the close relation of Sc and Sr to Ca in the periodic table and the similar superconducting properties under pressure, it could be expected that Ca under pressure should have more complex structures, as in Sc and Sr under pressure, rather than the observed sc structure. In fact, Olijnyk and Holzapfel[238] observed that their Ca sample transformed from sc to an unidentified complex structure at 42 GPa.

So far the higher pressure phases Ca-IV and Ca-V have attracted the most attention, and considerable progress has been made in identifying these phases through a combination of experimental[203, 250, 251] and theoretical[252, 253, 254] work. However, satisfactory agreement between experimental and theoretical work is still lacking. Ca-IV is identified as a Pnma space group by Yao *et al.*[252] but $P4_32_12$ symmetry by Ishikawa *et al.*[253] and Fujihisa *et al.*[251] Since the Pnma and $P4_32_12$ structures are quite different from each other, the disagreement is substantial. Ca-V seems clearly to have a Cmca space group[253, 251, 252], however, the calculated enthalpy in the Pnma structure is much lower than in other structures (including Cmca structure) at pressures over 140 GPa. Also in the experimental work of Fujihisa *et al.*[251], the fittings of their XRD patterns to the anticipated $P4_32_12$ and Cmca space groups were not satisfactory and other possibilities still exist. In the recent work of Arapan, Mao, and Ahuja[254], an incommensurate structure similar to Sr-V and Ba-IV structures was proposed for Ca-V phase. Therefore the nature of the Ca-IV and Ca-V phases is still not fully settled.

4.3.3 Objective of this Study

While understanding the structure of Ca-IV and Ca-V and its impressive superconducting T_c is one goal of the present work, our focus has been to understand the enigmatic “sc” Ca-III phase that is present from 32-109 GPa, where relatively high T_c emerges and increases with pressure, a phase that XRD at room temperature (T_R) identifies as primitive simple cubic. In this pressure range sc Ca becomes favored over the more closely packed fcc and bcc structures, but the dynamical (in)stability was not calculated by Ahuja *et al.*[255]

We report here first principles calculations of the enthalpy of five crystal structures (sc, $I\bar{4}3m$, $P4_32_12$, $Cmca$, and $Pnma$), and linear response calculations of EPC, that helps to clarify both the structural and superconducting questions. Over most of the 30-150 GPa range, we find at least three crystal phases whose enthalpies indicate they will compete strongly at room temperature. The sc phase is badly unstable dynamically (at $T=0$), but the observed “sc” diffraction pattern can be understood as a locally noncrystalline, highly anharmonic phase derived from a spatially inhomogeneous and dynamically fluctuating combination of these structures, with most of them being straightforward distortions from the sc structure. The picture that arises is one of high pressure “crushing” high symmetry crystal structures of Ca into a non-close-packed, highly locally distorted structure which nevertheless is an excellent superconductor in which T_c increases strongly with pressure. This interpretation impacts yet another precept of superconductivity: disorder normally decreases good conductivity, and disorder *per se* is rarely favorable for superconductivity.

Disorder is typically thought to decrease the superconducting critical temperature T_c , for example, by broadening peaks in the density of states $N(E)$ thus leading to lower values of $N(E_F)$. However, disorder is sometimes observed to enhance super-

conductivity. In the extensively studied A15 compounds, disorder does produce a remarkable reduction in T_c for Nb_3Ge , V_3Si , and Nb_3Al , but it enhances T_c from 1 to 5 K in Mo_3Ge .^[256] Disorder is found to enhance the bulk T_c of Mo films and Mo/Si multilayers.^[257] The influence of disorder on the superconductivity transition temperature of simple amorphous metals was studied theoretically by Krasny and Kovalenko.^[258] They argued that because the structure factor of amorphous metals doesn't have a unique form due to the absence of long-range order, it may lead to the softening of the phonon spectrum, and to the appearance of incoherent electron scattering which, in turn, may lead to an increase of the EP coupling strength λ , compared to the corresponding metals in the crystalline state. As a result, T_c may be higher in a disordered state than in the crystalline state though the Debye temperature may be lowered.

4.3.4 Computational Methods

We have used the full-potential local-orbital (FPLO) code,^[47] the full-potential linearized-augmented plane-wave (FP LAPW) + local orbitals (lo) method as implemented in WIEN2K,^[51] the Qbox code^[259], and the PWscf code ^[43] (now named Quantum ESPRESSO) to do various structural optimizations and electronic structure calculations, and checking for consistency among the results. For the enthalpy calculations we used the PWscf code.^[43] We use a norm-conserving pseudopotential of Ca in Qbox and a Vanderbilt ultrasoft pseudopotential^[36] of Ca in Pwscf, while both the FPLO and WIEN2K codes are all-electron and full potential codes. The linear-response calculations of phonon spectra and electron-phonon spectral function $\alpha^2F(\omega)$ were done using the all-electron, full potential LMTART code.^[49]

The parameters used in PWscf for the structural optimizations and enthalpy cal-

culations were: wavefunction plane-wave cutoff energy of 60 Ry, density plane-wave cutoff energy of 360 Ry, k mesh samplings (respectively, number of irreducible k points) $24*24*24$ (455), $32*32*32$ (897), $24*24*8$ (455), $24*24*24$ (3614), $24*32*32$ (6562) for sc, $I\bar{4}3m$, $P4_32_12$, Cmca, and Pnma structure, respectively. Increasing the number of k points lowers the enthalpy by only 1-2 meV/ Ca almost uniformly for all structures, resulting in negligible change in volume, lattice constants, and internal coordinates. In these calculations, we used a Vanderbilt ultrasoft pseudopotential[36] with Perdew-Burke-Ernzerhof[23] (PBE) exchange correlation functional and nonlinear core-correction, which included semicore $3s3p$ states as well as $4s3d$ states in valence states.

Structure Optimization. The dynamic instability of the sc phase of Ca suggested relaxation of the structure using molecular dynamics (MD) methods. Our MD calculations with the Qbox code resulted in a four-atom bcc cell with space group $I\bar{4}3m$ (#217) that is dynamically stable at least from 40 GPa to 110 GPa. In this structure, Ca occupies the $8c$ Wyckoff position with atomic coordinate (x, x, x) , with $x \approx 0.22$. Since $x=0.25$ will restore the sc structure, this $I\bar{4}3m$ structure is easily seen to be a straightforward distortion from the simple cubic structure.

Ishikawa *et al.*[253] suggested that Ca forms an orthorhombic structure at 120 GPa. Our MD calculations confirmed the stability of this structure, which has space group Cmca, which is a base-centered orthorhombic structure with Ca at Wyckoff position $8f$ $(0, y, z)$, where $x \sim 0.34$ and $y \sim 0.19$. Since $x=0.25$ and $y=0.25$ and appropriate lattice constants will restore the simple cubic structure, this Cmca is also readily recognized as a distortion from the sc structure. Linear response calculations also show that this structure is dynamically stable over a wide pressure range.

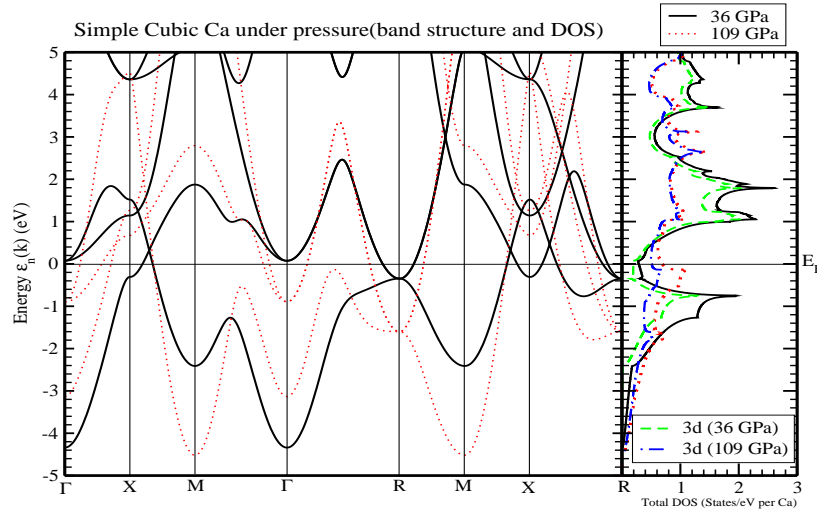


Figure 4.3.1: Band structure and DOS of sc Ca at 36 GPa ($a=2.70 \text{ \AA}$, $0.451 V_0$) and 109 GPa ($a=2.35 \text{ \AA}$, $0.297 V_0$). The high symmetry points are $\Gamma(0, 0, 0)$, $X(1, 0, 0)$, $M(1, 1, 0)$ and $R(1, 1, 1)$ in the units of $(\pi/a, \pi/a, \pi/a)$.

4.3.5 Simple Cubic Calcium

Although sc Ca is unstable, the crystal structure and its electronic structure is still a valuable reference from which to investigate the trend when pressure increases. It is common that s electrons will transfer to d electrons in metals under pressure. At about 36 GPa ($0.451 V_0$), the occupation number of $3d$ states is 1.03. It increases to 1.47 at 109 GPa ($0.297 V_0$). The valence states are mostly $3d$ character, with some $4s$ and $4p$ character. (see Fig. 4.3.1)

The bands are very dispersive already at 36 GPa and they are further broadened with increasing pressure. For example, the bands along X-M direction spans from -2.4 eV to +1.6 eV at 36 GPa, and broadens to -4.5 eV to +4.5 eV at 109 GPa. These are typical d -like bands. The broadening is also reflected in the total density of states (DOS) and $3d$ projected DOS (PDOS) plot. As mentioned above, Ca doesn't

superconduct at 36 GPa but becomes a good superconductor ($T_C=23$ K) at 109 GPa. Then one question comes that why it undergoes such dramatic change. First of all, the total DOS $N(E)$ at E_F increases by a factor of two from 0.3 states/eV at 36 GPa to 0.7 states/eV at 109 GPa. The increase of $N(E_F)$ can favor superconductivity. The more important reason is the change of band structure around Fermi level due to the increasing pressure, which leads to the broadening and shifting of bands. The change of bands will change the size and topology of its Fermi surfaces. There are three pieces of Fermi surfaces at 36 GPa, one small two-dimensional piece around X and two small pieces around R. (See Fig. 4.3.2) With increasing pressure, all the three pieces grow in size and two new pieces emerge around Γ (one cube like and the other p orbital like). At 109 GPa, the piece surround X becomes a large cube with side length of about $2\pi/3a$. The surface of the cube is very flat, indicating large nesting and potential huge electron-phonon couplings. Unfortunately, linear response calculations get imaginary frequencies in a large part of the BZ (see Fig. 4.3.3), suggesting instability of the sc structure. Nevertheless, since the average structure is sc (room temperature XRD suggests sc structure), the possible low temperature structures should be some small distortions of sc structure. As long as the distortion is small, the above argument is still valid.

4.3.6 $I\bar{4}3m$ Ca

As mentioned before, several groups have calculated that Ca is dynamically unstable over much of the Brillouin zone in the sc structure,[241, 242, 243] as shown in Fig. 4.3.3 The most unstable modes of sc Ca are transverse [001]-polarized zone boundary modes along the (110) directions. A linear combination of the eigenvectors of this mode at different zone boundary points leads to a body-centered four-atom cell in

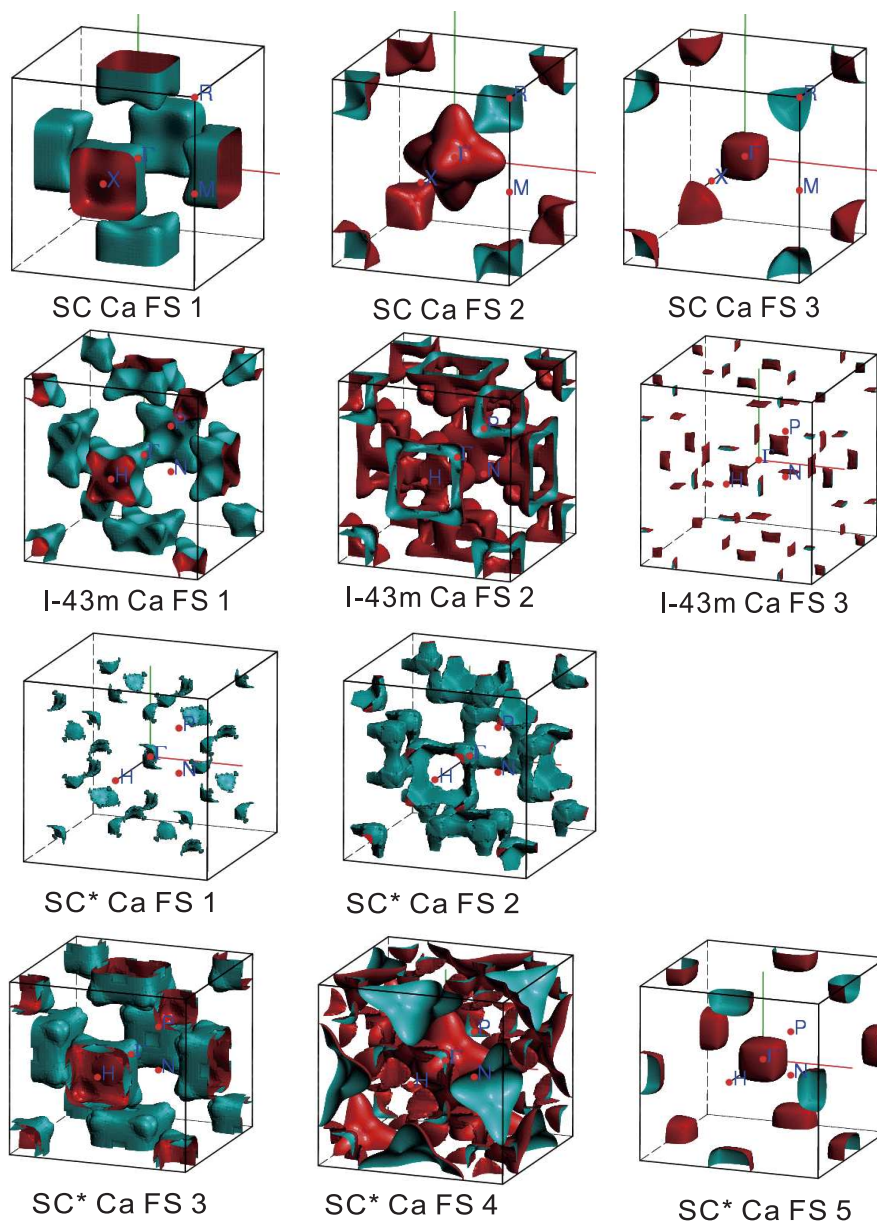


Figure 4.3.2: Fermi surface of sc Ca, $I\bar{4}3m$ Ca and the sc* Ca which takes the symmetry of $I\bar{4}3m$ space group, i.e., 8 atoms in the unit cell with $x=0.25$, at 109 GPa ($0.297 V_0$).

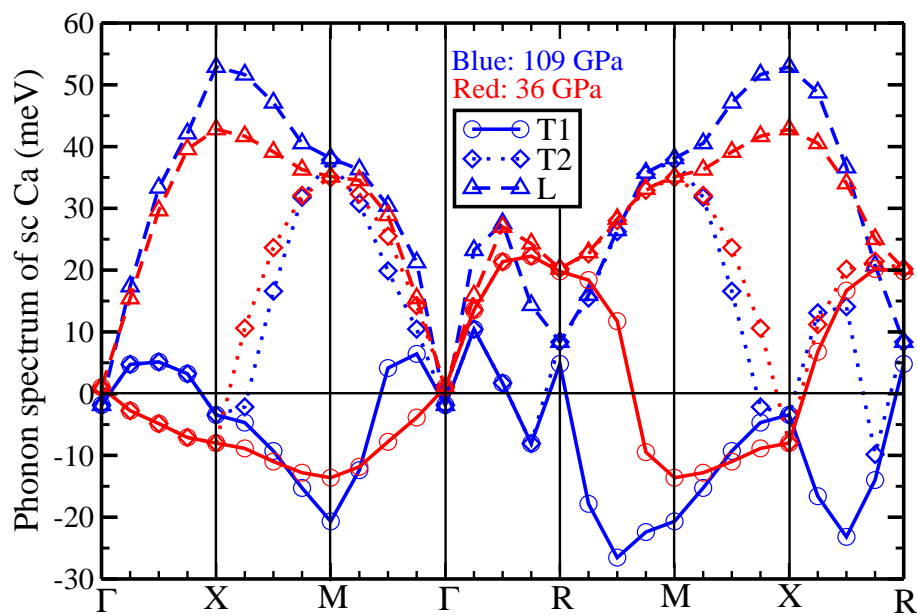


Figure 4.3.3: Phonon spectrum of sc Ca at 36 GPa and 109 GPa. The high symmetry points are $\Gamma(0, 0, 0)$, $X(0.5, 0, 0)$, $M(0.5, 0.5, 0)$ and $R(0.5, 0.5, 0.5)$ in the units of $(2\pi/a, 2\pi/a, 2\pi/a)$.

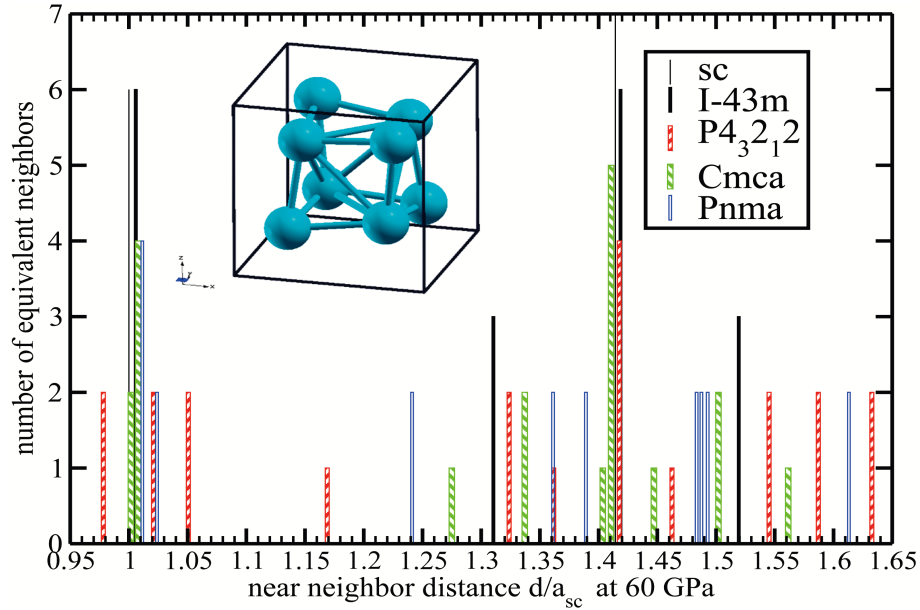


Figure 4.3.4: Local coordination of the five structures of Ca, plotted as number of neighbors versus the distance d relative to the cubic lattice constant a_{sc} with the same density. The inset shows the unit cube of the $I\bar{4}3m$ structure (which contains two primitive cells); this structure retains six near neighbors at equal distances but three different second neighbor distances. The $P4_32_12$ and $Pnma$ structures can be regarded to be seven-coordinated, albeit with one distance that is substantially larger than the other six.

the space group $I\bar{4}3m$, whose local coordination is shown in the cubic cell in the inset of Fig 4.3.4, and has a clear interpretation as a buckled sc lattice. This structure, when relaxed, becomes dynamically stable.

Since the $I\bar{4}3m$ structure is a straightforward distort from the sc structure. It is necessary to compare it with the sc structure energetically, along with the close-packed bcc structure, in the pressure range of 32-109 GPa. Fig. 4.3.5 shows the volume dependence of the total energy and resulting pressure. Above $0.40 V_0$ (low pressure), bcc has the lowest total energy, i.e., Ca prefers to stay in bcc structure, which is consistent with experimental observations. Then just below $0.40 V_0$ (about $0.395 V_0$), $I\bar{4}3m$ structure has the same total energy as bcc structure. Below 0.39

V_0 , $\bar{I}43m$ structure becomes the most stable structure. As for the sc structure, it has lower total energy than bcc structure at volumes below $0.36 V_0$, but its total energy is always higher than $\bar{I}43m$ structure across the whole volume range from $0.48 V_0$ to $0.28 V_0$. This suggests that Ca may never reside in the sc structure. Throughout the volume range, sc and $\bar{I}43m$ structure have about the same pressure, and bcc always gets about 6 GPa higher. Because bcc has a higher pressure at the same volume/Ca, the structure transition from bcc to $\bar{I}43m$ will take place around $0.395 V_0$, and may accompany with volume collapse. The $3d$ occupation number is also a little bit different: $\bar{I}43m$ structure gets 0.03 less than sc structure and bcc get 0.10 less.

The variation of the band structure and DOS under pressure of $\bar{I}43m$ structure has the same trend as in sc structure (band broadening and shifting). Bands are still quite dispersive, but less dispersive than in sc structure. DOS at E_F also increases as pressure increases with about 0.45 states/eV per Ca at 109 GPa, which is less than 0.70 states/eV per Ca of sc Ca at 109 GPa. The difference of bands between sc and $\bar{I}43m$ Ca gives different Fermi surface. The variation of the Fermi surface of $\bar{I}43m$ Ca under pressure shares a similar trend to sc Ca: small pieces become bigger and flat, new trivial pieces emerge. The growing and flattening of Fermi surfaces is a clear indication of increasing nesting and possible electron-phonon coupling, which is consistent with experiments and our linear response calculations. Comparing the Fermi surface of $\bar{I}43m$ and sc Ca at 109 GPa, the flat piece of Fermi surface of sc Ca is bigger and flatter than $\bar{I}43m$ Ca, which suggests that sc Ca, if stable, will have stronger e-p coupling and higher T_C . Shi *et al.* [260] used rigid muffin-tin approximation (RMTA) and obtained unrealistically large e-p coupling constant λ , η and thus T_C . For example, at $0.270 V_0$, RMTA gives $\lambda \sim 5.5$, $\eta \sim 21.45 \text{ eV/\AA}^2$,

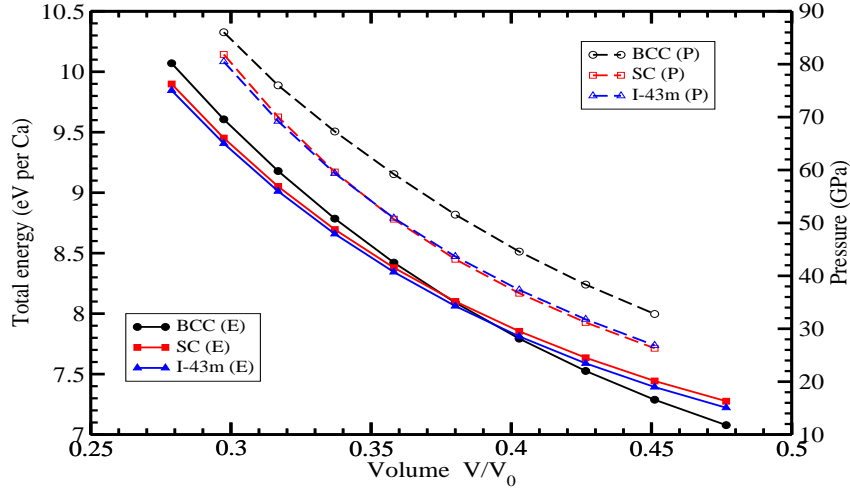


Figure 4.3.5: Plot of volume dependence total energy and pressure of bcc, sc and $I\bar{4}3m$ Ca.

and $T_C \sim 49$ K if using $\mu^*=0.13$. As a contrast, in the $I\bar{4}3m$ Ca, at $0.271 V_0$, linear response calculations give $\lambda \sim 2.2$, $\eta \sim 4.5 \text{ eV}/\text{\AA}^2$, and $T_C \sim 13$ K ($\mu^*=0.13$), all of them are much smaller than the results from RMTA calculations in the sc Ca. Note that there are no unstable modes (no imaginary phonon frequencies) for the $I\bar{4}3m$ structure generally. However, when there are *few (not many)* unstable modes at *few (not many)* \mathbf{q} points (for example, at the highest pressure 109 GPa), the \mathbf{q} points with unstable modes are replaced by their nearby \mathbf{q} points in calculating the e-p coupling constant and T_c . The point here is that structure symmetry is important in determining e-p coupling strength and resulting T_C .

Fig. 4.3.7 shows the phonon spectra and phonon DOS of $I\bar{4}3m$ Ca at 71 GPa and 109 GPa. At 71 GPa, the acoustic phonon softening happens around H and N point. The frequencies at H point are very low, leading to huge phonon softening. Then under higher pressure, the acoustic phonon modes at H and N points further soften, as showed for 109 GPa in Fig. 4.3.7. At 109 GPa, the softening of acoustic phonon

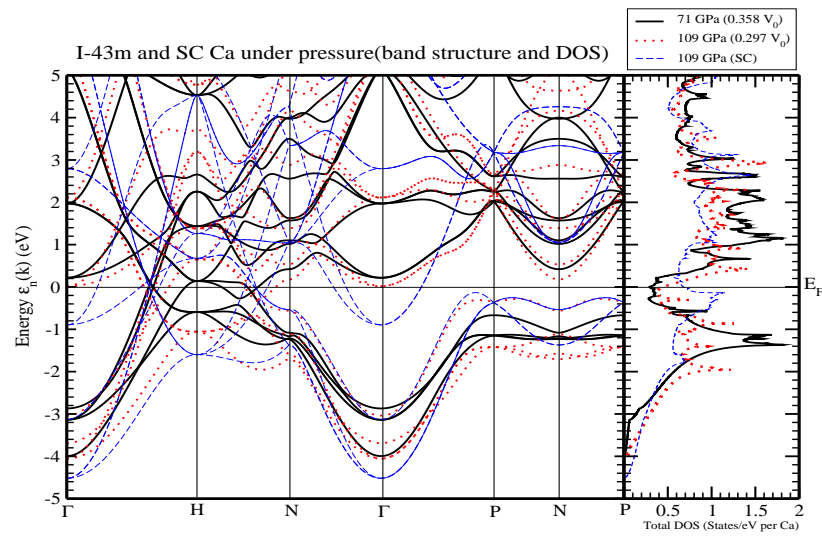


Figure 4.3.6: Band structure and DOS of I43m Ca at 71 GPa ($a=5.00 \text{ \AA}$, $0.358 V_0$) and 109 GPa ($a=4.70 \text{ \AA}$, $0.297 V_0$), and sc Ca at 109 GPa ($a=4.70 \text{ \AA}$, $0.297 V_0$) which takes the symmetry of I43m space group, i.e., 8 atoms in the unit cell with $x=0.25$. The high symmetry points are $\Gamma(0, 0, 0)$, H(1, 0, 0), N(0.5, 0.5, 0) and P(0.5, 0.5, 0.5) in the units of $(2\pi/a, 2\pi/a, 2\pi/a)$.

modes at H and H points is very impressive, the frequencies at H and N points are only half of the maximal frequencies in the same mode along the corresponding Γ -H and Γ -N line. When the high frequency phonons are pushed up to higher frequency with increasing pressure, the low frequency phonons further lower their frequencies, suggesting enhanced phonon softening of low-frequency modes and large e-p coupling in the low frequency range, which is clearly indicated in the α^2 and α^2F plot as shown in Fig. 4.3.13. At 71 GPa, α^2 remains an average value of 0.1 everywhere except a 0.3-peak below 1.5 THz. The α^2F then is similar with the phonon DOS, with many small peaks spreading over the entire frequency range. At a higher pressure 109 GPa, α^2 is about twice as large of that at 71 GPa almost everywhere, and large sharp peaks below 1.5 THz and around 3.5 THz. The α^2F at 109 GPa is also twice of that at 71 GPa everywhere, however, it is unexpectedly large from 1.0 THz to 4.0 THz, which further confirms that strong e-p coupling mainly focuses on low frequencies. The linewidth γ plot (not shown) suggests the largest contribution is from Γ -H line near the middle point. With increasing pressure the contribution from Γ -H line increases rapidly, while contributions from all other part change insignificantly. At 109 GPa, the peak value (near the middle point of Γ -H) along Γ -H is ten times the peak value at 71 GPa which suggests the strong e-p coupling comes mainly from phonons along Γ -H, especially the middle part of Γ -H. Plot of nesting function (see Fig. 4.3.8) confirms that the largest nesting happens in the area surrounding $(0.6, 0, 0)2\pi/a$ point, consistent with linear response calculation. The above results suggest strong e-p coupling exists in $\bar{I}43m$ Ca at high pressure, which comes mainly from the area around $(0.6, 0, 0)2\pi/a$ point.

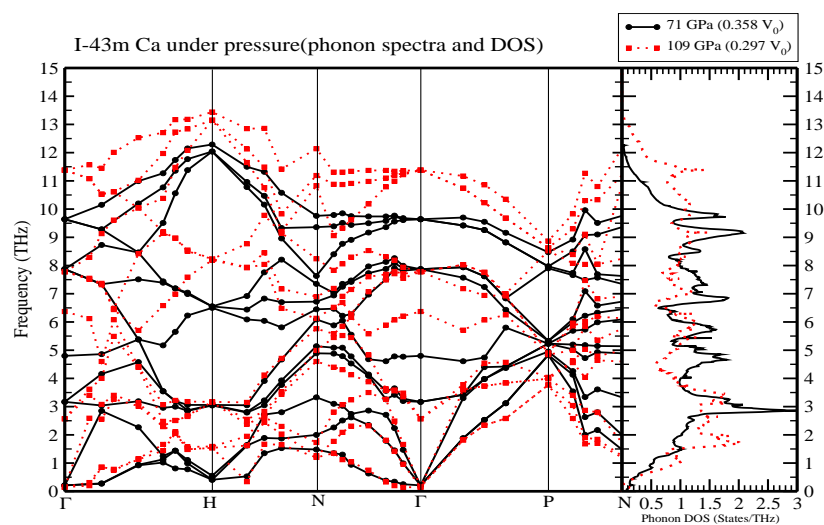


Figure 4.3.7: Phonon spectrum and phonon DOS of $I43m$ Ca at 71 GPa ($a=5.00 \text{ \AA}$, $0.358 V_0$) and 109 GPa ($a=4.70 \text{ \AA}$, $0.297 V_0$). The high symmetry points are $\Gamma(0, 0, 0)$, $H(1, 0, 0)$, $N(0.5, 0.5, 0)$ and $P(0.5, 0.5, 0.5)$ in the units of $(2\pi/a, 2\pi/a, 2\pi/a)$.

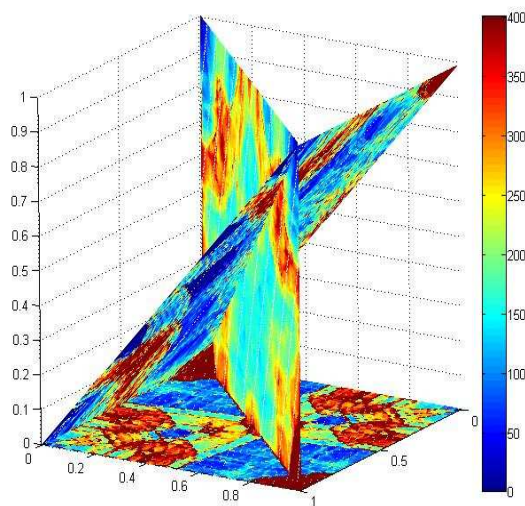


Figure 4.3.8: Nesting function $\xi(Q)$ of $I43m$ Ca on the (100), (110) and (111) planes at 83 GPa.

Table 4.2: Detailed structural data of the $\bar{I}43m$, $Pnma$, $Cmca$ and $P4_32_12$ Ca.

space group	No.	Wyckoff position	atomic coordinates	x	y	z
$\bar{I}43m$	217	8c	(x, x, x)	~ 0.2		
$Pnma$	62	4c	$(x, 1/4, z)$	~ 0.3		~ 0.6
$Cmca$	64	8f	$(0, y, z)$		~ 0.3	~ 0.2
$P4_32_12$	96	8b	(x, y, z)	~ 0	~ 0.3	~ 0.3

4.3.7 Other Possible Structures

The $\bar{I}43m$ structure is just one kind of distortion from the sc structure. There are many kinds of other possible distortions. Actually several other structures including $Pnma$, $Cmca$ and $P4_32_12$ were proposed for the high pressure Ca-IV and Ca-V phases.[251, 252, 253, 254] Their structural details are listed in Table 4.2 and their structures are pictured in Fig. 4.3.9. $\bar{I}43m$ is a body-centered cubic structure, $Pnma$ and $Cmca$ Ca are orthorhombic, and $P4_32_12$ has a tetragonal symmetry. All are closely related to sc structure. For example, $\bar{I}43m$ turns to simple cubic if $x=0.25$, and the $Cmca$ structure becomes a sc structure if $a = b = c$ and $y = z = 0.25$.

4.3.8 Enthalpy and Competing Phases

Since there are several possible structures with different symmetries, it is better to compare their total enthalpies instead of total energy. We have calculated enthalpy $H(P)$ curves for each structure in the range 40-220 GPa based on density functional methods using the PWscf code.[43] Several energy differences and relaxations were checked with the Qbox,[259] FPLO,[47] and Wien2K[51] codes. In the 40-70 GPa range, all five of the structures we have studied have enthalpies that differ by less than 20 meV/Ca (230 K/Ca), as shown in Fig. 4.3.10. In the 80-100 GPa range, the $P4_32_12$ phase is marginally the more stable phase. Three phases are degenerate, again within 20 meV/Ca, in the 100-130 GPa region and are almost exactly degenerate

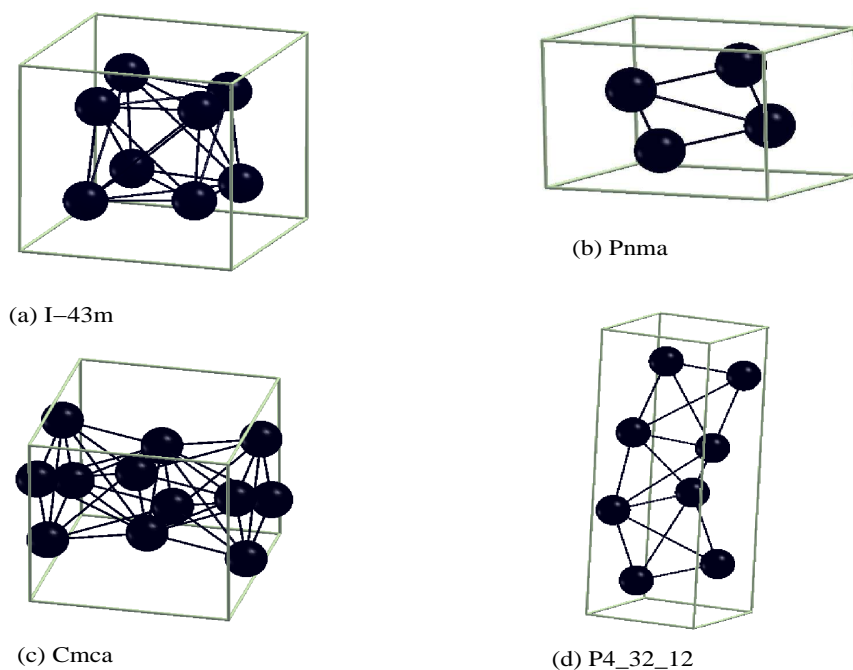


Figure 4.3.9: Structures of the $I\bar{4}3m$, $Pnma$, $Cmca$ and $P4_32_12$ Ca.

around 110-115 GPa. Thus at room temperature all five phases, including the sc one, are thermodynamically accessible up to 80-90 GPa, above which the sc and $I\bar{4}3m$ structures become inaccessible. The other three phases remain thermally accessible to 130 GPa. Above 140 GPa, the Pnma phase becomes increasingly more stable than the others.

Our results agree well with the results reported recently by Yao *et al.*[252] and Ishikawa *et al.*[253] in their corresponding pressure range. At low pressure, our result is apparently different from the result by Arapan, Mao, and Ahuja.[254] In their results, sc Ca has the lowest enthalpy from 40 GPa to 77 GPa, lower than the $P4_32_12$ and Cmca structures. A possible reason is that the authors might not have taken into account the change in shape and internal coordinates of the Cmca structure in the 70-80 GPa pressure range. In our calculation, $b/a=1.0003$ and internal coor-

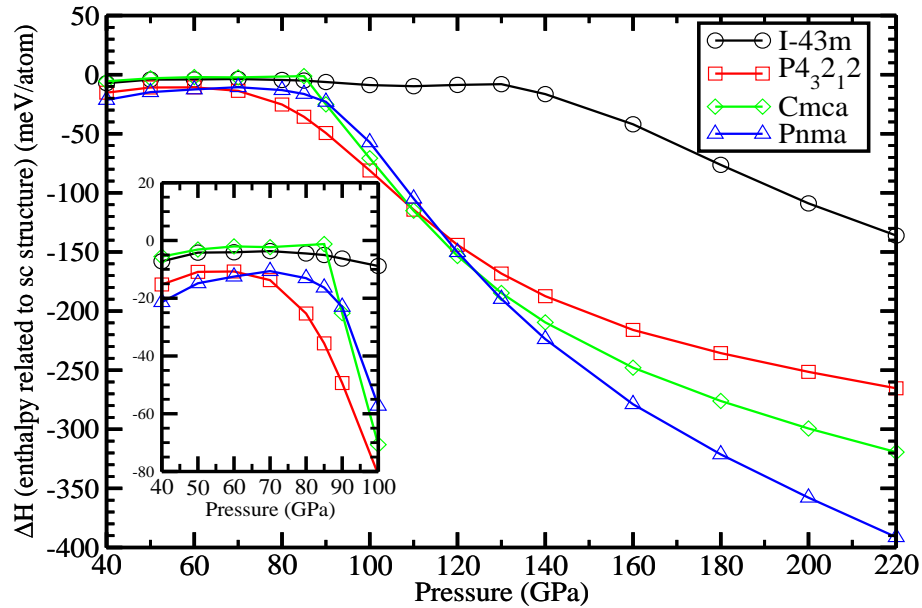


Figure 4.3.10: Plot of the enthalpy $H(P)$ of the four distorted Ca structures relative to that for Ca in the simple cubic structure. The inset gives an expanded picture of the 40-100 GPa regime.

coordinates $y=0.254$, $z=0.225$ at 70 GPa (and similarly below) change dramatically to $b/a=1.0594$, $y=0.349$ and $z=0.199$ at 80 GPa (and similarly above).

Although equally dense, quasi-degenerate, and related to the sc structure, these structures differ in important ways from the sc structure and each other. In Fig. 4.3.4 the distribution of (first and second) neighbor distances d , relative to the sc lattice constant a_{sc} , are pictured. The collection of distances cluster around $d/a_{sc} \sim 0.97 - 1.05$ and, more broadly, around $\sqrt{2}$. In an ensemble of nanocrystallites of these phases, the radial distribution function in the simplest picture should look like a broadened version of the sc one. For Ca the actual microscopic configuration at room temperature, where fluctuations (spacial and temporal) can occur among these phases (whose enthalpies differ by less than $k_B T_R$ per atom), will no doubt be much

more complex. However, this simplistic radial distribution plot makes it plausible that the resulting thermal and spatial distribution of Ca atoms will produce an XRD pattern more like simple cubic than any other simple possibility. Teweldeberhan and Bonev have noted the near degeneracy of some of these phases in the 40-80 GPa region, and suggest that the T=0 structure is Pnma in the 45-90 GPa range[243], which is consistent with our results if the P4₃2₁2 structure is not included.

4.3.9 Volume Collapse and First-order Isostructural Collapse

Figure 4.3.11 shows the behavior of V(P) relative to the smooth behavior in the sc phase. Around 75 GPa the Cmca structure suffers a rapid decrease in volume by 4-5%; whether actually discontinuous or not (see below) is probably not relevant to Ca at room temperature. Around 100 GPa, the Pnma phase undergoes a somewhat smaller but still very clear and rapid volume collapse (again, ~5%). The P4₃2₁2 system undergoes a somewhat milder (3%) collapse in the 80-100 GPa range. No collapse occurs for I $\bar{4}$ 3m until beyond 130 GPa, where the volume does decrease relative to the sc volume. Interestingly, at the highest pressures all structures return to within ~ 1% of the volume of the sc phase.

At 80 GPa the Cmca phase undergoes a discontinuous change that is not evident from the calculated V(P) results. However, by looking at all the structural parameters presented in Fig. 4.3.12, it is clear that the lattice constants change discontinuously at the volume collapse. This discontinuity signals some microscopic change in the electronic state, perhaps of the type proposed for high pressure lithium.[261, 262]

The overall picture that arises from these results is that, in most or all of the range 40-130 GPa, there are 3-5 crystal structures that are quasi-degenerate, and which can be expected to be competing thermodynamically at room temperature in

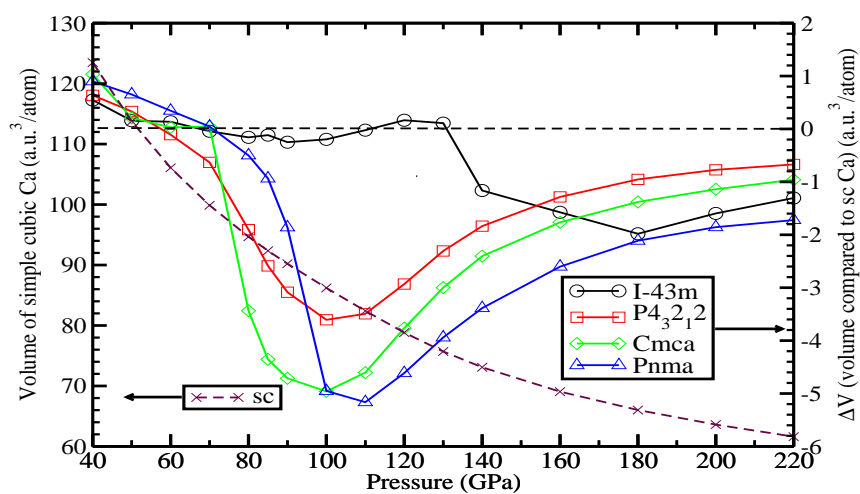


Figure 4.3.11: Plot (right hand axis) of the volume-pressure $V(P) - V_{sc}(P)$ behavior for each of the four distorted structures, relative to the behavior of sc Ca (shown as the dashed line and the left hand axis). The dips in the curves (70 GPa for Cmca, 80-100 GPa for $P4_32_12$, 90 GPa for Pnma, 140 GPa for $I\bar{4}3m$) reflect volume collapse regions.

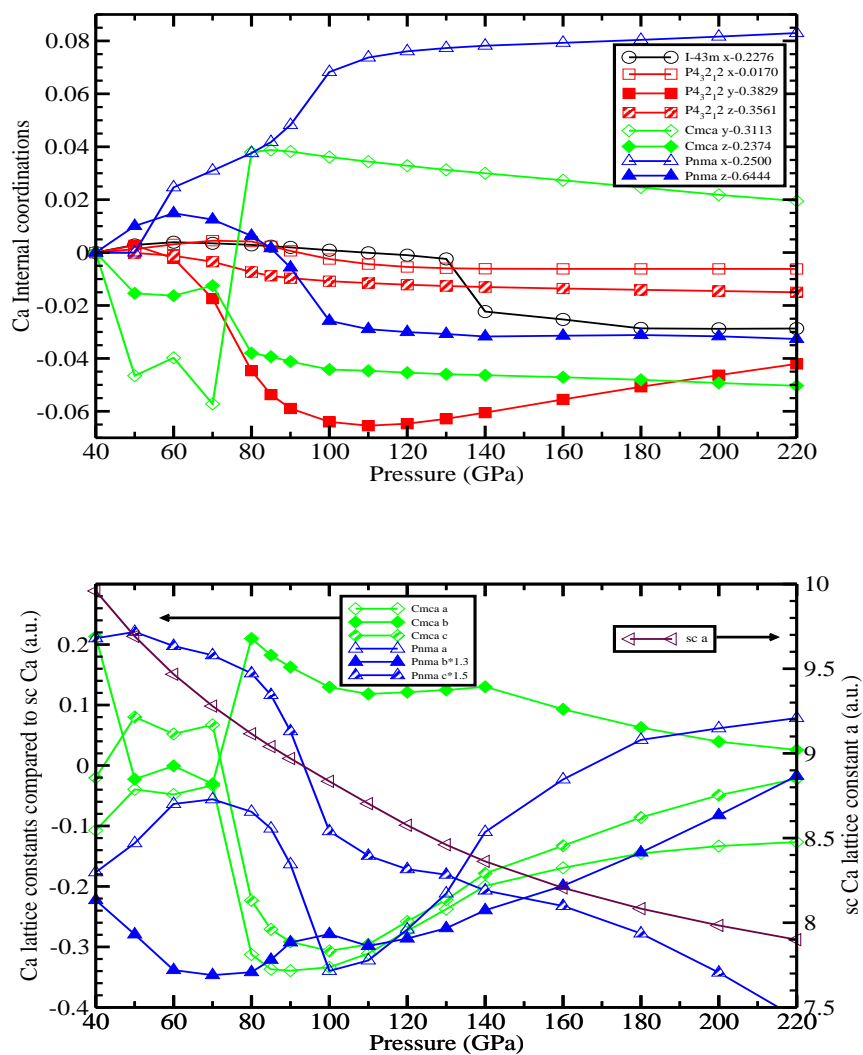


Figure 4.3.12: Top: Pressure variation of the internal structural parameters of the four distorted Ca structures. Bottom: Pressure variation of the lattice constants of the Cmca and Pnma structures (the corresponding behavior for $P4_32_12$ is smooth). Note the first-order change in the Cmca quantities near 75 GPa.

most of that range. While one might anticipate an instability of the simple cubic phase to a higher packing fraction phase, that interpretation is not supported in this system. For low symmetry phases “packing fraction” begins to lose its clarity, and in fact these structures have essentially equal densities in the 60-70 GPa range. The $P4_32_12$ and $Pnma$ phases can be viewed as 7-fold coordinated; one of the sc second-neighbors moves inward to a distance $d=1.17-1.25 a_{sc}$. However, the volume does change (rapidly or discontinuously) for three of the phases, which might be interpreted as attaining a somewhat larger packing fraction within each structural motif.

This collection of information elaborates on the initial, obvious observation that the “sc” phase Ca III cannot be simple cubic. Ca-III must be (at room temperature) a locally inhomogeneous and dynamically anharmonic structure for which a snapshot of the local structure will reveal some combination of, or interpolation between, these five crystal structures. Although Ca-III is not simple cubic and not even crystalline, it has one similarity to sc, in that each of these phases and presumably the actual, very complex, structure is *not* close-packed. Fujihisa *et al.*[251] have analyzed some of these structures around 150 GPa, where the 7-fold coordination becomes clearer. This case of high pressure “sc” Ca at room temperature may constitute yet another facet of the “weird structures” that occur in alkali and alkaline-earth metals under pressure.[263]

4.3.10 Stability and Lattice Dynamics

The structural stability of the (quasi-degenerate) structures we have studied provide insight into behavior of Ca under pressure. Linear response calculations were performed using the LMTART code[49] to evaluate EPC.

60-100 GPa. The $I\bar{4}3m$ and $Pnma$ structures are mostly dynamically stable from 60-100 GPa according to our linear response calculations, but there are very soft zone boundary modes that verge on instability (small imaginary frequencies) at some pressures. The $Cmca$ and $P4_32_12$ structures are unstable over this entire pressure range; note that their structures are close to the sc structure. However, they are close to stable with very soft phonons at 100 GPa, where they deviate far enough from the sc structure.

A rather common feature among these structures in this pressure range is softening of modes at the zone boundary, with an associated maximum in the spectral function $\alpha^2(\omega)$ that can be seen in Fig. 4.3.13 and Fig. 4.3.14. Such low frequency weight contributes strongly to λ , though the contribution to T_c is better judged[204] by $\langle \omega \rangle \lambda$ or even $\langle \omega^2 \rangle \lambda$. With increase of pressure, the peaks move towards lower frequency, λ increases, and the structures approach instability. These results are consistent with the changes of structure parameters we obtain in the process of calculating the enthalpies, where all four structures evolve further from the sc structure with increase of pressure.

Above 100 GPa. At the highest pressures studied (by us, and experimentally), the crystal structures deviate more strongly from the sc structure. Of the structures we have considered, the $P4_32_12$ one becomes favored and also is structurally stable around 110 GPa. This stability is consistent with the observed transition from the sc structure to the Ca-IV structure at room temperature. The dramatic drop in the electrical resistance at around 109 GPa is also consistent with a transition from a locally disordered phase to a crystalline material.[203]

In the pressure range of 110-140 GPa, the $P4_32_12$, $Cmca$, and $Pnma$ structures become quasi-degenerate again. Linear response calculations of the $Pnma$ structure

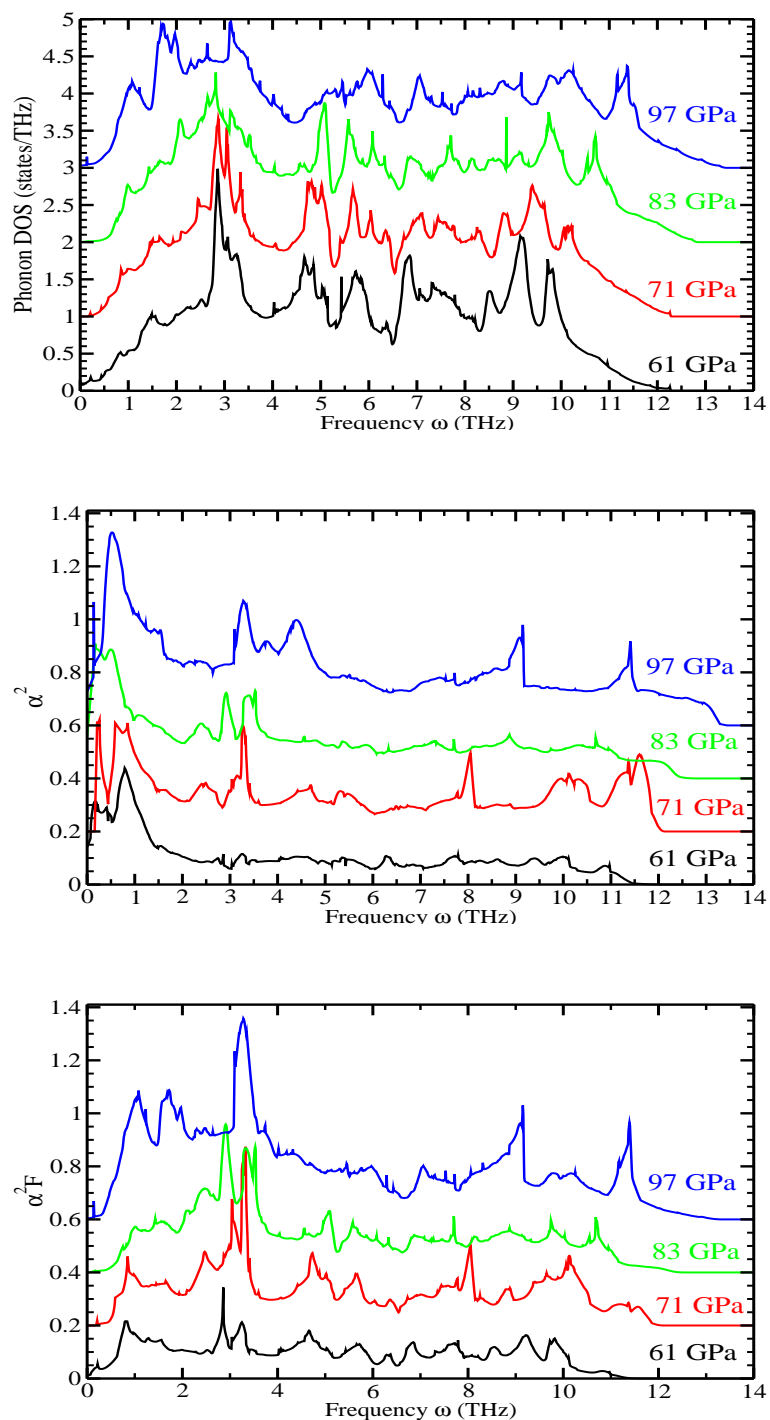


Figure 4.3.13: Plot of $\alpha^2 F(\omega)$ (lower panel), $\alpha^2(\omega)$ (middle panel), and phonon DOS (upper panel) of $I43m$ structure at about 61, 71, 83 and 97 GPa. This regime is characterized by strong coupling $\alpha^2(\omega)$ at very low frequency.

at 120 GPa and above, and of the Cmca structure at around 130 GPa indeed show strong coupling with $\lambda > 1.0$ in all the cases. Unlike what was found below 100 GPa, there are no longer very low frequency phonons (see Fig. 4.3.14 and Fig. 4.3.15). The coupling strength is spread over frequency, peaking for mid-range frequency phonons.

Another interesting feature arises in the $\alpha^2(\omega)$ curves, which reveal that the coupling matrix elements become relatively uniform across most of the frequency range (except the uninteresting acoustic modes below 2 THz) at pressures over 120 GPa in Pnma structure and at 130 GPa in Cmca structure; this behavior is evident in Fig. 4.3.14 and especially in Fig. 4.3.15 where the results for the Cmca structure at 130 GPa are pictured. This characteristic is fundamentally different from that below 100 GPa, discussed above.

At pressures over 140 GPa, the Pnma structure is clearly favored in our calculation, and linear response calculations indicate the structure is dynamically stable. The overall results are evident in Fig. 4.3.14, which shows that the structures remain stable (no imaginary frequencies) and the lattice stiffens smoothly with increasing pressure, and in Fig. 4.3.16 that shows that strong electron-phonon coupling persists and T_c remains high. In this high pressure range, the incommensurate structure proposed by Arapan, Mao, and Ahuja[254] at pressure over 130 GPa is also a possibility.

4.3.11 Coupling Strength and T_c

Fig. 4.3.16 shows the calculated λ , $\eta = M_{Ca} \langle \omega^2 \rangle \lambda$, and rms frequency $\langle \omega^2 \rangle^{1/2}$ versus pressure for a few structures and pressures. The calculated values of T_c are shown in the lower panel, using two values of Coulomb pseudopotential $\mu^*=0.10$ and 0.15 that bracket the commonly used values and therefore give an indication of the uncertainty due to the lack of knowledge of the value of μ^* and its pressure

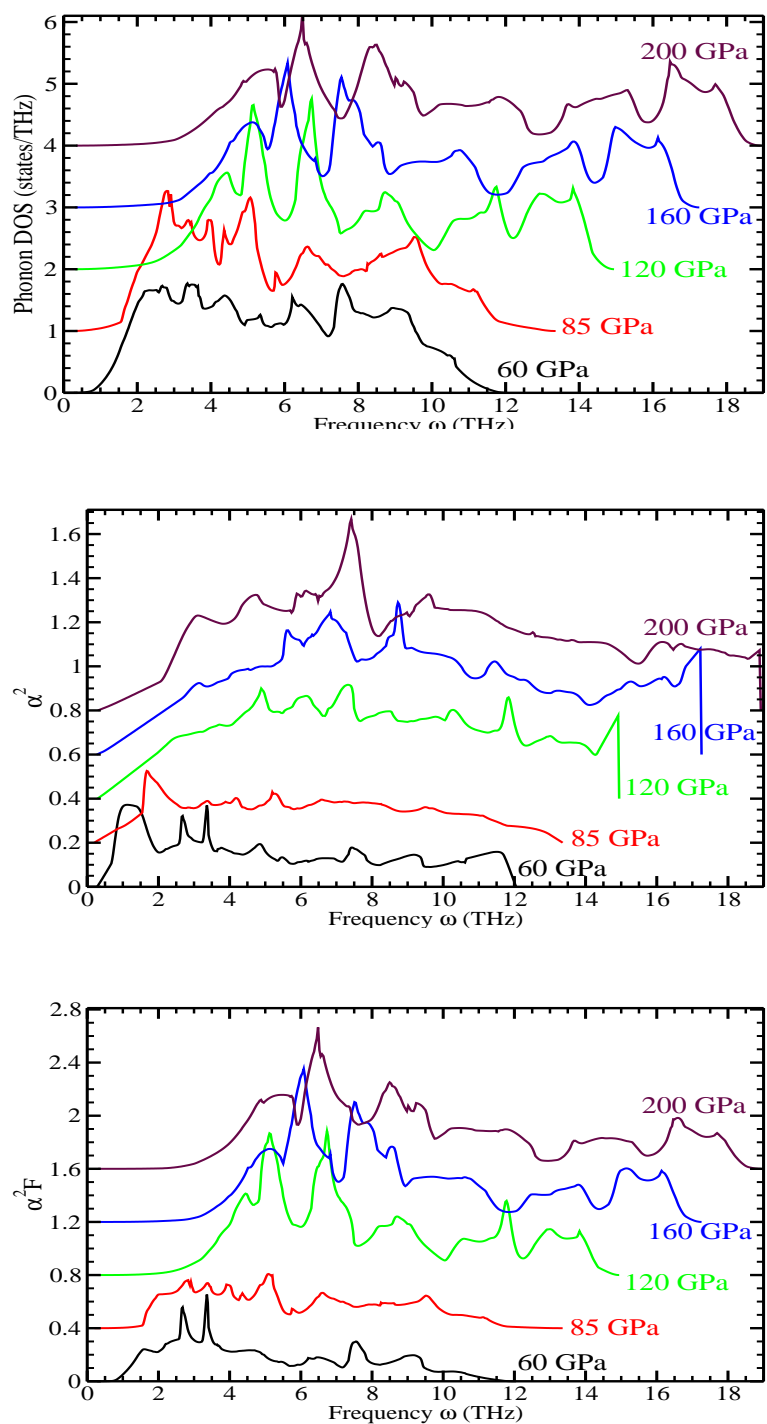


Figure 4.3.14: Plot of $\alpha^2 F(\omega)$ (bottom panel), $\alpha^2(\omega)$ (middle panel), and phonon DOS (upper panel) of Pnma structure at about 60, 85, 120, 160, and 200 GPa. The main trends are the stiffening of the modes with increasing pressure, and the retention of coupling strength $\alpha^2(\omega)$ over a wide frequency range.

dependence. Results are provided for Ca in $I\bar{4}3m$, Pnma and Cmca structures at a few pressures up to 220 GPa. In elemental metals and in compounds where coupling is dominated by one atom type, η has often been useful in characterizing contributions to T_c . [265] η increases with pressure monotonically by a factor of more than 6 from 60 GPa to 220 GPa. The coupling constant λ increases modestly up to 120 GPa then remains nearly constant at $\lambda = 1.2-1.4$. As pointed out elsewhere, [264] a dense zone sampling is needed to calculate λ accurately, so any small variation is probably not significant. Thus the increase in η beyond 120 GPa correlates well with the lattice stiffening (increase in $\langle \omega^2 \rangle$) in this pressure range.

The trend of the resulting T_c generally follows, but seems to overestimate somewhat, the experimental values [203]. For Cmca structure at about 130 GPa, the calculated EPC strength is $\lambda = 1.2$ and $T_c = 20-25K$ (for the two values of η). in very satisfactory agreement with the observed values of T_c in this pressure range. For Pnma structure, T_c increases rapidly in the 80-120 GPa region. At pressures above 120 GPa up to the maximum 220 GPa that we considered, the EPC constant λ is $\sim 1.2-1.4$ and the calculated T_c increases modestly from 25-30K at 120 GPa to 30-35K at 220 GPa. Neither the structure dependence nor the pressure dependence seems very important: the strong coupling and high T_c is more the rule than the exception. Ca at high pressure may be an excellent superconductor regardless of its structure.

4.3.12 Conclusions

Linear response calculations suggest simple cubic Ca in the pressure range of 32-109 GPa is not stable at low temperature. A straightforward distortion along the most unstable phonon modes leads sc to the $I\bar{4}3m$ structure. A total energy comparison of bcc, sc and $I\bar{4}3m$ Ca at various volumes suggests sc Ca may never exist at low

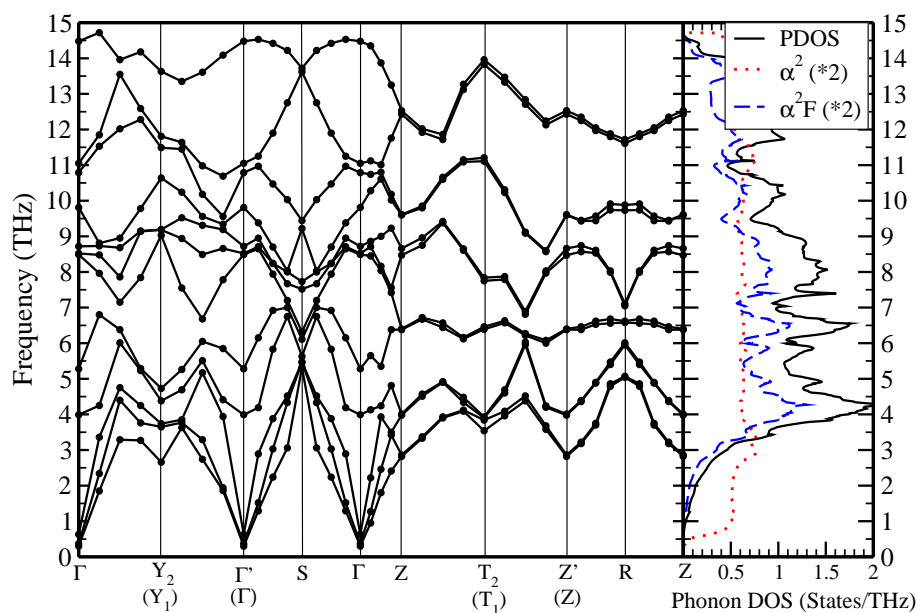


Figure 4.3.15: Phonon spectrum, phonon DOS, α^2 and α^2F of Cmca Ca at $0.251 V_0$ (~ 130 GPa from PWscf). The high symmetry points are $\Gamma(0, 0, 0)$, $Y_1(1, 0, 0)$, $Y_2(0, 1, 0)$, $\Gamma'(1, 1, 0)$, $S(0.5, 0.5, 0)$, $Z(0, 0, 0.5)$, $T_1(1, 0, 0.5)$, $T_2(0, 1, 0.5)$, $Z'(1, 1, 0.5)$ and $R(0.5, 0.5, 0.5)$ in the units of $(2\pi/a, 2\pi/b, 2\pi/c)$.

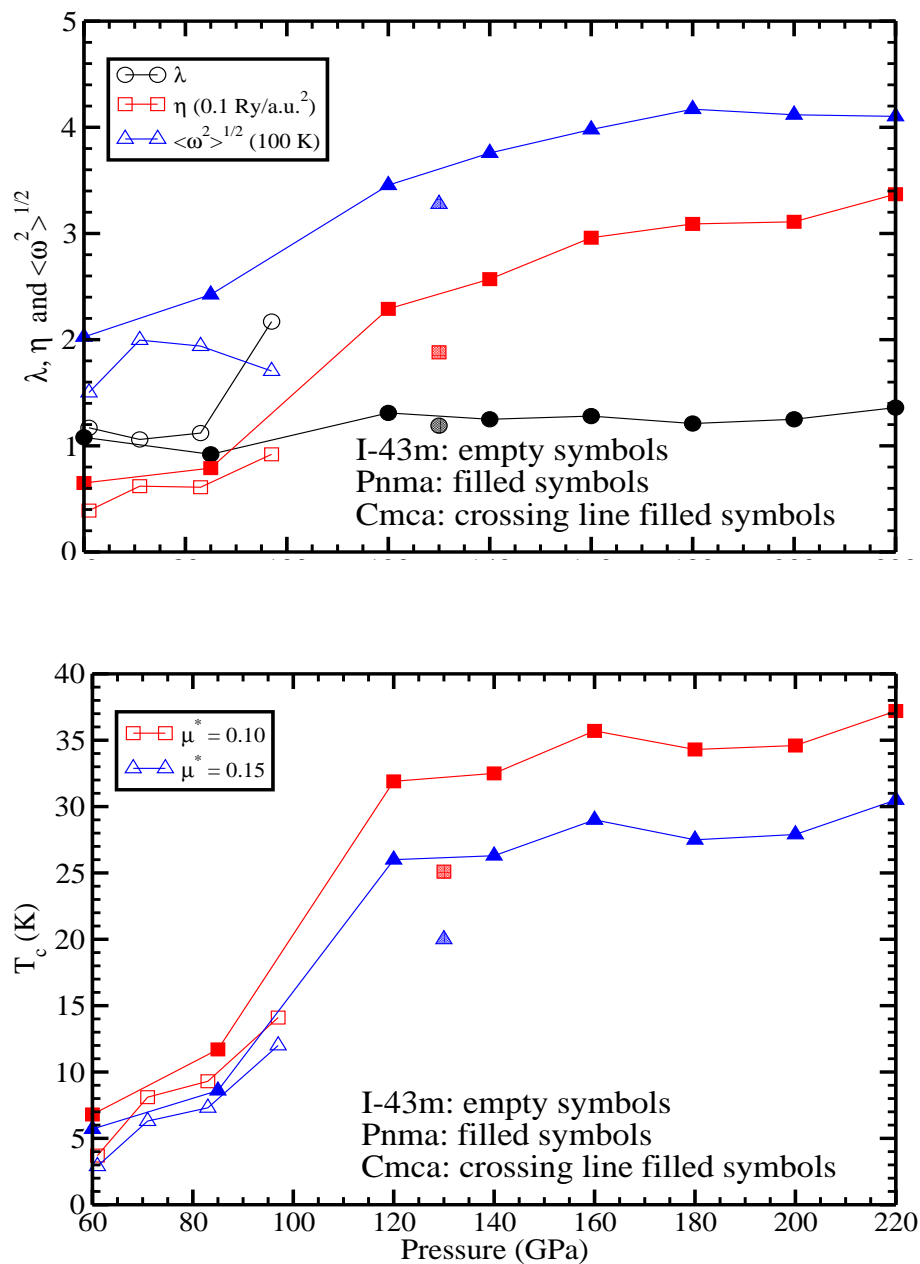


Figure 4.3.16: Upper panel: Calculated electron-phonon coupling constant λ , η and T_C of Ca in $\bar{I}43m$ (empty symbols), Pnma (filled symbols) and Cmca (crossing-line filled symbols) structures at a few pressures. Lower panel: T_C calculated from the Allen-Dynes equation, showing the dependence on the Coulomb pseudopotential for which two values, $\mu^*=0.10$ and 0.15 have been taken.

temperature, which is supported by the enthalpies of several sc-related structures at various pressures as well. Under pressure, there is a general trend of broadening of the bands around Fermi level, increasing of the DOS at E_F and of occupation number of Ca $3d$ electrons, of both sc and $I\bar{4}3m$ Ca. The evolutions of the Fermi surfaces of both sc and $I\bar{4}3m$ Ca under pressure generally enhance strongly nestings of electrons on the Fermi surfaces, which are contributed mainly by a flat piece of FS which grows in size under pressure. The calculated nesting function $\xi_{\mathbf{Q}}$ on the (100), (110) and (111) planes of $I\bar{4}3m$ Ca at 83 GPa reveals a peak around $\mathbf{Q} = (0.6, 0, 0)2\pi/a$ point, which is consistent with the topology of its Fermi surfaces and the mode $\lambda_{\mathbf{Q}}$ in linear response calculations. These are indicative of strong electron-phonon coupling, which is confirmed by linear response calculations.

Calculations of enthalpy versus pressure for five crystalline phases of Ca (simple cubic and four distortions from it) indicate quasi-degeneracy, with enthalpy differences small enough that one might expect a locally disordered, highly anharmonic, fluctuating structure at room temperature. Such a scenario seems to account qualitatively for the XRD observations of a “sc” structure, a rationale that is necessary because calculations indicate the actual sc structure itself is badly unstable (at least at $T=0$). At pressure below 100 GPa, the quasi-degenerate structures tend to have soft branches or occasionally lattice instabilities, which are associated with strong electron-phonon coupling. In the pressure range of 110 to 130 GPa three phases ($P4_32_12$, $Cmca$ and $Pnma$) again become quasi-degenerate, and again it seems likely there will be spacial and temporal fluctuations between the structures. Of course other structures may come into play as well; Arapan, Mao, and Ahuja[254] have proposed that the $Pnma$ structure competes with an incommensurate structure at high pressure.

As our other main result, we find that linear response calculation of the EPC strength and superconducting T_c accounts for its impressive superconductivity in the high pressure regime and accounts in a broad sense for the strong increase of T_c in the “sc” phase. At higher pressure beyond current experimental limit (i.e., 161 GPa), T_c still lies in the 20-30 K range for some phases that we have studied. In fact strong electron-phonon coupling seems to be present in several phases across a substantial high pressure range, although we have no simple picture why such strong coupling should arise. (The strong coupling in Li and Y likewise has no simply physical explanation.[58, 204]) These results may resolve some of the perplexing questions on the structure and record high T_c for an element, and should help in obtaining a more complete understanding of the rich phenomena that arise in simple metals at high pressure.

4.3.13 Acknowledgments

This work was supported by DOE through the Scientific Discovery through Advanced Computing program (SciDAC grant DE-FC02-06ER25794), and by DOE grant DE-FG02-04ER46111 with important interaction from the Computational Materials Science Network.

Chapter 5

The Iron-based Superconductors

5.1 Introduction to the Iron-based Superconductors

Since the discovery of copper oxide (cuprate) high temperature superconductors (HTS) in 1986,[188] there has been an extensive effort to find related superconductors in two-dimensional (2D) transition metal oxides (TMO), borides, nitrides, etc. Promising developments in this area include Li_xNbO_2 , [266], Sr_2RuO_4 , [267] Na_xCoO_2 , [268], and Cu_xTiSe_2 , [269] but all have superconducting critical temperature T_c of 5 K or less. The most striking discovery was that of electron-doped hafnium nitride semiconductor (HfNCl) [270] with $T_c = 25$ K. The other distinctive breakthrough, [198] MgB_2 ($T_c=40$ K), has strong 2D features but contains only s, p elements. Recently, design of possible TMO superconductors has been stimulated by a specific approach outlined by Chaloupka and Khaluillin. [271]

The simmering state of superconductor discovery has been re-ignited by discovery of a new class of layered transition metal pnictides $\mathcal{R}OT\text{Pn}$, where \mathcal{R} is a trivalent

rare earth ion, \mathcal{T} is a late transition metal ion, and Pn is a pnictogen atom. The breakthrough of $T_c=26$ K ($T_c^{onset}=32$ K) was reported[191] for $0.04 \leq x \leq 0.12$ electron doped $\text{LaO}_{1-x}\text{F}_x\text{FeAs}$, followed by the demonstration that hole-doping[272] in $\text{La}_{1-x}\text{Sr}_x\text{OFeAs}$, $0.09 \leq x \leq 0.20$, leads to a similar value of T_c . These values of T_c have now been superseded by the finding that replacement of La by Ce,[192] Pr,[193] Nd,[194] Sm,[195, 196] and Gd[197] result in $T_c = 41\text{-}55$ K, substantially higher than in any materials except for the cuprate HTS.

Very soon, a few other Fe based compounds were found to be superconducting when doped or compressed. Currently, the parent compounds of Fe-based superconductors include ZrCuSiAs-type $R\text{FeAsO}$ and $M'\text{FeAsF}$ (1111-type), ThCr_2Si_2 -type $M\text{Fe}_2\text{As}_2$ (122-type), Cu_2Sb -type $A\text{FeAs}$ (111-type), $\alpha\text{-PbO}$ -type FeTe and FeSe (11-type), and $\text{Fe}_2\text{As}_2\text{Sr}_4\text{X}_2\text{O}_6$ (22426-type) (R =rare earth metal; M' =Sr and Ca; M = Ba, Sr, Ca and Eu; A =Li and Na; X = Sc, Cr). [191, 192, 193, 194, 197, 273, 274, 275, 276, 277, 278, 279, 280]

In the vicinity of room temperature, these compounds crystallize in tetragonal symmetry with no magnetic order. The crystal structures of all the iron-pnictides share a common two-dimensional FePn layer, where Fe atoms form a 2D square sublattice with Pn atoms sit at the center of these square, but off the Fe plane (above and below the plane alternately). The FePn layer is different from the CuO layer in cuprates where the Cu and O atoms are in the same plane. The parent compounds of these iron-pnictides are metallic, while the parent compounds of cuprates are Mott insulators. At some lower temperature (which can be in the range of 100-210 K), they undergo a first or second order structural transition at T_S from tetragonal to orthorhombic, and an magnetic transition at T_N from non-magnetic to stripe-antiferromagnetic.[281, 282, 283, 284] The structural transition and magnetic order

transition can happen simultaneously or successively depending on the compound. It was confirmed both experimentally and theoretically that the magnetic order of Fe at low temperature is stripe-like antiferromagnetism often referred to as spin density wave (SDW). [281, 283, 284, 285, 286] Upon doping or compressing, the magnetic order goes away and the materials become superconducting. In the 1111-family (both $R\text{FeAsO}$ and $M'\text{FeAsF}$, R =rare earth and M' =Ca and Sr), T_N is lower than T_S , which seems to suggest that the magnetic transition is induced by the structural transition. In the $M\text{Fe}_2\text{As}_2$ (M =Ba, Sr, Ca, and Eu) compounds, $T_N=T_S$, i.e., the structural and magnetic transitions happen simultaneously (a first-order transition). Whether the magnetic transition is induced by the structural transition or not and what is the driving force of the structural transition are two important questions that are crucial to understand the formation of the stripe antiferromagnetic order in the parent compounds.

Many experiments have been done to measure various properties of these iron-pnictide compounds. The ordered magnetic moment of iron is typically less than $1.0 \mu_B$, which is much smaller than the calculated value ($\sim 2.0 \mu_B$) from first principle calculations. The superconducting gap is best fitted to s_{\pm} wave[287, 288] which is different from the $d_{x^2-y^2}$ symmetry in cuprate superconductors. The oxygen-isotope effect is much smaller than the iron-isotope effect[289], which verifies the superconductivity comes from the $\text{Fe}Pn$ layer. T_c is maximum when the $\text{Fe}-Pn$ -Fe angle is about 109.4° , suggesting that the height of the Pn atom is very important to superconductivity. Superconductivity can be induced by different ways including electron doping, hole doping, vacancy and applying pressure. The phase diagram of the iron-based superconductors is similar to the cuprate superconductors.

Hundreds of theoretical papers have been published since the first report[191] in

February, 2008. While much progress has been made on the understanding of these compounds, there are still fundamental questions remain unanswered, such as:

1. *Itinerant vs. localized*: Are the iron 3d electrons itinerant or localized?
2. *Driving force of phase transitions*: What is the relation of the structural transition and the magnetic transition? What is the underlying driving force?
3. *Failure of L(S)DA and GGA*: Since it has been confirmed from LDA+DMFT calculations[290] that LaFeAsO is a moderately correlated system, L(S)DA should work satisfactorily. Why L(S)DA fails to predict the correct position of As atom with an unacceptable large error of more than 0.1 Å? Why LSDA and GGA overestimate the ordered magnetic moment of iron in the stripe-AFM state by a huge amount?
4. *Pairing mechanism*: What is the pairing mechanism of superconductivity in these compounds? Is it spin fluctuation, orbital fluctuation, electron-lattice interaction or something else?

Although there are still many difficulties, it is believed that, with one more class of high T_c superconductors to study with, there are more chances to unveil the mechanism of high temperature superconductivity.

5.2 The Delicate Electronic and Magnetic Structure of LaFeAsO

This section contains work from two published papers[285, 291]: “*Electron-Hole Symmetry and Magnetic Coupling in Antiferromagnetic LaFeAsO*”, Z. P. Yin, S. Lebègue, M. J. Han, B. P. Neal, S. Y. Savrasov, and W. E. Pickett, Phys. Rev. Lett. **101**, 047001 (2008); and “*The delicate electronic and magnetic structure of the LaFePnO system (Pn=pnictogen)*”, S. Lebègue, Z. P. Yin, and W. E. Pickett, New Journal of

Physics **11**, 025004 (2009).

5.2.1 Background

The parent compound LaFeAsO is non-magnetic at room temperature. The transport, magnetic, and superconducting properties of LaFeAsO_{1-x}F_x depend strongly on doping.[191, 272, 292] Most interestingly, a kink is observed[192] in the resistivity of the stoichiometric (“undoped” but conducting) compound, which has been identified with the onset of antiferromagnetism (AFM). As a result, the original focus on the nonmagnetic LaFeAsO compound switched to an AFM ground state, in which the two Fe atoms in the primitive cell have oppositely oriented moments. Due to the structure of the FeAs layer, shown in Fig. 5.2.1, that requires two Fe atoms in the primitive cell, this ordering represents a $Q=0$ AFM state.

The basic electronic structure of this class of compounds was presented for LaFePO, superconducting at 5 K [293], by Lebègue.[294] The electronic structure of paramagnetic LaFeAsO is similar, and its (actual or incipient) magnetic instabilities have been described by Singh and Du,[295] who found that the Fermi level (E_F) lies on the edge of a peak in the density of states (DOS), making the electronic structure strongly electron-hole *asymmetric*. The Fermi surfaces are dominated by zone center and zone corner cylinders, which underlie several models of both magnetic[296] and superconducting.[287, 297, 298, 299] properties. Cao *et al.*[300] and Ma and Lu[301] demonstrated that a $Q=0$ AFM state (mentioned above) is energetically favored, but coincidentally (because the electronic structure is substantially different) still leaves E_F on the edge of a DOS peak, *i.e.* strongly particle-hole asymmetric. In both paramagnetic and $Q = 0$ AFM states a degenerate d_{xz}, d_{yz} pair of Fe orbitals remains roughly half-filled, suggesting possible spontaneous symmetry breaking to eliminate

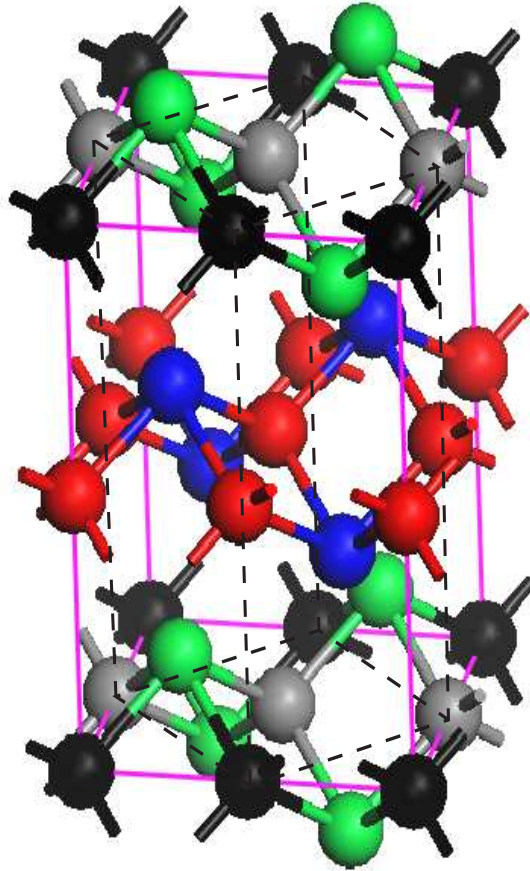


Figure 5.2.1: The Q_M antiferromagnetic structure of LaFeAsO , with different shades of Fe atoms (top and bottom planes) denoting the opposing directions of spins in the Q_M AFM phase. Fe atoms lie on a square sublattice coordinated tetrahedrally by As atoms, separated by LaO layers (center of figure) of similar structure. The dashed lines indicate the nonmagnetic primitive cell.

the degeneracy.[296, 302] Such degeneracies have attracted attention in transition metal oxides.[303]

Subsequently it was reported by Dong *et al.*[304] that a $\vec{Q}_M = (\pi, \pi, 0) \sqrt{2} \times \sqrt{2}$ AFM state lies substantially lower still in energy. The spin arrangement consists of Fe chains of aligned spins along one direction (which we take to be the x -axis) of the square Fe sublattice, with alternate chains having opposite spin direction. This \vec{Q}_M ordering is what might be expected from the (approximate) nesting of Fermi surfaces in the primitive cell, but the calculated moments are large ($1.72 \mu_B$ in the $Q=0$ phase, $1.87 \mu_B$ for Q_M) and thus is far removed from a ‘spin density wave’ description. Neutron scattering[281, 282] and x-ray scattering[282] have confirmed this in-plane ordering, and reveal that alternating planes of Fe spins are antialigned, *i.e.* the true ordering is (π, π, π) .

5.2.2 Crystal Structure

RFeAsO crystallizes in the ZrCuSiAs type structure [305, 306] (space group P4/nmm, $Z = 2$). LaFeAsO is made of alternating LaO and FeAs layers, as presented in Fig. 5.2.1. The Fe and O atoms lie in planes, while the As and La atoms are distributed on each side of these planes following a chessboard pattern. The crystal structure is fully described by the a and c lattice parameters, together with the internal coordinates of La and As. Experimentally, $a = 4.03533 \text{ \AA}$ and $c = 8.74090 \text{ \AA}$, while $z(\text{La}) = 0.1415$ and $z(\text{As}) = 0.6512$. However to describe correctly the antiferromagnetic structure, a $\sqrt{2}a \times \sqrt{2}a \times c$ cell must be used, with four Fe atoms per cell, as shown in full lines in Fig. 5.2.1. We will refer to this antiferromagnetic order as the Q_M AFM order, or equivalently as $(\pi, \pi, 0)$, while the Q_0 AFM order corresponds to an antiferromagnetic order of the original cell (dashed lines in Fig. 5.2.1) with two Fe atoms. Also, FM will

refer to a ferromagnetic arrangement of the spins, while NM means non-magnetic.

5.2.3 Calculation Method

To calculate the relevant quantities, we have used density functional theory (DFT) [1, 3], as implemented in two different electronic structure codes. The full potential local orbital (FPLO) code[47] was mainly used, while we double checked some of the calculations with Wien2k code [51]. For most of the FPLO and LAPW calculations, the Perdew and Wang 1992 (PW92)[20] exchange-correlation (XC) functional was used, but the effect of XC functional was checked using also LSDA(PZ)[18], the PBE (Perdew *et al.* 1996)[23], and another GGA (Perdew *et al.* 1992)[22] XC functionals. At each constant volume, the crystal structure was fully relaxed, i.e., c/a , $z(\text{La})$ and $z(\text{Pn})$ were relaxed. The errors were estimated to be within 0.5% for c/a , and 1.0% for $z(\text{La})$ and $z(\text{Pn})$. The relaxation was performed in the Q_M AFM structure, with 132 irreducible k points in the BZ. We double checked the total energy with a finer mesh with 320 irreducible k points in the BZ, and the difference is very small. After relaxation, all calculations were performed using dense meshes, with 320, 1027, and 637 irreducible k points in the BZ of the Q_M AFM, Q_0 AFM and NM structure, respectively. In the Q_M AFM structure, we used 464 irreducible k points in the BZ to double check the result, without any noticeable difference in the DOS nor band structure.

5.2.4 The Q_M AFM Ordering

To prepare for studying the superconducting state, it is necessary first to understand the normal state from which it emerges. We find the Q_M phase to be energetically favored over the $Q=0$ AFM phase by ~ 75 meV/Fe, which itself lies 87 meV/Fe below

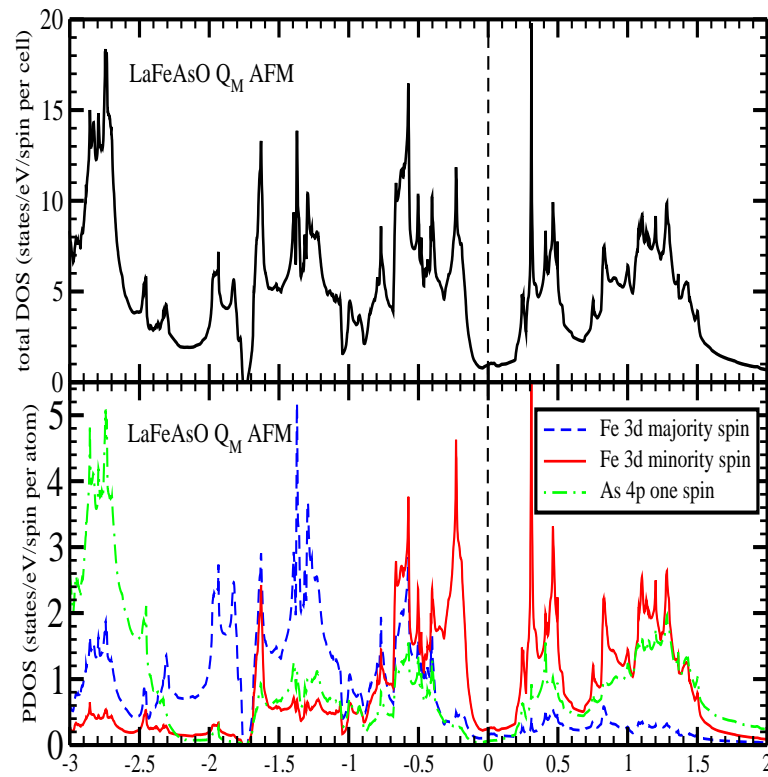


Figure 5.2.2: Top panel: total DOS for the Q_M AFM phase. Bottom panel: spin resolved Fe $3d$ DOS, showing majority filled and minority half-filled up to the pseudogap, and the As $4p$ DOS.

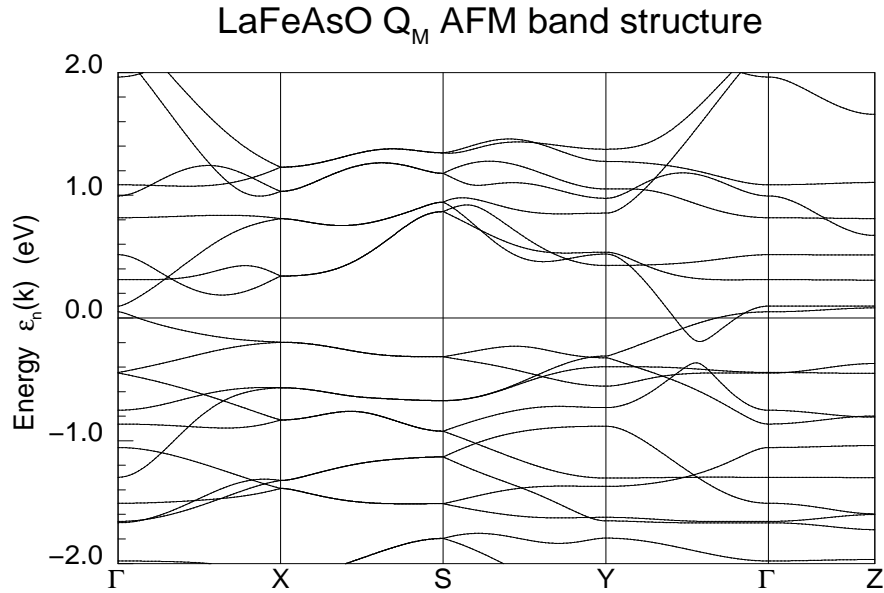


Figure 5.2.3: Band structure of the \vec{Q}_M AFM phase along high symmetry directions. Note that two dispersive bands and one narrow band cross E_F along Γ -Y, while only the one flatter band crosses E_F (very near $k=0$) along Γ -X.

the nonmagnetic phase. This energy difference is large enough that neither the $Q=0$ AFM, nor the nonmagnetic, phase will be thermally accessible at temperatures of interest. We neglect the antialignment of spins on the well separated adjacent FeAs layers, which will have little effect on the electronic and magnetic structure of a layer due to the weak interlayer hopping.

5.2.5 Electronic Structure

In either AFM phase, the Fe majority states are completely filled, thus the moment is determined by the occupation of the minority states. From the projected Fe 3d density of states (DOS) shown in Fig. 5.2.2, the minority states are almost exactly half-filled, giving 7.5 3d electrons and thus an Fe state that is no more than 0.5e from neutral. While the center of gravity of As 4p weight lies below that of Fe 3p bands,

there is strong mixing of these two characters on both sides of E_F , and the As 4p states are certainly unfilled.

Notably, the band structure and DOS is characterized by a pseudogap straddling E_F , closing only in a small region along the Γ -Y line near Γ . Since the moments, and hence the exchange energies, of the two AFM phases are very similar, the energy gain in the Q_M phase can be ascribed to the formation of the pseudogap. The system could be considered as *metallic* rather than semimetallic, in the sense that there are two dispersive bands crossing E_F along Γ -Y. One is 1.3 eV wide, comprised of Fe d_{xy} + As p_z character, the other of d_{yz} character is 0.9 eV wide. A third narrower (0.4 eV) band of $3d_{x^2-y^2}$ character crosses E_F near Γ . The crossing of the dispersive bands along Γ -Y are such as to leave only two small distinct 2D Fermi surfaces, shown in Fig. 5.2.4: an elliptical hole cylinder at Γ containing ~ 0.03 holes, and two symmetrically placed near-circular electron tubes midway along the Γ -Y axis. In the sense that the Fermi surfaces are small, the state is semimetallic. The bands near E_F have k_z dispersion of no more than 25 meV.

The d_{xz}, d_{yz} degeneracy is broken by the chains of aligned Fe spins in the Q_M phase. The rough characterization for the minority Fe orbitals is that d_{z^2} and $d_{x^2-y^2}$ states are partially filled, d_{xy} and d_{xz} states are empty, the d_{yz} states are mostly filled but giving rise to the hole Fermi surfaces. (Note that here the $x - y$ coordinate system is rotated by 45° from that usually used for the primitive cell, see Fig. 5.2.1)

A striking feature, crucial for accounting for observations, is that the DOS is (roughly) particle-hole symmetric, as is the observed superconducting behavior. All bands near E_F are essentially 2D, resulting in only slightly smeared 2D-like DOS discontinuities at the band edges with structure elsewhere due to band crossings and non-parabolic regions of the bands. The DOS has roughly a constant value of 0.25

states/(eV Fe spin) within 0.15-0.2 eV of E_F , with much flatter bands beyond. The hole and electron effective in-plane masses, obtained from $N(E) = m^*/(\pi\hbar^2)$ for each pocket, are $m_h^* = 0.33$, $m_e^* = 0.25$. An analogous band structure occurs in electron-doped HfNCl,[307] but there superconductivity appears before the heavy bands are occupied.

There are somewhat conflicting indications of the possible importance of electron-phonon coupling in this compound.[308, 309] Fig. 5.2.5 provides evidence of strong *magnetophonon* coupling: increase of the As height which changes the Fe-As distance affects the Fe moment at a rate of $6.8 \mu_B/\text{\AA}$, indicating an unusually large sensitivity to the Fe-As separation. Fig. 5.2.5 also reveals another important aspect: LDA is almost 0.1 \AA off in predicting the height of the As layer relative to Fe, a discrepancy that is uncomfortable large. Neglecting the Fe magnetism increases the discrepancy.

“Doping” (change of charge in the FeAs layers) is observed to cause the Néel temperature to decrease, and no magnetic order is apparent in superconducting samples. The effect of (rigid band or virtual crystal) doping on the Q_M electronic structure, either by electrons or holes, is to move E_F into a region of heavier carriers, by roughly a factor of 20 ($m_h^* \sim 6 \sim m_e^*$). About 0.1 carriers is sufficient to do this, which is just the amount of doping that results in superconductivity. The Fermi surfaces evolve accordingly as shown in Fig. 5.2.4: for electron doping the hole cylinder disappears, the electron tubes enlarge and merge; for hole doping the electron tubes decrease in size as the hole cylinder grows and distorts into a diamond-shaped cross section.

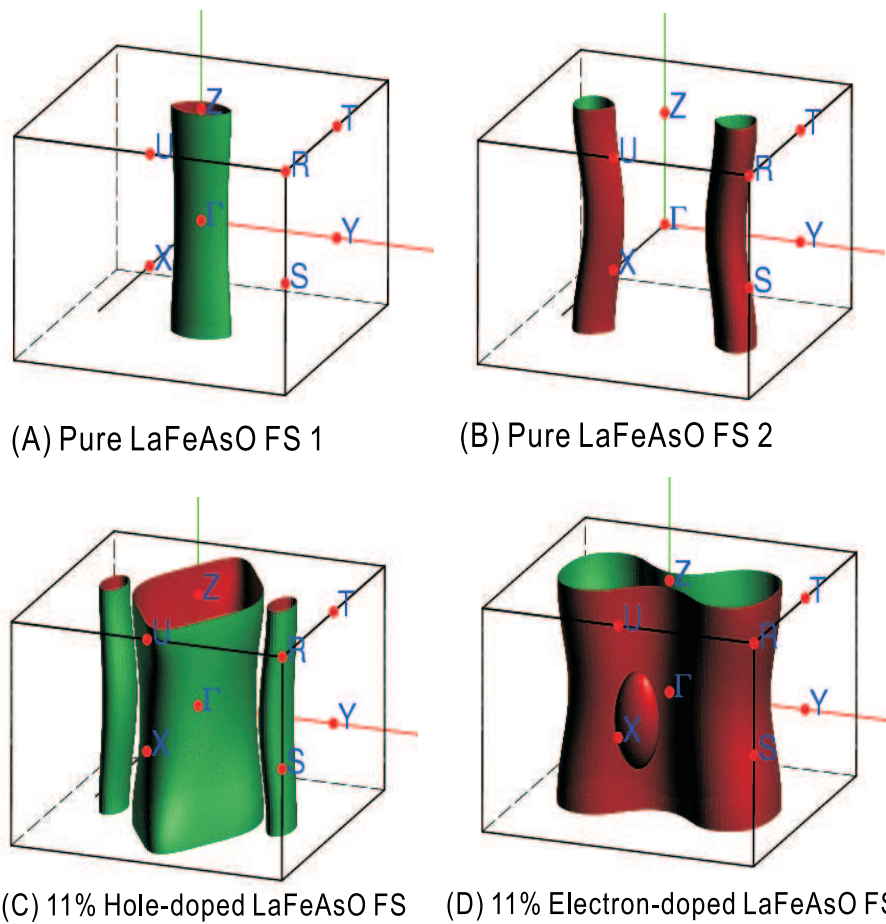


Figure 5.2.4: Fermi surfaces of LaFeAsO in the Q_M AFM phase. (A) and (B): the hole cylinders and electron tubes of the stoichiometric Q_M phase. (C) and (D): hole- and electron-doped surfaces doped away from the Q_M AFM phase.

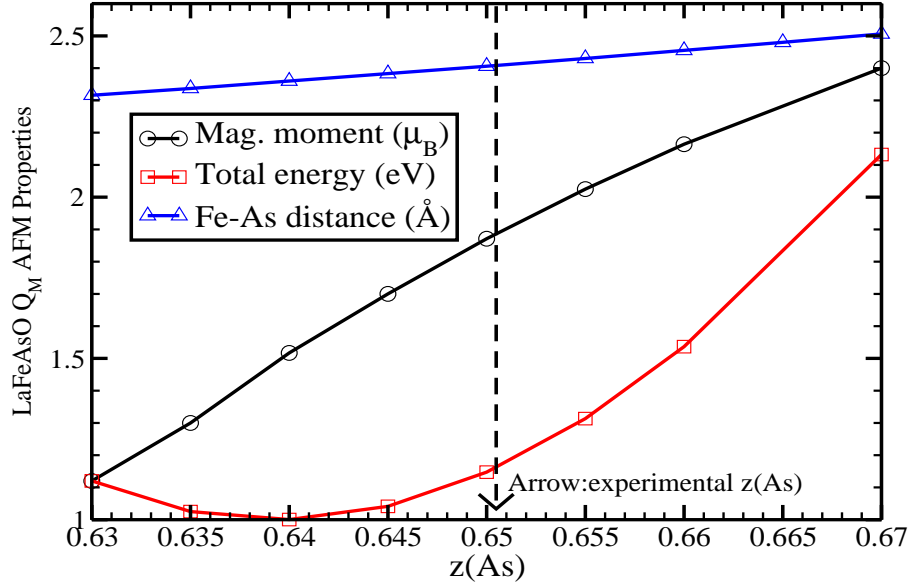


Figure 5.2.5: The magnitude of the Fe magnetic moment, the change in energy, and the Fe-As distance, as the As height z_{As} is varied.

5.2.6 Exchange Coupling

The spectrum of magnetic fluctuations is an important property of any AFM phase, and may bear strongly on the emergence of superconductivity. We have calculated from linear response theory the exchange couplings $J_{ij}(q)$ for all pairs $\{i,j\}$ within the unit cell, and by Fourier transform the real space exchange couplings $J_{ij}(R)$, for the transverse spin-wave Hamiltonian[310, 311]

$$H = - \sum_{\langle i,j \rangle} J_{ij} \hat{e}_i \cdot \hat{e}_j; \quad J_{ij}(R) = - \frac{d^2 E[\{\theta\}]}{\partial \theta_i(0) \partial \theta_j(R)}, \quad (5.2.1)$$

where $\theta_j(R)$ is the angle of the moment (with direction \hat{e}_j) of the j -th spin in the unit cell at R . For the Q_M AFM phase and experimental structural parameters, the

1st and 2nd neighbor couplings are (distinguishing parallel and perpendicular spins)

$$J_1^\perp = -550 \text{ K}; J_1^\parallel = +80 \text{ K}; J_2^\perp = -260 \text{ K}. \quad (5.2.2)$$

For comparison, the nearest neighbor coupling[310, 311] in elemental FM Fe is $J_1 \approx 1850 \text{ K}$, *i.e.* 3-4 times as strong. The signs are all supportive of the actual ordering, there is no frustration. The factor-of-7 difference between the two 1st neighbor couplings reflects the strong asymmetry between the x - and y -directions in the Q_M phase, which is also clear from the bands. The sensitivity to the Fe-As distance is strong: for $z(\text{As})=0.635$, where the moment is decreased by 40% (Fig. 5.2.5), the couplings change by roughly a factor of two: $J_1^\perp = -200 \text{ K}$, $J_1^\parallel = +130 \text{ K}$, $J_2^\perp = -140 \text{ K}$. The interlayer exchange constants will be much smaller and, although important for the (three dimensional) ordering, that coupling should leave the spin-wave spectrum nearly two-dimensional.

We emphasize that these exchange couplings apply only to small rotations of the moment (spin waves). The $Q=0$ phase couplings are different from those for the Q_M phase; furthermore, when FM alignment is enforced the magnetism disappears entirely. The magnetic coupling is phase-dependent, largely itinerant, and as mentioned above, it is sensitive to the Fe-As distance.

5.2.7 Influence of XC Functionals and Codes on the Electronic Structure of LaFeAsO

First, we studied the electronic structure of LaFeAsO in the experimental (tetragonal) crystal structure for different magnetic states (Q_M AFM, Q_0 AFM, FM and NM) using two different codes (FPLO7 and Wien2K) and different exchange-correlation

functionals. This is necessary in view of the large number of theoretical papers[295, 287, 312, 313, 286] which appeared recently and often contain strong disagreements. This was partly studied by Mazin *et al.*[314] Table 5.1 summarizes the results: the magnetic moment on the Fe atom together with the total energy differences for each magnetic state studied here. Independent of the code or the XC functional used, the Q_M AFM state is always found to be the ground state, which confirms our earlier report[285]. The magnetic moment for both AFM orders are considerably larger than the ordered moment reported from neutron diffraction and muon spin relaxation experiments($0.36 \mu_B$), while the one for the FM order is much smaller. For this last case, FPLO7 gives zero which indicates no magnetism with both PZ and PW92 XC functional; Wien2K gives about $0.36 \mu_B$ with GGA and PBE and $0.13 \mu_B$ with PW92. It appears therefore that the magnetic moment of Fe for the same state with different XC functionals varies by up to $0.5 \mu_B$, which is unexpectedly large, although GGA is known to enhance magnetism.[314] The difference between FPLO7 and Wien2K in predicting the Fe magnetic moment for each state may explain the total energy differences among them. Virtual doping (see next next subsection) by $0.1 e^-/Fe$ enhances the Fe magnetic moment in the Q_M AFM state but reduces it in the FM state for all the XC functionals used.

In the structural optimization (performed in the Q_M state), FPLO7 with PW92 (LDA) functional gives reasonable c/a and $z(La)$ in good agreement with experiment, but it predicted $z(As) \sim 0.139$, which is 0.011 off the experimental value, about 0.1 Å in length. However, Wien2K with PBE(GGA) XC functional gives an optimized $z(As) \sim 0.149$, which agrees well with experimental $z(As)$. Similar results are found in the XFe_2As_2 family ($X=Ba, Sr, Ca$) too. It suggests that, GGA (PBE) XC functional optimizes the FeAs-based system much better than LDA (PW92) XC functional.

Table 5.1: Calculated magnetic moment of Fe, the amounts of total energy per Fe lie below nonmagnetic state of FM, Q_0 AFM and Q_M AFM states from FPLO7 and Wien2K with different XC functionals of LaFeAsO with experimental structure. Positive Δ EE means lower total energy than NM state.

code	XC	mag. mom. (μ_B)			Δ EE (meV/Fe)		
		Q_M	Q_0	FM	Q_M	Q_0	FM
FPLO7	PW92	1.87	1.72	0.00	87.2	24.6	0
	PZ	1.70	1.31	0.00	62.2	6.9	0
WIEN2k	PW92	1.74	1.52	0.13	136.9	78.9	0
	GGA	2.09	1.87	0.36	149.1	65.2	3.7
	PBE	2.12	1.91	0.37	158.1	70.2	4.5
0.1 e ⁻ doped	PW92	1.86	—	0.08	125.2	—	-0.5
0.1 e ⁻ doped	GGA	2.14	—	0.26	139.7	—	-0.1
0.1 e ⁻ doped	PBE	2.16	—	0.27	149.6	—	2.1

And GGA should have better performance in dealing with the structure (including c/a , equilibrium volume and $z(\text{As})$) under pressure of this FeAs family. This is probably due to the layered structure of the FeAs family which results in large density gradient between layers, thus GGA has better description of the potential. But in the meantime, GGA (PBE) further overestimates the magnetic moment of Fe, which is already overestimated by LDA (PW92).

5.2.8 Effect of $z(\text{As})$ on the Electronic Structure of LaFeAsO

Then we studied how the electronic structure of LaFeAsO depends on the value of $z(\text{As})$.

Table 5.2 shows the difference between the experimental $z(\text{As})(\sim 0.150)$, the optimized $z(\text{As}) (\sim 0.139)$ and a middle value of 0.145 when using FPLO7 with PW92 XC functional: decreasing $z(\text{As})$ (reducing the Fe-As distance) rapidly reduces the differences in energy between the different magnetic orderings. At $z(\text{As}) = 0.145$, the magnetic moments of the Q_M and Q_0 states are reduced significantly in comparison

Table 5.2: Calculated magnetic moment of Fe, total energy relative to the nonmagnetic (ferromagnetic) states of NM/FM, Q_0 AFM and Q_M AFM of LaFeAsO with $z(\text{As}) = 0.150$ (experimental), 0.145, and 0.139 (optimized) from FPLO7 with PW92 XC functional.

$z(\text{As})$	mag. mom. (μ_B)			Δ EE (meV/Fe)		Fe 3d occ.#	
	Q_M	Q_0	FM	FM- Q_M	Q_0 - Q_M	maj.	min.
0.150	1.87	1.72	0.002	87.2	62.6	4.32	2.45
0.145	1.70	1.41	0.000	60.5	54.0	4.24	2.55
0.139	1.48	0.01	0.000	34.6	34.6	4.15	2.68

with $z(\text{As}) = 0.150$, and the difference in energy has changed by around 20%, indicating important changes in the electronic structure upon moving the As atom. For $z(\text{As}) = 0.139$, the Q_0 AFM state has lost its moment (become the NM state), while the magnetic moment of the Q_M state has decreased even more, with a changing rate of $6.8 \mu_B/\text{\AA}$, indicating strong magnetophonon coupling.[285] Therefore, using the experimental or optimized value for the internal coordinate of As gives quite different results and might explain several of the discrepancies seen in the previously published works.

In Figures 5.2.6 and 5.2.7, we present the corresponding band structures, total densities of states, and partial densities of states calculated for different values of $z(\text{As})$. Surprisingly, the band structure near E_F referred to the common Fermi level barely changes when $z(\text{As})$ decreases. Somewhat away from E_F , the bands below the Fermi level are pushed up in energy when $z(\text{As})$ is decreased, while the effect of the Fe-As distance on the bands above ϵ_F is less obvious, since they are pushed up or down depending on the direction of the Brillouin zone. For instance, along $\Gamma - X$ and $\Gamma - Z$ they are pushed down, so that a decrease of the pseudogap is expected, as shown by Fig. 5.2.6. The peaks of the DOS just above Fermi level move toward it when $z(\text{As})$ is reduced, while the DOS below the Fermi level is quite robust with less changes. The important decrease of the magnetic moment of Fe when the

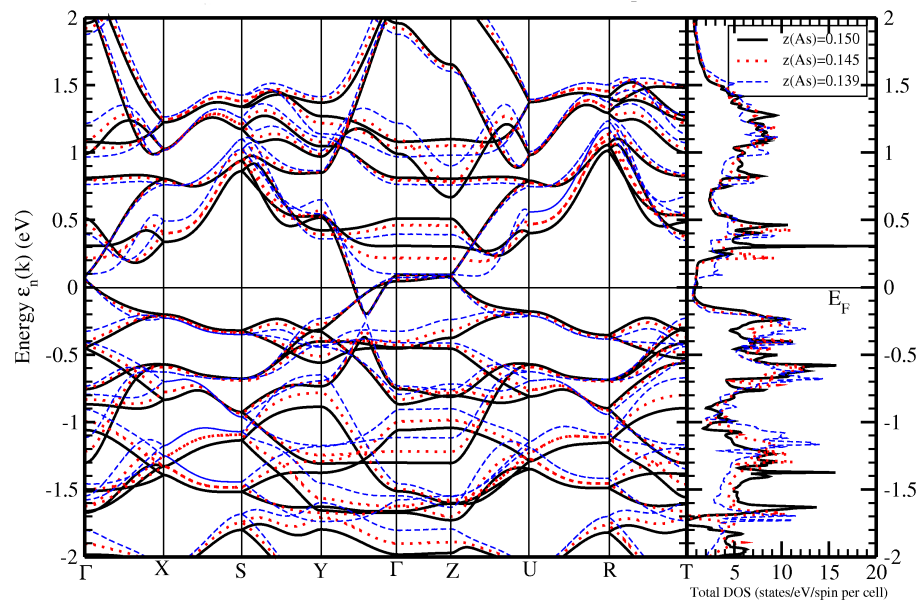


Figure 5.2.6: The bandstructure and total DOS of Q_M LaFeAsO at ambient pressure computed for $z(\text{As})=0.150$, $z(\text{As})=0.145$, $z(\text{As})=0.139$.

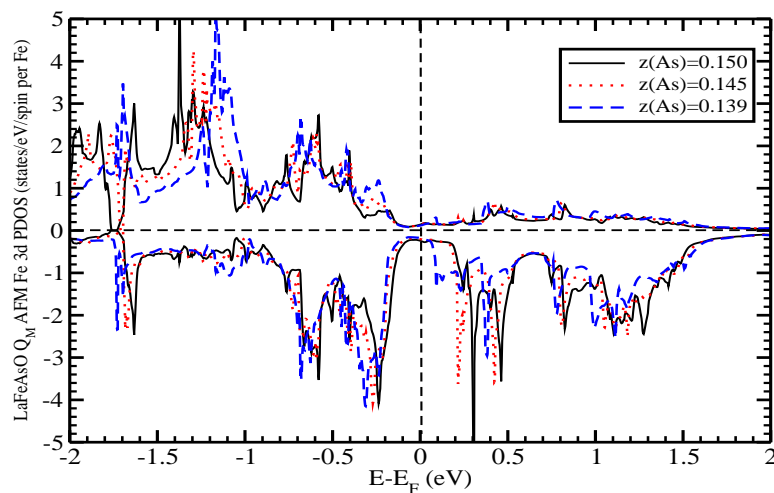


Figure 5.2.7: Plot of LaFeAsO Q_M AFM Fe 3d PDOS at ambient pressure with $z(\text{As})=0.150$, $z(\text{As})=0.145$, $z(\text{As})=0.139$.

Fe-As distance changes is understood by looking at the Fe-3d PDOS (Fig. 5.2.7) and the last column of table 5.2. Although the number of Fe-3d electrons remains approximately constant, the number of spin up electron decreases, while the number of spin down electrons is increased when $z(\text{As})$ is reduced, which overall leads to a decrease of the magnetic moment.

5.2.9 Effect of Virtual Crystal Doping on the Electronic Structure of LaFeAsO

Since superconductivity happens only in doped LaFeAsO, it is necessary to know how doping will affect the underlying electronic structure and the character of each magnetic state. Using the experimental lattice parameters, we performed virtual crystal doping calculations on LaFeAsO using Wien2K by changing the charge of O (doping with F) and La (doping with Ba, but simulating doping with Sr as well), and the corresponding number of valence electrons. The virtual crystal method is superior to a rigid band treatment because the change in carrier density is calculated self-consistently in the average potential of the alloy.

There is only a weak dependence of the calculated Fe magnetic moment on the electron doping level: 0.1 e^-/Fe doping enhances it from 2.12 μ_B to 2.16 μ_B (see Table 5.1). However, electron doping reduces the total energy difference (compared to NM) in both Q_M AFM and FM states. The main effect of virtual crystal doping is to change the Fermi level position, in roughly a rigid band fashion (see the caption of Fig. 5.2.8 for more details). The band structures of 0.1, and 0.2 e^-/Fe doped LaFeAsO in the Q_M AFM phase show only small differences; the charge goes into states that are heavily Fe character and the small change in the Fe 3d site energy with respect to that of As 4p states is minor.

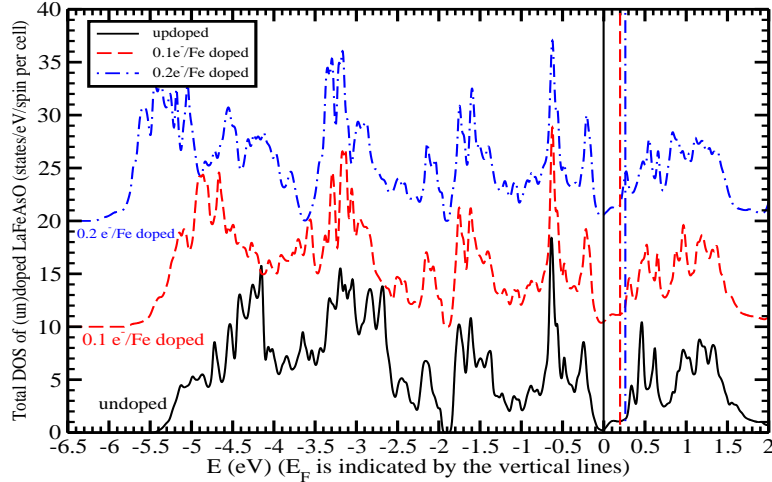


Figure 5.2.8: Plots of undoped, 0.1 and 0.2 electron-doped LaFeAsO Q_M AFM total DOS (displaced upward consecutively by 10 units for clarity, obtained using the virtual crystal approximation. Referenced to that of the undoped compound, the Fermi levels of 0.1 and 0.2 electron-doped DOS are shifted up by 0.20 eV and 0.26 eV, respectively.

Notably, the virtual crystal approximation continues to give strong magnetic states, whereas doping is observed to degrade and finally kill magnetism and promote superconductivity. Thus the destruction of magnetism requires some large effect not considered here, such as strong dynamical spin fluctuations.

5.2.10 Electric Field Gradients

We have calculated the electric field gradients (EFG) of each atom in LaFeAsO, studying both the effects of doping and of magnetic order. The structure used for these calculations is $a=4.0355 \text{ \AA}$, $c=8.7393 \text{ \AA}$, $z(\text{La})=0.142$, $z(\text{As})=0.650$, and the PBE(GGA) XC functional was used in the Wien2K code. (PW92 (LDA) XC functional gives similar results and thus the results are not presented here.) Since the

EFG is a traceless symmetric 3×3 matrix, only two of V_{xx} , V_{yy} , V_{zz} are independent. For cubic site symmetry, the EFG vanishes, hence the magnitude and sign of the EFG reflects the amount and character of anisotropy of the charge density. For the symmetries studied here, the off-diagonal components of the EFG tensor for all the four atoms are zero. For the Q_M AFM state, the V_{yz} component calculated separately for each spin for La and As is not zero, although the sum vanishes; the spin decomposition gives information about the anisotropy of the spin density that is not available from measurements of the EFG.

As shown in Table 5.3 and Table 5.4, the EFGs of both Fe and As in NM and FM states are very similar and they are doping insensitive, except for Fe where the EFG is comparatively small (in tetrahedral symmetry, the EFG is identically zero). Due to the breaking of the x-y symmetry in the Q_M phase, V_{xx} is no longer equal to V_{yy} . In this case, the EFGs are quite different from those in the NM and FM states, which shows once more that the electronic structure in the Q_M AFM order differs strongly from the ones of the NM and FM orders. Also, while hole doping (on the La site) and electron doping (on the O site) significantly change the EFG of Fe, the EFG of As is less affected. Using nuclear quadrupolar resonance (NQR) measurement, Grafe *et al.*[315] reported a quadrupole frequency $\nu_Q=10.9$ MHz and an asymmetry parameter $\eta=0.1$ of the As EFG in LaFeAsO_{0.9}F_{0.1}. This observation gives $V_{zz} \sim 3.00 \times 10^{21}$ V/m², which agrees reasonably well with our result of 2.6×10^{21} V/m² as shown in Table 5.4 in the NM state. Upon 0.1 electron or 0.1 hole doping, the EFGs are modified in a similar way for As but differently for Fe.

Table 5.3: The EFG of Fe in LaFeAsO with NM, FM and Q_M AFM states at different doping levels from Wien2K with PBE(GGA) XC functional. The unit is 10^{21} V/m².

Fe	doping	V_{xx}			V_{yy}		
		up	dn	total	up	dn	total
NM	undoped	0.11	0.11	0.22	0.11	0.11	0.22
	0.1h (La)	0.21	0.21	0.42	0.21	0.21	0.42
	0.1e (La)	0.01	0.01	0.02	0.01	0.01	0.02
	0.1e (O)	0.09	0.09	0.18	0.09	0.09	0.18
FM	undoped	0.51	-0.30	0.21	0.51	-0.30	0.21
	0.1h (La)	0.05	0.39	0.44	0.05	0.39	0.44
	0.1e (La)	0.31	-0.21	0.10	0.31	-0.21	0.10
	0.1e (O)	0.31	-0.20	0.11	0.31	-0.20	0.11
Q_M	undoped	0.22	0.03	0.25	-1.11	0.54	-0.57
	0.1h (La)	0.60	-1.13	-0.43	-1.15	1.04	-0.11
	0.1e (La)	-0.55	1.00	0.45	-1.05	0.24	-0.81
	0.1e (O)	-0.54	1.01	0.47	-1.07	0.32	-0.75
	0.2e (O)	-0.82	1.17	0.35	-1.02	0.52	-0.50

Table 5.4: The EFG of As in LaFeAsO with NM, FM and Q_M AFM states at different doping levels from Wien2K with PBE(GGA) XC functional. The unit is 10^{21} V/m².

As	doping	V_{xx}			V_{yy}		
		up	dn	total	up	dn	total
NM	undoped	0.69	0.69	1.38	0.69	0.69	1.38
	0.1h (La)	0.70	0.70	1.40	0.70	0.70	1.40
	0.1e (La)	0.65	0.65	1.31	0.65	0.65	1.31
	0.1e (O)	0.66	0.66	1.32	0.66	0.66	1.32
FM	undoped	0.55	0.81	1.36	0.55	0.81	1.36
	0.1h (La)	0.58	0.68	1.26	0.58	0.68	1.26
	0.1e (La)	0.56	0.74	1.30	0.56	0.74	1.30
	0.1e (O)	0.58	0.75	1.23	0.58	0.75	1.23
Q_M	undoped	-0.40	-0.40	-0.80	0.77	0.77	1.54
	0.1h (La)	-0.42	-0.42	-0.84	0.68	0.68	1.36
	0.1e (La)	-0.41	-0.41	-0.82	0.89	0.89	1.78
	0.1e (O)	-0.40	-0.40	-0.80	0.91	0.91	1.82
	0.2e (O)	-0.29	-0.29	-0.58	1.03	1.03	2.06

5.2.11 Effect of Pressure on the Electronic Structure of LaFeAsO

Applying pressure is often used as a way to probe how the resulting effect on the electronic structure impacts the superconducting critical temperature and other properties. A strong pressure effect was shown experimentally for the members of the LaFeAsO family[316, 317, 318], since for example $T_c = 43$ K could be reached under pressure for LaFeAsO_{1-x}F_x, in case of optimal doping[316]. To begin to understand such observations, it is necessary to determine how the electronic structure of the parent compound LaFeAsO is changed by pressure.

In Fig. 5.2.9, the magnetic moment of Fe in the Q_M AFM phase versus Fe-As distance is presented. Two different behaviours of the magnetic moment are observed. When $z(\text{As})$ is varied at constant volume (zero pressure), the decrease of the magnetic moment of Fe is parabolic. When pressure is applied and all internal positions are optimized (hence $z(\text{As})$ changes) the change is linear until the magnetic moment drops to zero. This linear behavior is followed also when the As height $z(\text{As})$ is shifted by 0.011 to compensate for the PW92 (LDA) error mentioned above.

Fig. 5.2.10 collects a number of results: the effect of pressure on the c/a ratio, the Fe-As distance, the total energy, the difference in energy between NM and QM states, and the magnetic moment on Fe. Under pressure, the c/a ratio, the Fe-As distance, and the magnetic moment of the Q_M AFM state drop linearly when volume is reduced. The PW92(LDA) predicts an equilibrium volume of 0.925 V_0 ; and the total energy differences between NM and Q_M AFM state gradually drops to zero at 0.78 V_0 .

The effect of pressure on the band structure is shown in Fig. 5.2.11. While the bands change positions under pressure, in the corresponding DOS (right panel of Fig. 5.2.11), the first peak above E_F is moved towards the Fermi level when pressure

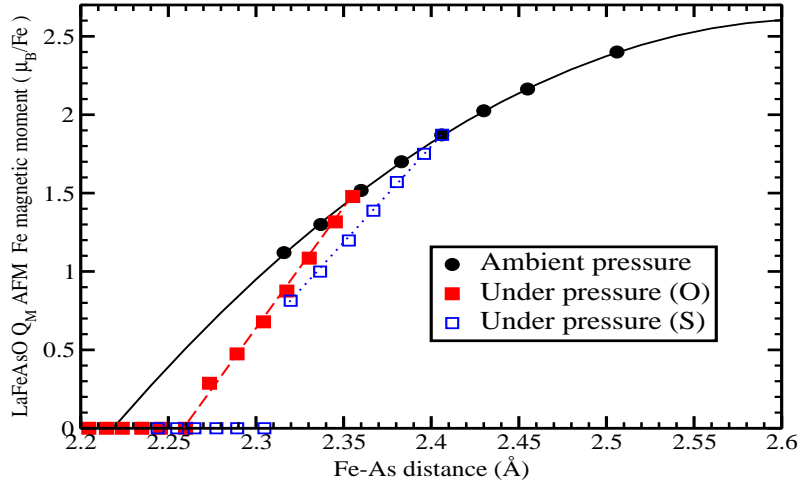


Figure 5.2.9: Plot of the magnetic moment of Fe atom in the Q_M AFM state of LaFeAsO as a function of the Fe-As distance, both at ambient pressure and under pressure.

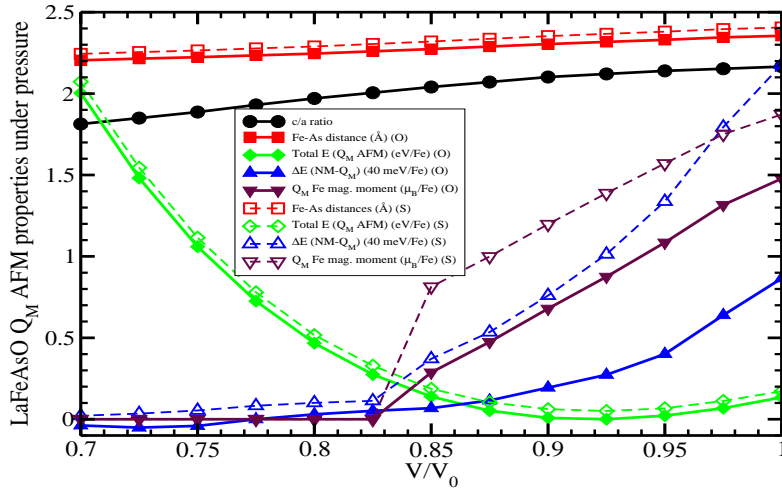


Figure 5.2.10: Plot of the optimized c/a ratio, the Fe-As distances (\AA), the total energy of the Q_M AFM state (eV), the total energy differences between NM and Q_M AFM state ($EE(\text{NM})-EE(Q_M \text{ AFM})$) (40 meV/Fe), the magnetic moment (μ_B) of the Q_M AFM states as a function of V/V_0 .

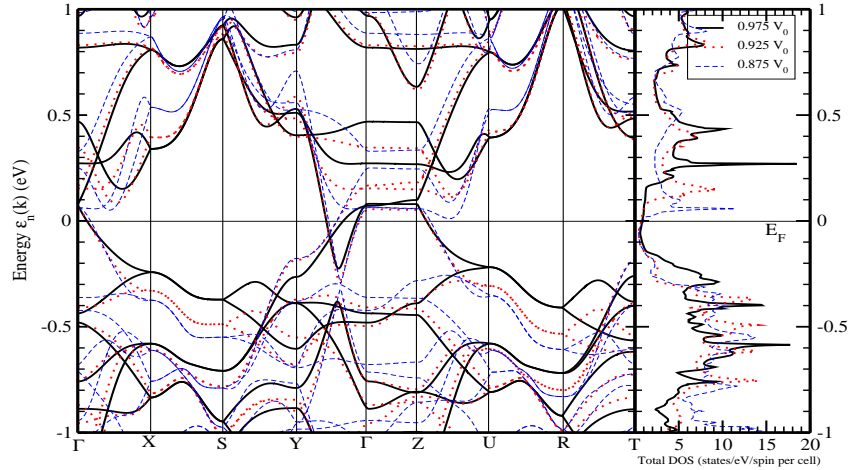


Figure 5.2.11: The bandstructure and total DOS of Q_M LaFeAsO computed for $0.975V_0$, $0.925 V_0$ and $0.875 V_0$. $z(\text{As})$ has been shifted.

is applied, but the DOS from -0.1 eV to E_F is left almost unchanged by pressure. Therefore pressure should induce important changes in the superconducting properties of electron-doped LaFeAsO, while they should be less important for hole-doped LaFeAsO.

The Fermi surface of Q_M LaFeAsO computed for different values of the volume is presented in Fig. 5.2.12. The first sheet is an almost perfect cylinder along the $\Gamma - Z$ line, while the second sheet is made of two ellipsoidal cylinders with some k_z bending. They appear to be very similar to the FS computed at ambient pressure[285]. The pressure has almost no effect on the first sheet, but it enhances the distortion of the second sheet.

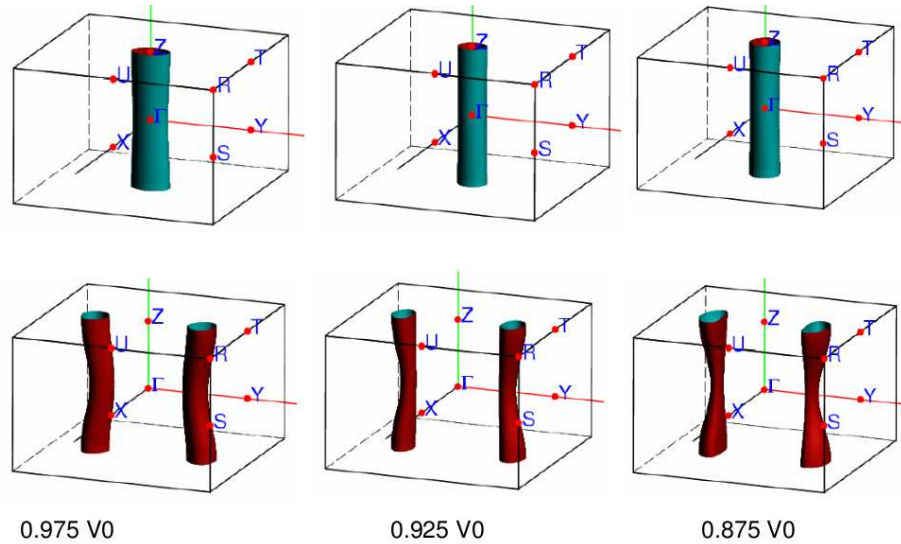


Figure 5.2.12: The Fermi surface of Q_M LaFeAsO computed for $0.975V_0$, $0.925 V_0$ and $0.875 V_0$. $z(\text{As})$ has been shifted.

5.2.12 Summary

The electronic and magnetic structure, and the strength of magnetic coupling, in the reference state of the new iron arsenide superconductors has been presented here, and the origin of the electron-hole symmetry of superconductivity has been clarified. The dependence of the Fe moment on the environment, and an unusually strong magnetophonon coupling, raises the possibility that magnetic fluctuations are involved in pairing, but that it is longitudinal fluctuations that are important here.

We have also studied the effects of XC functional, of the Fe-As distance, of doping, and of pressure, on the electronic structure of LaFeAsO. Calculations of the EFGs for all atoms in LaFeAsO have been reported, and compared with available experimental data with satisfactory agreements. It was found that (approximate) electron-hole symmetry versus doping, and strong magnetophonon coupling are primary characteristics of the LaFeAsO system, and are two of the ingredients that need

to be understood to proceed toward the discovery the mechanism of superconducting pairing.

5.2.13 Acknowledgments

This work was supported by DOE under Grant No. DE-FG02-04ER46111. We also acknowledge support from the France Berkeley Fund that enabled the initiation of this project.

5.3 The Effect of *Pn* and Rare Earth Atoms

This section contains work from “*The delicate electronic and magnetic structure of the LaFePnO system (Pn=pnicogen)*”, S. Lebègue, Z. P. Yin, and W. E. Pickett, *New Journal of Physics* **11**, 025004 (2009).

5.3.1 Background and Motivation

The layered conductors LaFePO and LaFeAsO, though isostructural and isovalent, display surprisingly different properties. The first is nonmagnetic and was initially reported as superconducting with critical temperature $T_c = 2-7$ K, [319, 320, 321, 322] while more recently there are indications[323, 324] that stoichiometric LaFePO may not be superconducting without the presence of oxygen vacancies. The second becomes antiferromagnetically ordered at $T_N \approx 140$ K[281, 325]with no report of superconductivity in the stoichiometric compound. The discovery of superconductivity at 26 K in carrier-doped LaFeAsO[191], followed by rapid improvement now up to $T_c=55$ K[274] in this class, is strikingly different from what is reported in LaFePO and these high values of T_c make these superconductors second only to the cuprates

in critical temperature. Several dozen preprints appeared within the two months after the original publication, and many hundred since, making this the most active field of new materials study in recent years (since the discovery in MgB_2 , at least).

A host of models and ideas about the “new physics” that must be operating in this class of compounds is appearing, pointing out the need to establish a clear underpinning of the basic electronic (and magnetic) structure of the system. The materials are strongly layered, quasi-two-dimensional in their electronic structure, by consensus. The electronic structure of LaFePO was described by Lebègue,[294] with the electronic structure and its neighboring magnetic instabilities of LaFeAsO being provided by Singh and Du[295]. Several illuminating papers have appeared since, outlining various aspects of the electronic and magnetic structure of LaFeAsO .

The extant electronic structure work has provided a great deal of necessary information, but still leaves many questions unanswered, and indeed some important questions are unaddressed so far. In this section we address some of these questions more specifically. Stoichiometric LaFeAsO is AFM; then ~ 0.05 carriers/Fe doping of either sign destroys magnetic order and impressive superconductivity arises.

The question we address here can be typified by the question: with the nonmagnetic electronic structure of LaFePO and LaFeAsO being so similar, why are their magnetic and superconducting behavior so different? Surely this difference must be understood and built into bare-bones models, or else such models risk explaining nothing, or explaining anything. There are increases in T_c due to replacement of La with other rare earth ions, and the variation in size of the rare earth is often a dominant factor in the observed trends in their compounds. Very important also is the magnetism in these materials, as magnetism is a central feature in the cuprate superconductors and in correlated electron superconductors. Another important question

is: what can be expected if other pnictide atoms can be incorporated into this system: Sb (or even Bi) on the large atom side, or N on the small atom end. We address these questions in this section.

5.3.2 Overall Results

Results presented here have used the same calculation method as above section.

LaFeAsO and LaFePO are isostructural and isovalent, but they have quite different properties. A deeper understanding of the differences of the electronic structure of these two compounds can provide insight into the competition between magnetic ordering and superconductivity. For similar reasons, the related compounds LaFeNO and LaFeSbO (although not studied experimentally yet) are potentially of high interest, so we also provide predictions for their electronic structure.

Table 5.5 displays the experimental structure parameters for LaFePO[319] and LaFeAsO[191] as well as the predicted structure for LaFeNO and LaFeSbO after optimization (see below for calculation details). As a result of the increasing size of the pnictogen atom, the Fe- Pn length changes. In particular, the Fe- Pn distance is consistent with the sum of the covalent radii of Fe and Pn , which reflects the covalent bonding nature between Fe and Pn atoms in this family. The slight increase of the La-O distance through the series is just a size effect related to the expansion of the volume .

The values of the Fe magnetic moment for LaFe Pn O with FM/NM, Q_0 AFM, Q_M AFM states, and their total energy differences are presented in Table 5.6. Apart from LaFePO, all the members of the LaFe Pn O family studied here have a large Fe magnetic moment in the Q_M AFM state, the corresponding total energy being significantly lower than the ones corresponding to FM/NM state.

<i>Pn</i>	<i>a</i> (Å)	<i>c</i> (Å)	<i>c/a</i>	<i>z</i> (La)	<i>z</i> (<i>Pn</i>)	La-O	Fe- <i>Pn</i>	Sum	Fe- <i>Pn</i> -Fe angles
N	3.7433	8.1120	2.167	0.169	0.102	2.320	2.046	2.00	132.4, 80.6
P	3.9636	8.5122	2.148	0.149	0.134	2.352	2.286	2.31	120.2, 75.6
As	4.0355	8.7393	2.166	0.142	0.151	2.369	2.411	2.44	113.6, 72.6
Sb	4.1960	9.2960	2.215	0.128	0.168	2.411	2.615	2.62	106.7, 69.1

Table 5.5: Structural parameters of LaFePnO ($Pn = \text{N, P, As, or Sb}$), as obtained experimentally for LaFePO [319] and LaFeAsO [191] or from our calculations for LaFeNO and LaFeSbO . Length units are in Å, $z(\text{La})$ and $z(Pn)$ are the internal coordinate of the lanthanum atom and the pnictide atom, and “Sum” means the sum of Fe covalent radius and the Pn covalent radius, which is quite close to the calculated value in all cases.

<i>Pn</i>	mag. mom. (μ_B)			Δ EE (meV/Fe)	
	Q_M	Q_0	FM	FM- Q_M	Q_0 - Q_M
N	1.85	0.88	0.027	73.5	70.7
P	0.56	—	0.087	2.1	—
As	1.87	1.72	0.002	87.2	62.6
Sb	2.45	2.39	0.000	276.5	80.8

Table 5.6: Calculated magnetic moment of Fe, total energy relative to the nonmagnetic (ferromagnetic) states of Q_0 AFM, and Q_M AFM states of LaFePnO from FPLO7 with PW92 XC functional.

5.3.3 LaFePO

LaFePO was the first member of the iron-oxypnictide family to be reported to be superconducting[319]. The corresponding electronic structure was studied by Lebègue using ab-initio calculations[294], but considering only a non-magnetic ground-state. Since then LaFePO has been studied using various experimental tools: by using photoemission[326, 327, 328], it was shown that the Fe $3d$ electrons are itinerant, and that there is no pseudogap in LaFePO . Also, magnetic measurements revealed[329, 323] that LaFePO is a paramagnet, while electron-loss spectroscopy[330] implied a significant La-P hybridization. The absence of long-range order in LaFePO was confirmed by Mössbauer spectroscopy [321] and it was proposed that LaFePO and doped LaFeAsO could have different mechanisms to drive the superconductivity in

these compounds. Also, further theoretical studies were performed[329, 330, 328] but without studying all the possible magnetic states.

In our calculations, we find that for FM order Fe has a weak magnetic moment of about $0.09 \mu_B$, with a total energy very close to the NM one; this result is much like what is found in LaFeAsO. A remarkable difference is that the Q_0 AFM state cannot be obtained. However, we found the Q_M AFM state to be the lowest in energy, but only by about 2.1 meV/Fe, which is about two orders of magnitude less than in LaFeAsO. LaFePO, therefore, presents the situation where all of the three possible magnetic states are all very close in energy to the nonmagnetic state, in contrast with LaFeAsO for which the Q_M AFM order was clearly the ground state. Thus LaFePO is surely near magnetic quantum criticality.

The band structure of Q_M AFM LaFePO is displayed in Fig. 5.3.1 together with total DOS for both Q_M AFM and NM states. The band structure of Q_M AFM LaFePO is quite different from that of LaFeAsO with the same Q_M order, with the most significant differences along Γ -X, Γ -Y and Γ -Z lines. The difference is because the breaking of the x - y symmetry is much smaller in the Q_M AFM LaFePO compared to LaFeAsO, because the calculated Fe moment is only $0.56 \mu_B$ in LaFePO (it is $1.87 \mu_B$ in LaFeAsO with the same calculational method). The corresponding DOS is also different from that of LaFeAsO: there is structure within the pseudogap around Fermi level in LaFePO (See Fig. 5.3.1). The difference in total DOS at E_F is significant: it is only 0.2 states/eV/spin per Fe for LaFeAsO, but it is 0.6 states/eV/spin per Fe for LaFePO. In the NM state of LaFePO, it is even larger with 1.6 states/eV/spin per Fe. The DOS of Q_M AFM LaFePO is fairly flat from the Fermi level (set to 0.0 eV) to 0.6 eV, so that electron doping of LaFePO will increase the Fermi level, but will hardly change $N(E_F)$ (in a rigid band picture).

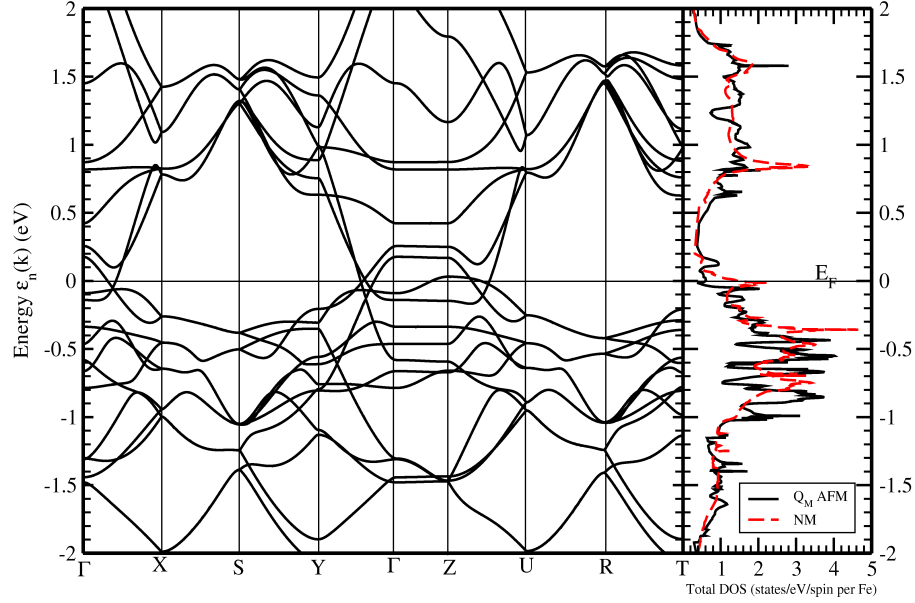


Figure 5.3.1: Plot of LaFePO band structure in Q_M AFM state and total DOS in both Q_M AFM and NM states at ambient conditions with experimental lattice parameters.

An important consequence is that there will be no expected enhancement of T_C coming from $N(E_F)$ upon electron doping. In order to see a significant increase of $N(E_F)$ in Q_M AFM LaFePO, an electron doping level of at least $1.2 e^-/\text{Fe}$ is required, which seems unrealistically large based on the current experimental information. This conclusion remains valid in the case of NM LaFePO, since apart from a peak around Fermi level, the DOS is about the same as for the Q_M AFM state. Again, the behavior is quite different from the one of Q_M AFM LaFeAsO: $0.1 e^-/\text{Fe}$ doping will increase its $N(E_F)$ by a factor of 6: from $0.2 \text{ states/eV/spin per Fe}$ to $1.2 \text{ states/eV/spin per Fe}$.

The Fermi surface of Q_M AFM LaFePO is shown in Fig. 5.3.2. Compared to the Fermi surface of Q_M AFM LaFeAsO presented earlier by Yin *et al.*[285], the piece enclosing the Γ -Z line (containing holes) increases in size and its $x - y$ cross section becomes more circular rather than elliptic. There is another piece (absent

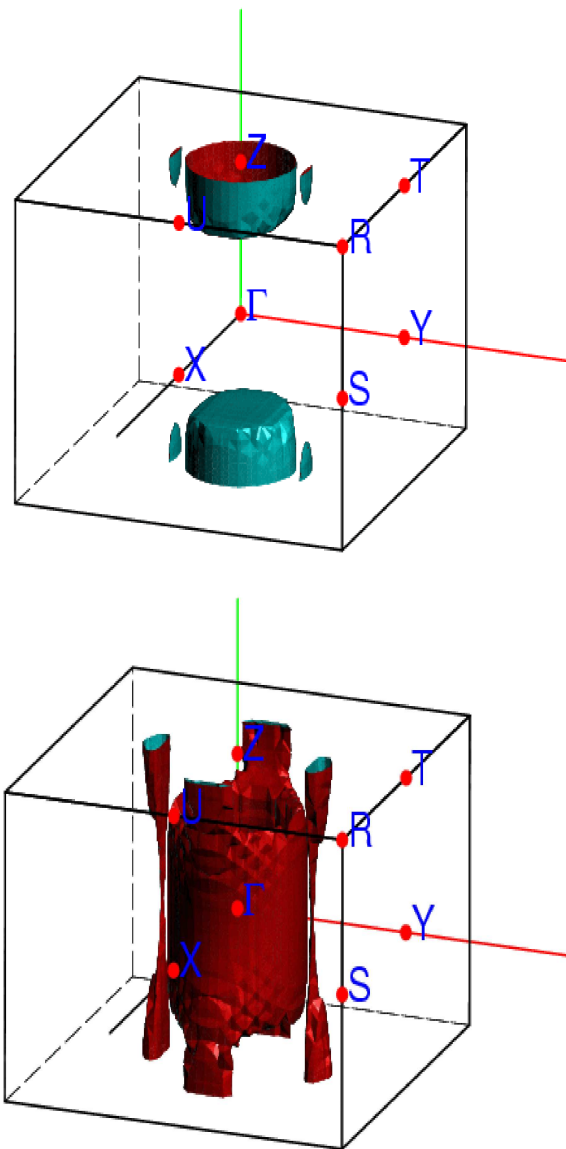


Figure 5.3.2: Fermi surface of Q_M AFM LaFePO, showing the very strong differences compared to LaFeAsO.

in LaFeAsO) also enclosing the Γ -Z line with the same shape but larger in size and containing electrons instead of holes. The two symmetric electron-type pieces of Fermi surface lying along Γ -Y direction in LaFeAsO reduces a lot in size in LaFePO but it has two additional similar pieces lying along Γ -X direction. In LaFePO, it has one more hole-type piece of Fermi surface surround Z point, which is a small cylinder. It is, understandably, quite different from the Fermi surface of NM LaFePO presented earlier[294].

Therefore, while they are isostructural and significantly covalent, LaFePO and LaFeAsO present quite important differences in their respective electronic structures. These differences must form the underpinning of any explanation of why LaFePO is superconducting with a T_c which is almost electron-doping independent, while pure LaFeAsO is not superconducting and becomes so only upon doping.

5.3.4 LaFeSbO

Since the experimental crystal structure of LaFeSbO is not reported yet, we conducted calculations to obtain the structure. The procedure we used is the following: starting from the experimental volume V_0 of LaFeAsO (but with As replaced by Sb), we first optimized c/a , $z(\text{La})$ and $z(\text{Sb})$. Then we chose a higher volume and again optimized the parameters, finally finding the volume that has the lowest total energy. Using this scheme, the optimized volume is $1.046 V_0$ while for LaFeAsO the equilibrium volume is about $0.919 V_0$. Assuming that PW92 overbinds equally for LaFeSbO as for LaFeAsO, the experimental equilibrium volume for LaFeSbO should be $1.046/0.919=1.138 V_0$. Therefore, we performed calculations for a range of volume from $V = V_0$ to $V = 1.150 V_0$, the corresponding structural parameters being presented in Table 5.7. A later calculation in the Q_M AFM phase using PBE

V/V_0	a (Å)	c (Å)	c/a	$z(\text{La})$	$z(\text{Sb})$
1.000	4.092	8.500	2.077	0.137	0.165
1.050	4.118	8.812	2.140	0.133	0.163
1.100	4.141	9.131	2.205	0.129	0.161
1.125	4.155	9.274	2.232	0.128	0.160
1.138	4.163	9.347	2.245	0.127	0.160
1.150	4.169	9.418	2.259	0.126	0.159

Table 5.7: Optimized structure parameters for LaFeSbO at several volumes. The accuracy for c/a is within 0.3%, and within 0.8% for $z(\text{La})$ and $z(\text{Sb})$. A later calculation in the Q_M AFM phase using PBE XC functional gives $a=4.196$ Å, $c=9.296$ Å, $z(\text{La})=0.128$, $z(\text{Sb})=0.168$ at ambient pressure. ($V=1.150 V_0$.)

XC functional gives $a=4.196$ Å, $c=9.296$ Å, $z(\text{La})=0.128$, $z(\text{Sb})=0.168$ at ambient pressure. ($V=1.150 V_0$.)

Since for LaFeAsO in the Q_M AFM phase PW92 underestimated $z(\text{As})$ by 0.011 at its experimental volume, we corrected $z(\text{Sb})$ by adding 0.011 to the optimized $z(\text{Sb})$ (we refer to this position at the “shifted $z(\text{Sb})$ ”). The shifted $z(\text{Sb})$ at $1.150 V_0$ is 0.170, close to $z(\text{Sb})=0.168$ obtained from PBE result, which is confirmed to predict fairly accurate structural parameters including lattice constants and atomic coordinates. Both for the NM and Q_M AFM case, there are very small differences near E_F between the optimized $z(\text{As})$ and shifted $z(\text{As})$ in the band structure and DOS, as seen in Fig 5.3.3. However, shifting $z(\text{Sb})$ induces important changes in the energy differences between NM and Q_M AFM states, as shown in Table 5.8. Also, the magnetic moment of Fe, and the energy differences among NM/FM, Q_0 AFM and Q_M AFM are strongly dependent on the volume. With decreasing volume, the difference in energy between the different magnetic states decreases quickly.

At $1.138 V_0$ (or $1.150 V_0$ from PBE result), the inferred equilibrium volume of LaFeSbO, the properties of NM/FM, Q_0 AFM, and Q_M AFM are very similar to the ones of LaFeAsO at its experimental volume. Thus from these results we expect that

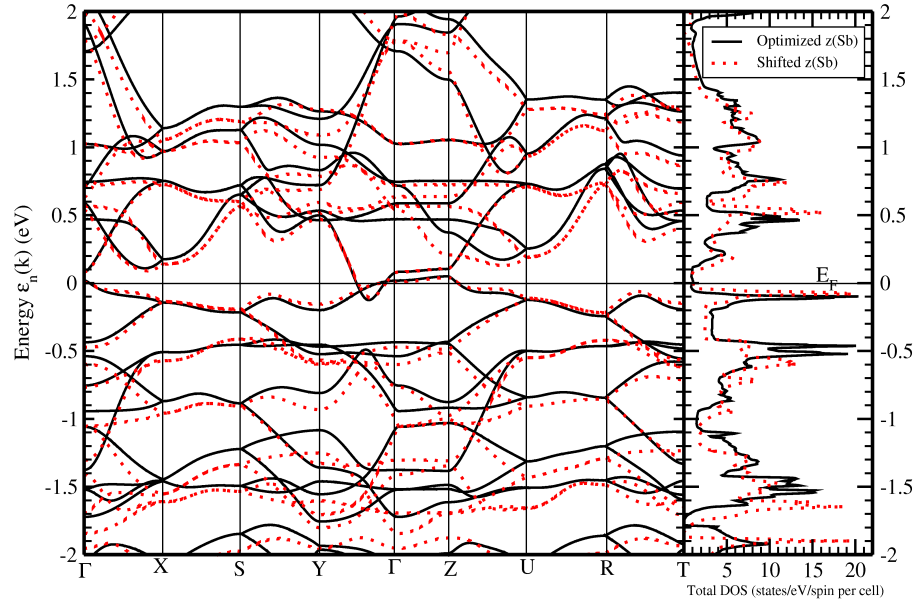


Figure 5.3.3: Plot of Q_M AFM LaFeSbO band structure and total DOS at $1.138 V_0$ with both optimized and shifted $z(\text{Sb})$.

V/V_0	mag. mom. (μ_B)			ΔEE (meV/Fe)	
	Q_M	Q_0	FM	FM- Q_M	Q_0 - Q_M
1.000	1.58	1.12	0.36	60.1	60.1
1.050	1.87	1.74	0.44	95.6	68.0
1.100	2.09	2.00	0.00	147.6	70.7
1.125	2.17	2.10	0.00	172.6	71.8
1.138	2.23	2.16	0.00	190.6	72.5
1.150	2.26	2.19	0.00	199.0	72.0
1.050	2.17	2.08	0.72	158.1	78.0
1.100	2.35	2.00	0.00	223.8	80.8
1.125	2.42	2.37	0.00	271.6	81.8
1.138	2.47	2.42	0.00	293.8	82.4
1.150	2.49	2.45	0.00	287.6	82.1

Table 5.8: Calculated magnetic moment of Fe, total energy relative to the nonmagnetic (ferromagnetic) states of Q_0 AFM and Q_M AFM with the optimized structure of LaFeSbO at several volumes from FPLO7 with PW92 XC functional. Upper part: $z(\text{Sb})$ is optimized. Lower part: $z(\text{Sb})$ is optimized and shifted.

doped LaFeSbO should have similar properties (viz, value of T_c) as LaFeAsO.

5.3.5 LaFeNO

The structure of LaFeNO is also not reported experimentally. In order to obtain it, the same procedure as for LaFeSbO was used. The lowest total energy is at $0.762 V'_0$ (here V'_0 is the experimental volume of LaFePO.). Again assuming PW92 makes a similar error as it makes in LaFeAsO, we estimate its equilibrium volume to be close to $0.825 V'_0$. At $0.825 V'_0$ and for larger volume, the total energy of the Q_M AFM state is well below that of the FM/NM state (see Table 5.9). Therefore, LaFeNO, if it exists, should be in the Q_M AFM ordered state at low temperature, which is similar to LaFeAsO and LaFeSbO. A later calculation in the Q_M AFM phase using PBE XC functional gives $a= 3.743 \text{ \AA}$, $c= 8.112 \text{ \AA}$, $z(\text{La})=0.169$, $z(\text{Sb})=0.102$ at ambient pressure, corresponding to a equilibrium volume of $0.85 V'_0$, which is very close to (with in 3% of) $0.825 V'_0$ estimated from PW92 result.

Compared to the other *LaFePnO* compounds, LaFeNO is even closer to being a semimetal when the volume is equal to $0.825 V'_0$, and it becomes a small gap insulator at $0.850 V'_0$ and a higher carrier density metal at $0.800 V'_0$ (see Fig. 5.3.4). The DOS for $0.825 V'_0$ shows a pseudogap around E_F , but the DOS is somewhat less flat than it is for LaFeAsO.

When LaFeNO is calculated to be insulating (for volumes larger than $0.825 V'_0$), the gap can be taken to *define* a distinction between bonding (occupied) and antibonding (unoccupied) states. The appearance of this gap in LaFeNO is quite surprising: although there is clear separation of valence and conduction bands over most of the zones for LaFeAsO, there is no way to ascribe the small FSs to simple overlapping valence and conduction bands: in LaFeAsO and LaFeSbO, the bonding and

V/V'_0	mag. mom. (μ_B)			ΔEE (meV/Fe)	
	Q_M	Q_0	NM/FM	NM/FM- Q_M	Q_0 - Q_M
0.900	2.21	1.69	1.64	209.8	135.9
0.875	2.06	1.51	0.03	114.9	99.2
0.850	1.88	1.14	0.03	74.3	68.1
0.825	1.63	0.80	0.03	41.0	40.0
0.800	1.26	—	0.00	18.4	—
0.787	1.08	—	0.00	11.3	—
0.775	0.90	—	0.00	7.0	—
0.762	0.00	—	0.00	1.3	—
0.750	0.00	—	0.00	1.4	—
0.725	0.00	—	0.00	1.2	—
0.700	0.00	—	0.00	0.9	—

Table 5.9: Calculated magnetic moment of Fe in LaFeNO, total energy relative to the nonmagnetic (ferromagnetic) states of Q_0 AFM and Q_M AFM with the optimized structure at several volumes, but shifted $z(N)$ up by 0.011, as a compensation PW92 does to LaFeAsO, where PW92 underestimates $z(As)$ by 0.011.

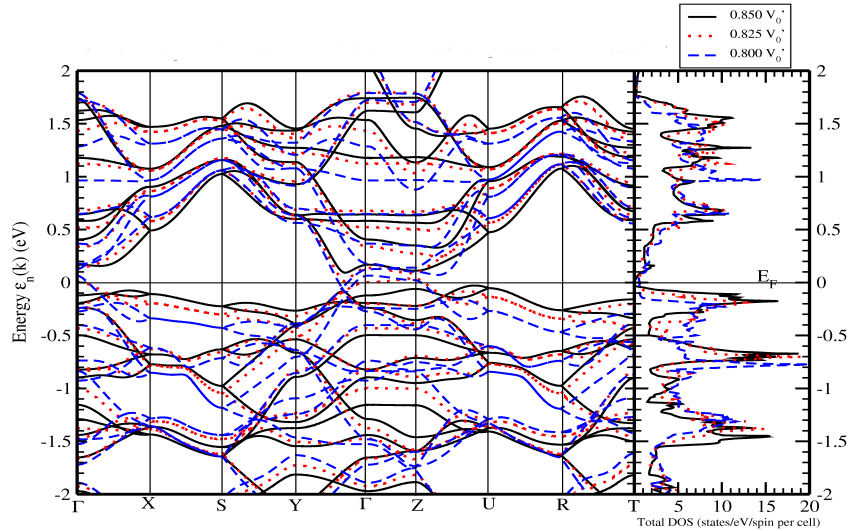


Figure 5.3.4: Plot of LaFeNO Q_M AFM band structure and total DOS at $0.850V'_0$, $0.825 V'_0$ and $0.800 V'_0$ with shifted $z(N)$.

antibonding bands are never completely separated from each other. In LaFeNO this separation finally becomes apparent, as an actual bandgap does appear.

5.3.6 Role of the Rare Earth Atom in *RFeAsO*

After LaFeAsO was discovered, after appropriate variation of the carrier concentration, to be superconducting at 26 K, much substitution on the rare earth (*R*) site has been done, with impressive increases in the critical temperature. Since all are evidently trivalent and donate three valence electrons to the FeAs layer, it becomes important to uncover the influence of the R atom: is it some aspect of the chemistry, which does differ among the rare earths? is it an effect of size? or can there be some other subtle effect?

Table 5.10 is a collection of the lattice constants a and c , volume V of the primitive cell, T_c onset of *RFeAsO* reported from experiment.[196, 273, 331, 332] Both lattice constants, hence the volume, decrease monotonically as the atomic number increases, but T_c increases only from La to Gd, whereupon drops for heavier rare earths. Since we have found that small details affect the electronic and magnetic structure – especially $z(\text{As})$ – it is reasonable to assess the size effect. We have performed calculations on Ce, Nd and Gd, using LSDA+U with $U=7.0$ eV and $J=1$ eV applied to the R atom to occupy the $4f$ shell appropriately and keep the $4f$ states away from the Fermi level. Our results indicate that all have very similar DOS and band structure with LaFeAsO. To investigate further, we checked GdFeAsO using the crystal structure of LaFeAsO. The resulting band structure and DOS are almost identical to the original results for Gd, thus there seems to be no appreciable effect of the differing chemistries of Gd and La. This negative result supports the idea that the size difference may be dominant, though seemingly small. The difference in size

Table 5.10: Collection of the lattice constants a (Å) and c (Å), volume V (Å³) of the primitive cell, T_c onset s (onset, middle, and zero, in K) of *RFeAsO* reported from experiments.

element	Z	a (Å)	c (Å)	V (Å ³)	$T_{C,onset}$ (K)
La	57	4.033	8.739	142.14	31.2
Ce	58	3.998	8.652	138.29	46.5
Pr	59	3.985	8.595	136.49	51.3
Nd	60	3.965	8.572	134.76	53.5
Sm	62	3.933	8.495	131.40	55.0
Gd	64	3.915	8.447	129.47	56.3
Tb	65	3.899	8.403	127.74	52
Dy	66	3.843	8.284	122.30	45.3

(hence a , c , and the internal coordinates) influences not only the band structure and DOS, but also the magnetic properties. Fixed spin moment calculations in the FM state gives the lowest total energy at $0.2 \mu_B/\text{Fe}$ in LaFeAsO, and $0.5 \mu_B/\text{Fe}$ in both GdFeAsO and La-replaced GdFeAsO.

5.3.7 Summary

We have investigated in some detail the electronic structure and magnetic properties of the LaFe*PnO* class of novel superconductors using ab-initio methods. The related materials LaFePO, LaFeSbO, and LaFeNO were investigated and their properties were compared to those of LaFeAsO. From these comparisons, it appears that LaFePO is significantly different from the other materials studied here; this difference might explain why, at stoichiometry, LaFePO is superconducting while LaFeAsO is antiferromagnetic. Also, in view of their similarities with LaFeAsO, either pure or doped LaFeSbO and LaFeNO are potential candidates as superconductors.

5.3.8 Acknowledgments

This work was supported by DOE under Grant No. DE-FG02-04ER46111. We also acknowledge support from the France Berkeley Fund that enabled the initiation of this project.

5.4 Antiphase Magnetic Boundaries

This section contains work[333] from “*Antiphase magnetic boundaries in iron-based superconductors: A first-principle density-functional theory study*”, Z. P. Yin and W. E. Pickett, Phys. Rev. B **80**, 144522 (2009).

5.4.1 Motivation

Much theoretical work has been reported since the first discovery [191] of $\text{LaFeAsO}_{1-x}\text{F}_x$, with many aspects of these compounds having been addressed,[285, 286, 295, 291, 287, 313, 314, 334] but with many questions unresolved. A central question is what occurs at the SDW-to-SC (superconducting) phase transition, and what drives this change, and more fundamentally what microscopic picture is most useful in this enterprise. In the $R\text{FeAsO}$ compounds, doping with carriers of either sign leads to this transition, even though there seems little that is special about the band-filling in the stoichiometric compounds. In the $M\text{Fe}_2\text{As}_2$ system, the SDW-to-SC transition can be driven with pressure (relatively modest, by research standards) without any doping whatever, apparently confirming that doping level is not an essential control parameter. Some delicate characteristic seems to be involved, and one way of addressing the loss of magnetic order is to consider alternative types of magnetic order, and their energies.

Many results, experimental and theoretical, indicate itinerant magnetism in this system, and LSDA calculations without strong interaction effects included correctly predict the type of antiferromagnetism observed. There is however the general feature that the calculated ordered moment of Fe is larger than the observed value. For example, neutron scattering experiment[281] obtained the ordered Fe magnetic moment of $0.36 \mu_B$ in LaFeAsO, while calculations[285, 291, 314] result in the much larger values 1.8 - $2.1 \mu_B$. Neutron diffraction and neutron scattering experiments [335, 336, 337] estimated the Fe magnetic moment in the SDW state of $M\text{Fe}_2\text{As}_2$ ($M=\text{Ba}, \text{Sr}, \text{Ca}$) to be in the range of $0.8 \mu_B$ to $1.0 \mu_B$ but our calculations (this work) give 1.6 - $1.9 \mu_B$. This kind of (large) discrepancy of the ordered magnetic moment is unusual in Fe-based magnets, and there are efforts underway to understand the discrepancy as well as the mechanism underlying magnetic interactions.[338] In addition, ^{57}Fe Mössbauer experiments [282, 339, 340, 341, 342, 343, 344, 345] and ^{75}As NMR measurements [283, 284, 315] further confirm the disagreement in magnetic moments and electric field gradients between experiments and ab initio calculations in the SDW state.

To explain these significant disagreements, it is likely that spin fluctuations in some guise play a role in these compounds. The SDW instability is a common interpretation of the magnetic order in these compounds, [192, 281, 346, 347] which implicates the influence of spin fluctuation in the magnetically disordered state. An inelastic neutron scattering study on a single-crystal sample of BaFe_2As_2 by Matan *et al.* [348] showed anisotropic scattering around the antiferromagnetic wave vectors, suggestive of two dimensional spin fluctuation in BaFe_2As_2 . Such possibilities must be reconciled with the existence of high energy spin excitations in the SDW state of BaFe_2As_2 as observed by Ewings *et al.* [349].

One of the simplest spin excitations is that arising from antiphase boundaries

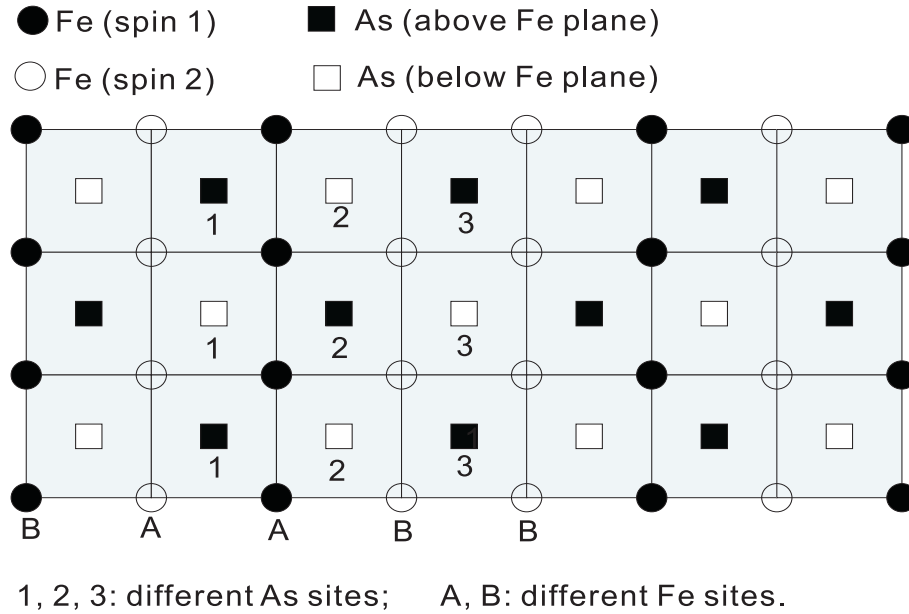


Figure 5.4.1: The structure of FeAs layer in the Q-SDW state showing the antiphase boundary in the center of the figure. Fe spin 1 (filled circle) and spin 2 (empty circle) have two different sites A (‘bulklike’) and B (‘boundary-like’). As above Fe plane (filled square) and below Fe plane (empty square) have three sites 1, 2, 3 whose local environments differ.

in the SDW phase. Mazin and Johannes have introduced such “antiphasons” and their dynamic fluctuations as being central for understanding the various phenomena observed in this class of materials.[350] The structural transition followed by the antiferromagnetic transition, the change of slope and a peak in the differential resistivity $d\rho(T)/dT$ at the phase transitions, and the invariance of the resistivity anisotropy over the entire temperature range can be qualitatively understood in their scenario by considering dynamic antiphase boundaries (twinning of magnetic domains).[350]

In this section, we consider a class of magnetic arrangements derived from the stripe-like AFM phase: static periodic magnetic arrangements (SDWs) representing antiphase boundaries that require doubled, quadrupled, and octupled supercells. We denote these orders as D-SDW, Q-SDW and O-SDW, respectively. Figure 5.4.1 shows

the magnetic arrangements of Fe in the Q-SDW phase. Its unit cell is a $4 \times 1 \times 1$ supercell of the SDW unit cell. Antiphase boundaries occur at the edge and the center of its unit cell along a-axis (antiparallel/alternating Fe spins), the same as in the D-SDW and O-SDW states, the unit cells of which are $2 \times 1 \times 1$ and $8 \times 1 \times 1$ supercells of the SDW unit cell, respectively. The D-SDW phase can also be viewed as a double stripe SDW phase. Based on the results of these states, we consider the effect of antiphase boundary spin fluctuations in explaining various experimental results, which was discussed to some extent by Mazin and Johannes.[350] The antiphase magnetic boundaries we consider here are the simplest possible and yet explain semi-quantitatively many experimental results by assuming that the dynamic average over antiphase magnetic boundaries can be modeled by averaging over several model antiphase boundaries. Our picture presumes that the antiphase boundary within the magnetically ordered state is in some sense a representative spin excitation in the FeAs-based compounds.

The calculations are done using the full-potential linearized-augmented plane-wave (FP-LAPW) + local orbital (lo) method as implemented in the WIEN2K code [51], with both PW91[20] and PBE[23] exchange-correlation (XC) functionals. Several results have been double checked using the full-potential local-orbital (FPLO) code[47] with PW91 XC potential.

5.4.2 LDA VS. GGA

Whereas the local density approximation (LDA) for the exchange-correlation (XC) potential usually obtains internal coordinates accurately, it has been found[291, 314] that LDA makes unusually large errors when predicting the As height $z(\text{As})$ in these compounds in either NM or SDW states. The generalized gradient approximation

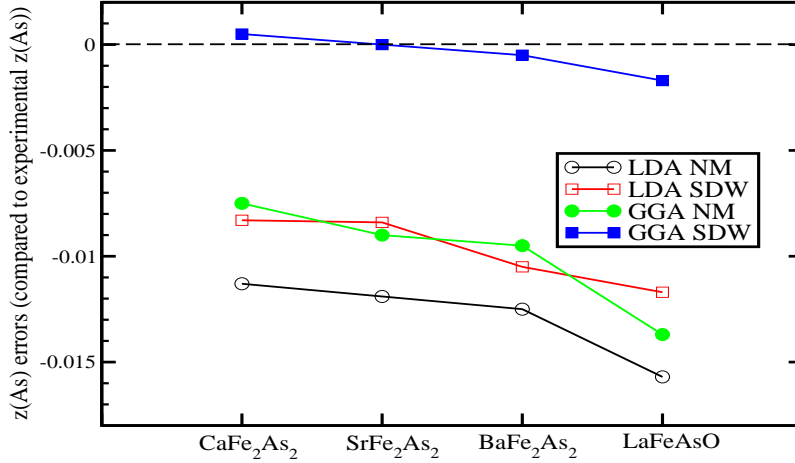


Figure 5.4.2: The calculated errors of $z(\text{As})$ compared to experimental values in the NM and SDW states when using LDA (PW92) and GGA (PBE) XC functionals in CaFe_2As_2 , SrFe_2As_2 , BaFe_2As_2 , and LaFeAsO .

(GGA) makes similar errors in the NM state, however, GGA predicts very good values of $z(\text{As})$ in the SDW phase, as shown in Fig. 5.4.2. Further calculations indicate that GGA done in the SDW phase also predict very good equilibrium lattice constants a , b and c compared to experimental values. (Figure not shown) One drawback of GGA is that it enhances magnetism[314, 291] in these compounds over the LDA prediction, which is already too large compared to its observed value. For example, using experimental structural parameters, GGA (PBE) gives a Fe spin magnetic moment larger than LDA (PW91) by $0.3 \mu_B$ in the SDW state, and more than $0.6 \mu_B$ in the D-SDW state. The magnetic moment changes the charge density, roughly in proportion to the moment. For this reason, we have used Wien2K with PW91 (LDA) XC functional with its more reasonable moments to calculate the EFG and hyperfine field using experimental structural parameters. We note that PBE and PW91 produce about the same EFG in the NM state.

5.4.3 The Magnetic Moment and Hyperfine Field of Iron

In the various antiphase boundary SDW states, the Fe atoms can assume two different characters: high-spin A site away from the antiphase boundaries and low-spin B site at the antiphase boundaries, as shown in Fig. 5.4.1. The Fe atoms with the same site (A or B) in these states have about the same magnetic moment and hyperfine field. For example, in BaFe₂As₂ in the static Q-SDW state, the spin magnetic moment and hyperfine field for Fe at A site are 1.59 μ_B and 12.6 T, and for Fe at B site are 0.83 μ_B and 6.2 T. In the O-SDW state, the spin magnetic moments and hyperfine fields for the three (slightly different) A sites are 1.59, 1.60, 1.67 μ_B and 12.6, 13.5, 1.37 T, respectively, and are 0.83 μ_B and 6.1 T for Fe at B site.

As mentioned above, there are significant differences of the ordered magnetic moment of Fe in the SDW state between calculated values and values observed in neutron scattering (diffraction) experiments and/or Mössbauer experiments. Table 5.11 shows Fe spin magnetic moment and hyperfine field in the SDW and static D-SDW state calculated by FPLO7 and Wien2K using PW91 XC functional.

5.4.4 The Energy Differences

Since Fe atoms in all these antiphase boundary SDW states have basically two spin states (high-spin state at A sites and low-spin state at B sites), in a local moment picture one might expect that energy differences could be related to just the two corresponding energies. From our comparison of energies we have found that this picture gives a useful account of the energetic differences.

The SDW and the D-SDW state are the simple cells in this regard. The former doesn't have any low spin Fe and the latter doesn't have any high spin Fe, so these two define the high spin (low energy) and low spin (high energy) "states" of the Fe

Table 5.11: The experimental magnetic moment of Fe m_{Fe} (in unit of μ_B) and the hyperfine field B_{hf} (in unit of Tesla) for Fe, and values calculated in the SDW and D-SDW ordered phases, using Wien2K with PW91 for the MFe_2As_2 (M =Ba, Sr, Ca), LaFeAsO and SrFeAsF compounds. The experimental values are in all cases much closer to the D-SDW values (with its maximally dense antiphase boundaries) than to the SDW values. [281, 340, 337, 335, 336, 343, 344, 345] For the Fe magnetic moment, results from both FPLO (denoted as FP) and Wien2k(denoted as WK) are given. Because these methods (and other methods) differ somewhat in their assignment of the moment to an Fe atom, the difference gives some indication of how strictly a value should be presumed.

compound	exp		SDW			D-SDW		
	m_{Fe}	B_{hf}	m_{Fe}		B_{hf}	m_{Fe}		B_{hf}
			FP	WK	WK	FP	WK	WK
BaFe ₂ As ₂	0.8	5.5	1.78	1.65	13.6	0.90	0.80	5.4
SrFe ₂ As ₂	0.94	8.9	1.80	1.68	13.9	0.98	0.91	6.1
CaFe ₂ As ₂	0.8	—	1.63	1.53	12.4	0.77	0.71	4.7
LaFeAsO	0.36	—	1.87	1.77	14.9	0.50	0.48	3.6
SrFeAsF	—	4.8	—	1.66	14.5	—	0.32	2.3

atom. Table 5.12 shows the total energies per Fe (in meV) of the magnetic phases compared to the non-magnetic stater, for BaFe₂As₂, SrFe₂As₂, CaFe₂As₂, LaFeAsO and SrFeAsF. The high spin and low spin energies vary from system to system. The energy of the Q-SDW state has also been calculated, and it can be compared with the average of high spin and low spin moment energies (last column in Table 5.12). The reasonable agreement indicates that corrections beyond this simple picture are minor.

The energy cost to create an antiphase boundary is (roughly) simply the cost of two extra low spin Fe atoms versus the high spin that would result without the antiphase boundary. This difference is found to vary by over a factor of two, in the range of 40-90 meV per Fe for this set of five compounds. The reason for the variation is not apparent; for example, it is not directly proportional to the Fe moment (or its square).

Table 5.12: Calculated total energies (meV/Fe) compared to NM state of the various SDW states (SDW, D-SDW, Q-SDW) in the $M\text{Fe}_2\text{As}_2$ ($M=\text{Ba}, \text{Sr}, \text{Ca}$), LaFeAsO and SrFeAsF compounds. The energy tabulated in the last column, labeled Q' , is the average of the high spin (SDW) and low spin (D-SDW) energies. illustrating that the energy of the Q-SDW ordered phase follows this average reasonably well. The level of agreement indicates to what degree ‘high spin’ and ‘low spin’ is a reasonable picture of the energetics at an antiphase boundary.

compound	SDW	D	Q	Q'
BaFe_2As_2	-73	-6	-36	-39
SrFe_2As_2	-91	-11	-46	-51
CaFe_2As_2	-66	-8	-33	-37
LaFeAsO	-143	-61	-94	-102
SrFeAsF	-73	0	-40	-37

Analogous calculations were also carried out for the large O-SDW cell for BaFe_2As_2 . As for the other compounds and antiphase supercells, the Fe moments could be characterized by a low spin atom at the boundary and high spin Fe elsewhere. The energy could also be accounted for similarly, analogously to Table 5.12.

5.4.5 The Electric Field Gradient

The EFG at the nucleus of an atom is sensitive to the anisotropy of the electron charge distribution around the atom. A magnitude and/or symmetry change of the EFG implies the local environment around the atom changes, which can be caused by changes in bonding, structure, or magnetic ordering. In BaFe_2As_2 during the simultaneously structure transition from tetragonal to orthorhombic and magnetic order transition from non-magnetic to SDW order at about 135 K, the EFG component V_c along the crystal c-axis drops rapidly by 10% and the asymmetry parameter $\eta = \frac{|V_a - V_b|}{|V_c|}$ jumps from zero to larger than one, indicating the principle axis for the largest component V_{zz} is changed from along c-axis to in the ab plane.[283] The abrupt EFG change reflects a large change in the electron charge distribution around As sites and highly

anisotropic charge distribution in the ab plane. A similar thing happens in CaFe_2As_2 except that the V_c component of CaFe_2As_2 in the non-magnetic state is *five times* that in BaFe_2As_2 , and doubles its value at the structural and magnetic transition at 167 K when it goes to the SDW phase.[284] The different behaviour of the EFG change across the phase transition in BaFe_2As_2 and CaFe_2As_2 may be due to the out-of-plane alkaline-earth atom (Ba and Ca in this case), which influences the charge distribution around As atoms. It also indicates that three dimensionality is more important in $M\text{Fe}_2\text{As}_2$ than in $R\text{FeAsO}$, which is evident in the layer distance of the FeAs layers reflected in the c lattice constant of these compounds. The c lattice constant of CaFe_2As_2 is significantly smaller than BaFe_2As_2 , so that the interlayer interaction of the FeAs layers is stronger in CaFe_2As_2 , therefore the charge distribution in CaFe_2As_2 is more three dimensional like than in BaFe_2As_2 , which can be clearly seen in their Fermi surfaces (not shown).

EFG of As Atoms

The EFG of As can be obtained from the quadrupole frequency in nuclear quadrupolar resonance (NQR) measurement in nuclear magnetic resonance (NMR) experiment. The NQR frequency can be written as

$$\nu_Q = \frac{3eQV_{zz}(1 + \eta^2/3)^{1/2}}{2I(2I - 1)h}, \quad (5.4.1)$$

where Q ($\sim 0.3b$, $b=10^{-24} \text{ cm}^2$) is the ^{75}As quadrupolar moment, V_{zz} is the zz component of As EFG,

$$\eta = \frac{|V_{xx} - V_{yy}|}{|V_{zz}|} \quad (5.4.2)$$

is the asymmetry parameter of the EFG, $I=3/2$ is the ^{75}As nuclear spin, h is the Planck constant. In $\text{LaO}_{0.9}\text{F}_{0.1}\text{FeAs}$, Grafe *et al.*[315] reported $\nu_Q=10.9$ MHz, and $\eta=0.1$, which gives $V_{zz} \sim 3.00 \times 10^{21}$ V/m². (Note: for the value of EFG, the unit 10^{21} V/m² is commonly used, and we will adopt this unit for all EFG values below) The experimental value 3.0 agrees satisfactorily with our result[291] of 2.7 calculated by Wien2K code.

In BaFe_2As_2 and CaFe_2As_2 , NMR experiments suggest the V_c component of the EFGs of As are 0.83 and 3.39 respectively at high temperature in the NM states,[283, 284] while our calculated values are 1.02 and 2.35, respectively. The difference is in the right direction and right order of magnitude though not quantitatively accurate. However, the EFGs calculated in the SDW state don't match experimental observations at all. In BaFe_2As_2 from 135 K down to very low temperature, V_c remains around 0.62 and $\eta = \frac{|V_a - V_b|}{|V_c|}$ changes from 0.9 to 1.2. Our calculated results in the SDW state gives $V_a=1.34$, $V_b=-1.47$, and $V_c=-0.13$, which gives $\eta \approx 20$. The calculated results substantially underestimate V_c and overemphasize the anisotropy in the ab plane.

We now consider whether these discrepancies can be clarified if antiphase boundary is considered. In the static D-SDW, Q-SDW and O-SDW states, the surrounding environment of As sites change. Depending on the magnitudes (high spin or low spin) and directions (parallel or antiparallel) of the spins of their nearest and next nearest neighboring Fe atoms, As atoms generally have three different sites (1, 2, and 3) as shown in Fig. 5.4.1. In the static D-SDW state, As atoms have similar site 1' and 3'. As shown in Table 5.13, the calculated quantities for these states cannot directly explain the experimental observed values neither.

However, they may be understandable if the antiphase boundary is dynamic, i.e.,

Table 5.13: The calculated EFG component V_a , V_b , V_c (in unit of 10^{21} V/m²), the asymmetry parameter η , spin magnetic moment of As (μ_B), hyperfine field at the As nuclei (Tesla) of BaFe₂As₂ in the SDW, D-SDW, Q-SDW and O-SDW states. Experimentally, V_c is around 0.62, η is in the range of 0.9 to 1.2, and the internal field at As site parallel to c axis is about 1.4 T.[283] See text for notation.

state	site	V_a	V_b	V_c	η	B_{hf}
SDW	1	1.21	-1.32	0.11	23.0	0
D-SDW	1'	0.63	0.07	-0.70	0.8	0
	3'	0.66	0.37	-1.03	0.28	2.1
Q-SDW	1	1.17	-1.38	0.21	12.1	0
	2	0.99	-0.72	-0.27	6.33	1.0
	3	0.90	0.51	-1.41	0.28	2.1
O-SDW	1	1.25	-1.44	0.19	14.2	0
	2	0.98	-0.71	-0.27	6.26	1.1
	3	0.87	0.50	-1.37	0.27	2.3

any As atom in a given measurement can change from site 1 to site 2 and/or site 3, when its nearby Fe atoms flip their spin directions. These time fluctuations have been represented by an average over configurations, and we consider briefly what arises from a configuration average over our SDW phase and three short-period ordered cells (having different densities of anti-phase boundaries). In the O-SDW state, for example, if an As samples 25%, 25% and 50% “time” as As sites 1, 2 and 3, respectively during the experimental measurement, then the expectation values are $V_a=0.99$, $V_b=-0.29$, $V_c=-0.71$, $\eta=1.80$, $B_{hf}=1.43$ T. This simple consideration already matches much better with experimental[283] observed $V_c \sim 0.62$, $H_{in}=1.4$ T, except η which is around 1.2. The actual situation could be much more complicated, being an average over all the sites in all the static D-SDW, Q-SDW and O-SDW states, and other more complicated states. Considering the relatively small differences of the EFGs at the same site for Q-SDW and O-SDW order, As sites in other static antiphase boundary SDW states should be able to be classified to site 1, 2 and 3 as in the Q-SDW and O-SDW states.

EFG of Fe Atoms

The EFG of Fe can be obtained from the electric quadrupole splitting parameter derived from Mössbauer measurements. The electric quadrupole splitting parameter can be written as

$$\Delta = \frac{3eQV_{zz}(1 + \eta^2/3)^{1/2}}{2I(2I - 1)}, \quad (5.4.3)$$

which equals $E_\gamma \Delta E_Q / c$, where $Q \sim 0.16b$ is the ^{57}Fe quadrupolar moment, E_γ is the energy of the γ ray emitted by the $^{57}\text{Co}/\text{Rh}$ source, ΔE_Q is the electric quadrupole splitting parameter from Mössbauer data given in the unit of speed, and c is the speed of light in vacuum. By fitting the Mössbauer spectra, one also obtains the isomer shift δ and average hyperfine field B_{hf} .

We consider whether the dynamic antiphase boundary spin fluctuation picture can also clarify the comparison between calculated and observed EFG of Fe. We take SrFe_2As_2 as an example. As shown in Table 5.14, in the NM state, the calculated value $V_Q=0.98$ agrees well with the $V_Q \approx 0.83$ at room temperature. V_Q calculated in the SDW state (0.68) agrees rather well with experimental value about 0.58 at 4.2 K. V_Q calculated in the D-SDW state (0.80) is somewhat larger than that in the SDW state. Regarding EFG, the biggest difference between SDW and D-SDW is the asymmetry parameter—it is 0.61 in the SDW and only 0.11 in the latter. Further experiments are required to clarify this difference.

5.4.6 Summary

Experiments generally indicate that an itinerant magnetic moment, magnetic (SDW) instability, and spin fluctuations are common features of the Fe-based superconductors. In this section, we have studied the energetics, charge density distribution

Table 5.14: The calculated EFG component V_a , V_b , V_c (in unit of 10^{21} V/m²), the asymmetry parameter $\eta=|V_{xx}-V_{yy}|/|V_{zz}|$ (here $|V_{zz}| > |V_{xx}|$ and $|V_{yy}|$), $V_Q=|V_{zz}|/(1+\eta^2/3)^{1/2}$ of Fe in SrFe₂As₂ in the NM, SDW, D-SDW, Q-SDW and O-SDW states. Experimentally, V_Q is around 0.83 at room temperature in the non-magnetic state, and it is about 0.58 at 4.2 K.[344]

state	site	V_a	V_b	V_c	η	V_Q
NM	0	-0.49	-0.49	0.98	0	0.98
SDW	A	-0.58	-0.14	0.72	0.61	0.68
D-SDW	B	-0.30	-0.51	0.81	0.26	0.80
Q-SDW	A	-0.63	-0.06	0.69	0.83	0.62
	B	-0.56	-0.49	1.05	0.07	1.05

(through calculation of the electric field gradients, hyperfine fields and magnetic moments) for ordered supercells with varying densities of antiphase magnetic boundaries, namely the SDW, D-SDW, Q-SDW and (for very limited cases) O-SDW phases. Supposing dynamic magnetic antiphase boundaries are present, and that the spectroscopic experiments average over them, we can begin to clarify several seemingly contradictory experimental and computational results.

Our calculations tend to support the idea that antiphase boundary magnetic configurations can be important in understanding data. The fact that the decrease in moment is confined to the antiphase boundary Fe atom does not mean that a local moment picture is appropriate; in fact, exactly this same type of local spin density calculations provide a description of magnetic interaction that is at odds with a local moment picture.[338] The calculated energy cost to create an antiphase boundary is however rather high for the cases we have considered, and this value would seem to restrict formation of antiphase boundaries at temperatures of interest. Calculations that treat actual disorder, and dynamics as well, would be very helpful in furthering understanding in this area.

5.4.7 Acknowledgments

This work was supported by DOE under Grant No. DE-FG02-04ER46111. I also acknowledge support from the France Berkeley Fund that enabled the initiation of this project.

5.5 Wannier Functions of Fe 3d Orbitals

We have constructed real-space Wannier functions of Fe 3d orbitals in both NM and Q_M AFM phases of these iron pnictide compounds using the FPLO8 code[47] with LDA XC functional[20] (PW92) and the same experimental lattice constants and internal atomic coordinates for the compounds LaFeAsO, LaFePO, CaFeAsF, SrFeAsF, BaFe₂As₂, SrFe₂As₂, and CaFe₂As₂, as used in the previous Section 5.2, 5.3, and 5.4. For the other two hypothetical compounds LaFeNO and LaFeSbO, the lattice constants and internal atomic coordinates are taken from the optimized equilibrium values of first principle calculations presented in Section 5.3, which were done in the Q_M AFM phase using GGA (PBE) XC functional[23], since such calculations were proven to predict reasonably good equilibrium lattice constants and internal atomic coordinates in the real iron pnictide compounds compared to experimental values. (see Section 5.3 and 5.4.) The Wannier functions used here are maximally localized atomic orbitals (distinct from the maximally localized Wannier functions proposed by Vanderbilt *et al.*[60, 61]), and preserve the angular momentum symmetry of the corresponding orbital as well as the point group symmetry of the corresponding atomic site.

Since the FeAs layers are the same (differ only by the lattice constants and height of As) in these compounds, we pick LaFeAsO as an example to show the Wannier

functions of Fe $3d$ orbitals and the resulting tight binding bands, which try to fit to the corresponding DFT-LSDA Fe-derived bands, in both NM and stripe AFM phases. The Wannier functions for Fe $3d$ orbitals are constructed in both NM and stripe AFM phases, with the same input parameters. The energy window used is from -1.5 eV and 1.5 eV, with a smearing energy $\Delta E=0.5$ eV. Only the Fe $3d$ orbitals are included in the process, leaving out As $4p$ orbitals. The resulting tight-binding bands fit generally very well with the corresponding DFT-LSDA Fe-derived bands in both NM and stripe AFM phases, except at the top of the Fe $3d$ bands (at about 2 eV), where the Fe $3d$ bands mix more strongly with other bands, as shown in Fig. 5.5.1.

The Wannier functions for each Fe $3d$ orbital are shown in Fig. 5.5.2. In the NM phase, all five Wannier functions are well localized at the Fe site. In the Q_M AFM phase, the Wannier functions for $3d_{yz}$, $3d_{x^2-y^2}$ and $3d_{z^2}$ orbitals are very similar to the corresponding Wannier functions in the NM phase. However, the Wannier functions for $3d_{xz}$ and $3d_{xy}$ orbitals, especially for the d_{xz} orbital, are more delocalized in the Q_M AFM phase, with significant density at its nearest-neighbor As sites. Therefore, the $3d_{xz}$ and $3d_{xy}$ orbitals mix much more strongly with nearest-neighbor As $4p$ orbitals in the Q_M phase than in the NM phase, and give rise to different hopping parameters to the Fe $3d$ orbitals of its neighboring Fe atoms. The change of Wannier functions from NM to Q_M AFM state suggests the Fe $3d_{xz}$ and $3d_{xy}$ orbitals participate actively in bonding with its nearest-neighbor As atoms in the Q_M AFM phase, and may explain the fact that the lattice constants $a < b$ (a is along the aligned spin direction) in the Q_M AFM phase. The resulting hopping parameters with similarities and differences between the NM and Q_M AFM phases and the indications are presented and discussed in the next section.

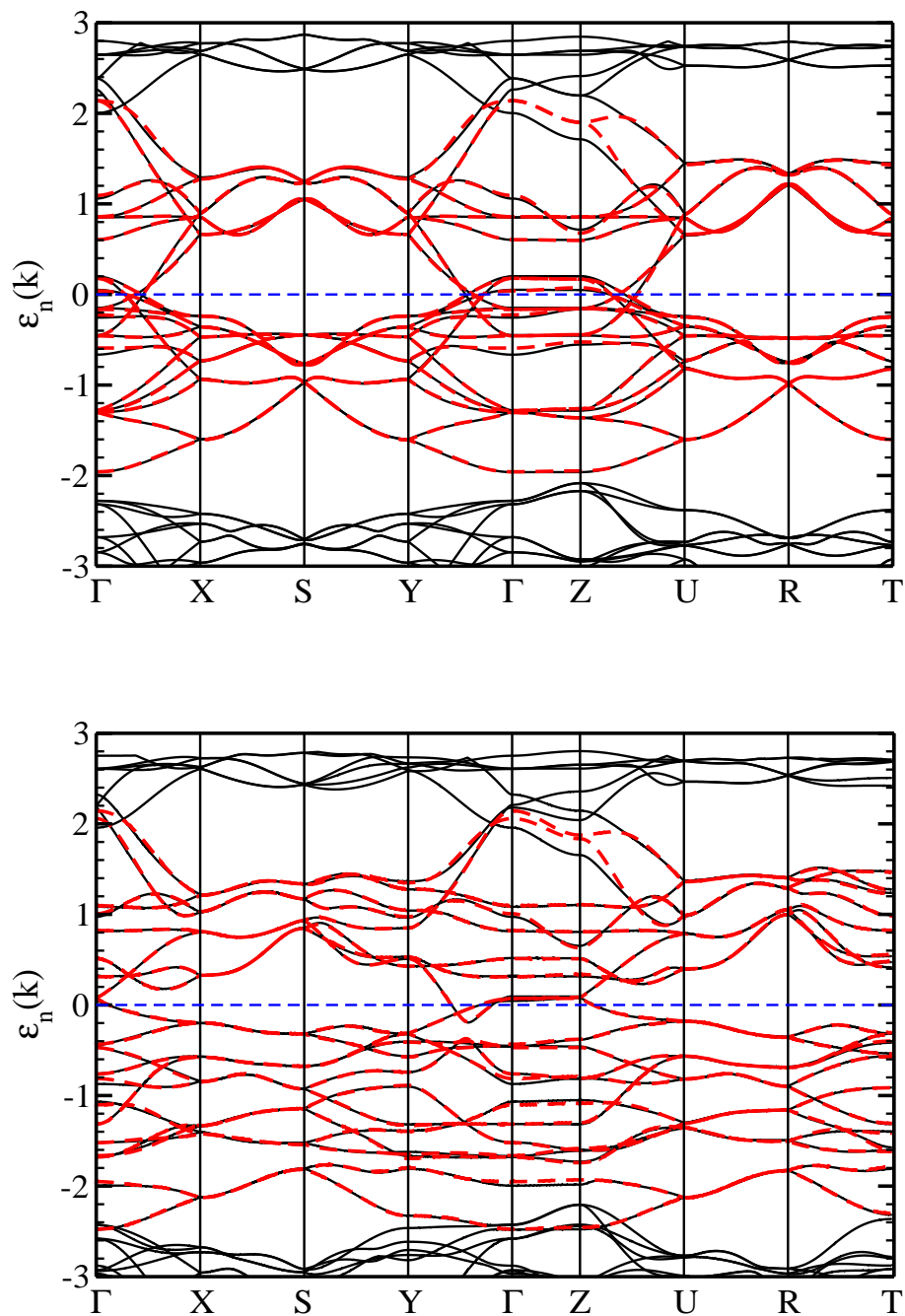


Figure 5.5.1: LaFeAsO band structure in the NM (top panel) and Q_M AFM (bottom panel) phases. Dash (red) lines are the Fe 3d tight-binding bands fitting to the DFT-LSDA Fe-derived bands (solid black), which generally have very good overall agreements.

5.6 Origin of the NM to Stripe-AFM Transition: a Tight Binding Analysis

5.6.1 Background and Motivation

Despite a great deal of work, there are still basic questions remain unresolved. One of them is: what causes the structural transition from tetragonal to orthorhombic in the parent compounds of iron-based superconductors? It is especially challenging in the 1111-compounds (e.g. LaFeAsO), where the structural transition is observed (when lowering the temperature) to occur before the magnetic transition (from non-magnetic to stripe antiferromagnetic, we denote it as Q_M AFM). It is natural to think that the stripe antiferromagnetic ordering of Fe provides the driving “force” of the structural transition because it induces anisotropy. The question then is: why is the structural transition observed first in LaFeAsO experimentally? (See Table III in reference[351] for a summary of the structural transition temperature T_S and stripe antiferromagnetic transition temperature T_N of several iron pnictide compounds.)

Noting that the structural transition and magnetic transition occurs simultaneously in the 122-compounds (e.g. BaFe₂As₂), a possible argument is that the magnetism is there at the structural transition but is greatly suppressed by strong fluctuation so that long range magnetic ordering is difficult to detect experimentally (for example, NMR and neutron scattering experiments whose time resolutions are slow). With a time resolution of 10^{-15} s, photoemission experiments by Bondino *et al.*[352] inferred a dynamic magnetic moment of Fe with magnitude of $1 \mu_B$ in the nonmagnetic phase of CeFeAsO_{0.89}F_{0.11}, which is comparable to the static magnetic moment of Fe in the undoped antiferromagnetic CeFeAsO compound. The fluctuation strength should be much stronger in 1111-compounds than 122-compounds based on

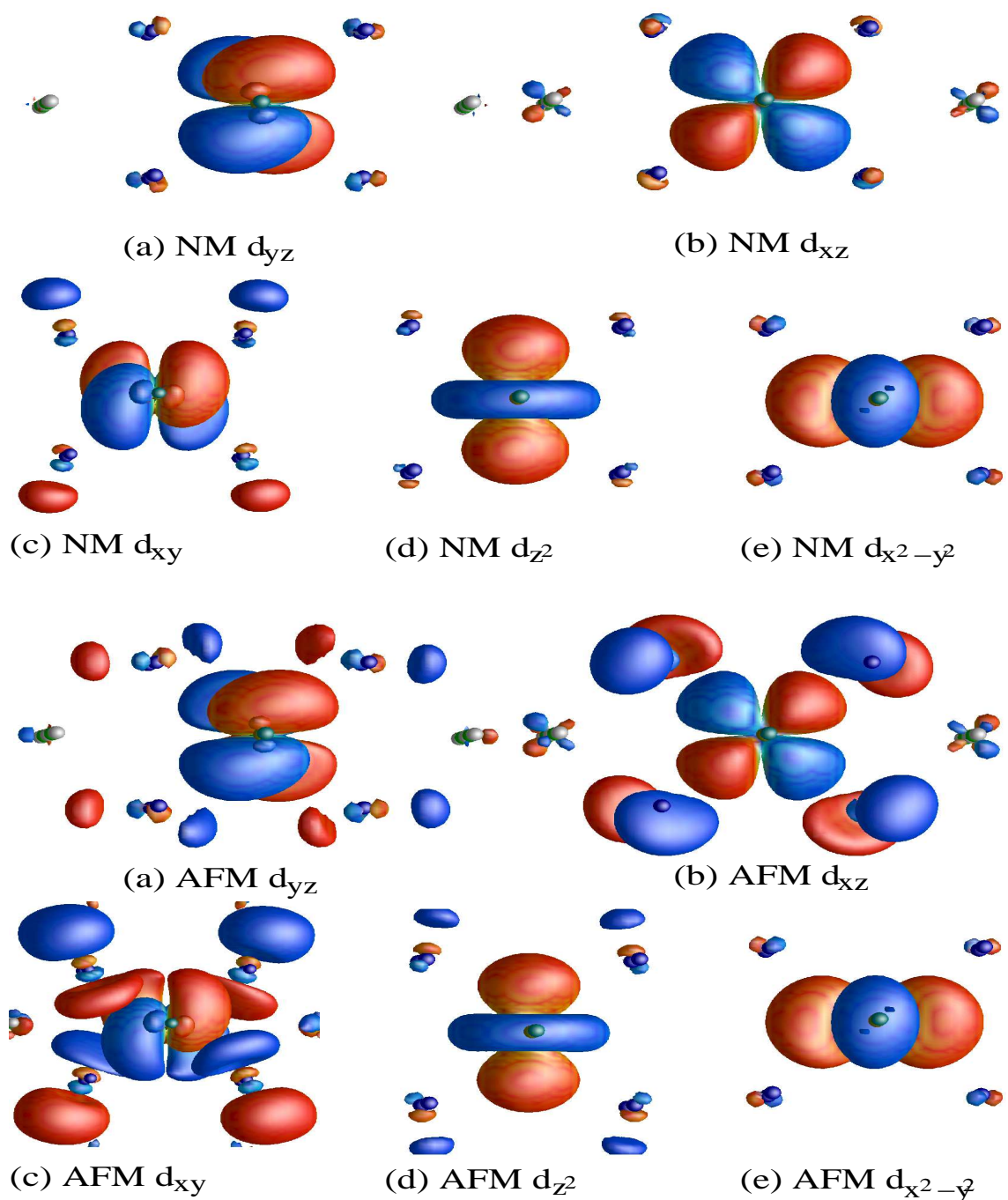


Figure 5.5.2: LaFeAsO Wannier functions of Fe 3d orbitals in the NM (top panel) and Q_M AFM (bottom panel) phases: showing (a) $3d_{yz}$, (b) $3d_{xz}$, (c) $3d_{xy}$, (d) $3d_{z^2}$ and (e) $3d_{x^2-y^2}$. In the NM phase, these Wannier functions are well localized at the Fe site, however, in the Q_M AFM phase, the Wannier functions for $3d_{xy}$ and $3d_{xz}$ orbitals are more delocalized, especially for the d_{xz} orbital, with significant density at the nearest-neighbor As sites. The isosurface is at the same value (density) in each panel.

the fact that the measured Fe ordered magnetic moment in 1111-compounds ($\sim 0.4 \mu_B$) is much less than in 122-compounds ($\sim 0.9 \mu_B$) and they are much smaller than DFT predicted value ($\sim 2 \mu_B$).[351, 285] One possible reason is that the interlayer interaction of the FeAs layers is much stronger in 122-compounds than 1111-compounds because the interlayer distance in 122-compounds ($\sim 5.9\text{-}6.5 \text{ \AA}$) is significantly smaller than 1111-compounds ($\sim 8.2\text{-}9.0 \text{ \AA}$).[351] The interlayer interaction may help to stabilize the ordered Fe magnetic moment by reducing fluctuations.

5.6.2 The Fe $3d_{yz}$ and $3d_{xz}$ Bands in LaFeAsO and LaFePO

Regarding the electronic structures (such as band structures, density of states, total energy, magnetic moment, etc.) in these compounds, a very important issue is the role of pnictide atom. Since the calculated Fe magnetic moment is much larger than its experimentally measured value in these parent compounds, the electronic structure in the Q_M AFM phase cannot be taken too seriously. Some have tried to produce the experimental magnetic moment in their calculations, usually by applying a negative Coulomb interaction U parameter in LDA+ U method.[353, 354] In this section, we compare also a parallel system of LaFeAsO, namely LaFePO. The total energy of LaFePO in the Q_M AFM phase is slightly lower than the nonmagnetic phase by 2 meV/Fe.[291] The calculated Fe magnetic moment in the Q_M AFM phase is $0.52 \mu_B$, which is relatively close to the measured magnetic moment $0.36 \mu_B$ in the Q_M AFM phase of LaFeAsO.[291, 281] The band structures of LaFeAsO and LaFePO in the nonmagnetic and Q_M AFM phase are shown in Fig. 5.6.1 and 5.6.2, with highlighted Fe $3d_{yz}$ and $3d_{xz}$ characters. (We choose x direction along the stripe direction with aligned Fe spins, as shown in Fig. 5.6.3, then y direction is parallel to the anti-aligned Fe spins.) The nonmagnetic band structures of the two compounds are very

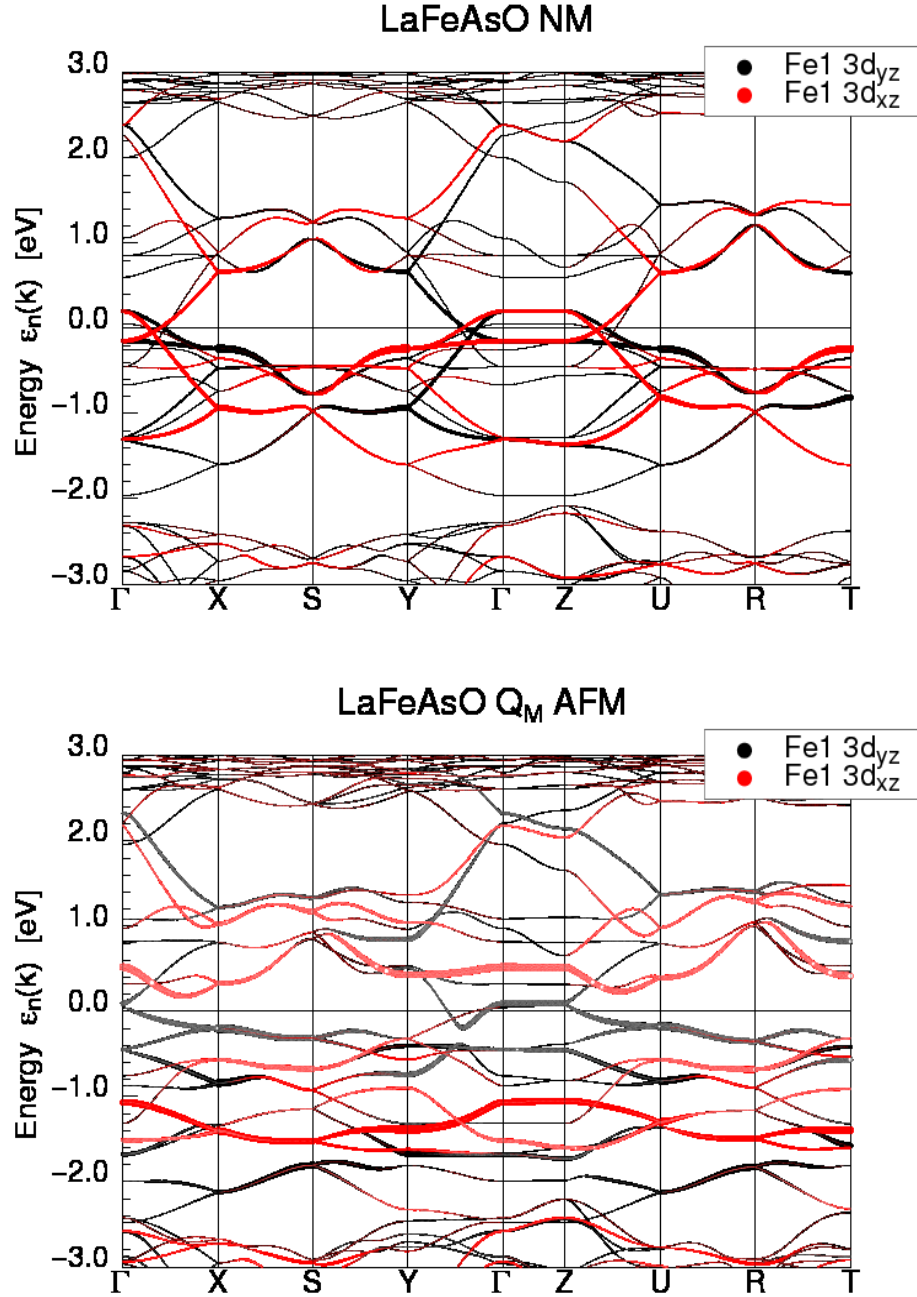


Figure 5.6.1: LaFeAsO band structure with highlighted Fe $3d_{yz}$ and $3d_{xz}$ fatband characters in the NM (top panel) and Q_M AFM (bottom panel) phases. Compared to the NM phase, the Fe $3d_{xz}$ bands near Fermi level in the Q_M AFM phase, especially along $\Gamma - X$ and $\Gamma - Y$ directions, change dramatically due to the formation of the stripe antiferromagnetism with large ordered Fe magnetic moment of $1.9 \mu_B$.

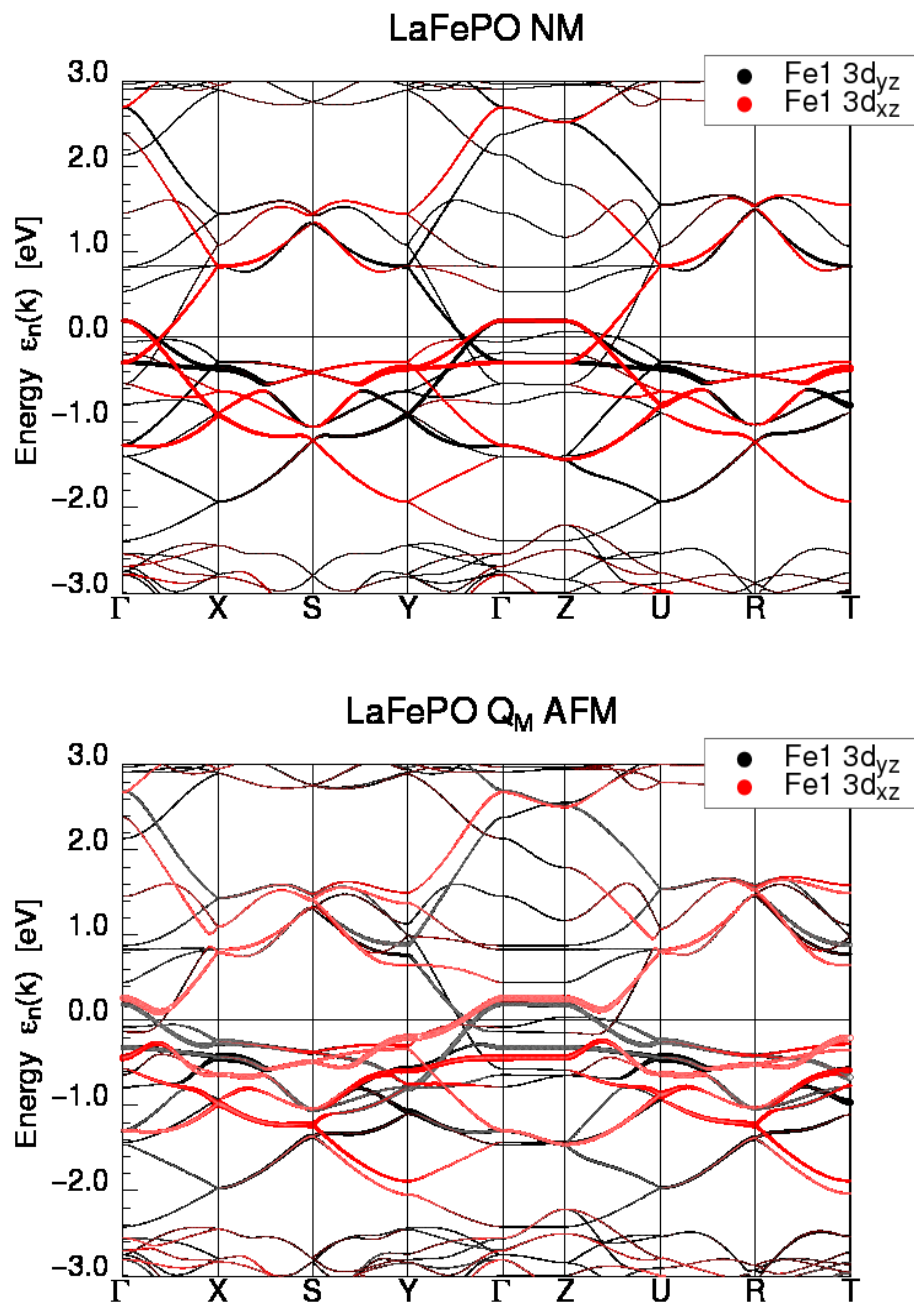


Figure 5.6.2: LaFePO band structure with highlighted Fe $3d_{yz}$ and $3d_{xz}$ fatband characters in the NM (top panel) and Q_M AFM (bottom panel) phase. Compared to LaFeAsO, the Fe $3d_{xz}$ bands near Fermi level in the Q_M AFM phase change less significantly from the NM phase, due to the relatively small ordered Fe magnetic moment of $0.5 \mu_B$.

similar, differing only in some fine details. However, the band structures in the Q_M AFM phase of the two compounds differ substantially, which can only be due to the difference in the Fe magnetic moment (1.9 vs. $0.5 \mu_B$). [285, 291] The similarities and differences indirectly provide a way to study the effect of magnetic fluctuation on these compounds.

Figure 5.6.2 shows the influence of a weak stripe antiferromagnetism ($0.5 \mu_B$) on the nonmagnetic band structure. The overall band structure remains the same except for some bands near the Fermi energy, where the main change is the separating of the Fe $3d_{xz}$ bands away from the Fermi level, which causes disappearance and change of topology of certain pieces of the Fermi surface of the Fe $3d_{xz}$ bands. Note that the Fe $3d_{yz}$ bands change insignificantly. This difference indicates that even a weak stripe antiferromagnetism has a very strong symmetry breaking effect on the $3d_{xz}$ and $3d_{yz}$ bands, which are equivalent in the nonmagnetic state. As a result, even a weak stripe antiferromagnetism induces a large anisotropy, let alone the much stronger (calculated) antiferromagnetism in FeAs-based compounds. (The much bigger anisotropy in the stripe AFM phase in LaFeAsO is evident by comparing Fig. 5.6.1 and 5.6.2.)

5.6.3 Possible Microscopic Orbital Ordering of the Fe $3d_{xz}$ and $3d_{yz}$ Orbitals

Due to the strong influence of stripe antiferromagnetism on the band structure, the orbital ordering of the Fe $3d_{xz}$ and $3d_{yz}$ electrons bears further consideration. Figure 5.6.3 shows two possible orbital orderings, both of which give rise to the Q_M AFM structure. t_{xy} denotes the hopping parameter of the $d_{xz} - d_{xz}$ hopping in the y

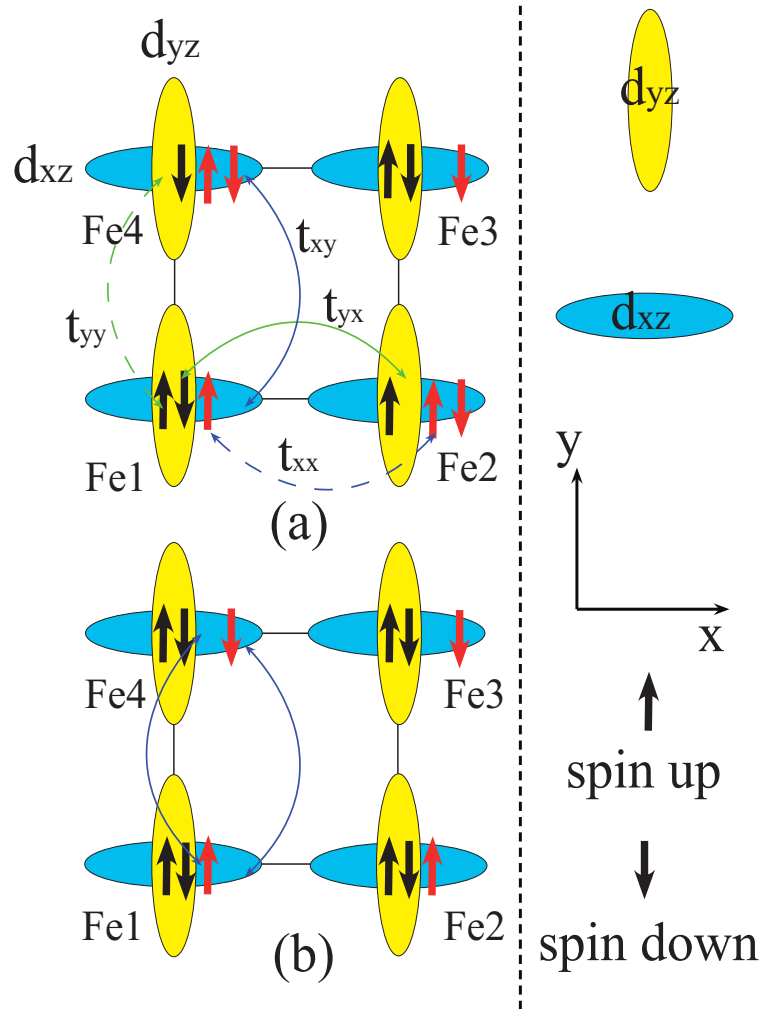


Figure 5.6.3: Possible orbital orderings of iron in iron-pnictides. Left panel: Both (a) and (b) form the Q_M AFM ordering. However, (a) is favored because it gains more kinetic energy from nearest-neighbor hoppings according to second-order perturbation theory (see text). Right panel (from top to bottom) shows the simplified symbols for Fe $3d_{yz}$ and $3d_{xz}$ orbitals, the chosen x and y directions, up arrows for spin up electrons and down arrows for spin down electrons, where black arrows for $3d_{yz}$ orbital and red arrows for $3d_{xz}$ orbital.

direction, and t_{yx} the $d_{yz} - d_{yz}$ hopping in the x direction. In the nonmagnetic case,

$$t_{xy} = t_{yx} = t \quad (5.6.1)$$

and they differ by a small amount in the Q_M AFM state. t_{xx} denotes the $d_{xz} - d_{xz}$ hopping in the x direction, and t_{yy} the $d_{yz} - d_{yz}$ hopping in the y direction (see Fig. 5.6.3).

Let U and U' denote the intra-orbital and inter-orbital Coulomb repulsion, and J_H the inter-orbital Hund's exchange. According to second-order perturbation theory, the kinetic energy gain from the $d_{yz} - d_{yz}$ hopping in the x direction (Fig. 5.6.3a) is

$$\Delta E_{yx} = -t_{yx}^2 / (U' - J_H). \quad (5.6.2)$$

A similar kinetic gain of

$$\Delta E_{xy} = -t_{xy}^2 / (U' - J_H) \quad (5.6.3)$$

comes from the $d_{xz} - d_{xz}$ hopping in the y direction (Fig. 5.6.3a). t_{xx} and t_{yy} are much smaller and can be neglected (see Table 5.15). Therefore, the total energy gain from NN hopping of Fig. 5.6.3a is

$$\Delta E(a) = \Delta E_{xy} + \Delta E_{yx} = -2t^2 / (U' - J_H), \quad (5.6.4)$$

while it is

$$\Delta E(b) = -2t^2 / U \quad (5.6.5)$$

for Fig. 5.6.3b. Because U is larger than $U' - J_H$, the orbital ordering in Fig. 5.6.3a is favored over Fig. 5.6.3b, by kinetic fluctuations. This result is in contrast to that

of Lee *et al.*[355] who didn't consider the effect of t_{yx} .

Table 5.15: The hopping parameters (in eV) of LaFeAsO in the nonmagnetic and Q_M AFM state. The onsite energies (in eV) of the d_{z^2} , $d_{x^2-y^2}$, d_{yz} , d_{xz} , and d_{xy} in the NM and Q_M AFM (both spin up and spin down) are (-0.11, -0.27, 0.02, 0.02, 0.18), (-0.95, -1.14, -0.67, -0.70, -0.50), (0.18, 0.07, 0.23, 0.21, 0.40), respectively.

Fe1		yz			xz		
		NM	Q_M up	Q_M dn	NM	Q_M up	Q_M dn
Fe2	z^2	-0.12	-0.16	-0.08	0	0	0
	$x^2 - y^2$	0.34	0.42	0.28	0	0	0
	yz	-0.33	-0.42	-0.29	0	0	0
	xz	0	0	0	-0.06	-0.29	0.09
	xy	0	0	0	-0.22	-0.21	-0.20
Fe4	z^2	0	0	0	-0.12	-0.11	-0.15
	$x^2 - y^2$	0	0	0	-0.34	-0.39	-0.34
	yz	-0.06	-0.09	-0.09	0	0	0
	xz	0	0	0	-0.33	-0.35	-0.35
	xy	-0.22	-0.20	-0.27	0	0	0
Fe3	z^2	-0.10	-0.10	-0.11	-0.10	-0.12	-0.10
	$x^2 - y^2$	0.10	0.09	-0.10	-0.10	-0.09	-0.09
	yz	0.22	0.23	0.24	0.08	0.12	0.08
	xz	0.08	0.08	0.12	0.22	0.24	0.24
	xy	0.01	0	-0.01	0.01	-0.03	0.02

5.6.4 Tight Binding Hopping Parameters and Discussions

Using these Wannier functions as the basis of the local orbitals in the tight binding method as discussed in Section 5.5, the hopping parameters are then obtained from matrix elements of the Wannier Hamiltonian from the FPLO8 code. The corresponding band structures of LaFeAsO and LaFePO are already shown in Fig. 5.6.1 and Fig. 5.6.2 and the resulting tight binding bands (not shown) fit very well the corresponding DFT-LSDA Fe-derived bands in both NM and stripe AFM phases. Table 5.15 shows the hopping parameters of the Fe1 $3d_{yz}$ and $3d_{xz}$ orbitals to all the $3d$ orbitals of its nearest neighbor Fe2 and Fe4 atoms and next nearest neighbor Fe3

atom in LaFeAsO compound. (See Fig. 5.6.3 for the definition of each Fe atom.) The hopping parameters reported here are very similar to the corresponding hopping parameters reported by Lee *et al.*[355] and Haule *et al.*[356], but are not directly comparable to those reported by Cao *et al.*[300] who mainly considered the hoppings from As $4p$ orbitals to Fe $3d$ orbitals and to its nearest neighbor As $4p$ orbitals. As shown in Table 5.15, in the NM phase, $t_{xy} = t_{yx} \gg t_{xx} = t_{yy}$, which suggests that the hopping (through As atoms) of $d_{xz} - d_{xz}$ ($d_{yz} - d_{yz}$) in the y (x) direction of the electrons in Fe $3d_{xz}$ ($3d_{yz}$) orbital is favored over the x (y) direction. The hopping process for Fe $3d_{xz}$ ($3d_{yz}$) electrons is anisotropic. Global tetragonal symmetry is retained because the Fe $3d_{xz}$ and $3d_{yz}$ electrons hop in different directions, which enforces the equivalence of the x and y directions.

In the Q_M AFM phase, the corresponding hopping parameters (both spin up and spin down) are either the same or very close to the NM value, except for one case. The special one is the $d_{xz} - d_{xz}$ hopping in the x direction of a majority-spin electron, whose absolute value increases significantly from the NM case (from -0.06 to -0.29, see the highlighted numbers in Table 5.15). This opens an extra hopping channel in addition to the original $d_{xz} - d_{xz}$ hopping in the y direction. In the NM state, the electrons in the d_{xz} or d_{yz} orbitals can only hop in one direction (in the sense that the hopping parameters in other directions are relatively small). The dramatic change of the $3d_{xz}$ bands near Fermi level from NM to Q_M AFM can be traced to this difference.

The transition to the Q_M AFM state is understandable because it provides an extra kinetic energy gain of

$$\Delta E_{xx} = -t_{xx}^2 / (U' - J_H) \quad (5.6.6)$$

Table 5.16: The hopping parameters (in eV) of LaFePO in the nonmagnetic and Q_M AFM state. The onsite energies (in eV) of the d_{z^2} , $d_{x^2-y^2}$, d_{yz} , d_{xz} , and d_{xy} in the NM and Q_M AFM (both spin up and spin down) are $(-0.17, -0.27, -0.04, -0.04, 0.23)$, $(-0.35, -0.44, -0.19, -0.21, 0.13)$, $(-0.04, -0.14, 0.07, 0.07, 0.30)$, respectively.

Fe1		yz			xz		
		NM	Q_M up	Q_M dn	NM	Q_M up	Q_M dn
Fe2	z^2	-0.06	-0.07	-0.05	0	0	0
	$x^2 - y^2$	0.42	0.44	0.41	0	0	0
	yz	-0.37	-0.37	-0.34	0	0	0
	xz	0	0	0	-0.09	-0.15	-0.03
	xy	0	0	0	-0.23	-0.23	-0.23
Fe4	z^2	0	0	0	-0.06	-0.06	-0.06
	$x^2 - y^2$	0	0	0	-0.42	-0.43	-0.42
	yz	-0.09	-0.09	-0.09	0	0	0
	xz	0	0	0	-0.36	-0.36	-0.36
	xy	-0.23	-0.22	-0.24	0	0	0
Fe3	z^2	-0.09	-0.08	-0.08	-0.09	-0.09	-0.08
	$x^2 - y^2$	-0.13	0.13	-0.13	-0.13	-0.12	-0.13
	yz	0.25	0.25	0.25	0.09	0.10	0.09
	xz	0.09	0.08	0.10	0.25	0.25	0.25
	xy	-0.04	-0.05	-0.04	-0.04	-0.05	-0.04

from the hopping process of $d_{xz} - d_{xz}$ hopping in the x direction, which is comparable with ΔE_{xy} . (Note that ΔE_{xx} is negligible in the NM state.) The anisotropy arises because the majority-spin electron in the $3d_{xz}$ orbital can hop in both directions, while others can only hop in one direction. The anisotropy would favor the structural transition such that the lattice constant along the aligned-spin direction (x direction in this section) becomes shorter than the other direction (y direction in this section, thus $a < b$), due to this additional hopping channel.

The strength of this additional hopping channel reflects the ordered Fe magnetic moment in the Q_M AFM state, which is evident by comparing the case of LaFeAsO and LaFePO (see Table 5.15 and 5.16). The iron atom in the Q_M AFM state in the former compound has a large ordered magnetic moment of $1.9 \mu_B$ while in the latter

compound it is very weak, only $0.5 \mu_B$, in DFT-LSDA calculations. The difference in the ordered Fe magnetic moment is consistent with the change of hopping parameter of $d_{xz} - d_{zx}$ in the x direction of the spin up electron from the NM to the Q_M AFM state, as shown in Table 5.15 and Table 5.16. In LaFeAsO, it changes from -0.06 to -0.29 while in LaFePO, it changes only from -0.09 to -0.15. Note that, as pictured in Fig. 5.6.3a, the $3d_{xz}$ spin up electron of Fe1 atom cannot hop in the x direction due to the Pauli principle. In order to take advantage of this extra kinetic energy gain of ΔE_{xx} , the spin up occupation number of $3d_{xz}$ orbital should not be one but instead must fluctuate, which results in a reduced magnetic moment and is possibly one mechanism of orbital fluctuation.

Table 5.17: The hopping parameters t_{xy} , t_{yx} , t_{xx} and t_{yy} in the NM and Q_M AFM phases of a few iron-pnictides.

compound (mag. mom.)		yz			xz		
		NM	Q_M		NM	Q_M	
			up	dn		up	dn
LaFeAsO ($1.90 \mu_B$)	t_{yx}/t_{xy}	-0.33	-0.42	-0.29	-0.33	-0.35	-0.35
	t_{yy}/t_{xx}	-0.06	-0.09	-0.09	-0.06	-0.29	0.09
LaFePO ($0.52 \mu_B$)	t_{yx}/t_{xy}	-0.37	-0.37	-0.34	-0.36	-0.36	-0.36
	t_{yy}/t_{xx}	-0.09	-0.09	-0.09	-0.09	-0.15	-0.03
LaFeNO ($1.86 \mu_B$)	t_{yx}/t_{xy}	-0.30	-0.33	-0.27	-0.30	-0.31	-0.31
	t_{yy}/t_{xx}	-0.03	-0.05	-0.05	-0.03	-0.14	0.06
LaFeSbO ($2.45 \mu_B$)	t_{yx}/t_{xy}	-0.26	-0.39	-0.21	-0.26	-0.28	-0.27
	t_{yy}/t_{xx}	-0.07	-0.11	-0.11	-0.07	-0.38	0.16
CaFeAsF ($1.75 \mu_B$)	t_{yx}/t_{xy}	-0.36	-0.43	-0.34	-0.36	-0.37	-0.37
	t_{yy}/t_{xx}	-0.06	-0.08	-0.08	-0.06	-0.27	0.08
SrFeAsF ($1.96 \mu_B$)	t_{yx}/t_{xy}	-0.35	-0.43	-0.31	-0.35	-0.37	-0.37
	t_{yy}/t_{xx}	-0.08	-0.10	-0.10	-0.08	-0.31	0.08
BaFe ₂ As ₂ ($1.88 \mu_B$)	t_{yx}/t_{xy}	-0.32	-0.40	-0.29	-0.32	-0.34	-0.34
	t_{yy}/t_{xx}	-0.08	-0.10	-0.10	-0.08	-0.28	0.07
SrFe ₂ As ₂ ($1.78 \mu_B$)	t_{yx}/t_{xy}	-0.33	-0.40	-0.31	-0.33	-0.34	-0.35
	t_{yy}/t_{xx}	-0.08	-0.10	-0.10	-0.08	-0.28	0.06
CaFe ₂ As ₂ ($1.67 \mu_B$)	t_{yx}/t_{xy}	-0.33	-0.38	-0.32	-0.33	-0.35	-0.35
	t_{yy}/t_{xx}	-0.08	-0.10	-0.10	-0.08	-0.28	0.06

Further Observations

Similar hopping parameters compared to LaFeAsO have been obtained for the CaFeAsF, SrFeAsF, and $M\text{Fe}_2\text{As}_2$ ($M=\text{Ba}, \text{Sr}, \text{Ca}$) compounds, (which have similar FeAs layers), as shown in Table 5.17. However, replacing As in LaFeAsO with other pnictides (N, P and Sb) results in similar t_{xy} , t_{yx} and t_{yy} but different t_{xx} . Compared to LaFeAsO, the t_{xx} for the majority spin electron in the Q_M AFM phase is reduced for LaOFeN and LaOFeP, but enhanced in LaFeSbO. The importance of the pnictide for the formation of the Q_M AFM phase is evident.

Another important factor is the interlayer hoppings. The interlayer distance of FeAs layers in 1111-compounds is in the range of 8.2 -9.0 Å and it is much smaller in 122-compounds, ranging from 5.9 Å to 6.5 Å. The interlayer hopping parameters of Fe 3d electrons in the z direction are negligible in 1111-compounds but become substantial for certain hoppings in 122-compounds, especially in CaFe_2As_2 , whose interlayer distance of FeAs layers is only 5.9 Å. For example, certain interlayer hopping parameters are as large as 0.15 eV for d_{xy} and d_{z^2} orbitals, and 0.07 eV for d_{yz} , d_{xz} and $d_{x^2-y^2}$ orbitals, calculated in the Q_M AFM phase for CaFe_2As_2 . The large interlayer hopping parameters in the Fe $3d_{xy}$ orbital couple to the fact that the $3d_{xy}$ orbital are distorted from its symmetric atomic shape to its nearest neighbor As atoms above and below the Fe plane, as shown in Fig. 5.5.2. This distort in the z direction can favor interlayer hoppings, especially when the interlayer distance is small, as in the case of CaFe_2As_2 . For comparison, the interlayer hopping parameters (if not zero) are less than 0.01 eV in LaFeAsO. The increasing hopping of Fe 3d electrons in the z direction increases the interlayer coupling and may inhibit fluctuations and thereby help to stabilize the ordered Fe magnetic moment in the Q_M AFM phase. The k_z dispersion correlates with the experimental observations that

the measured Fe magnetic moments in the Q_M AFM phase are significantly larger in 122-compounds ($\sim 0.9 \mu_B$) than 1111-compounds ($\sim 0.4 \mu_B$).

5.6.5 Summary

In summary, we compare the band structure of LaFeAsO and LaFePO in the NM and Q_M AFM phase and find that the stripe antiferromagnetism affects very differently the Fe $3d_{xz}$ and $3d_{yz}$ bands, even when the stripe antiferromagnetism is weak. We construct a tight-binding representation for Fe $3d$ electrons and calculate the hopping parameters by using Wannier functions. The resulting hopping parameters indicate the electrons in Fe $3d_{xz}$ and $3d_{yz}$ orbitals are anisotropic in the x and y direction in the hopping process to nearest neighbor Fe. The equivalence of the x and y directions is broken when only the majority-spin electron in Fe $3d_{xz}$ (or $3d_{yz}$) orbital can hop in both x and y directions, which forms the stripe antiferromagnetism, and may drive the structural transition to orthorhombic symmetry. The anisotropy in hopping also favors orbital fluctuation which can gain extra kinetic energy from the enhanced hopping process, and in the meantime, reduces the ordered Fe magnetic moment in the Q_M phase. By comparing the hopping parameters of several 1111-compounds and 122-compounds, we find that the pnictide atom is influential in the formation of Q_M AFM phase. Interlayer hoppings of the Fe $3d$ electrons in the z direction may also help to stabilize the Fe magnetic moment in the Q_M AFM phase.

5.6.6 Acknowledgments

I thank Q. Yin and E. R. Ylvisaker for helpful discussions, and K. Koepnik for implementing the calculations of Wannier functions in FPLO code. This work was supported by DOE grant DE-FG02-04ER46111.

Bibliography

- [1] P. Hohenberg and W. Kohn, Phys. Rev. **136**, B864 (1964).
- [2] M. Born and R. Oppenheimer, Annalen der Physik **84**, 457 (1927).
- [3] W. Kohn and L. J. Sham, Phys. Rev. **140**: A1133 (1965).
- [4] D. R. Hartree, Proc. Cam. Phil. Soc. **24**, 89 (1928).
- [5] V. Z. Fock, Z. Phys. **61**, 209 (1930).
- [6] M. Born and K. Huang, *Dynamic Theory of Crystal Lattices*. Oxford: Oxford University Press (1954).
- [7] L. H. Thomas, Proc. Cambridge Phil. Roy. Soc. **23**, 542 (1927).
- [8] E. Fermi, Rend. Accad. Naz. Lincei **6**, 602 (1927).
- [9] P. A. M. Dirac, Proc. Cambridge Phil. Roy. Soc. **26**, 376 (1930).
- [10] E. Teller, Rev. Mod. Phys. **34**, 627 (1962).
- [11] M. Levy, Proc. Nat. Acad. Sci. USA **76**, 6062 (1979).
- [12] R. O. Jones and O. Gunnarsson, Rev. Mod. Phys. **61**, 689 (1989).
- [13] N. D. Mermin, Phys. Rev. **137**, A1441 (1965).

- [14] E. Runge and E. K. U. Gross, Phys. Rev. Lett. **52**, 997 (1984).
- [15] U. von Barth and L. Hedin, J. Phys. C: Solid State Phys. **5**, 1629 (1972).
- [16] D. M. Ceperley and B. J. Alder, Phys. Rev. Lett. **45**, 566 (1980).
- [17] S. H. Vosko, L. Wilk and M. Nusair, Can. J. Phys. **58**, 1200 (1980).
- [18] J. P. Perdew and A. Zunger, Phys. Rev. B **23**, 5048 (1981).
- [19] L. A. Cole and J. P. Perdew, Phys. Rev. A **25**, 1265 (1982).
- [20] J. P. Perdew and Y. Wang, Phys. Rev. B **45**, 13244 (1992).
- [21] A. D. Becke, Phys. Rev. A **38**, 3098 (1988).
- [22] J. P. Perdew, J. A. Chevary, S. H. Vosko, K. A. Jackson, M. R. Pederson, and C. Fiolhais, Phys. Rev. B **46**, 6671 (1992).
- [23] J. P. Perdew, K. Burke, and M. Ernzerhof, Phys. Rev. Lett. **77**, 3865 (1996).
- [24] R. M. Martin, *Electronic Structure - Basic Theory and Practical Methods*, Cambridge University Press (2004).
- [25] A. Svane and O. Gunnarsson, Phys. Rev. Lett. **65**, 1148 (1990).
- [26] S. Massida, M. Posternak and A. Baldereschi, Phys. Rev. B **48**, 5058 (1993).
- [27] L. Hedin, Phys. Rev. **139**, A796 (1965).
- [28] V. I. Anisimov, F. Aryasetiawan and A. I. Lichtenstein, J. Phys. Condens. Matter **9**, 767 (1997).
- [29] J. C. Slater, *Quantum Theory of Atomic Structure*, (McGraw-Hill, New York, 1960), Vol. 1.

- [30] F. M. F. de Groot, J. C. Thole, and G. A. Sawatzky, Phys. Rev. B **42**, 5459 (1990).
- [31] V. I. Anisimov, J. Zaanen and O. K. Andersen, Phys. Rev. B **44**, 943 (1991).
- [32] Czyzyk and G. A. Sawatzky, Phys. Rev. B **49**, 14211 (1994).
- [33] V. I. Anisimov, I. V. Solovyev, M. A. Korotin, M. T. Czyzyk. and G. A. Sawatzky, Phys. Rev. B **48**, 16929 (1993).
- [34] E. R. Ylvisaker, W. E. Pickett and K. Koepernik, Phys. Rev. B **79**, 035103 (2009).
- [35] D. R. Hamann, M. Shlüter, and C. Chiang, Phys. Rev. Lett. **43**, 1494 (1979).
- [36] D. Vanderbilt, Phys. Rev. B **41**, 7892 (1990).
- [37] W. C. Herring, Phys. Rev. **57**, 1169 (1940).
- [38] W. C. Herring and A. G. Hill, Phys. Rev. **58**, 132 (1940).
- [39] F. Herman, Rev. Mod. Phys. **30**, 102 (1958).
- [40] P. E. Blöchl, Phys. Rev. B **50**, 17953 (1994).
- [41] G. Kresse and D. Joubert, Phys. Rev. B **59**, 1758 (1999).
- [42] N. A. W. Holzwarth, G. E. Matthews, A. R. Tackett, and R. B. Dunning, Phys. Rev. B **55**, 2055 (1997).
- [43] <http://www.quantum-espresso.org/>.
- [44] <http://www.abinit.org/>.

- [45] <http://cms.mpi.univie.ac.at/vasp/>.
- [46] J. C. Slater and G. F. Koster, Phys. Rev. **94**, 1498 (1954).
- [47] K. Koepnik and H. Eschrig Phys. Rev. B **59**, 1743 (1999).
- [48] O. K. Anderson, Phys. Rev B **12**, 3060 (1975).
- [49] S. Y. Savrasov, Phys. Rev. B **54**, 16470 (1996); S. Y. Savrasov, D. Y. Savrasov, *ibid* **54** 16487 (1996).
- [50] D.J. Singh, *Plane Waves, Pseudopotentials and the LAPW Method*, Kluwer Academic Publishers, Boston, Dordrecht, London (1994).
- [51] P. Blaha, K. Schwarz, G. K. H. Madsen, D. Kvasnicka and J. Luitz, WIEN2K, (K. Schwarz, Techn. Univ. Wien, Austria, 2001).
- [52] S. Y. Savrasov, Phys. Rev. Lett. **69**, 2819 (1992).
- [53] X. Gonze, D. C. Allan, and M. P. Teter, Phys. Rev. Lett. **68**, 3603 (1992).
- [54] S. Y. Savrasov and D. Y. Savrasov, Phys. Rev. B **54**, 16487 (1996).
- [55] P. B. Allen, Phys. Rev. B **6**, 2577 (1972).
- [56] W. L. McMillan, Phys. Rev. **167**, 331 (1968)
- [57] P. B. Allen and R. C. Dynes, Phys. Rev. B **12**, 905 (1975).
- [58] D. Kasinathan, J. Kuneš, A. Lazicki, H. Rosner, C. S. Yoo, R. T. Scalettar, and W. E. Pickett, Phys. Rev. Lett. **96**, 047004 (2006).
- [59] G. H. Wannier, Phys. Rev. **52**, 191 (1937).

- [60] N. Marzari and D. Vanderbilt, Phys. Rev. B **56**, 12847 (1997).
- [61] I. Souza, N. Marzari, and D. Vanderbilt, Phys. Rev. B **65**, 035109 (2001).
- [62] W. Ku, H. Rosner, W. E. Pickett, and R. T. Scalettar, Phys. Rev. Lett. **89**, 167204 (2002).
- [63] E. R. Ylvisaker and W. E. Pickett, Phys. Rev. B **74**, 075104 (2006).
- [64] Z. P. Yin and W. E. Pickett, Phys. Rev. B **74**, 205106 (2006).
- [65] A. K. McMahan, C. Huscroft, R. T. Scalettar, and E. L. Pollock, J. Computer-Aided Materials Design **5**, 131 (1998); cond-mat/9805064.
- [66] N. C. Cunningham, N. Velisavljevic, and Y. K. Vohra, Phys. Rev. B **71**, 012108 (2005).
- [67] C.-S. Yoo, B. Maddox, and V. Iota, Mater. Res. Soc. Symp. Proc. Vol. **1104** (2008).
- [68] R. Patterson, C. K. Saw, and J. Akella, J. Appl. Phys. **95**, 5443 (2004).
- [69] D. Errandonea, R. Boehler, and M. Ross, Phys. Rev. Lett. **85**, 3444 (2000).
- [70] B. Johansson, Philos. Mag. **30**, 30 (1974).
- [71] J. W. Allen and R. M. Martin, Phys. Rev. Lett. **49**, 1106 (1982).
- [72] M. Lavagna, C. Lacroix, and M. Cyrot, Phys. Lett. **90A**, 210 (1982); J. Phys. F **13**, 1008 (1983).
- [73] H. Hua, Y. K. Vohra, J. Akella, S. T. Weir, R. Ahuja, and B. Johansson, Rev. High Pressure Sci. Technol. **7**, 233 (1988).

- [74] J. Akella, G. S. Smith, and A. P. Jephcoat, *J. Phys. Chem. Solids* **49**, 573 (1988).
- [75] B. R. Maddox, A. Lazicki, C. S. Yoo, V. Iota, M. Chen, A. K. McMahan, M. Y. Hu, P. Chow, R. T. Scalettar, and W. E. Pickett, *Phys. Rev. Lett.* **96**, 256403 (2006).
- [76] J. W. Allen and R. M. Martin, *Phys. Rev. Lett.* **49**, 1106 (1982).
- [77] M. Lavanga, C. Lacroix, and M. Cyrot, *Phys. Lett.* **90A**, 210 (1982).
- [78] K. Held, A. K. McMahan, and R. T. Scalettar, *Phys. Rev. Lett.* **87**, 276404 (2001).
- [79] A. K. McMahan, *Phys. Rev. B* **72**, 115125 (2005).
- [80] A. Svane, W. M. Temmerman, Z. Szotek, J. Laegsgaard, and H. Winter, *Intl. J. Quant. Chem.* **77**, 799 (2000).
- [81] D. Kasinathan, J. Kunes, K. Koepernik, C. V. Diaconu, R. L. Martin, I. Prodan, C. E. Scuseria, N. Spaldin, L. Petit, T. C. Schulthess, and W. E. Pickett, *cond-mat/0605430*.
- [82] B. Johansson and A. Rosengren, *Phys. Rev. B* **11**, 2836 (1975).
- [83] L. B. Robinson, F. Milstein, and A. Jayaraman, *Phys. Rev.* **134**, A187 (1964).
- [84] D. D. Jackson, C. Aracne-Ruddle, V. Malba, S. T. Weir, S. A. Catledge, and Y. K. Vohra, *Rev. Sci. Instr.* **74**, 2467 (2003).
- [85] D. D. Jackson, V. Malba, S. T. Weir, P. A. Baker, and Y. K. Vohra, *Phys. Rev. B* **71**, 184416 (2005).
- [86] P. Kurz, B. Bihlmayer, and S. Blügel, *J. Phys.: Condens. Matt.* **14**, 6353 (2002).

- [87] A. B. Shick, A. I. Liechtenstein, and W. E. Pickett, Phys. Rev. B **60**, 10763 (1999).
- [88] M. D. Johannes and W. E. Pickett, Phys. Rev. B **72**, 195116 (2005).
- [89] A. B. Shick, W. E. Pickett, and C. S. Fadley, J. Appl. Phys. **87**, 5878 (2000).
- [90] O. Gunnarsson, E. Koch, and R. M. Martin, Phys. Rev. B **54**, R11026 (1996).
- [91] O. Gunnarsson, E. Koch, and R. M. Martin, Phys. Rev. B **56**, 1146 (1997).
- [92] E. Koch, O. Gunnarsson, and R. M. Martin, Comp. Phys. Commun. **127**, 137 (2000).
- [93] Z. P. Yin and W. E. Pickett, Phys. Rev. B **77**, 035135 (2008).
- [94] H. Nagamatsu, N. Hakagawa, T. Muranaka, Y. Zenitani and J. Akimitsu, Nature (London) **410**, 63 (2001).
- [95] J. An and W. E. Pickett, Phys. Rev. Lett. **86**, 4366 (2001).
- [96] W. N. Lipscomb, J. Chem. Phys. **33**, 275 (1960).
- [97] W. N. Lipscomb, J. Less-Common Metals **82**, 1 (1981).
- [98] Y. Imai, M. Mukaida, M. Ueda, and A. Watanabe, Intermetallics **9**, 721 (2001).
- [99] M. Takeda, T. Fukuda, F. Domingo, and T. Miura, J. Solid State Chem. **177**, 471 (2004).
- [100] C.-H. Chen, T. Aizawa, N. Iyi, A. Sato, and S. Otani, J. Alloys Compnds. **366**, L6 (2004).
- [101] L. W. Rupp Jr. and P. H. Schmidt, J. Phys. Chem. Solids **30**, 1059 (1969).

- [102] S. Muranaka and S. Kawai, *J. Crystal Growth* **26**, 165 (1974).
- [103] J. L. Gavilano, B. Ambrosini, H. R. Ott, D. P. Young, and Z. Fisk, *Physica B* **281&282**, 428 (2000).
- [104] J. L. Gavilano, B. Ambrosini, H. R. Ott, D. P. Young, and Z. Fisk, *Physica B* **284-288**, 1359 (2000).
- [105] K. Schmitt, C. Stückl, H. Ripplinger, and B. Albert, *Solid State Science* **3**, 321 (2001).
- [106] S. Otani, T. Aizawa, and Y. Yajima, *J. Crystal Growth* **234**, 431 (2002).
- [107] C.-H. Chen, Y. Xuan, and S. Otani, *J. Alloys Compds.* 350, L4 (2003).
- [108] P. Teredesai, D. V. S. Muthu, N. Chandrabhas, S. Meenakshi, V. Vijayakumar, P. Modak, R. S. Rao, B. K. Godwal, S. K. Sikka, and A. K. Sood, *Solid State Commun.* **129**, 91 (2004).
- [109] S.-K. Mo, G.-H. Gweon, J. D. Denlinger, H.-D. Kim, J. W. Allen, C. G. Olson, H. Höchst, J. L. Sarrao, and Z. Fisk, *Physica B* **312-313**, 668 (2002).
- [110] P. G. Perkins and A. V. J. Sweeney, *J. Less-Common Metals* **47**, 165 (1976).
- [111] A. Ammar, M. Ménétrier, A. Villesuzanne, S. Matar, B. Chevalier, J. Etourneau, G. Villeneuve, J. Rodriguez-Carvajal, H.-J. Koo, A. I. Smirnov, and M.-H. Whangbo, *Inorg. Chem.* **43**, 4974 (2004).
- [112] Z. Fisk and M. B. Maple, *Solid State Commun.* **39**, 1189 (1981).
- [113] J. Etourneau, *J. Less-Common Metals* **110**, 267 (1985).

- [114] J. Etourneau, J. P. Mercurio, A. Berrada and P. Hagenmuller, *J. Less-Common Metals* **67**, 531 (1979).
- [115] Z. Fisk, A. S. Cooper, P. H. Schmidt and R. N. Castellano, *Mat. Res. Bull.* **7**, 285 (1972).
- [116] B. Jäger, S. Paluch, W. Wolf, P. Herzig, O. J. Zogal, N. Shitsevalova, and Y. Paderno, *J. Alloys Compds.* **383**, 232 (2004).
- [117] S. Otani, Y. Xuan, Y. Yajima, and T. Mori, *J. Alloys and Compunds* **361**, L1 (2003).
- [118] S. Otani, M. M. Korsukova, T. Mitsuhashi, and N. Kieda, *J. Crystal Growth*, **217**, 378 (2000).
- [119] T. Tanaka and Yoshio Ishizawa, *J. Phys. C* **18**, 4933 (1985).
- [120] J. Günster, T. Tanaka, and R. Souda, *Phys. Rev. B* **56**, 15962 (1997).
- [121] K. Kato, I. Kawada, C. Oshima and S. Kawai, *Acta Cryst.* **B30**, 2933 (1974).
- [122] S. V. Meschel and O. J. Kleppa, *J. Alloys Compds.* **226** 243 (1995).
- [123] A. Zalkin and D. H. Templeton, *Acta Cryst.* **6**, 269 (1953).
- [124] A. Zalkin and D. H. Templeton, *J. Chem. Phys.* **18**, 391 (1950).
- [125] P. Salamakha, A. P. Goncalves, O. Sologub, and M. Almeida, *J. Alloys Compds.* **316**, L4 (2001).
- [126] B. J. Mean, K. H. Kang, J. H. Kim, I. N. Hyun, M. Lee, and B. K. Cho, *Physica B* **378-380**, 598 (2006).

- [127] S. Ji, C. Song, K. Koo, K.-B. Lee, Y. J. Park, J.-H. Park, H. J. Shin, J. S. Rhyee, B. H. Oh, and B. K. Cho, *Phys. Rev. Lett.* **91**, 257205 (2003).
- [128] M. T. Garland, J. P. Wiff, J. Bauer, R. Guerin and J.-Y. Saillard, *Solid State Sciences* **5**, 705 (2003).
- [129] K. H. J. Buschow and J. H. N. Creighton, *J. Chem. Phys.* **57**, 3910 (1972).
- [130] S. W. Lovesey, J. F. Rodríguez, J. A. Blanco and P. J. Brown, *Phys. Rev. B* **70**, 172414 (2004).
- [131] J. A. Blanco, P. J. Brown, A. Stunault, K. Katsumata, F. Iga and S. Michimura, *Phys. Rev. B* **73**, 212411 (2006).
- [132] B. J. Mean, K. H. Kang, J. H. Kim, I. N. Hyun, M. Lee, and B. K. Cho, *Physica B* **378-380**, 600 (2006).
- [133] J. C. Gianduzzo, R. Georges, B. Chevalier, J. Etourneau, P. Hagenmuller, G. Will, and W. Schäfer, *J. Less-Common Metals* **82**, 29 (1981).
- [134] F. Elf, W. Schäfer and G. Will, *Solid State Commun.* **40**, 579 (1981).
- [135] Z. Heiba, W. Schäfer, E. Jansen and G. Will, *J. Phys. Chem. Solids* **47**, 651 (1986).
- [136] G. Will, W. Schäfer, F. Pfeiffer and F. Elf, *J. Less-Common Metals* **82**, 349 (1981).
- [137] G. Will, Z. Heiba, W. Schäfer, and E. Jansen, *AIP Conf. Proc.* **140**, 130 (1986).
- [138] D. Okuyama, T. Matsumura, H. Nakao, and Y. Murakami, arXiv: cond-mat/0506304.

- [139] R. Watanuki, H. Mitamura, T. Sakakibara, G. Sato, and K. Suzuki, *Physica B* **378-380**, 594 (2006).
- [140] T. Matsumura, D. Okuyama, H. Nakao, and Y. Murakami, *Photon Factory Activity Report 2004 #24 Part B* (2005).
- [141] E. M. Dudnik, Y. A. Kochierzinsky, Y. B. Paderno, N. Y. Shitsevalova, E. A. Shishkin and I. E. Kir'yakova, *J. Less-Common Metals* **67**, 281 (1979).
- [142] W. Schäfer, G. Will, and K. H. J. Buschow, *J. Magnetism and Magnetic Materials* **3**, 61 (1976).
- [143] R. Watanuki, G. Sato, K. Suzuki, M. Ishihara, T. Yanagisawa, Y. Nemoto, and T. Goto, *J. Phys. Soc. Japan* **74**, 2169 (2005).
- [144] G. Will and W. Schäfer, *J. Less-Common Metals* **67**, 31 (1979).
- [145] L. I. Derkachenko, V. N. Gurin, and M. M. Korsukova, *J. Solid State Chem.* **133**, 296 (1997).
- [146] R. Schmitt, B. Blaschkowski, K. Eichele, and H. J. Meyer, *Inorg. Chem.* **45**, 3067 (2006).
- [147] D. R. Noakes, G. K. Shenoy, D. Niarchos, A. M. Umarji, and A. T. Aldred, *Phys. Rev. B* **27**, 4317 (1983).
- [148] P. C. Canfield, S. L. Bud'ko, B. K. Cho, W. P. Beyermann, and A. Yatskar, *J. Alloys & Compnds.* **250**, 596 (1997).
- [149] A. Kokalj, *Comp. Mater. Sci.* **28**, 155 (2003). The code is available from <http://www.xcrysden.org/>.

- [150] T. Lundström, *Pure & Appl. Chem.* **57**, 1383 (1985).
- [151] A. Vegas, L. A. Martinez-Cruz, A. Ramos-Gallardo, and A. Romero, *Z. f. Krist.* **210**, 574 (1995).
- [152] M. D. Johannes and W. E. Pickett, *Phys. Rev. B* **72**, 195116 (2005).
- [153] P. Larson, W. R. L. Lambrecht, A. Chantis, and M. van Schilfgaarde, *Phys. Rev. B* **75**, 045114 (2007).
- [154] J. Kuneš and W. E. Pickett, *J. Phys. Soc. Japan* **74**, 1408 (2005).
- [155] G. A. Wigger, F. Baumberger, and Z.-X. Shen, Z. P. Yin, W. E. Pickett, S. Maquilon, and Z. Fisk, *Phys. Rev. B* **76**, 035106 (2007).
- [156] G.R. Stewart, *Rev. Mod. Phys.* **73**, 797 (2001).
- [157] B. Bogenberger and H. v. Lohneysen, *Phys. Rev. Lett.* **74**, 1016 (1995).
- [158] F.M. Grosche, S.R. Julian, N.D. Mathur, and G.G. Lonzarich, *Physica B*, **223-224**, 50 (1996).
- [159] I.R. Walker, F.M. Grosche, D.M. Freye, and G.G. Lonzarich, *Physica C*, **282-287**, 303 (1997).
- [160] P. Estrella, A. de Visser, F. R. de Boer, G. J. Nieuwenhuys, L. C. J. Pereira, and M. Almeida, *Physica B* **259-261**, 409 (1999).
- [161] J. Kondo, *Prog. Theor. Phys.* **32**, 37 (1964).
- [162] M.A. Ruderman and C. Kittel, *Phys. Rev.* **96**, 99 (1954).
- [163] K. Ishida, D. E. MacLaughlin, O. O. Bernal, R. H. Heffner, G. J. Nieuwenhuys, O. Trovarelli, C. Geibel, and F. Steglich, *Physica B* **326**, 403 (2003).

- [164] O. Trovarelli, C. Geibel, S. Mederle, C. Langhammer, F.M. Grosche, P. Gegenwart, M. Lang, G. Sparn, and F. Steglich, *Phys. Rev. Lett.* **85**, 626 (2000).
- [165] P. Gegenwart, J. Custers, C. Geibel, K. Neumaier, T. Tayama, K. Tenya, O. Trovarelli, and F. Steglich, *Phys. Rev. Lett.* **89**, 056402 (2002).
- [166] O. Trovarelli, J. Custers, P. Gegenwart, C. Geibel, P. Hinze, S. Mederle, G. Sparn and F. Steglich, *Physica B* **312-313**, 401 (2002).
- [167] J. Custers, P. Gegenwart, H. Wilhelm, K. Neumaier, Y. Tokiwa, O. Trovarelli, C. Geibel, F. Steglich, C. Pépin and P. Coleman, *Nature* **424**, 524 (2003).
- [168] K. Ishida, K. Okamoto, Y. Kawasaki, Y. Kitaoka, O. Trovarelli, C. Geibel, and F. Steglich *Phys. Rev. Lett.* **89**, 107202 (2002).
- [169] S. Paschen, T. Luhmann, S. Wirth, P. Gegenwart, O. Trovarelli, C. Geibel, F. Steglich, P. Coleman, Q. Si, *Nature* **432**, 881 (2004).
- [170] M.R. Norman, *Phys. Rev. B* **71**, 220405(R) (2005).
- [171] Q. Si, S. Rabello, K. Ingersent and J.L. Smith, *Nature* **413**, 804 (2001).
- [172] S. Hüfner, *Photoelectron Spectroscopy* (Springer Verlag, Berlin, 1995).
- [173] P.W. Anderson, *Phys. Rev.* **124**, 41 (1961).
- [174] M.D. Johannes and W.E. Pickett, *Phys. Rev. B* **72**, 195116 (2005).
- [175] S. Danzenbächer, Y. Kucherenko, C. Laubschat, D.V. Vyalikh, Z. Hossain, C. Geibel, N. Mannella, X.J. Zhou, W. Yang, Z.-X. Shen and S.L. Molodstov, *Phys. Rev. B* **75**, 045109 (2007).

- [176] For other examples, consider K. Takegara and Y. Kaneta, *J. Phys. Soc. Jpn.* **60**, 4009 (1991); I. I. Mazin and S. L. Molodtsov, *Phys. Rev. B* **72**, 172504 (2005).
- [177] W. Meissner and R. Ochsenfeld, *Naturwiss.* **21**, 787 (1933).
- [178] H. Kamerlingh Onnes, *Leiden Comm.* **120b**, **122b**, **124c** (1911).
- [179] F. London and H. London, *Proc. Roy. Soc. (London)* **A149**, 71 (1935).
- [180] V. L. Ginzburg and L. D. Landau, *Zh. Eksp. Teor. Fiz.* **20**, 1064 (1950).
- [181] A. A. Abrikosov, *Zh. Eksp. Teor. Fiz.* **32**, 1442 (1957).
- [182] E. Maxwell, *Phys. Rev.* **78**, 477 (1950).
- [183] C. A. Reynolds, B. Serin, W. H. Wright, and L. B. Nesbitt, *Phys. Rev.* **78**, 487 (1950).
- [184] J. Bardeen, L. N. Cooper, and J. R. Schrieffer, *Phys. Rev.* **108**, 1175 (1957).
- [185] N. N. Bogoliubov, *Zh. Eksp. Teor. Fiz.* **34**, 58 (1958).
- [186] L. P. Gor'kov, *Zh. Eksp. Teor. Fiz.* **36**, 1918 (1959).
- [187] W. E. Pickett, *Physica C* **468**, 126 (2008).
- [188] J. G. Bednorz and K. A. Müller, *Z. Physik B* **64**, 189 (1986).
- [189] M. Wu, J. Ashburn, C. Torng, G. Peng, F. Szofran, P. Hor, and C. Chu, *Phys. Rev. Lett.* **58**, 908 (1987).
- [190] V. Z. Kresin, S. A. Wolf, *Rev. Mod. Phys.* **81**, 481 (2009).

- [191] Y. Kamihara, T. Watanabe, M. Hirano, and H. Hosono, *J. Amer. Chem. Soc.* **130**, 3296 (2008).
- [192] G. F. Chen, Z. Li, D. Wu, G. Li, W. Z. Hu, J. Dong, P. Zheng, J. L. Luo, and N. L. Wang, *Phys. Rev. Lett.* **100**, 247002 (2008).
- [193] Z.-A. Ren, J. Yang, W. Lu, W. Yi, G.-C. Che, X.-L. Dong, L.-L. Sun, and Z.-X. Zhao, *Materials Research Innovations* **12**, 105, (2008).
- [194] Z.-A. Ren, J. Yang, W. Lu, W. Yi, X.-L. Shen, Z.-C. Li, G.-C. Che, X.-L. Dong, L.-L. Sun, F. Zhao, and Z.-X. Zhao, *Europhys. Lett.* **82**, 57002 (2008).
- [195] X. H. Chen, T. Wu, G. Wu, R. H. Liu, H. Chen, and D. F. Fang, *Nature* **453**,761 (2008).
- [196] Z.-A. Ren, G.-C. Che, X.-L. Dong, J. Yang, W. Lu, W. Yi, X.-L. Shen, Z.-C. Li, L.-L. Sun, F. Zhou, and Z.-X. Zhao, *Europhys. Lett.* **83**, 17002 (2008).
- [197] P. Cheng, L. Fang, H. Yang, X. Zhu, G. Mu, H. Luo, Z. Wang, and H.-H. Wen, *Science in China G* **51**(6), 719-722 (2008).
- [198] J. Nagamatsu, N. Nakagawa, T. Muranaka, Y. Zenitani, and J. Akimitsu, *Nature* **410**, 63 (2001).
- [199] K. Shimizu, H. Kimura, D. Takao, and K. Amaya, *Nature* **419**, 597 (2002).
- [200] V. V. Struzhkin, M. I. Erements, W. Gan, H.-K. Mao, and R. J. Hemley, *Science* **298**, 1213 (2002).
- [201] S. Deemyad and J. S. Schilling, *Phys. Rev. Lett.* **91**, 167001 (2003).
- [202] J. J. Hamlin, V. G. Tissen, and J. S. Schilling, *Phys. Rev. B* **73**, 094522 (2006).

- [203] T. Yabuuchi, T. Matsuoka, Y. Nakamoto and K. Shimizu, *J. Phys. Soc. Jpn.*, **75**, 083703 (2006).
- [204] Z. P. Yin, S. Y. Savrasov, and W. E. Pickett, *Phys. Rev. B* **74**, 094519 (2006).
- [205] N. W. Ashcroft, *Nature* **419**, 569 (2002)
- [206] M. I. Eremets, V. V. Struzhkin, H.-K. Mao, R. J. Hemley, *Physica B* **329-333**, 1312 (2003).
- [207] J. S. Schilling, in *Treatise on High Temperature Superconductivity*, edited by J. R. Schrieffer (Springer-Verlag, Hamburg, 2006); cond-mat/0604090.
- [208] C. Buzea and K. Robbie, *Semicond. Sci. Technol.* **18**, R1 (2005) and reference therein.
- [209] N. W. Ashcroft, *Phys. Rev. Lett.* **21**, 1748 (1968).
- [210] K. A. Johnson, N. W. Ashcroft, *Nature* **403**, 632 (2003).
- [211] M. Stadelé, R. M. Martin, *Phys. Rev. Lett.* **84**, 6070 (2000).
- [212] H. Balster and J. Wittig, *J. Low Temp. Phys.* **21**, 377 (1975).
- [213] V. G. Tissen, E. G. Ponyatovskii, M. V. Nefedova, F. Porsch, and W. B. Holzapfel, *Phys. Rev. B* **53**, 8238 (1996).
- [214] W. E. Pickett, A. J. Freeman, D. D. Koelling, *Phys. Rev. B* **22**, 2695 (1980) and reference therein.
- [215] H. Wühl, A. Eichler, and J. Wittig, *Phys. Rev. Lett.* **31**, 1393 (1973).
- [216] M. Hanfland, I. Loa, K. Syassen, U. Schwarz, and K. Takemura, *Solid State Commun.* **112**, 123 (1999).

- [217] M. Hanfland, K. Syassen, N. E. Christensen, and D. L. Novikov, *Nature* **408**, 174 (2000).
- [218] Y. K. Vohra, H. Olijnik, W. Grosshans, and W. B. Holzapfel, *Phys. Rev. Lett.* **47**, 1065 (1981) and references therein.
- [219] W. A. Grosshans and W. B. Holzapfel, *Phys. Rev. B* **45**, 5171 (1992).
- [220] J. Wittig, *Phys. Rev. Lett.* **24**, 812 (1970).
- [221] J. Melsen, J. M. Wills, B. Johansson and O. Eriksson, *Phys. Rev. B* **48**, 15574 (1993).
- [222] F. H. Spedding, A. H. Daane and K. W. Herrmann, *Acta Cryst.* **9**, 599 (1956).
- [223] T. L. Loucks, *Phys. Rev.* **144**, 504 (1968).
- [224] S. J. Crowe, S. B. Dugdale, Zs. Major, M. A. Alam, J. A. Duffy and S. B. Palmer, *Europhys. Lett.* **65**, 235 (2004).
- [225] M. Ross and A. K. McMahan, *Phys. Rev. B* **26**, 4088 (1982).
- [226] S. K. sinha, T. O. Brun, L. D. Muhlestein, and J. Sakurai, *Phys. Rev. B* **1**, 2430 (1970).
- [227] G. Bergmann and D. Rainer, *Z. Physik A* **263**, 59 (1973).
- [228] Carbotte has argued that $\lambda\omega^2$ may be an even better indication of the coupling strength; see J. P. Carbotte, *Rev. Mod. Phys.* **62**, 1067 (1990) and references therein.
- [229] J.J. Hamlin and J.S. Schilling, *Phys. Rev. B* **76**, 012505 (2007).

- [230] G. Gaspari and B. L. Gyorffy, Phys. Rev. Lett. **28**, 801 (1972).
- [231] D. A. Papaconstantopoulos, L. L. Boyer, B. M. Klein, A. R. Williams, V. L. Morruzzi, and J. F. Janak, Phys. Rev. B **15**, 4221 (1977).
- [232] W. E. Pickett, Phys. Rev. B **25**, 745 (1982).
- [233] R. C. Dynes and J. M. Rowell, Phys. Rev. B **11**, 1884 (1975).
- [234] Z. P. Yin, F. Gygi, and W. E. Pickett, arXiv:0911.0040.
- [235] M. Debessai, J. J. Hamlin and J. S. Schilling, Phys. Rev. B **78**, 064519 (2008).
- [236] G. Profeta, C. Franchini, N. N. Lathiotakis, A. Floris, A. Sanna, M. A. L. Marques, M. Lüders, S. Massidda, E. K. U. Gross and A. Continenza, Phys. Rev. Lett. **96**, 047003 (2006).
- [237] P. P. Singh, Phys. Rev. B **75** 125101 (2007).
- [238] H. Olijnyk and W. B. Holzapfel, Phys. Lett. **100A**, 191 (1984).
- [239] A. V. Hippel, J. Chem. Phys., Vol. 16, No. 4, pp. 372 (1948).
- [240] W. H. Beamer and C. R. Maxwell, J. Chem. Phys., Vol. 17, No. 12, pp. 1293 (1949).
- [241] Z. P. Yin and W. E. Pickett, (2007, unpublished).
- [242] A. Bergara, (2007, unpublished).
- [243] A. M. Teweldeberhan and S. A. Bonev, Phys. Rev. B **78**, 140101(R) (2008).
- [244] S. Mizobata, T. Matsuoka and K. Shimizu, J. Phys. Soc. Jpn. **76**, 23 (2007).

- [245] A. Phusittrakool, T. Bovornratanaraks, R. Ahuja, and U. Pinsook, Phys. Rev. B **77**, 174118 (2008).
- [246] T. Bovornratanaraks, D. R. Allan, S. A. Belmonte, M. I. McMahon, and R. J. Nelmes, Phys. Rev. B **73**, 144112 (2006).
- [247] M. I. McMahon, T. Bovornratanaraks, D. R. Allan, S. A. Belmonte, and R. J. Nelmes, Phys. Rev. B **61**, 3135 (2000).
- [248] Y. C. Zhao, F. Porsch, and W. B. Holzapfel, Phys. Rev. B **54**, 9715 (1996).
- [249] M. Debessai, J. J. Hamlin, and J. S. Schilling, Phys. Rev. B **78**, 064519 (2008).
- [250] T. Yabuuchi, Y. Nakamoto, K. Shimizu and T. Kikegawa, J. Phys. Soc. Jpn., **74**, 2391 (2005).
- [251] H. Fujihisa, Y. Nakamoto, K. Shimizu, T. Yabuuchi and Y. Gotoh, Phys. Rev. Lett. **101**, 095503 (2008).
- [252] Y. Yao, J. S. Tse, Z. Song, D. D. Klug, J. Sun and Y. LePage, Phys. Rev. B **78**, 054506 (2008).
- [253] T. Ishikawa, A. Ichikawa, H. Nagara, M. Geshi, K. Kusakabe and N. Suzuki, Phys. Rev. B **77**, 020101(R) (2008).
- [254] S. Arapan, H.-K. Mao, and R. Ahuja, PNAS **105**, 20627 (2008).
- [255] R. Ahuja, O. Eriksson, J. M. Wills and B. Johansson, Phys. Rev. Lett. **75**, 3473 (1995).
- [256] J. Ruvalds and C. M. Soukoulis, Phys. Rev. Lett. **43**, 1263 (1979).

- [257] N. Y. Fogel, E. I. Buchstab, A. S. Pokhila, A. I. Erenburg, and V. Langer, Phys. Rev. B **53**, 71 (1996).
- [258] Y. P. Krasny and N.P. Kovalenko, Physica B **162**, 128 (1990).
- [259] F. Gygi, <http://eslab.ucdavis.edu/>.
- [260] S. Lei, D. A. Papaconstantopoulos and M. J. Mehl, Phys. Rev. B **75**, 024512 (2007).
- [261] T. Matsuoka, S. Onoda, M. Kaneshige, Y. Nakamoto, K. Shimizu, T. Kagayama and Y. Ohishi, J. Phys: Conf. Ser. **121**, 052003 (2008).
- [262] H. Hanfland, K. Syassen, N. E. Christensen and D. L. Novikov, Nature **408**, 174 (2000).
- [263] T. N. Kolobyanina, Phys. Usp. **45**, 1203 (2002).
- [264] D. Kasinathan, K. Koepernik, J. Kunes, H. Rosner, and W. E. Pickett, Physics C **460-462**, 133 (2007).
- [265] W. E. Pickett, Phys. Rev. B **25**, 745 (1982).
- [266] M. J. Geselbracht, T. J. Richardson, and A. M. Stacy, Nature **345**, 324 (1990).
- [267] Y. Maeno, H. Hashimoto, K. Yoshida, S. Nishizaki, T. Jujita, J. G. Bednorz, and F. Lichtenberg, Nature **372**, 532 (1994).
- [268] K. Takada, H. Sakurai, E. Takayama-Muromachi, F. Izumi, R. A. Dilanian, and T. Sasaki, Nature **422**, 53 (2003).

- [269] E. Morosan, H. W. Zandbergen, B. S. Dennis, J. W. G. Bos, Y. Onose, T. Klimczuk, A. P. Ramirez, N. P. Ong, and R. J. Cava, *Nature Phys.* **2**, 544 (2006).
- [270] S. Yamanaka, K.-I. Hotehama, and H. Kawaji, *Nature* **392**, 580 (1998).
- [271] J. Chaloupka and G. Khaliullin, *Phys. Rev. Lett.* **100**, 016404 (2008).
- [272] H.-H. Wen, G. Mu, L. Fang, H. Yang, and X. Zhu, *Europhys. Lett.* **82**, 17009 (2008).
- [273] C. Wang, L.-J. Li, S. Chi, Z.-W. Zhu, Z. Ren, Y.-K. Li, Y.-T. Wang, X. Lin, Y.-K. Luo, S. Jiang, X.-F. Xu, G.-H. Cao, and Z.-A. Xu, *Europhys. Lett* **83**, 67006 (2008).
- [274] Z.-A. Ren, W. Lu, J. Yang, W. Yi, X.-L. Shen, Z.-C. Li, G.-C. Che, X.-L. Dong, L.-L. Sun, F. Zhou, and Z.-X. Zhao, *Chin. Phys. Lett.* **25**, 2215 (2008).
- [275] M. Rotter, M. Tegel, and D. Johrendt, *Phys. Rev. Lett.* **101**, 107006 (2008).
- [276] K. Sasmal, B. Lv, B. Lorenz, A. M. Guloy, F. Chen, Y. Y. Xue, and C. W. Chu, *Phys. Rev. Lett.* **101**, 107007 (2008)
- [277] M. S. Torikachvili, S. L. Bud'ko, N. Ni, and P. C. Canfield, *Phys. Rev. Lett.* **101**, 057006 (2008).
- [278] J. H. Tapp, Z. J. Tang, B. Lv, K. Sasmal, B. Lorenz, P. C.W. Chu, and A. M. Guloy, *Phys. Rev. B* **78**, 060505(R) (2008).
- [279] D. R. Parker, M. J. Pitcher, P. J. Baker, I. Franke, T. Lancaster, S. J. Blundell, and S. J. Clarke, *Chem. Commun. (Cambridge)* (**2009**), 2189.

- [280] S. Matsuishi, Y. Inoue, T. Nomura, M. Hirano, and H. Hosono, *J. Phys. Soc. Jpn.* **77**, 113709 (2008).
- [281] C. de la Cruz, Q. Huang, J. W. Lynn, J. Li, W. Ratcliff, J. L. Zarestsky, H. A. Mook, C. F. Chen, J. L. Luo, N. L. Wang, and P. Dai, *Nature* **453**, 899 (2008).
- [282] M. A. McGuire, A. D. Christenson, A. S. sefat, R. Jin, E. A. Payzant, B. C. Sales, M. D. Lumsden, and D. Mandrus, *Phys. Rev. B* **78**, 094517 (2008).
- [283] K. Kitagawa, N. Katayama, K. Ohgushi, M. Yoshida, and M. Takigawa, *J. Phys. Soc. Jpn.* **77**, 114709 (2008).
- [284] S.-H. Baek, N. J. Curro, T. Klimczuk, E. D. Bauer, F. Ronning, and J. D. Thompson, *Phys. Rev. B* **79**, 052504 (2009).
- [285] Z. P. Yin, S. Lebègue, M. J. Han, B. P. Neal, S. Y. Savrasov, and W. E. Pickett, *Phys. Rev. Lett.* **101**, 047001 (2008).
- [286] T. Yildirim, *Phys. Rev. Lett.* **101**, 057010 (2008).
- [287] I. I. Mazin, D. J. Singh, M. D. Johannes, and M. H. Du, *Phys. Rev. Lett.* **101**, 057003 (2008).
- [288] Y. Nagai, N. Hayashi, N. Nakai, H. Nakamura, M. Okumura, and M. Machida, *New J. Phys.* **10**, 103026 (2008).
- [289] R. H. Liu, T. Wu, G. Wu, H. Chen, X. F. Wang, Y. L. Xie, J. J. Yin, Y. J. Yan, Q. J. Li, B. C. Shi, W. S. Chu, Z. Y. Wu, and X. H. Chen, *Nature* **459**, 64 (2009).
- [290] M. Aichhorn, L. Pourovskii, V. Vildosola, M. Ferrero, O. Parcollet, T. Miyake, A. Georges, and S. Biermann, *Phys. Rev. B* **80**, 085101 (2009).

- [291] S. Lebègue, Z. P. Yin, and W. E. Pickett, *New Journal of Physics* **11**, 025004 (2009).
- [292] A. S. Sefat, M. A. McGuire, B. C. Sales, R. Jin, J. Y. Howe, and D. Mandrus, *Phys. Rev. B* **77**, 174503 (2008).
- [293] T. Watanabe, H. Yanagi, T. Kamiya, Y. Kamihara, H. Hiramatsu, M. Hirano, and H. Hosono, *Inorg. Chem.* **46**, 7719 (2007).
- [294] S. Lebègue, *Phys. Rev. B* **75**, 035110 (2007).
- [295] D. J. Singh and M.-H. Du, *Phys. Rev. Lett.* **100**, 237003 (2008).
- [296] H.-J. Zhang, G. Xu, X. Dai, and Z. Fang, *Chin. Phys. Lett.* **26**, 017401 (2009).
- [297] X. Han, Y. Chen, and Z. D. Wang, *Europhys. Lett.* **82**, 37007 (2008).
- [298] X. Dai, Z. Fang, Y. Zhou, and F.-C. Zhang, *Phys. Rev. Lett.* **101**, 057008 (2008).
- [299] K. Kuroki, S. Onari, R. Arita, H. Usui, Y. Tanaka, H. Kontani, and H. Aoki, *Phys. Rev. Lett.* **101**, 087004 (2008).
- [300] C. Cao, P. J. Hirschfeld, and H.-P. Cheng, *Phys. Rev. B* **77**, 220506(R) (2008).
- [301] F. Ma and Z.-Y. Lu, *Phys. Rev. B* **78**, 033111 (2008).
- [302] T. Li, *J. Phys.: Condens. Matter* **20**, 425203 (2008).
- [303] Y. Tsujimoto, C. Tassel, N. Hayashi, T. Watanabe, H. Kageyama, K. Yoshimura, M. Takano, M. Ceretti, C. Ritter, and W. Paulus, *Nature* **450**, 1062 (2007).

- [304] J. Dong, H. J. Zhang, G. Xu, Z. Li, G. Li, W. Z. Hu, D. Wu, G. F. Chen, X. Dai, J. L. Luo, Z. Fang, and N. L. Wang, *Europhys. Lett.* **83**, 27006 (2008).
- [305] B. I. Zimmer, W. Jeitschko, J. H. Albering, R. Glaum, and M. Reehuis, *J. Alloy Comp.* **229**, 238 (1995).
- [306] P. Quebe, L. J. Terbuchte, and W. Jeitschko, *J. Alloy Comp.* **302**, 70 (2000).
- [307] R. Weht, A. Filipetti, and W. E. Pickett, *Europhys. Lett.* **48**, 320 (1999).
- [308] L. Boeri, O. V. Dolgov, and A. A. Golubov *Phys. Rev. Lett.* **101**, 026403 (2008).
- [309] H. Eschrig, arXiv:0804.0186.
- [310] A. I. Liechtenstein, M. I. Katsnelson, V. P. Antropov, and V. A. Gubanov, *J. Magn. Magn. Mat.* **67**, 65 (1987).
- [311] X. Wan, Q. Yin, and S. Y. Savrasov, *Phys. Rev. Lett.* **97**, 266403 (2006).
- [312] S. Ishibashi, K. Terakura, and H. Hosono, *J. Phys. Soc. Jpn.* **77**, 053709 (2008).
- [313] F. Ma, Z.-Y. Lu, and T. Xiang, *Phys. Rev. B* **78**, 224517 (2008).
- [314] I. I. Mazin, M. D. Johannes, L. Boeri, K. Koepernik, and D. J. Singh, *Phys. Rev. B* **78**, 085104 (2008).
- [315] H.-J. Grafe, D. Paar, N. J. Curro, G. Behr, J. Werner, J. Hamann-Borrero, C. Hess, N. Leps, R. Klingeler, and B. Büchner, *Phys. Rev. Lett.* **101**, 047003 (2008).
- [316] H. Takahashi, K. Igawa, K. Arii, Y. Kamihara, M. Hirano, and H. Hosono, *Nature* **453**, 376 (2008).

- [317] W. Lu, J. Yang, X. L. Dong, Z. A. Ren, G. C. Che, and Z. X. Zhao, *New Journal of Physics* **10**, 063026 (2008).
- [318] B. Lorenz, K. Sasmal, R. P. Chaudhury, X. H. Chen, R. H. Liu, T. Wu, and C. W. Chu *Phys. Rev. B* **78**, 012505 (2008).
- [319] Y. Kamihara, H. Hiramatsu, M. Hirano, R. Kawamura, H. Yanagi, T. Kamiya, and H. Hosono, *J. Am. Chem. Soc.* **128**, 10012 (2006).
- [320] C. Y. Liang, R. C. Che, H. X. Yang, H. F. Tian, R. J. Xiao, J. B. Lu, R. Li, and J. Q. Li *Supercond. Sci. Technol.* **20**, 687 (2007).
- [321] M. Tegel, I. Schellenberg, R. Pttgen, and D. Johrendt *Z. Naturforsch. B - Chem. Sci.* **63**, 1057 (2008).
- [322] J. J. Hamlin, R. E. Baumbach, D. A. Zocco, T. A. Sayles, and M. B. Maple, *J. Phys.: Condens. Matter* **20**, 365220 (2008).
- [323] T. M. McQueen, M. Regulacio, A. J. Williams, Q. Huang, J. W. Lynn, Y. S. Hor, D. V. West, M. A. Green, and R. J. Cava *Phys. Rev. B* **78**, 024521 (2008).
- [324] J. G. Analytis, J.-H. Chu, A. S. Erickson, C. Kucharczyk, A. Serafin, A. Carrington, C. Cox, S. M. Kauzlarich, H. Hope, and I. R. Fisher, arXiv:0810.5368 (2008).
- [325] T. Nomura, S. W. Kim, Y. Kamihara, M. Hirano, P. V. Sushko, K. Kato, M. Takata, A. L. Shluger, and H. Hosono, *Supercond. Sci. Technol.* **21**, 125028 (2008).

- [326] Y. Ishida, T. Shimojima, K. Ishizaka, T. Kiss, M. Okawa, T. Togashi, S. Watanabe, X.-Y. Wang, C.-T. Chen, Y. Kamihara, M. Hirano, H. Hosono, and S. Shin Phys. Rev. B **79**, 060503(R) (2009).
- [327] W. Malaeb, T. Yoshida, T. Kataoka, A. Fujimori, M. Kubota, K. Ono, H. Usui, K. Kuroki, R. Arita, H. Aoki, Y. Kamihara, M. Hirano, and H. Hosono, J. Phys. Soc. Jpn. **77**, 093714 (2008).
- [328] D. H. Lu, M. Yi, S.-K. Mo, A. S. Erickson, J. Analytis, J.-H. Chu, D. J. Singh, Z. Hussain, T. H. Geballe, I. R. Fisher, and Z.-X. Shen, Nature **455**, 81 (2008).
- [329] Y. Kamihara, M. Hirano, H. Yanagi, T. Kamiya, Y. Saitoh, E. Ikenaga, K. Kobayashi, and H. Hosono, Phys. Rev. B **77**, 214515 (2008).
- [330] R. C. Che, R. J. Xiao, C. Y. Liang, H. X. Yang, C. Ma, H. L. Shi, and J. Q. Li, Phys. Rev. B **77**, 184518 (2008).
- [331] J.-W. G. Bos, G. B. S. Penny, J. A. Rodgers, D. A. Sokolov, A. D. Huxley, and J. P. Attfield, Chem. Commun. **31**, 3634 (2008).
- [332] L.-J. Li, Y.-K. Li, Z. Ren, Y.-K. Luo, X. Lin, M. He, Q. Tao, Z.-W. Zhu, G.-H. Cao, and Z.-A. Xu, Phys. Rev. B **78**, 132506 (2008).
- [333] Z. P. Yin and W. E. Pickett, Phys. Rev. B **80**, 144522 (2009).
- [334] K. Haule, J. H. Shim, and G. Kotliar, Phys. Rev. Lett. **100**, 226402 (2008).
- [335] Y. Su, P. Link, A. Schneidewind, T. Wolf, P. Adelmann, Y. Xiao, M. Meven, R. Mittal, M. Rotter, D. Johrendt, T. Brueckel, and M. Loewenhaupt, Phys. Rev. B **79**, 064504 (2009).

- [336] J. Zhao, W. Ratcliff, J. W. Lynn, G. F. Chen, J. L. Luo, N. L. Wang, J. Hu, and P. Dai, Phys. Rev. B **78**, 140504 (R) (2008).
- [337] A. I. Goldman, D.N. Argyriou, B. Ouladdiaf, T. Chatterji, A. Kreyssig, S. Nandi, N. Ni, S. L. Bud'ko, P. C. Canfield, and R. J. McQueeney, Phys. Rev. B **78**, 100506(R) (2008).
- [338] M. D. Johannes and I. I. Mazin, Phys. Rev. B **79**, 220510(R) (2009).
- [339] S. Kitao, Y. Kobayashi, S. Higashitaniguchi, M. Saito, Y. Kamihara, M. Hirano, T. Mitsui, H. Hosono, and M. Seto, J. Phys. Soc. Jpn. **77** 103706 (2008)
- [340] H.-H. Klauss, H. Luetkens, R. Klingeler, C. Hess, F.J. Litterst, M. Kraken, M. M. Korshunov, I. Eremin, S.-L. Drechsler, R. Khasanov, A. Amato, J. Hamann-Borro, N. Leps, A. Kondrat, G. Behr, J. Werner, and B. Buechner, Phys. Rev. Lett. **101**, 077005 (2008).
- [341] I. Nowik, I. Felner, V. P. S. Awana, A. Vajpayee, and H. Kishan, J. Phys.: Condens. Matter **20**, 292201 (2008).
- [342] I. Nowik and I. Felner, J. Supercond. Nov. Magn. **21**, 297 (2008).
- [343] M. Rotter, M. Tegel and D. Johrendt, I. Schellenberg, W. Hermes, and R. Pöttgen, Phys. Rev. B **78**, 020503(R) (2008).
- [344] M. Tegel, M. Rotter, V. Weiss, F. M. Schappacher, R. Poettgen, and D. Johrendt, J. Phys.: Condens. Matter **20**, 452201 (2008).
- [345] M. Tegel, S. Johansson, V. Weiss, I. Schellenberg, W. Hermes, R. Poettgen, and D. Johrendt, Europhys. Lett. **84**, 67007 (2008).

- [346] A. J. Drew, Ch. Niedermayer, P. J. Baker, F. L. Pratt, S. J. Blundell, T. Lancaster, R. H. Liu, G. Wu, X. H. Chen, I. Watanabe, V. K. Malik, A. Dubroka, M. Röessle, K. W. Kim, C. Baines, and C. Bernhard, *Nature Mater.* **8**, 310 (2009).
- [347] W. Z. Hu, J. Dong, G. Li, Z. Li, P. Zheng, G. F. Chen, J. L. Luo, and N. L. Wang, *Phys. Rev. Lett.* **101**, 257005 (2008).
- [348] K. Matan, R. Morinaga, K. Iida, and T. J. Sato, *Phys. Rev. B* **79**, 054526 (2009).
- [349] R. A. Ewings, T. G. Perring, R. I. Bewley, T. Guidi, M. J. Pitcher, D. R. Parker, S. J. Clarke, and A. T. Boothroyd, *Phys. Rev. B* **78**, 220501(R) (2008).
- [350] I. I. Mazin and M. D. Johannes, *Nature Physics* **5**, 141 (2009).
- [351] K. Ishida, Y. Nakai, H. Hosono, *J. Phys. Soc. Jpn.* **78**, 062001 (2009).
- [352] F. Bondino, E. Magnano, M. Malvestuto, F. Parmigiani, M. A. McGuire, A. S. Sefat, B. C. Sales, R. Jin, D. Mandrus, E. W. Plummer, D. J. Singh, and N. Mannella, *Phys. Rev. Lett.* **101**, 267001 (2008).
- [353] J. Dai, Z. Y. Li, J. L. Yang, and J. G. Hou, arXiv:0808.0065 (2008).
- [354] M. D. Johannes, private communication (2009).
- [355] C.-C. Lee, W.-G. Yin, and W. Ku, arXiv:0905.2957 (2009).
- [356] K. Haule and G. Kotliar, *New J. Phys.* **11**, 025021 (2009).